



UNIVERSITY OF
BIRMINGHAM

MODELLING AND OPTIMIZATION OF HIGH TEMPERATURE DIFFERENCE (HTD) GAMMA- TYPE STIRLING ENGINE PROTOTYPE

By

Suliman Alfarawi

*A thesis submitted to the
University of Birmingham for the*

Degree of Doctor of Philosophy

School of Mechanical Engineering
College of Engineering and Physical Sciences
The University of Birmingham
September - 2017

UNIVERSITY OF
BIRMINGHAM

University of Birmingham Research Archive

e-theses repository

This unpublished thesis/dissertation is copyright of the author and/or third parties. The intellectual property rights of the author or third parties in respect of this work are as defined by The Copyright Designs and Patents Act 1988 or as modified by any successor legislation.

Any use made of information contained in this thesis/dissertation must be in accordance with that legislation and must be properly acknowledged. Further distribution or reproduction in any format is prohibited without the permission of the copyright holder.

ABSTRACT

Finding solutions for increasing energy demands is being globally pursued. One of the promising solutions is the utilization of renewable forms of energy with thermo-mechanical conversion systems such as Stirling engines. Nowadays, effort is made in industry and academia to promote the development of Stirling technology. In this context, this thesis was first focused on modelling of High Temperature Difference (HTD) gamma-type Stirling engine prototype (ST05-CNC) and investigating means of improving its performance. Secondly, newly parallel-geometry mini-channel regenerators (with hydraulic diameters of 0.5, 1, 1.5 mm) and their test facility were developed and fabricated to enhance engine performance.

Both thermodynamic and CFD models were comprehensively developed to simulate the engine and have been successfully validated against experimental data. The modified second-order analysis with different thermal, frictional and mechanical losses was adopted in the thermodynamic model. The CFD model was based on a combined approach of dynamic meshing of compression and expansion spaces, non-isothermal flow modelling in free flow domains and non-equilibrium thermal modelling in porous domains of the engine such as regenerator and cooler. The simulation results showed that the performance of the engine can be improved with a minimum alteration of the current layout by the following;

- At speeds up to 500 rpm, there is no significant difference in generated power using helium and nitrogen. However, helium tends to increase engine shaft power at higher speeds (712W at 1100 rpm) while the power generated using nitrogen is totally decayed.
- Reducing the connecting pipe diameter from 30mm to 15mm can enhance the shaft power by up to 20% as the dead volume is reduced by 75%.

- Although the shaft power can be increased by 5% when the phase angle is increased from 90° to 105°, phase angle can be adjusted to normally 90° for practical reasons.
- The heater tube diameter can be kept as 6mm as the original layout. Degradation of engine performance occurs at values far from this value due to reduction in surface area or the increase in heater dead volume.

Theoretically, engine power can be increased by maximizing the operational temperature difference between the heat source and sink. The feasibility of utilizing the cryogenic energy storage using surplus electricity or renewable energy sources to maximize the shaft power was investigated. It was found that lowering the cooling temperature -50 °C can enhance the shaft power by 49% for helium reaching 1000 W and 35% for Nitrogen reaching 700 W.

A combined approach based on experiment and CFD as an alternative to single-blow method was used to investigate heat transfer and flow friction in three fabricated mini-channel regenerators fabricated using 3D printing technology. It was found that the 0.5mm channel regenerator had the highest interstitial heat transfer coefficient compared to other investigated configurations due to the increased surface area of the matrix. On the other hand, using materials with higher heat capacity and lower thermal conductivity such as ceramic ZrO₂ and Monel 400 can have good potential to generate power compared to random fibre.

ACKNOWLEDGEMENTS

My sincere thanks and gratitude are due to my **ALMIGHTY, ALLAH**, who helped and blessed me.

To my wife, **Nagat** and my daughters, **Mariem, Sajeda** and **Retaj**: because I owe it all to you.

Many Thanks!

For their supervision, valuable guidance, and continues support during my PhD research, I extend my sincere thanks to:

Dr. Raya Al-Dadah and Dr. Saad Mahmoud

I would like to thank Mr Simon Rowan for helping me to construct my test rig and for his continuous assessment and commissioning of the test facilities.

I would like to thank all my family and friends for their moral support during my PhD study.

CONTENTS

ABSTRACT	I
ACKNOWLEDGEMENTS	III
CONTENTS	IV
LIST OF FIGURES.....	VIII
LIST OF TABLES.....	XII
NOMENCLATURE	XIII
LIST OF PUBLICATIONS	XVII
CHAPTER 1.....	1
INTRODUCTION	1
1.1 Introduction.....	1
1.2 Stirling cycle engine history	1
1.3 Theoretical cycle.....	4
1.4 Real cycle of Stirling engine.....	6
1.4.1 Real motion	6
1.4.2 Leakage of working fluid	7
1.4.3 Pumping and mechanical losses	8
1.4.4 Real gas and turbulence	8
1.4.5 Dead spaces	9
1.4.6 Real heat exchangers	9
1.4.7 Thermal losses	10
1.5 Engine configurations	10
1.6 Engine heat exchangers	12
1.6.1 Heater.....	12
1.6.2 Cooler	14
1.6.3 Regenerator.....	15
1.7 Stirling engine applications	16
1.7.1 Solar power generation.....	16
1.7.2 Computer chip cooling	17
1.7.3 Stirling engine powered submarines	18
1.7.4 Domestic heat and power	19
1.7.5 Stirling engine powered automobiles	20
1.7.6 Stirling cryocooler	21

1.8	Motivation.....	22
1.9	Aims and objectives and thesis structure	23
CHAPTER 2.....		27
LITERATURE REVIEW		27
2.1	Introduction.....	27
2.2	Review of different analysis approaches	27
2.2.1	Zeroth-order analysis	29
2.2.2	First-order analysis	29
2.2.3	Second-order analysis.....	34
2.2.4	Third-order analysis.....	41
2.2.5	Fourth-order analysis	43
2.3	Review of previous experimental work	48
2.4	Review on transient testing techniques of heat exchangers.....	53
2.5	Summary and knowledge gap	57
CHAPTER 3.....		59
EXPERIMENTAL TEST FACILITY OF THE RESEARCH ENGINE.....		59
3.1	Introduction.....	59
3.2	Engine description	59
3.3	Instrumentations and performance analysis.....	64
3.4	Uncertainty analysis.....	68
CHAPTER 4.....		71
ENGINE THERMODYNAMIC MODELLING		71
4.1	Introduction.....	71
4.2	Thermodynamic model	72
4.3	Derivation of real volume variation.....	73
4.4	Ideal adiabatic model	75
4.5	Losses consideration	79
4.6	Method of solution.....	85
4.7	Model validation	87
4.8	Summary.....	91
CHAPTER 5.....		92
ENGINE CFD MODELLING		92
5.1	Introduction.....	92
5.2	Heat transfer in porous media	92
5.2.1	Local thermal equilibrium	92

5.2.2	Local thermal non-equilibrium.....	94
5.3	Moving mesh	96
5.4	Linear translation	97
5.5	Governing equations	99
5.6	Permeability, Forchheimer Drag Coefficient and Nusselt number.....	103
5.6.1	Regenerator.....	103
5.6.2	Cooler	104
5.7	Meshing sequence.....	107
5.8	Boundary Conditions and Solution Scheme	109
5.9	Model Validation	110
5.9.1	Replication of a previously published work ‘CFD Simulation of porous regenerative displacer LTD Stirling engine’	110
5.9.2	Validation with experimental data of the engine under research	112
5.10	Summary	114
CHAPTER 6.....		116
DEVELOPMENT OF CHANNEL REGENERATORS.....		116
6.1	Introduction.....	116
6.2	Conventional and parallel-geometry regenerators	116
6.3	Mini-channel regenerator.....	117
6.4	CFD model.....	121
6.5	Fluid flow and heat transfer in channels	121
6.6	Governing equations and solution methodology	125
6.7	Regenerator modelling.....	131
6.8	Regenerator test facility	136
6.9	Theoretical model for transient testing method	141
6.10	Data analysis and uncertainty	147
6.11	Summary	148
CHAPTER 7.....		150
RESULTS AND DISCUSSION.....		150
7.1	Introduction.....	150
7.2	Results of thermodynamic model	150
7.3	Parametric study of developed thermodynamic model.....	155
7.3.1	Effect of phase angle	155
7.3.2	Effect of regenerator matrix type.....	155
7.3.3	Effect of gas type.....	156

7.3.4	Effect of low temperature cooling	157
7.3.5	Effect of dead volume (connecting pipe)	159
7.3.6	Effect of heater tube diameter	160
7.4	Results of engine 2D CFD model	161
7.5	Parametric study using the developed CFD model.....	168
7.5.1	Effect of phase angle	168
7.5.2	Effect of dead volume (connecting pipe)	172
7.5.3	Effect of regenerator porosity.....	175
7.6	3D half engine CFD modelling.....	176
7.7	3D engine sector CFD modelling	179
7.8	Results of channel regenerators	182
7.8.1	Transient testing method results	182
7.8.2	Engine performance with mini-channel regenerators.....	191
7.8.3	Summary.....	196
CHAPTER 8.....		197
CONCLUSIONS AND RECOMMENDATIONS		197
REFERENCES		201
APPENDIX A.....		213
APPENDIX B.....		215

LIST OF FIGURES

Figure 1.1 Model of hot-air engine built by Robert Stirling in 1816 to prove his idea [1].	2
Figure 1.2 Stirling’s improved engine [3].	3
Figure 1.3 Ideal thermodynamic cycle representation, a) PV diagram. b) TS diagram.	4
Figure 1.4 Stirling and Carnot cycle [7].	6
Figure 1.5 Motion diagram of a gamma-configuration Stirling engine, a) ideal, b) real [7].	7
Figure 1.6 Engine components and configurations [9].	11
Figure 1.7 Drive mechanisms, (a): yoke drive, (b): rhombic drive, (c): crank drive [10].	11
Figure 1.8 Stirling engine heater types, (a) annular [10], (b) tubular [13], (c) finned [14].	13
Figure 1.9 Typical cooling arrangement in the Stirling engine [10].	14
Figure 1.10 Stirling regenerator configurations, a) woven screen [20], b) random fibre [19], c) wrapped-foil [10], d) metal foam [21].	15
Figure 1.11 Solar-powered Stirling engine [24].	17
Figure 1.12 Chip cooling by Stirling engine [26].	18
Figure 1.13: Stirling engine-powered submarine [27].	18
Figure 1.14 Stirling engine powered CHP [28].	19
Figure 1.15 Stirling engine powered automobiles [29].	20
Figure 1.16 Stirling cryocooler [30].	21
Figure 2.1 Different categories for Stirling engine analysis.	28
Figure 2.2 Stirling engine research percentage in open literature of the three types.	28
Figure 2.3 Overview of thesis structure.	24
Figure 3.1 Engine components: 1-Heater, 2-Displacer piston, 3-Regenerator, 4-Cooler, 5-Connecting pipe, 6-Power piston.	60
Figure 3.2 Electrical heater hood (EHH70).	61
Figure 3.3 Cooler of the engine.	62
Figure 3.4 Regenerator of the engine	63
Figure 3.5 Thermocouples positions of the test engine, a) actual, b) schematic.	64
Figure 3.6 Pressure sensor location.	65
Figure 3.7 whole test facility of the engine.	66
Figure 3.8 LabVIEW experimental data screen-shot.	67
Figure 4.1 Reconfigured adiabatic model with six engine cells.	72
Figure 4.2 Sketch of conventional crank mechanism.	73
Figure 4.3 Regenerator temperature profile.	76
Figure 4.4 Schematic diagram of forced work [134].	83
Figure 4.5: Flow chart of the developed algorithm.	86
Figure 4.6 Comparison of indicated PV diagrams between the model and experiment at fixed charge pressure (10bar) and different heater temperatures, (a) at 450 °C and (b) at 650 °C. .	87
Figure 4.7 Comparison of indicated PV diagrams between the model and experiment at Fixed heater temperature (650 °C) and different charge pressures, (a) at 4 bar and (b) at 10 bar.	88
Figure 4.8 Comparison of N ₂ results between the present model and experiment at constant charge pressure (10 bar) and different heater temperatures, (a) shaft power and (b) engine efficiency.	89

Figure 4.9 Comparison of N ₂ results between the present model and experiment at constant heater temperature (650 °C) and different charge pressures, (a) shaft power and (b) engine efficiency.	90
Figure 4.10 Comparison of N ₂ results of shaft power versus engine speed between the present model and experiment at constant charge pressure (10 bar) and different heater temperatures (450 °C and 650 °C).	91
Figure 5.1 Motion of solid object along a linear path inside a complicated domain [148].	98
Figure 5.2 The temperature fields of a moving object and its surrounding over time [148].	99
Figure 5.3 Porous media domains, (a) regenerator, (b) cooler.	100
Figure 5.4 Velocity contours inside a sector of the real engine cooler.	105
Figure 5.5 Pressure contours inside a sector of the real engine cooler.	105
Figure 5.6 Temperature contours inside a sector of the real engine cooler.	105
Figure 5.7 Pressure drop through cooler using steady state simulations.	106
Figure 5.8 The 2D computational domain of the engine.	107
Figure 5.9: Meshing of engine domains.	108
Figure 5.10 LTD gamma-type Stirling engine.	110
Figure 5.11 Temperature contours of the simulated engine during the 10 th cycle.	111
Figure 5.12 Comparison of CFD results and experiment.	111
Figure 5.13 Effect of regenerator porosity on indicated PV diagram.	112
Figure 5.14 Comparison of indicated PV diagrams between CFD model and experiment at normal operating conditions.	113
Figure 5.15 Comparison between CFD model and experimental results at constant charge pressure (10 bar) and different heater temperature, (a) indicated power and (b) cooling power.	114
Figure 6.1 Conceptual design of mini-channel regenerator.	118
Figure 6.2 Thermal penetration depth vs. engine speed.	119
Figure 6.3 Geometrical parameters of channels regenerator.	119
Figure 6.4 Radial pitch definition in terms of regenerator parameters (not to scale).	120
Figure 6.5 The developing velocity profile of a fluid entering a tube [133].	122
Figure 6.6 The developing temperature profile of a fluid entering a tube [133].	123
Figure 6.7 Computational domain of the tube.	126
Figure 6.8 Meshing sequence, a) coarse, b) normal, c) fine and d) finer, e) extra-fine.	127
Figure 6.9 Velocity contours (m/s) along the tube.	128
Figure 6.10 Sectional velocity contours (m/s) at different positions of the pipe.	128
Figure 6.11 Temperature contours (K) along the tube.	128
Figure 6.12 Sectional temperature contours (K) at different positions of the pipe.	129
Figure 6.13 Pressure contours along the tube.	129
Figure 6.14 Nusselt number for laminar developing pipe flow.	130
Figure 6.17 Temperature contours for 1.5mm channels regenerator at speed of 100 rpm and time of 30s.	132
Figure 6.18 Temperature contours for 1.5mm channels regenerator at speed of 1000 rpm and time of 30s.	132
Figure 6.19 Pressure loss per unit length vs. maximum gas inlet velocity to the regenerator for different channels regenerators.	133
Figure 6.20 Darcy friction factor vs. Reynolds number for different channels regenerators.	134
Figure 6.21 Nusselt number vs. Reynolds number for different channels regenerators.	135

Figure 6.22 3D printed 0.5mm MCRHX.....	136
Figure 6.23 schematic of experimental test facility.....	137
Figure 6.24 Test section components, (a) Heater, (b) Anemometer, (c) Variac transformer, (d) Conical converter, (e) Housing cylinder, (f) MCRHX and filler assembly, (g) Assembled test section, (h) Data logger and (i) Inclined micromanometer.	139
Figure 6.25 Positions of thermocouples at inlet and outlet of MCRHX.	140
Figure 6.26: Computational domain of 3D sector of the heat exchanger.....	144
Figure 7.1 Variation of total, expansion, compression volumes versus crank angle.	151
Figure 7.2 Cyclic pressure vs. crank angle over a cycle.....	151
Figure 7.3 Variation of space temperatures vs. crank angle.....	152
Figure 7.4 Energy rates vs. crank angle within engine spaces.	153
Figure 7.5 Mass flow rates vs. crank angle, a) engine spaces b) spaces interfaces.	154
Figure 7.6 Effect of phase angle on engine performance, (a) shaft power and (b) engine efficiency.	155
Figure 7.7 Effect of regenerator matrix on engine performance, (a) shaft power and (b) engine efficiency.	156
Figure 7.8 Effect of gas type on engine performance, (a) shaft power and (b) engine efficiency.	157
Figure 7.9 Effect of cold end temperature on engine performance at different hot end temperatures for helium (a, b) and nitrogen (c, d).....	158
Figure 7.10 Effect of connecting pipe diameter on engine performance, shaft power and engine efficiency.	159
Figure 7.11 Effect of heater tube diameter on engine, a) shaft power and b) thermal efficiency.	160
Figure 7.12: PV diagrams for expansion and compression volumes within an engine cycle at 500 rpm.....	161
Figure 7.13 Velocity contours during the 5 th cycle (t = 0.6 s) at different crank angles, a) $\Theta = 0^\circ, 360^\circ$, b) $\Theta = 90^\circ$, c) $\Theta = 180^\circ$, d) $\Theta = 270^\circ$	163
Figure 7.14 Pressure contours during the 5 th cycle (t = 0.6 s) at different crank angles, a) $\Theta = 0^\circ, 360^\circ$, b) $\Theta = 90^\circ$, c) $\Theta = 180^\circ$, d) $\Theta = 270^\circ$	164
Figure 7.15 Temperature contours during the 5 th cycle (t = 0.6 s) at different crank angles, a) $\Theta = 0^\circ, 360^\circ$, b) $\Theta = 90^\circ$, c) $\Theta = 180^\circ$, d) $\Theta = 270^\circ$	165
Figure 7.16 Temperature contours of porous domains during the 5 th cycle (t = 0.6 s) at engine normal operating conditions, (a) Regenerator, (b) Cooler.....	166
Figure 7.17 Spaces cyclic temperatures vs. crank angle during the 5 th cycle at engine normal operating conditions.	167
Figure 7.18 Gas and matrix variation in the regenerator over one cycle.....	168
Figure 7.19 Total volume vs. crank angle at different phase angles.	169
Figure 7.20 Pressure drop across the regenerator vs. crank angle at different phase angles..	170
Figure 7.21 Indicated PV diagrams at different phase angles.	171
Figure 7.22 Indicated power and indicated power loss at different phase angles.	172
Figure 7.23 Effect of connecting pipe diameter on velocity streamlines during the 5 th cycle (a) original pipe and (b) reduced pipe.....	173
Figure 7.24 Effect of connecting pipe diameter on engine performance, (a) indicated power and (b) cooling power.	174
Figure 7.25: Indicated power vs. different regenerator porosities.....	175

Figure 7.26: Cooling power vs. different regenerator porosities.....	176
Figure 7.27: 3D meshing of appendix gap.	177
Figure 7.28 3D half engine temperature contours during fifth cycle at different crank angles, a) $\Theta = 0^\circ, 360^\circ$, b) $\Theta = 90^\circ$, c) $\Theta = 180^\circ$, d) $\Theta = 270^\circ$	178
Figure 7.29: Computational domain of 18-degree 3D sector of the engine.	179
Figure 7.30 (3D) sector temperature contours during fifth cycle at different crank angles, a) $\Theta = 0^\circ, 360^\circ$, b) $\Theta = 90^\circ$, c) $\Theta = 180^\circ$, d) $\Theta = 270^\circ$	180
Figure 7.31 Indicated PV diagrams of different CFD modelling.....	181
Figure 7.32 Sample of temperature contours (in $^\circ\text{C}$) of the three MCRHXs at 10 SCFM and $t = 3600\text{s}$	183
Figure 7.33 Comparison of inlet and outlet temperatures histories for 1.5mm MCRHX.....	184
Figure 7.34 Comparison of inlet and outlet temperatures histories for 1mm MCRHX.....	185
Figure 7.35 Comparison of inlet and outlet temperatures histories for 0.5mm MCRHX.....	186
Figure 7.36 interstitial heat transfer coefficients vs. Reynolds number for the three heat exchangers.	188
Figure 7.37 Average Nusselt number vs. Reynolds number for the three heat exchangers...	189
Figure 7.38 comparison of pressure drop across the three heat exchangers between CFD and experiment.	190
Figure 7.39 Friction factor vs. Reynolds number for the three MCRHXs.	191
Figure 7.40 Indicated PV diagrams for channels regenerator and random fibre.....	192
Figure 7.41 Indicated power for channels regenerator and random fibre.	192
Figure 7.42 Cooling power for channels regenerator and random fibre.	193
Figure 7.43 Indicated and cooling powers for different matrix materials.	195

LIST OF TABLES

Table 3.1 Engine's geometrical and operational parameters.....	60
Table 3.2 Uncertainty analysis for measured parameters.....	70
Table 4.1 Data used for calculation of engine mechanism effectiveness.....	84
Table 5.1 Mesh sequence and CFD results.....	108
Table 6.1 Regenerator material thermal properties (SS304).....	118
Table 6.2 Regenerators configurations and parameters.....	120
Table 6.3 Mesh sequence and CFD results.....	127
Table 6.4 Comparison between CFD results and analytical data for fully developed tube flow.	130
Table 6.5 Equivalent porous media characteristics of the five proposed regenerators.	136
Table 6.6 (ζ) values under different flow conditions.....	145
Table 7.1 Random fibre configurations	155
Table 7.2: CFD comparison of indicated PV powers.....	182
Table 7.3 Material thermal properties of regenerator matrix [88].....	194

NOMENCLATURE

Symbols	Description	Unit
A_f	Internal wetted area	(m ²)
A_{ff}	Free flow area	(m ²)
A_h	Heater internal wetted area	(m ²)
A_{k1}	Connecting pipe internal wetted area	(m ²)
A_{k2}	Cooler internal wetted area	(m ²)
A_r	Regenerator internal wetted area	(m ²)
a_{fs}	Solid surface area per unit volume	(1/m)
B_n	Beale number	[-]
C_p	Gas heat capacity at constant pressure	(J/kg. K)
C_{ps}	Solid heat capacity	(J/kg. K)
C_v	Gas heat capacity at constant volume	(J/kg. K)
CVC	Compression clearance volumes	(m ³)
CVE	Expansion clearance volumes	(m ³)
D_d	Displacer diameter	(m)
d_{ch}	Channel diameter	(m)
d_h	Hydraulic diameter	(m)
d_r	Regenerator hydraulic diameter	(m)
d_w	Mesh wire diameter	(μ m)
E	Mechanism effectiveness	[-]
f	Friction factor	[-]
f_D	Darcy friction factor	[-]
f_r	Reynolds friction factor	[-]
f_F	Fanning Friction factor	[-]
f_{req}	Engine frequency	(Hz)
Gz	Graetz number	[-]
h	Average heat transfer coefficient	(W/m ² . K)
h_h	Heater heat transfer coefficient	(W/m ² . K)
h_{k1}	Pipe heat transfer coefficient	(W/m ² . K)
h_{k2}	Cooler transfer coefficient	(W/m ² . K)
h_x	Local heat transfer coefficient	(W/m ² . K)
J	Colburn j-factor	[-]
J_d	Displacer annular gap	(m)
K	Permeability	(m ²)
k	Gas thermal conductivity	(W/m. K)
k_d	Displacer thermal conductivity	(W/m. K)
$\overline{k_e}$	Equivalent thermal conductivity	(W/m. K)
k_r	Regenerator thermal conductivity	(W/m. K)
k_s	Solid thermal conductivity	(W/m. K)
L	Heat exchanger length	(m)

l_r	Regenerator effective length	(m)
m	Total mass of gas	(kg)
\dot{m}	Mass flow rate	(kg/s)
NTU	Number of transfer units	[-]
Nu	Nusselt number	[-]
$\overline{Nu_D}$	Average Nusselt number for developing pipe flow	[-]
n	Engine speed	(rpm)
Pe	Peclet number	[-]
P_r	Radial pitch	(m)
P_{rn}	Prandtl number	[-]
P_ϕ	Angular pitch	(°)
p	Instantaneous gas pressure,	Pa
p_{ch}	Charge pressure,	Pa
$Q_{act,h}$	Actual heat transferred to heater	(J)
Q_c	Heat transferred to cooler	(J)
$Q_{d,loss}$	Conduction heat loss	(J)
Q_h	Heat transferred to heater	(J)
Q_{hot}	Heat transferred to heater	(J)
Q_k	Heat transferred to cooler	(J)
Q_r	Heat transferred to regenerator	(J)
Q_{reg}	Heat transferred to regenerator	(J)
$Q_{r,loss}$	Regenerator heat loss	(J)
$Q_{r,max}$	Maximum regenerator heat loss	(J)
$Q_{r,min}$	Minimum regenerator heat loss	(J)
$Q_{sh,loss}$	Shuttle heat loss	(J)
q''	Heat flux	(W/m ²)
q''_{-net}	Net heat flux	(W/m ²)
q''_{-tot}	Total heat flux	(W/m ²)
q_x	Local heat flux	(W/m ²)
R	Gas constant	(J/kg. K)
Re	Reynolds number	[-]
r	Crank radius	(m)
r_i	Sector inner radius	(m)
r_o	Sector outer radius	(m)
S	Fabrication clearance	(m)
T	Gas phase temperature	(K)
T_c	Compression space temperature	(K)
T_{ck1}	Conditional temperature compression cell / pipe	(K)
T_e	Expansion space temperature	(K)
T_{gh}	Actual heater gas temperature	(K)
T_{gk}	Actual cooler gas temperature	(K)
T_h	Ideal heater gas temperature	(K)

T_{he}	Conditional temperature expansion cell / heater	(K)
T_k	Ideal cooler gas temperature	(K)
$T_{m,b}$	Mean bulk fluid temperature	(K)
T_r	Ideal regenerator gas temperature	(K)
T_s	Solid phase temperature	(K)
T_w	Wall temperature	(K)
T_{wh}	Heater wall temperature	(K)
T_{wk}	Cooler wall temperature	(K)
t	Time	(s)
U_m	Flow mean velocity	(m/s)
u	Gas velocity	(m/s)
\mathbf{u}	Gas velocity vector	(m/s)
V_c	Compression volume variation	(m ³)
V_e	Expansion volume variation	(m ³)
V_{k1}	Connecting pipe void volume	(m ³)
V_{k2}	Cooler void volume	(m ³)
V_r	Regenerator void volume	(m ³)
V_{SC}	Compression swept volumes	(m ³)
V_{SE}	Expansion swept volumes	(m ³)
\bar{W}	Forced work	(W)
W_{loss}	Pumping loss	(W)
W	The power output of the engine	(W)
W_{comp}	Compression work of the engine	(J)
W_{exp}	Expansion work of the engine	(J)
\dot{W}_s	Shaft power	(W)
W_s	Shaft work	(J)
X_c	Power piston displacement	(m)
X_e	Displacer piston displacement	(m)
Z_d	Displacer stroke	(m)

Greek letters	Description	Unit
Δ	Difference	[-]
β_F	Forchheimer drag coefficient	(kg/m ⁴)
γ	Specific heat ratios	[-]
δ	Thermal penetration depth	(m)
ε	Porosity	[-]
θ	Crank angle	(rad)
Θ	Temperature incremental rate	[-]
ν	Air kinematic viscosity	(m ² /s)
λ_c	Crank radius to compression connecting rod ratio	[-]
λ_e	Crank radius to expansion connecting rod ratio	[-]
μ	Gas dynamic viscosity	(Pa. s)

ζ	Overweighing constant	[-]
ρ	Gas density	(kg/m ³)
ρ_s	Solid density	(kg/m ³)
τ	Time scale	[-]
ω	Angular velocity	(rad/s)

Acronyms	Description
2D	Two dimensional
3D	Three dimensional
CFD	Computational fluid dynamics
GPU3	Ground power unit No (3)
HTD	High temperature difference
LTD	Low temperature difference
MCRHX	Mini-channel regenerative heat exchanger
SCFM	Standard cubic feet per minute

LIST OF PUBLICATIONS

1. **Alfarawi S**, Webb-Martin M, Mahmoud S, AL-Dadah R. Thermal Analysis of Stirling Engine to Power Automotive Alternator Using Heat from Exhaust Gases. *Energy Procedia*. 2014 Dec 31; 61:2395-2398.
2. **Alfarawi S**, AL-Dadah R, Mahmoud S. Enhanced thermodynamic modelling of a gamma-type Stirling engine. *Applied Thermal Engineering*. 2016 Aug 5; 106:1380-1390.
3. **Alfarawi S**, AL-Dadah R, Mahmoud S. Influence of phase angle and dead volume on gamma-type Stirling engine power using CFD simulation. *Energy Conversion and Management*. 2016 Sep 15; 124:130-140.
4. **Alfarawi S**, AL-Dadah R, Mahmoud S. CFD Modelling of a Gamma-type Stirling Engine. *Proceeding of Heat Powered Cycles Conference, Nottingham University, ISBN 978-0-9563329-5-0; 177-184, 27th -29th June 2016.*
5. **Alfarawi S**, AL-Dadah R, Mahmoud S. Potentiality of new miniature-channels Stirling regenerator. *Energy Conversion and Management*. 2017 Feb 1; 133:264-274.
6. **Alfarawi S**, AL-Dadah R, Mahmoud S. Transient investigation of mini-channel regenerative heat exchangers: Combined experimental and CFD approach. *Applied Thermal Engineering*. 2017 Jul 5; 125:346-358.
7. Almajri A, Mahmoud S, AL-Dadah R, **Alfarawi S**, Jayakody H. CFD Parametric Study of Alpha Stirling Engine Performance. *Proceeding of the 17th International Stirling Engine Conference, Northumbria University, 24th -26th August 2016.*

CHAPTER 1

INTRODUCTION

1.1 Introduction

In this chapter, an overview of Stirling engine was presented. In this regard, the history of the engine, the main differences between the ideal and real cycles, engine configurations and different applications of the engine are described. Finally, the objectives of the current research were outlined.

1.2 Stirling cycle engine history

By the early nineteenth century, the industrial revolution had reached the peak of its development. It was a golden era of important innovations and measurable advancement in science and technology. Mechanical engines had been the driving force for the thriving industry in a variety of applications such as mining and manufacturing processes. One of the engines emerged at this time was the Stirling engine. It was invented by Robert Stirling in 1816 [1] and was introduced two years later to compete with the existing famous steam engine. However, the steam engines, at this time, were reportedly problematic with explosion-prone boilers and safety issues were a major concern. Therefore, the Stirling engine was initially introduced to be utilized locally for water pumping purpose [2]. The original model of the engine, shown in Figure 1-1, works in a closed cycle and used air as its working fluid.

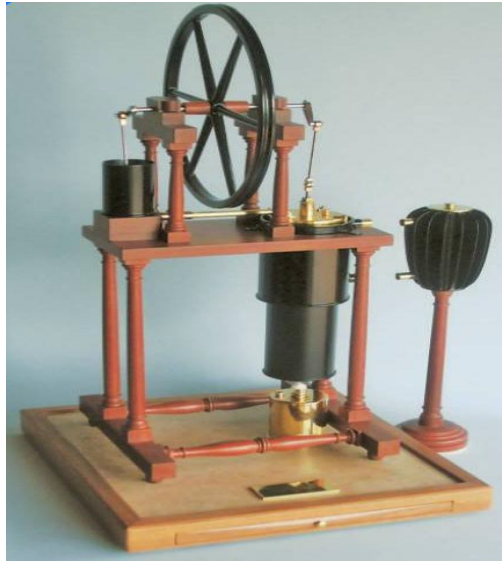


Figure 1-1 Model of hot-air engine built by Robert Stirling in 1816 to prove his idea [1].

In addition to this, the engine is set up with a thermal regenerator which is a form of a heat exchanger that absorbs and releases the heat from the working fluid in an alternating manner. This made the engine more thermally efficient than other engines at that time. Full-scale engines were used for pumping water for almost two years and produced two horse-power (1.49 kW). However, this engine did not produce as much power as the steam engine. Moreover, there was a key concern of the metallurgical capability of some engine parts to withstand the high temperatures required to maintain the engine in continuous operation.

Later, Robert Stirling introduced a second model of the engine aiming to boost the power output, as illustrated in Figure 1-2. This engine, which was installed to drive the machinery at a Dundee iron foundry in 1843 [3], was based on double-acting piston prime mover capable of producing thirty-seven horse-power.

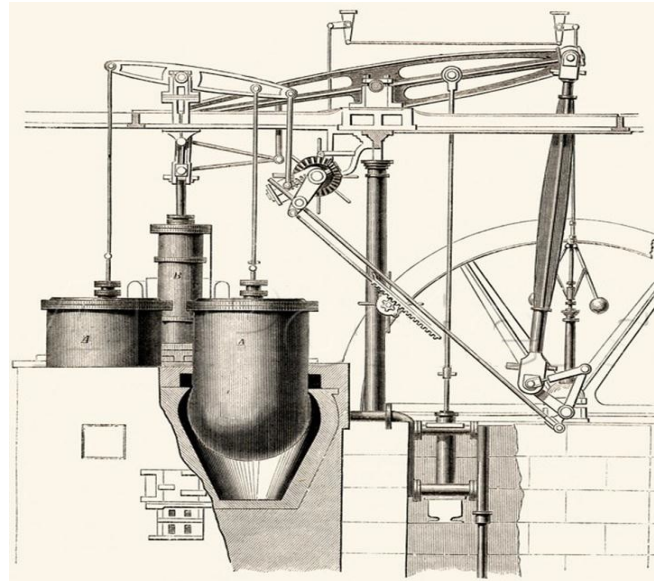


Figure 1-2 Stirling's improved engine [3].

Although this engine was competitive with steam engines at the time in terms of a relatively quiet operation, safety and efficiency metallurgical problems associated with the engine parts made of cast iron were problematic and within a few years interest in Stirling engines declined while steam engines continued to develop.

Stirling engines were neglected for many years as new engines types emerged to compete with steam engines, such as internal combustion engines (Otto and Diesel) and electric motors. In 1936, when new promising materials were discovered such as, stainless steel alongside the technological advancement in machining, Philips (a Dutch electronics company) conducted extensive research to develop the Stirling engine to power radio receivers [4]. By 1950 efficient versions of Stirling engine were introduced capable of producing 16 W (small engine) to 6 kW (larger engine), which stimulated interest again in the engine.

1.3 Theoretical cycle

The Stirling engine is described by Walker [5] as: “A device which operates on a closed regenerative thermodynamic cycle, with cyclic compression and expansion of the working fluid at different temperature levels and where the flow is controlled by volume changes, so that there is a net conversion of heat to work or vice versa”. Stirling engines work on the basis of a theoretical thermodynamic cycle which is greatly different from the real behaviour of the engine but it is useful to describe its main processes to understand the ideal behaviour. The working gas inside the engine undergoes four processes as shown in Figure 1-3;

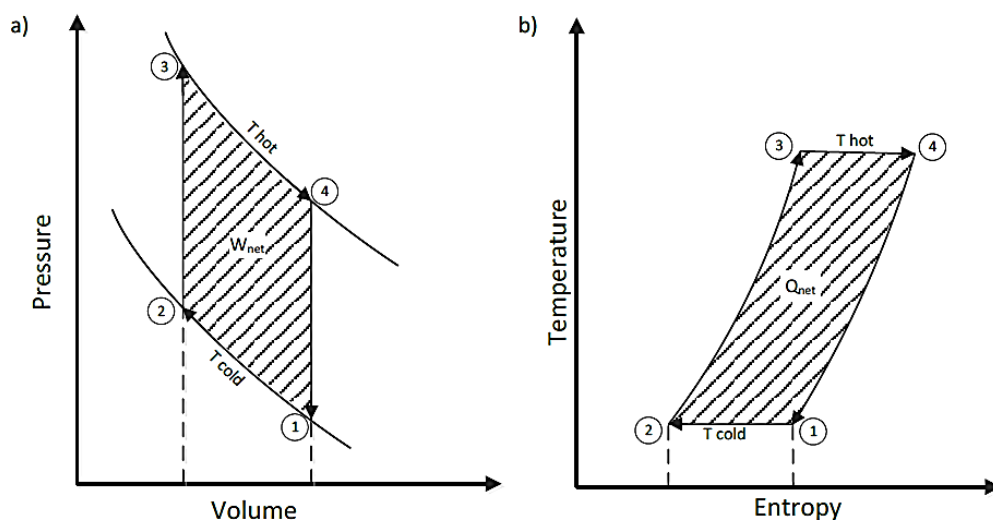


Figure 1-3 Ideal thermodynamic cycle representation, a) PV diagram. b) TS diagram.

1-2 Isothermal compression

The working gas is compressed by the compression-space piston as the piston moves from the top dead centre (TDC) towards the bottom dead centre (BDC). During this transformation, heat is ideally transferred to an external heat sink maintaining a constant temperature of the working gas. As a result, the entropy is reduced due to the heat transferred to the sink, as seen on the T-S diagram.

2-3 Isochoric heat addition

The working gas is forced to move towards the expansion space through the regenerator matrix due to the combined movement of hot and cold pistons. In this process, the gas volume is kept constant, while its temperature increases from minimum to maximum temperatures of the cycle as a result of the heat transfer from the regenerator with the corresponding entropy increment.

3-4 Isothermal expansion

The working gas expands by the expansion-space piston at constant temperature of the hot end. During this phase, the heat is absorbed from an external heat source at an infinite heat transfer rate to maintain the constant temperature. Due to heat input, the entropy increases.

4-1 Isochoric heat rejection

The working gas is displaced to the compression space through the regenerator matrix due to the combined movement of hot and cold pistons. In this transformation, due to the heat transferred from the gas to the regenerator matrix, gas volume is maintained constant and its temperature is reduced from maximum to minimum temperature.

Ideally, all the four processes are reversible and the amount of heat exchanged between gas and regenerator matrix during heat addition (2-3) and rejection (4-1) are equal. The heat transfers between the system and the surroundings are supplied or removed at constant temperature which imply that heat transfer rates are infinite in regenerator matrix and between the gas and the space walls. This ideal regeneration makes the Stirling cycle efficiency approaches the Carnot cycle efficiency between same temperature ends.

As depicted in Figure 1-4, the replacement of two isentropic processes in the Carnot cycle (1 2C 3 4C 1) with two isochoric processes in Stirling cycle (1 2 3 4 1) results in increasing area of the Stirling PV diagram. Therefore, higher work is obtained from the Stirling cycle at lower pressures and swept volumes compared to the Carnot cycle. The mechanical efficiency of the ideal Stirling engine is comparable to all reciprocating heat engines working at the same operational conditions [6].

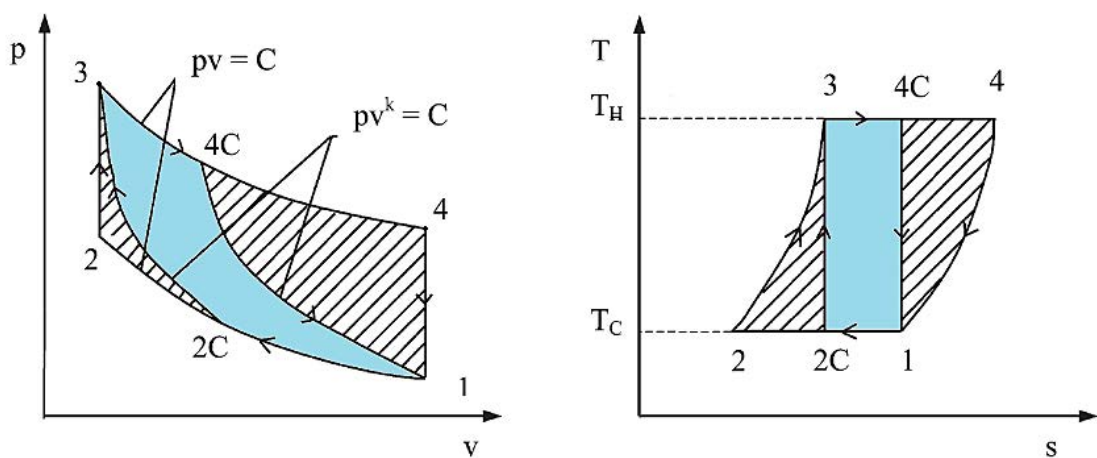


Figure 1-4 Stirling and Carnot cycle [7].

The real cycle is considerably penalized due to the irreversibility and non-ideal nature of transport mechanisms occurring inside the different components of the engine.

1.4 Real cycle of Stirling engine

1.4.1 Real motion

There is a difference between the drive motion of the practical engine and that of ideal cycle. Figure 1-5 is presented as an example of ideal and real motion for gamma-type Stirling engine. It is practically impossible to reproduce discontinuous motion of the pistons in the ideal cycle

due to the continuous motion of the drive mechanism in real engines. Many attempts have been made by researchers to design and optimize drive mechanisms to resemble the ideal motion behaviour, but a significant difference still remains and sinusoidal motion is predominant. As a result of this difference, a considerable amount of work is lost (40-60%) [5] in real cycle due to the overlapping of the four processes over the continuous cycle which results in a smooth continuous envelope of the PV diagram.

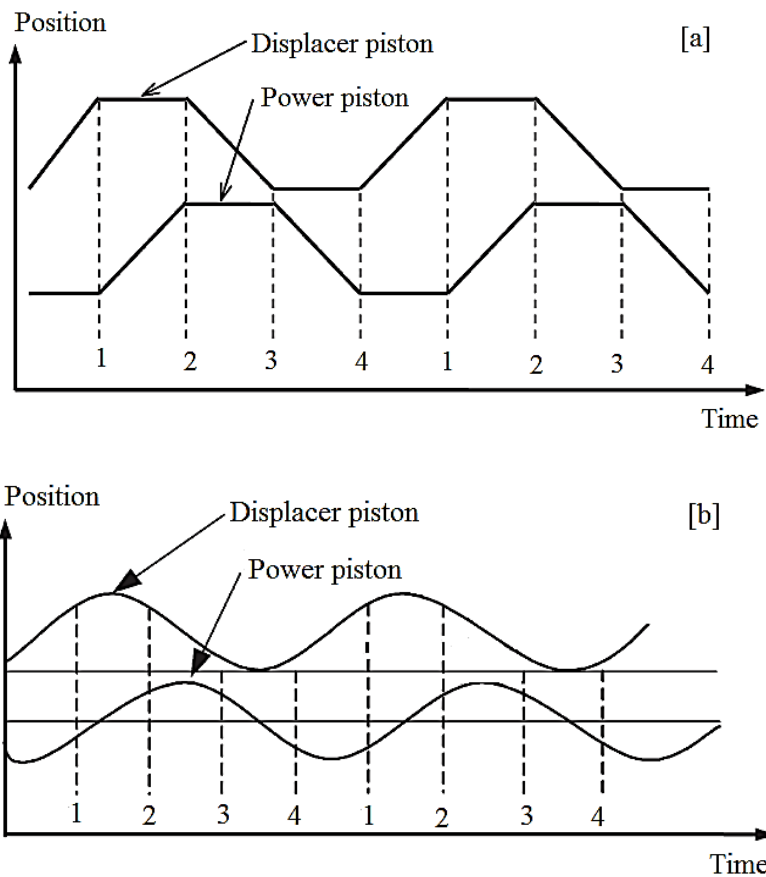


Figure 1-5 Motion diagram of a gamma-configuration Stirling engine, a) ideal, b) real [7].

1.4.2 Leakage of working fluid

The typical type of seals in Stirling engines are the traditional ring type or clearance seals; the design concept of the seals is based on running without oil lubrication. The seals may not be

perfectly tight as this may cause local overheating with the moving surfaces. Therefore, leakage through the seals may not be avoidable. This principally results in a reduction in the PV cycle due to the loss of the internal pressure as gas mass is reduced. Thermodynamic effects connected to the leakage losses are the reduction of the internal fluid mass in the engine [5, 8].

1.4.3 Pumping and mechanical losses

In addition to the power loss due to real seals and a real drive mechanism, pumping losses due to the pressure drop across the different parts of the engine including the three heat exchangers and piping sections, can contribute to the loss in power output of the engine. The mechanical losses are due to the frictional forces between the mechanical parts; between the sealing ring and the cylinder, in the shaft seal, the frictional torque in all rolling bearings and in the flywheel aerodynamic resistance. These losses are normally accounted for the brake efficiency of the real engine [5, 8].

1.4.4 Real gas and turbulence

As a result of the non ideality of the working gas and the irreversibilities of transport mechanisms in the real cycle, gas spring hysteresis losses is one of the ideal and real cycles difference. The hysteresis losses are associated with transient heat transfer fluctuation between the gas and the surrounding solid walls and can be significant if the compression and expansion spaces are far from the two idealized extremes of isothermal and adiabatic. Therefore, the work output of the engine is impaired as inefficient heat transfer is experienced. On the other hand, as a result of turbulence effects, a portion of fluid energy is dissipated inside the porous micro structures due to generated vortexes or eddies depending on the geometry of the engine [8].

1.4.5 Dead spaces

In theory, the unswept volume of the working space is called ‘dead space’ which is not swept by the movement of the pistons which means that the gas cannot totally expand or be compressed and part of the gas would remain in these spaces. This includes cylinder clearance spaces, void volumes of regenerator, heater, cooler and piping. Unlike the ideal cycle, real engines can have up to 50% dead volume of its total gas volume resulting in reducing engine power output [5].

1.4.6 Real heat exchangers

Engine performance is significantly dependent on each heat exchanger effectiveness including heater, cooler and regenerator. Another difference between ideal and real cycles is that in real heat exchangers, the assumption of infinite heat transfer rate is poor and hence isothermal compression and expansion processes are not practical. In fact, some parts of Stirling engine continuously experience high temperatures which in turn are limited by the metallurgical limits. One way to improve the heat exchangers efficiency is to increase its surface area. However, larger heat exchangers may imply higher dead volume and an elevated frictional loss. Therefore, the optimum design is normally a compromise between the positive effects of increased heat transfer and negative effects of increased pressure drop.

Another aspect of loss is related to the global efficiency, specifically if the engine is externally heated by combustion or flue gases as heat sources. Direct loss is represented by the exhaust gas flow which reduces the global efficiency of the system. The regenerator is a key heat exchanger in Stirling engines, and it experiences different mechanisms of loss that affects its performance. Imperfect regeneration is another difference between ideal and real cycle. During

the regeneration, it is practically impossible to heat and cool the working gas to the working spaces temperatures due to the finite heat transfer rates between gas and solid matrix. Regenerator effectiveness is considerably affected by the heat transfer surface area, porous material heat capacity and the temperature differences between solid and gas phase and optimum design of the matrix is required [5, 8].

1.4.7 Thermal losses

In Stirling engines, thermal losses which occur in the expansion space and regenerator may significantly alter the working gas temperatures to an extent depending on the type of heat source. The appendix gap which is the gas domain confined between the displacer and housing cylinder, is relatively exposed to a combined type of loss due to the movement of the displacer between the extreme positions and extreme temperatures. When the displacer is at the TDC position, heat is absorbed by the displacer due to convection and conduction and then it is rejected to cold gas in appendix gap at BDC position; this type of loss is well-known as shuttle losses. The secondary effect associated to the shuttle loss is the high flow-resistance when the gas is pumped through the appendix gap in parallel with the flow path through the heat exchangers. The combined effect of shuttle and hysteresis loss can degrade work potential of the engine [8].

1.5 Engine configurations

The typical components of Stirling engine, depending on engine type as shown in Figure 1-6, are; power piston, displacer piston, heater, cooler and regenerator. Stirling engines are mechanically arranged into three configurations; namely, alpha, beta and gamma. For all of the three configurations, the cycle is thermodynamically similar.

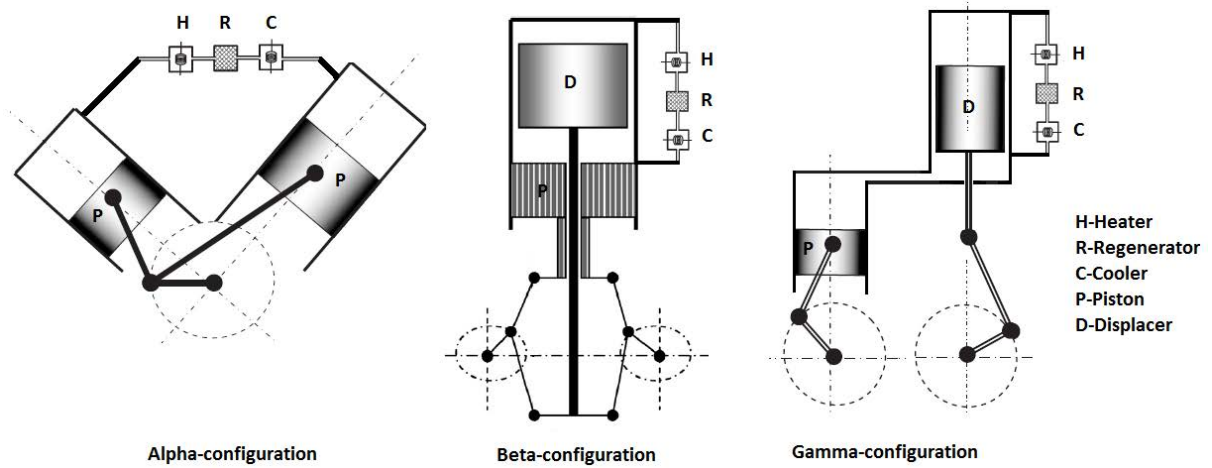


Figure 1-6 Engine components and configurations [9].

In alpha Stirling, hot and cold pistons mounted in separate cylinders work on each side of the regenerator. The gas completes the closed thermodynamic cycle of expansion and compression in the hot and cold cylinders, respectively. The V-arrangement and the yoke drive (Ross linkage) are often applied to this type of engine as shown in Figure 1-7-(a). For larger engines, the alpha may be made double-acting, as in the Franchot, Rinia, or the Siemens engines.

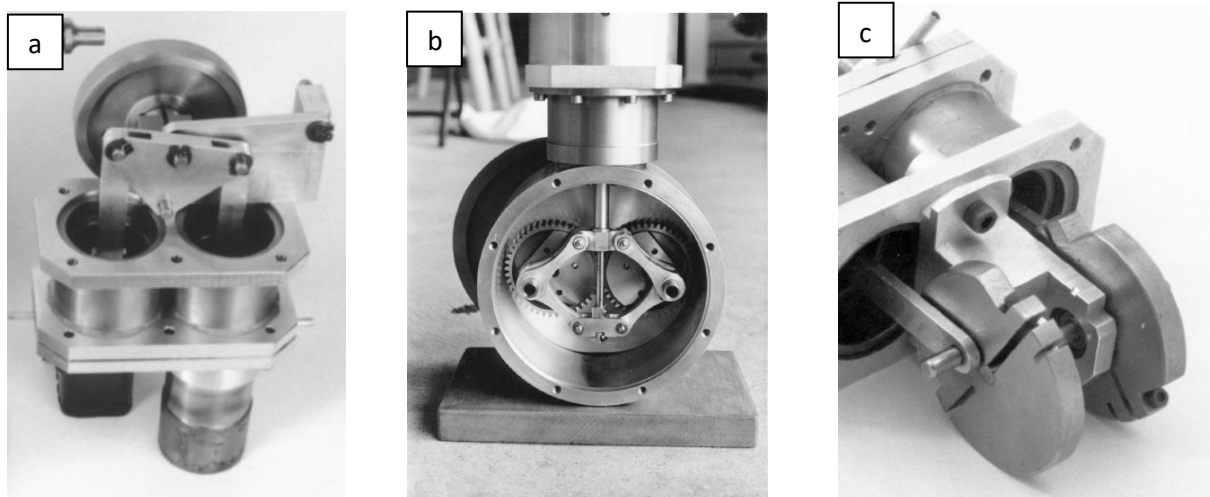


Figure 1-7 Drive mechanisms, (a): yoke drive, (b): rhombic drive, (c): crank drive [10].

The beta Stirling basically consists of power piston and displacer incorporated in the same cylinder as shown in Figure 1-6. The displacer acts to move or displace the gas back and forth without affecting the gas pressure, while the power piston compresses the gas when it is in the cold. One mechanical disadvantage is that a drive rod from the displacer extends through the piston. On the other hand, higher compression, efficiency, and power can be obtained due to lower dead volume. The rhombic drive is often applied to this type of engine as shown in Figure 1-7-(b).

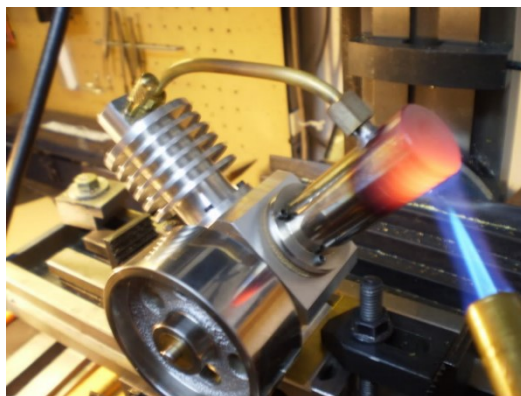
In gamma Stirling, the power piston and displacer are located in separate cylinders. The power piston, which is located at the cold side of the cylinder, compresses or expands the gas being pushed into the cylinder. This configuration of the engine is mechanically more efficient than the others [5]. The shortcoming is higher dead volumes specifically the connecting pipe that connects both the compression space and the lower part of the expansion space. The standard crank drive is often applied to this type of engine as shown in Figure 1-7-(c).

1.6 Engine heat exchangers

1.6.1 Heater

The heater transfers the heat absorbed from the heat source to the working gas and it is located near the expansion space of the engine. As the engine is externally heated, the heat source could be from the combustion of a fuel (fossil fuel, biomass, biogas), solar heat, geothermal or even waste heat source. Depending on the type of heat source, heater design parameters are determined and consequently this defines the engine operation. The heater void volume is crucial parameter that affects engine performance; oversizing the heater volume would degrade the engine power due to the increased dead volume. On the other hand, downsizing of the heater

would imbalance the heat required for its operation and may cause the engine to stop. Therefore, heater design is a balance between high heat transfer, low pumping losses and low dead volume. Since the power output of the engine increases with higher heater temperatures, materials with high temperature loads such as advanced super-alloys, refractory-metal alloys, and ceramics should be selected if high temperature heat source is targeted [11]. The general heat transfer mechanisms occur in the heater are; convective and radiative heat transfer from the external heat source to the external area of the heater tubes, conductive heat transfer from the outer to the inner surface of the heat exchanger and convective heat transfer from the inner surface to the working fluid. Different heater designs have evolved and can be classified into: annular, tubular and finned heat exchangers [12], as shown in Figure 1-8.



(a)



(b)



(c)

Figure 1-8 Stirling engine heater types, (a) annular [10], (b) tubular [13], (c) finned [14].

In the annular type, the gas is heated inside single or two concentric cylinders. The tubular heater contains the gas inside a number of small diameter tubes surrounded by the other heat exchanging fluid. Both types can be finned-structured to maximize the heat transfer area.

1.6.2 Cooler

In order to maintain a temperature gradient across the engine, the cooler in Stirling engine is required to handle twice the cooling power of traditional IC engines [5]. The common types adopted in Stirling engines are air-cooled and water-cooled configurations [9]. Figure 1-9 presents the typical arrangement of cooler heat exchangers in the Stirling engine. The inner gas passages are cooled by an external fluid (water or air) usually in a cross-flow configuration perpendicular to the channels containing the inner gas. The cooler heat exchanger can be of a shell and tube type where the tubes contain the gas to be cooled and the cooling medium is in the shell side [15, 16].

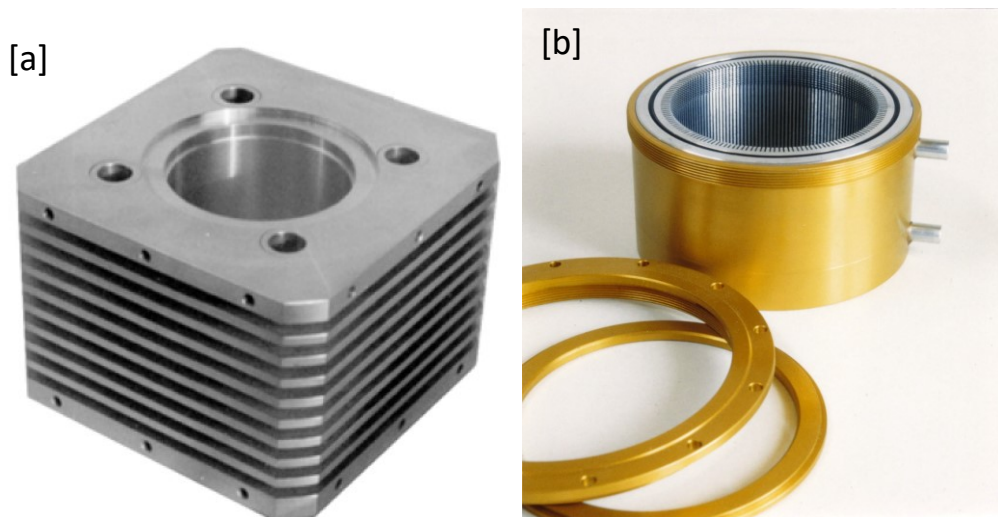


Figure 1-9 Typical cooling arrangement in the Stirling engine, (a) Air-cooled, (b) Water-cooled [10].

1.6.3 Regenerator

The regenerator is a key component of the engine. It is an internal heat exchanger that acts as a thermal sponge when absorbing and releasing heat at a portion of the cycle, thus, engine power and efficiency are enhanced. The heat being absorbed and released to the gas in the regenerator during one cycle is typically four times the heat that passes through the heater during one cycle [17]. Such an engine without a regenerator, its heater would need to take in five times as much heat during a cycle so that engine power generated is the same as it did with a regenerator [18, 19]. Several types of regenerators are used for Stirling engines including simple clearance gaps, stacks of woven-wire screens, random-fiber, packed-sphere, wrapped-foil, tube-bundles, metal foam and parallel plate regenerator [19]. The conventional regenerator type adopted in Stirling engines is the wire mesh or random fibre as shown in Figure 1-10.

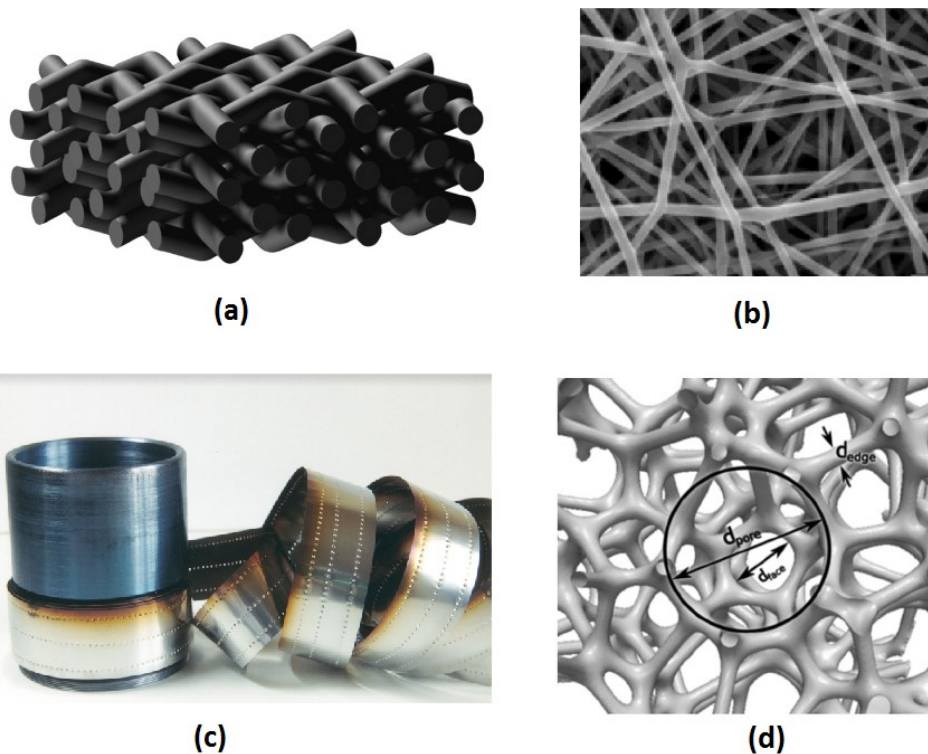


Figure 1-10 Stirling regenerator configurations, a) woven screen [20], b) random fibre [19], c) wrapped-foil [10], d) metal foam [21].

Some advantageous features exist in the wire matrix regenerator as:

- a. high convective heat transfers between the solid and the gas due to the extended surface area of wires and this is similar to a cross flow over repeated cylinder-shaped wires.
- b. Low axial conduction in flow direction

However, the downside of this type of regenerator is the high flow friction resulting from flow separation, eddies associated with stagnation areas that can degrade the engine performance. The regenerator has to have several features for better performance that might be contradicting and this lays a great effort for a designer to find the optimum configuration based on [17, 22];

- a. Minimum pressure drop
- b. Maximum convective heat transfer
- c. Minimum axial conduction in flow direction

1.7 Stirling engine applications

1.7.1 Solar power generation

Previously, steam turbines utilized solar energy for large-scale electricity generation [23]. As a viable source of energy, the sun can potentially run Stirling engines to generate electricity on small scale basis. A parabolic dish collector (shaped as satellite dish) shown in Figure 1-11, comprised of a matrix of dish-shaped mirrors, is used to concentrate the solar irradiation onto a focal point wherein the hot-end head of Stirling engine is positioned. In this system, hydrogen or helium are used as the working fluid in the engine [24].



Figure 1-11 Solar-powered Stirling engine [24].

The system is integrated with dual-axis tracking mechanism to track the sun in the sky and the engine is connected with an alternator which converts the mechanical work produced by the engine into electricity. The heat-to-electricity conversion efficiencies of these systems reach 40 %, while each system is capable of generating electricity from 7 kW to 25 kW [25]. Solar-powered Stirling engines were reported to be the cheapest for up to 100 kW electricity [24].

1.7.2 Computer chip cooling

This is one of the innovative concepts of miniature Stirling engines, shown in Figure 1-12, adopted for PC processor cooling. The heat dissipated from the processor components is used to heat the engine and thus operating the cooling fan attached to the engine. The developer, Micro-Star International Co., claimed that the engine is seventy percent efficient which means that the engine converts seventy percent of heat generated by chip components into mechanical work to rotate the cooling fan [26].



Figure 1-12 Chip cooling by Stirling engine [26].

1.7.3 Stirling engine powered submarines

Because of its quiet operation, Stirling engines have been developed to be used in military submarines, shown in Figure 1-13. The engine, which generates 75 kW, works as a backup to the main diesel engine to be used for propulsion or charging the batteries. With this technology, developed by (ThyssenKrupp Marine Systems) in Sweden, the submarine can remain submerged from days to weeks without surfacing to charge the batteries [27].



Figure 1-13: Stirling engine-powered submarine [27].

1.7.4 Domestic heat and power

One of the great developments of Stirling engine is to be used in domestic combined heat and power (CHP) application. Organ [2] stated that “Stirling engine is now a commercial reality as the core component of domestic CHP”.

One of the possibilities to use the engine is that gas-fired boiler can be integrated with Stirling engine in a compact package. The engine is driven by the temperature difference of hot and cold water of the boiler to generate electricity for home usage. These compact units, shown in Figure 1-14, such as SIEMENS unit, is capable of producing 5 kW as heat and 1 kW as electricity [28].

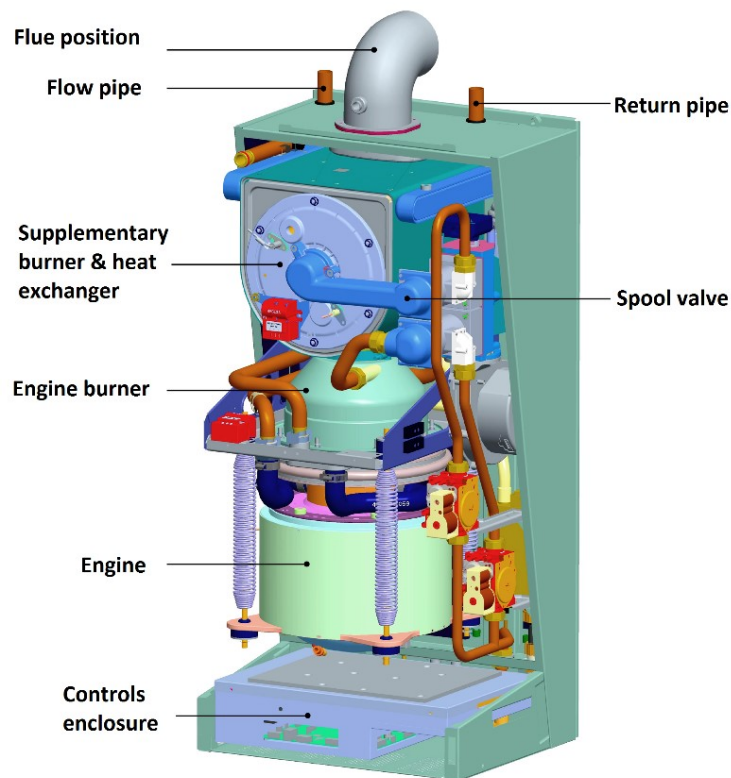


Figure 1-14 Stirling engine powered CHP [28].

1.7.5 Stirling engine powered automobiles

The Stirling engine powered automobiles, shown in Figure 1-15, were not a success when they were developed and introduced to replace the internal combustion engine automobiles in 1979 by NASA projects, General Motors and Ford [29].

The lack of success was attributed to issues of long warm-up period of the engine, the difficulty of increasing the engine speed and the larger size of the engine. Even when some relatively efficient models were proposed, funding to develop more efficient models was not adequate. Nowadays, considerable efforts are being made to incorporating Stirling engines into hybrid-electric engines [30].

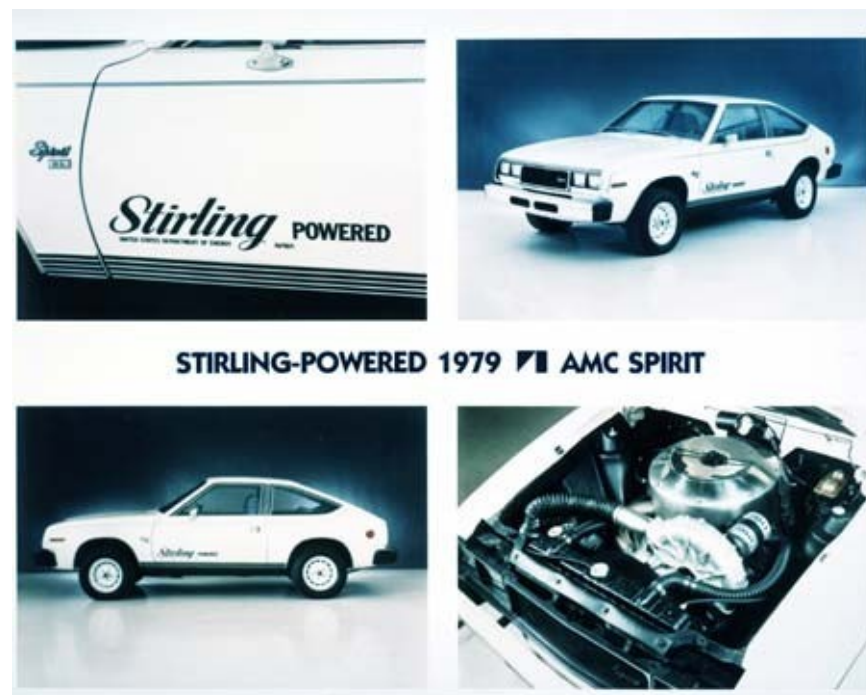


Figure 1-15 Stirling engine powered automobiles [29].

1.7.6 Stirling cryocooler

Because the Stirling cycle can be reversed, Stirling engines are used as a heat pump (Stirling cryocooler) which converts the input mechanical power into temperature difference between two reservoirs causing cooling effects as in refrigeration systems. The mechanical components of Stirling engine and Stirling cryocooler are similar except the cycle is reversed, as shown in Figure 1-16. Stirling cryocooler can cover a wide range of cooling powers from miniature models to large industrial machines, and generate temperatures below 100K reaching even less than 10K in research applications [31].

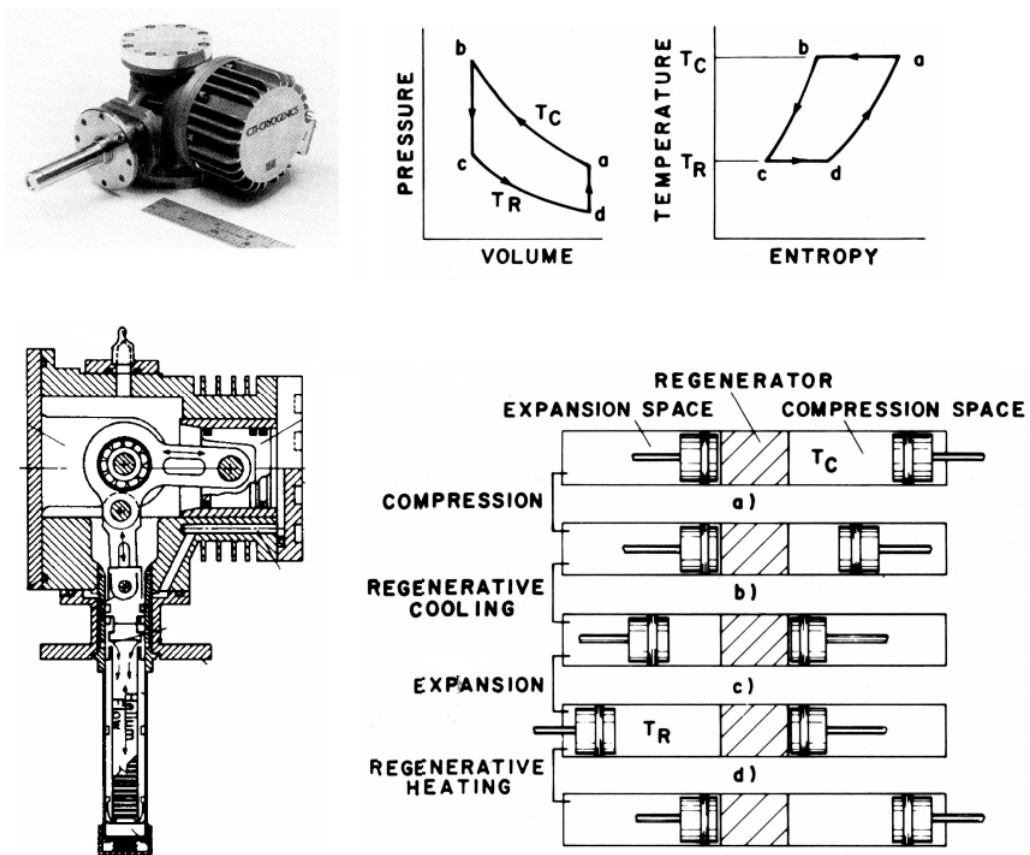


Figure 1-16 Stirling cryocooler [31].

1.8 Motivation

Fossil fuels, as a conventional source of heat energy, are being continuously burned and alarmingly exploited resulting in CO₂ emissions that contribute to global warming. Renewable energy resources (such as solar and geothermal energy) exist abundantly all over the world [32]. It is worth noting that the hourly solar energy received by earth is significantly more than the energy consumed globally by other energy sources in one year [33]. Moreover, about 20-50% of low-grade waste heat generated by industries are rejected into atmosphere. Thus, ways of exploiting these alternative sources of energy are being sought to preserve fossil fuels as well as to reduce the greenhouse effects.

The Stirling engine is an externally-fired combustion engine, so there is no fuel or gas exchanged between the inside and outside of the engine. It is thermally regenerative, simple in construction, virtually silent and safe in operation, and intrinsically flexible, able to adopt any heat source such as solar, biomass, geothermal energy otherwise waste heat. However, the low specific power and the high initial cost of the engine hinder development, optimization and commercial implementation of Stirling machines. The potential of Stirling engines to use renewable forms of energy as heat sources is highly regarded. This appears to outweigh the increasing concern about engine prices, which is affecting commercialization. During the last thirty years Stirling engine technology has shown some successful concepts in different areas such as domestic combined heat and power, military submarines, refrigeration systems, cooling of computer chips, hybrid-electric automobile and electricity generation [34]. Many researchers believe that Stirling engines have good potential in the area of domestic combined heat and power (CHP) applications and electricity generation [28].

Cryogenic fluids including liquid air/LN₂ have been acknowledged as energy storage mediums with high storage density of 0.77 [MJ/kg]. Surplus electricity (off-peak) and/or renewable energy sources can be used to liquefy air/N₂ in which energy can be stored and transported using the well-developed cryogenic industry infrastructure. Therefore, integrating Stirling engines with the stored cold energy is feasible and motivating. There has been ongoing research into developing Stirling engine technology, most of which has been based on the optimization of design and operation to develop cost-effective, durable, efficient engine in the near future. However, accurate modelling of Stirling engine using comprehensive CFD analysis is still challenging. The successful development of an efficient and cost-effective Stirling engine using CFD modelling will have a significant impact on the recovery of the available waste heat sources leading to significant reduction in fossil fuel consumption and CO₂ emissions.

1.9 Aims and objectives and thesis structure

The main aim of this work is to model and enhance the performance of (HTD) gamma-type Stirling engine prototype (ST05-CNC) through the following objectives;

- 1) the development and validation of an enhanced thermodynamic model and a comprehensive CFD model to simulate the gamma-type Stirling engine prototype (ST05 CNC).
- 2) investigating the potential use of cryogenic energy storage to maximize engine shaft power.
- 3) an investigation of the potentiality of new channel regenerators in Stirling engine applications.

- 4) the fabrication of three mini-channel regenerators and their test facility to conduct transient testing and to investigate their performance using a combined experimental and CFD approach.

The thesis is structured as presented in Figure 1-17; chapters 1 and 2 present an overview of Stirling engine history and the literature survey of research carried out on the engine in open literature. Chapter 3 is devoted to give an overview of the engine test facility available at University of Birmingham. The engine components, instrumentations, measurements are described.

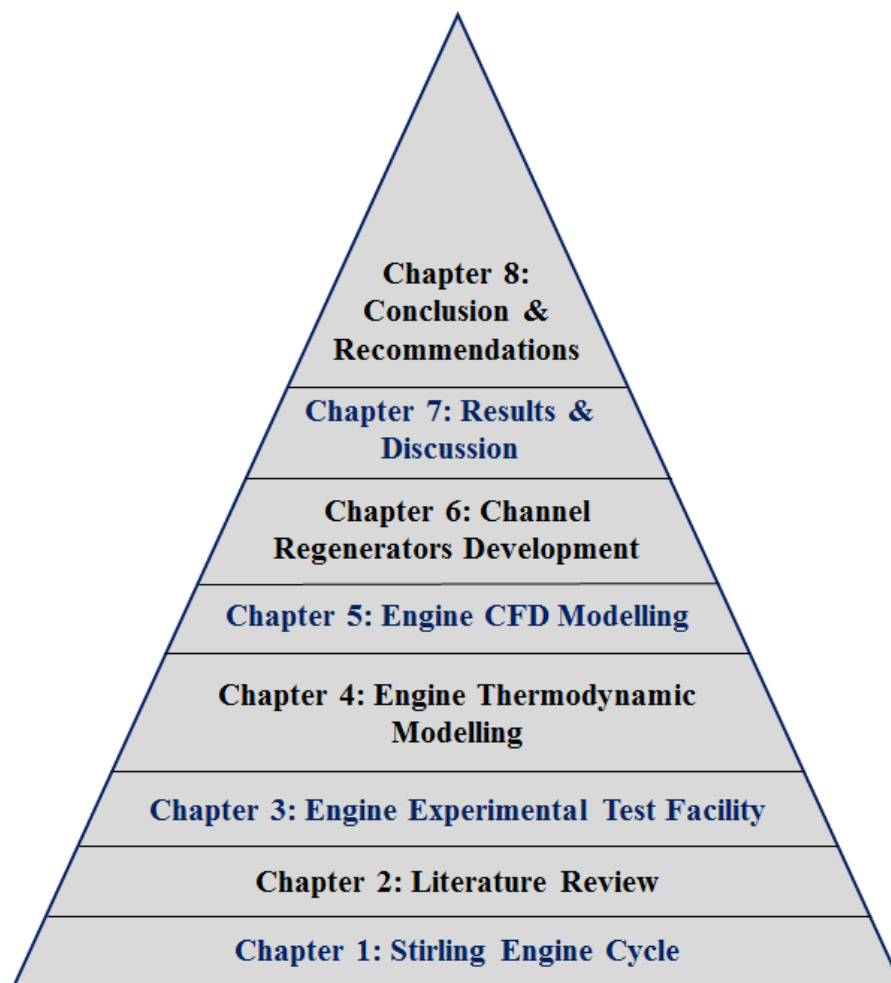


Figure 1-17 Overview of thesis structure.

Chapter 4 describes the thermodynamic analysis using non-ideal adiabatic modelling for gamma-type Stirling engine. The engine is reconfigured with six engine cells to include the connecting pipe into the analysis. Random fibre correlations for flow friction and heat transfer, based on oscillatory flow testing, are adopted to model the regenerator. The real pistons motion is adopted and hence the real volume variation is included in the model. The pumping losses in the heat exchangers are evaluated depending on the type of flow regime. Meanwhile, thermal losses such as shuttle and conduction losses are accounted for. Moreover, mechanical losses are also included to predict engine shaft power.

Chapter 5 describes the methodology of developing the CFD model using a commercially available software (COMSOL Multiphysics 5.2) to investigate some effects of geometrical and operational parameters on engine performance and hence improvements of the current engine will be suggested.

In chapter 6, five regenerator's configurations were designed with different circular channel diameters and different porosities. Initially the regenerator was designed as a whole piece with circular channels cutting through. The five configurations were tested virtually prior to fabrication using the validated CFD model of the engine. The test facility to perform transient testing of the fabricated MCRHXs was designed and manufactured. Transient testing using CFD conjugated heat transfer of 3D sector of each MCRHX was performed in combination with experiments. Therefore, heat flux, radial and axial conduction losses were included in the model. Meanwhile, the measured inlet temperature profile was inputted to the CFD model. Direct curve matching of outlet temperature histories between CFD and experiment were performed and Nusselt number and friction factor correlations for each configuration were obtained. Discussion of all results from the thermodynamic model, CFD model of the engine

and CFD model and experimental results of the regenerators will be presented in chapter 7. Finally, chapter 8 will conclude the work carried out in this project and recommendations for further future work.

CHAPTER 2

LITERATURE REVIEW

2.1 Introduction

In early 1816 Stirling engines were built based on the observation that air expands when heated and compresses when cooled. However, mathematical analysis of such engine was first attempted in 1971. Since then, models have been emerging through a continues process of refinement and improvements of Stirling engine theory. In this chapter, a comprehensive review was presented to highlight the previous theoretical and experimental work done on kinematic Stirling engines. Other studies regarding the development of parallel-geometry Stirling regenerators were reviewed as well. This chapter concludes with a gap of research on Stirling engine under study.

2.2 Review of different analysis approaches

Different analysis approaches are classified, as depicted in Figure 2-1, with Martini's [35] nomenclature according to their hierarchal order rather than the order of discretization in time and space, into zeroth-, first-, second-, third- and forth- order models. These models are descending according to their complexity, accuracy and computational time.

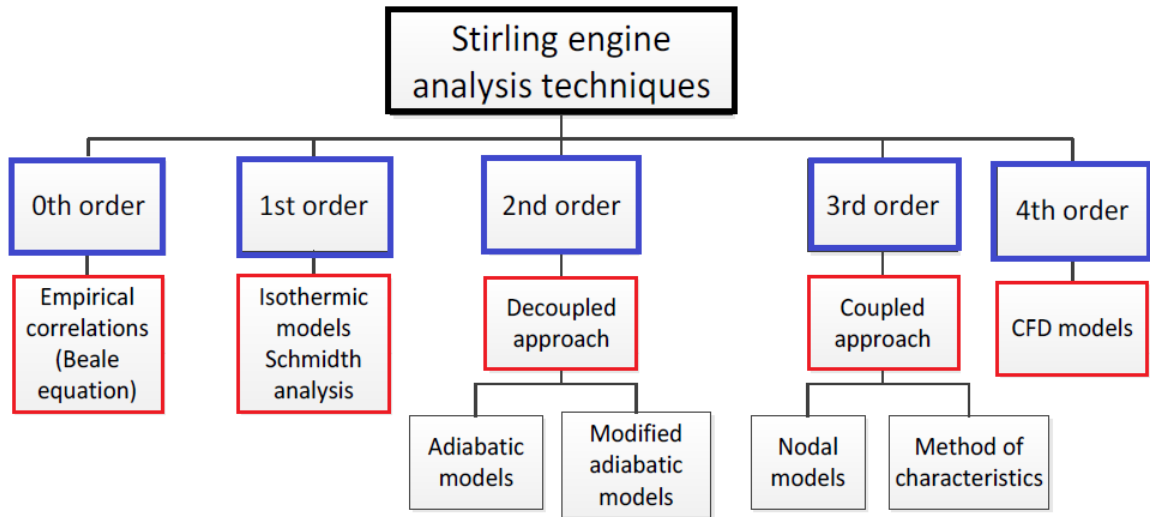


Figure 2-1 Different categories for Stirling engine analysis.

Based on literature survey conducted in this work, it was demonstrated that beta and gamma type Stirling engines are widely used in research compared to alpha type, as depicted in Figure 2-2.

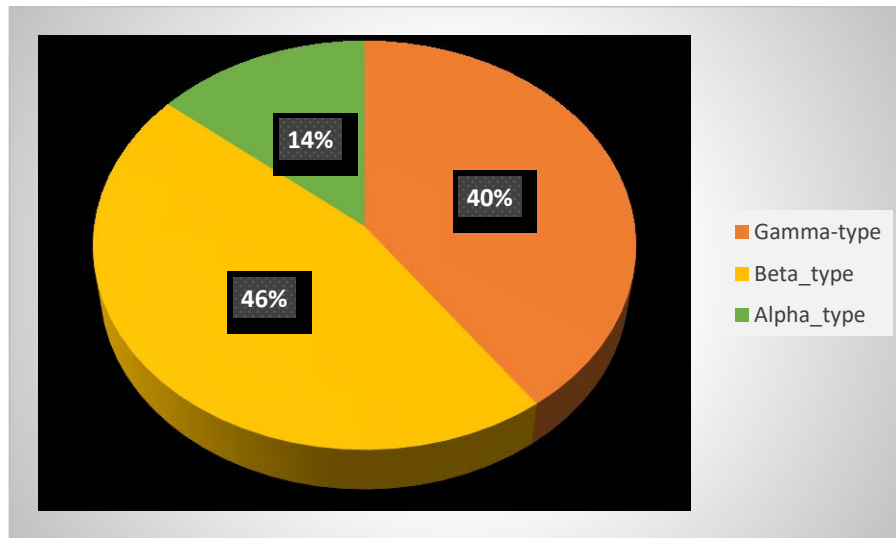


Figure 2-2 Stirling engine research percentage in open literature of the three types.

2.2.1 Zeroth-order analysis

Zero order analysis is based on an empirical correlation to predict the power output of an engine. Beale et al [36] proposed a correlation based on extensive experimental work of certain layouts of Stirling engines. He observed that engines that operate under given conditions with similar ratios of temperature, swept volumes, dead volume and phase angle, can be correlated by one empirical formula to represent the engine power in terms of power piston swept volume, charge pressure and engine frequency.

$$W = B_n \cdot p_{ch} \cdot V_{SC} \cdot f_{req} \quad 2.1$$

The original Beale number (B_n) is typically assumed to be 0.015. However, this figure can deviate considerably at higher temperature ratios. Later, West [37], developed this approach to predict the power output, using a generalized Beale number at different operational parameters taking into account the effect of temperature ratio.

2.2.2 First-order analysis

The first order analysis was first introduced by Schmidt [38] who developed a closed-form analytical approach based on algebraic equations of mass and energy conservation which allow predicting the engine power and efficiency for the case of sinusoidal volume variation. Schmidt theory is based on the assumption of isothermal working spaces of compression and expansion. This analysis is highly idealized and no heat transfer and internal pumping losses are considered. Usually, the power and efficiency predicted by Schmidt analysis, are overestimated by a margin of 30% or even more [39]. However, first-order analysis can be a good starting point to explore engine performance on a basic level.

Senft [40] performed analytical study on optimum Stirling geometry for gamma-type, based on classic Schmidt thermodynamic analysis. He showed that maximum indicated work does not necessarily generate the highest shaft power output. The results showed that not only the mechanism effectiveness affects the output of the shaft but also do the shape of the cycle and the buffer pressure. For a given operating condition, optimum values of swept volumes ratio and phase angle exist to give maximum break power output.

Bert et al [41] proposed a three-zone finite-time thermodynamic model (FTT) to simulate and optimize gamma-type Stirling engine with a nominal electrical power of 1 kWe. FTT is a non-equilibrium theory that provides the bounds and extremes for irreversible thermodynamics processes and it is used to find the optimal path or mode operation of any thermal system including heat engines. Effects of speed, gas type, hot end temperature and filling pressure on engine performance were investigated. The pistons kinematics were optimized using particle swarm optimization (PSO) for maximum power. Their results showed that in the optimized crank-connecting rod system, the phase angle varies from 90° at the beginning of the cycle to 100° at the maximum position of each piston.

Li et al [42] proposed a coupled finite speed and isothermal models to analyse a solar-powered gamma-type Stirling engine. A filling material in regenerator gap was not considered in this low temperature difference (LTD) Stirling engine. Different loss mechanisms affecting the engine performance were considered. They found that the key loss mechanisms are the regenerator gap heat loss and the work loss due to gas leakage through piston/ cylinder walls. Some engine improvements; using insulating material for displacer and cylinder walls and reducing the clearance leakage, were proposed.

Formosa and Despesse [43] developed an analytical model based on first-order analysis for free piston Stirling engine simulation. Heat losses and irreversibilities of the engine were included in their model. Although, isothermal assumption was used, the model was validated with reasonable accuracy against the experimental data published by Martini [35] of ground power unit (GPU3) engine built by General Motors. GPU3 data is widely referenced in open literature for the validation of different analysis methods.

Eid [44] investigated the effect of a regenerative displacer on a beta-type Stirling engine using Schmidt theory. The displacer cylinder was filled with homogenous layers of woven sheets. The optimum dimensions of heater, cooler, regenerator, piston stroke and displacer stroke were investigated. It was found that the proposed engine with a regenerative displacer was able to deliver 20% more power than that of the GPU3 engine which had non-regenerative displacer. Also, this reduced the engine space when the regenerator was incorporated inside the displacer.

El-Ehwany et al [45] evaluated the performance of an alpha type Stirling engine using two elbow-bend heat exchangers as heater and cooler. The eight heat exchangers with different dimensions were tested experimentally for steady flow in a previous investigation by the same authors and the data of heat transfer and pressure drop were correlated and used as inputs to the simulation code which was based on Schmidt analysis. The optimum parameters of stroke/bore ratio, phase angle and speed on engine performance were proposed. The engine performance was compared to similar prototypes in literature. The results revealed that the altered engine generates 13% more power at lower range of speed than those in the literature at high level of thermal efficiency due to the reduced hydraulic losses in the heater and the cooler.

Martaj et al [46] presented an energetic, entropic and exergetic analyse of LTD gamma-type Stirling engine based on steady state operation. Using a zero-dimensional numerical model, the engine was split into three isothermal control volumes, including the heater, cooler and regenerator. Energy, mass, entropy and exergy balance was carried out on each cell based on a function of crank angle (kinematic-thermodynamic coupling). The results showed that it was possible to optimize engine components based on best efficiency and minimum production of entropy. The results revealed that the increase in regenerator's dead volume had reduced the thermal and exergy efficiencies for the whole engine.

Puech and Tishkova [47] performed a classical thermodynamic analysis on a Stirling engine with linear and sinusoidal volumetric variations based on an isothermal assumption. The work output and the heat stored in the regenerator during a complete cycle were investigated. Their results showed that the dead volume has no impact on the efficiency in the ideal case of perfect regeneration which contradicts previously published results. On the other hand, they showed that efficiency reduction due to imperfect regeneration was significantly amplified with increasing the dead volume. They proposed an approximation formula that is useful for characterization of both the imperfection and the dead volume in the regenerator for discontinuous and sinusoidal motions of the pistons.

Cheng and Yang [48] performed a theoretical analysis to investigate the effect of geometrical parameters on the three types of Stirling engine. The theoretical model adopted is simple idealized one but aimed to compare the real cycle characteristics. Optimum combination of phase angle and swept volume ratios to maximize shaft work was proposed for each type at any given operating conditions. The results showed that beta-type engine generates the highest shaft work while gamma-type generates the lowest. Also, the results revealed that gamma-type is the

most capable to run with low temperature difference application while alpha-type is the worst for that application due to reduced shaft work with increased temperature ratio.

Cheng and Yang [49] performed an analytical study to optimize a rhombic drive mechanism of a beta-type Stirling engine for maximum shaft power. The volumes and pressure variations in the engine chambers were transformed into a dimensionless form in terms of piston and displacer displacements. Similarly, Schmidt analysis, incorporated with Senft's theory, was built in a dimensionless thermodynamic model, to return dimensionless shaft work. Optimum values of geometrical parameters were investigated and proposed. It was found that the produced work of the engine is sensitive to the increase in the dead volume.

Recently, Hosseinzade et al [50] developed a closed-form first order thermal model called (PFST) for gamma-type Stirling engine simulation based on combined polytropic-finite speed thermodynamics analysis. Finite speed thermodynamics (FST) is based on mathematical expression of first law of thermodynamics for processes with finite speed that caused internal irreversibility including; finite speed of piston, friction and throttling. The expansion and compression processes were based on polytropic assumption. Different losses including pressure throttling, mechanical friction and finite motion of pistons were considered in their analysis to estimate engine shaft power. Their simulation results when compared to GPU3 engine data revealed same order of accuracy in prediction compared to other recent second-order numerical models; but still it suffers from the absence of some engine parameters such as variable cold end temperature and no information of indicated power was provided.

First-order analysis is idealized but can capture the Stirling engines characteristics and behaviours. It is not expensive in terms of computational time; however, it can be only used for initial prediction of engines performance.

2.2.3 Second-order analysis

Finkelstein [51] improved the modelling accuracy further by developing the ideal adiabatic analysis. The engine is simplified into five cell units including the three heat exchangers (heater, cooler and regenerator), with the assumption that both expansion and compression spaces are adiabatic. For each space a set of ordinary differential equations of mass and energy equations is integrated numerically to obtain parameters cyclic variation. The isothermal assumption still applies in all heat exchangers. Then an improved model called (Simple analysis) was proposed based on an ideal adiabatic analysis but with heater and cooler gas temperatures recalculated using the regenerator effectiveness. This implied evaluating and subtracting power and thermal losses from ideal cycle analysis in a decoupled approach to obtain the actual engine performance. This analysis takes into account conduction thermal losses as well as the pumping losses in the heat exchangers. Later, the quasi steady flow approach for Stirling engine simulation was published by Urielli and Berchowitz [8].

The non-ideality of heat exchangers was introduced into second-order analysis. The pressure values in expansion and compression spaces were rectified based on the pressure drop in the heat exchangers. An improved accuracy of the (Simple) analysis mentioned earlier was reported when the model was compared to engine experimental data of GPU3. Later, the Simple analysis was modified by many researchers to include different loss mechanisms such as evaluating the shuttle heat transfer loss, the gas enthalpy transfer, the hysteresis heat transfer loss along with conduction heat transfer loss and the pumping losses evaluation.

Two commercially available codes exist based on second-order analysis; SNAPpro (Stirling Numerical Analysis Program) developed by Altman [52] and PROSA (PROgram for Second-order analysis) developed by Thomas and Pittman [53]. Paula et al [54] used PROSA simulator to build a prototype Stirling engine named Amazon, aimed to generate 8 kW electric power in remote areas. The results obtained from PROSA were compared to Schmidt analysis based model. It was found that the Schmidt model results are 6.8% higher than those of PROSA software.

There have been numerous numerical models in open literature to analyse and optimize Stirling engines using second-order approach. Cheng et al [13] developed a non-ideal adiabatic model for a domestic-scale 300-W Stirling engine. The developed engine was tested using helium and air as working gases at different charge pressures and hot end temperatures. They also investigated the effect of wire mesh number on engine performance and an optimum value was found. 20% maximum deviation was reported when model results compared to experimental results. It was found that power generated by helium-charged engine was superior to air. Furthermore, a maximum shaft power of the engine of 390 W was reached at 1400 rpm with 1.2 kW input heat transfer rate (32.2% thermal efficiency) using wire mesh (#120) in the regenerator at optimum operating conditions of 8 bars and 850 °C as charged pressure and the heating temperature, respectively.

Hachem et al [55] developed a numerical model, based on classical quasi-steady approach, to optimize gamma-type Stirling engine. Their results showed that the maximum losses were recorded in the regenerator including viscous, conduction and imperfection losses. The effect of key operational parameters, such as engine speed, hot end temperature and charge pressure on engine performance were investigated and they found that the engine speed can alter thermal

losses mechanisms and optimum value should exist. Increasing initial filling pressure and hot end temperature were the two influential parameters on the increase of engine brake power.

Araoz et al [56] developed a thermodynamic model based on second-order analysis to simulate gamma-type Stirling engine. The forced work and mechanical efficiency, based on Senft theory, were considered to predict engine shaft power. According to their results, they found that the engine low power output was attributed to the reduced mechanical efficiency of the system. The dynamics of volume variation and drive mechanism were suggested for further improvements to increase the engine shaft power.

Mabrouk et al [57] introduced analytical model to predict displacer gap losses in beta- and gamma-type Stirling engines. The results of velocity and temperature distributions in the displacer were introduced to the classical non-ideal adiabatic analysis to study the GPU3 Stirling engine as a case study. Their results showed that displacer gap losses are minimum when clearance thickness in the range of [50-70] microns and also minimum when the operating frequency of the engine in the range between [25-35] Hz.

Parlak et al [58] performed a thermodynamic analysis of gamma-type Stirling engine using quasi steady flow model based on Urielli and Berchowicz work [8]. Pressure drop in engine spaces and thermal losses were considered in their model. The main feature of their model was the calculation of pressure inside each working space based on the pressure drop in heat exchangers.

Tlili and Sa'ed [59] investigated theoretically the effect of Ross Yoke drive mechanism on alpha-type Stirling engine using second order modelling method. They argued that, opposite to

what has been published in literature about the low performance of Yoke drive alpha-type Stirling engine, using this type of drive mechanism can minimize the vibration and the lateral forces on the pistons leading to efficient energy conversion.

Timoumi et al [60] developed a thermodynamic model for GPU3 based on a quasi-steady flow second-order analysis with a deviation of 15%. He considered different losses in the model such as shuttle losses, flow resistance, heat conduction losses and gas spring hysteresis losses in the compression and expansion spaces.

Gheith et al [61] investigated numerically and experimentally the heater of gamma type Stirling engine. The optimal values of operating parameters that maximize the heater performance and therefore of the Stirling engine were examined using classical quasi-steady second-order model. Four operating parameters including; hot end temperature (300–500 °C), charge pressure (3–8 bar), cooling water flow rate (0.2–3 l/min) and frequency (2–7 Hz) were selected in this study. It was found that all investigated parameters have significant impact on the exchanged heat and the efficiency of the heater. A frequency of 6.1 Hz, charge pressure of 7 bar, a hot end temperature of 500 °C and a 3 l/min of cooling water flow rate were found to provide heater with best performance.

Kraitong [62] developed a thermodynamic model to simulate a LTD solar Stirling engine, based on second-order analysis taking into account hydraulic and mechanical losses in the engine's working spaces. The model was linked to genetic algorithm for engine optimisation. Parametric optimization of displacer stroke, power piston stroke and thickness of the regenerator was carried out and noticeable enhancement in engine performance was achieved.

The obtained optimal design parameters were further compared to a 3D CFD model to validate its accuracy.

Schulz and Schwendig [63] developed a second-order thermodynamic model for Stirling engines simulation taking into account the real gas effects and considering turbulent flow in the heat exchangers. During simulation, Nusselt number for laminar and turbulent flow conditions was computed. Good agreement was found between model predictions and the experimental data for a Vuilleumier engine.

Mahkamov and Ingham [64] applied a second-order mathematical model on 1 kW alpha-type solar Stirling engine to investigate the influence of mechanical losses on its performance. Different thermal and hydraulic losses were considered in the model. The mechanical losses were calculated based on the cyclic variation of the frictional force between the sealing ring and the cylinder, in the shaft seal, the frictional torque in all rolling bearings and in the flywheel aerodynamic resistance. The results showed that 50% loss in the indicated power was due to the mechanical losses.

Paul and Engeda [65] developed a thermodynamic model for beta-type Stirling engine simulation based on ideal adiabatic plus simple heat exchanger including cooler-regenerator manifold, regenerator-heater manifold and appendix gap. The model included external components such as the fan, combustor and preheater. The model prediction of engine power was compared to GPU-3 experimental data and found to be within $\pm 14\%$ of deviation at different engine speeds and charge pressures. The same authors [66] in other work, designed a Stirling engine that uses lower quality fuels based on modifying GPU-3 engine. The modified engine was expected to generate 5 kWe at a combustion gas temperature of 900 °C. The engine

was modelled using the adiabatic thermodynamic analysis with decoupled losses. The results showed that the surface area of the heater is a key parameter to determine the system performance. Best efficiency of 23.6% was obtained at increased heater surface area at the expense of the increased dead volume.

Shendage et al [67] investigated the effect of geometrical dimensions of a regenerator on beta-type Stirling engine performance. They used a thermodynamic analysis based on second-order simulation to evaluate engine performance. Different losses were accounted for in the analysis including reheat, shuttle conduction, pumping and heat exchangers effectiveness. The number of wire sheets in the regenerator were varied depending on the pressure drop, dead volume and the thermal penetration depth. They proposed a length of the regenerator of 22 mm that balanced the conflicting increased heat transfer and pressure drop due to the increase number of sheets which gave a regenerator an optimum effectiveness of 0.965.

Oberweis and Al-Shemmer [68] developed a thermodynamic model, to investigate the effects of the working gases such as hydrogen, helium and air, and charge pressure in the range of 1 to 15 bar, on a gamma-type Stirling engine performance. The developed model was based on Simple analysis taking into account the heat losses due to conduction caused by imperfect regeneration and heat exchangers pumping losses. The results showed that lower power losses were observed when using lower density working gases. The power output showed an increasing trend with increasing the charge pressure while the engine efficiency is increased up to 7.5 bar and then no significant change was depicted above this value.

Recent researchers incorporated finite speed thermodynamics with adiabatic analysis or new polytropic analysis. Hosseinzade and Sayyaadi [69] proposed a numerical adiabatic model

called (CAFS) which combines adiabatic analysis and finite speed thermodynamics (FST). Different loss mechanisms in the original Simple analysis were considered as well as the finite speed of pistons. It was shown that the deviation of the developed thermal model in predicting brake power, indicated power and thermal efficiency with +69.7%, +33.6% and +14.9%, respectively when compared to the experimental data of GPU-3 Stirling engine. Geometrical and operational parameters based on five objective functions were proposed and optimized.

Babaelahi and Sayyaadi [70] proposed a new thermal model called Simple-II which is based on modification of the original Simple analysis developed by Urielli and Berchowitz [8]. They included the gas leakage from the piston to the buffer space and the displacer shuttle losses into the differential equation of the model. They improved the accuracy of the model by including; the effect of piston finite motion using FST, mechanical frictional losses and the non-ideal heat exchangers.

In recent work of Babaelahi and Sayyaadi [71], they proposed a new thermal model called (PSVL) based on the assumption of polytropic processes of compression and expansion. Similar to Simple-II analysis, the different thermal and mechanical frictional losses were accounted for. The more recent work of authors [72] showed a modification of the original (PSVL) model in which the polytropic heat losses are coupled to convective heat transfer based on thermal resistance between gas and environment. Instead of linear temperature distribution of the regenerator, an exponential gas temperature distribution was proposed. Similarly, the FST is coupled with the new polytropic-convective model. The results were compared to the GPU-3 engine data and the previous models and significant accuracy of model predictions was reported.

From the above review, it can be concluded that the second-order analysis results in a reasonable accuracy, if the thermodynamic model includes the different loss mechanisms occurring in the engine, and requires less computational time. Therefore, it is very suitable for both early stages of engine design and optimization tasks.

2.2.4 Third-order analysis

The third order analysis proposed by Finkelstein [73], is a nodal analysis which includes applying the conservation of mass, momentum and energy at nodal points of the engine. The governing equations are solved implicitly in space and time. The transient start-up behaviour was not modelled as the periodic solution was used. This approach adds more complexity by coupling different energy losses into the governing equations. Therefore, this model may not be suitable for optimization purposes due to the increased computational time. There are few examples of codes which were reviewed by Dyson et al [74] based on third-order analysis. GLIMPS is a simulation code developed by Gedeon in 1986 and then in 1994 he proposed Sage code, which was based on the same methods in GLIMPS but it had a good feature of a friendly GUI, graphical user interface. It was reported that the application of the Sage code on Stirling simulation was first conducted by NASA. HFAST is another code developed by Huang [75] which was based on a linearized harmonic analysis. The periodic steady-state equations of mass, momentum and energy were solved in frequency domain.

Hooshang et al [76] proposed a model for gamma-type Stirling engine optimization based on neural network concepts. The thermodynamic code based on a third-order analysis was used to produce a dataset to recognise the relationship between inputs and outputs using a neural network and to search for optimum design parameters. The results showed that engine power and efficiency can be optimized to 878 W and 13.21% compared to a base case of 500 W and

8.5% by optimizing the three engine parameters of displacer stroke, phase angle and frequency of the engine.

Hoegel et al [77] investigated the influence of different operating parameters on alpha-type Stirling engine performance working with a low temperature heat source in the range of 100-200 °C. They used Sage software based on third-order analysis to find the optimum indicated power and efficiency of the engine. Fluid dynamics and thermodynamics imperfections were taken into account while friction, leakage and mechanical losses were omitted from study. Their results showed that for the considered LTD Stirling engine, the optimum frequency was found to be 30 Hz. The optimum phase angle was found to be higher than 90° that is normally assumed in HTD Stirling engines. They suggested that the optimum phase angle is around 160° and which was independent on engine frequency. Furthermore, heat exchanger design was optimized and a higher porosity for the regenerator was proposed.

Hooshang et al [78] developed a combined dynamic-thermodynamic model for gamma-type Stirling engine simulation. The dynamic response based on engine kinematic relations were linked to 1D third-order thermodynamic analysis code to evaluate the instant variation of engine parameters such as velocity, density, convective heat transfer and temperature in each engine chamber. Their code was able to predict engine power and rejected heat rate compared to experiment within maximum deviation of 11% and 18%, respectively.

Toghyani et al [79] conducted multi-objective optimization on a GPU-3 Stirling engine using third order thermodynamic code (Nlog). Four decision variables were considered in the optimization process to maximize engine brake power and thermal efficiency and minimize pressure drop; (hot end temperature, stroke, charge pressure and engine speed). It was shown

that by using Fuzzy decision making, power output and efficiency were enhanced by 600 W and 5.7%, respectively with the new optimize variables.

2.2.5 Fourth-order analysis

As the Stirling engine works by gas expansion and compression processes, the main physical processes involved are unsteady, transient, oscillating, laminar or turbulent, compressible flow and heat transfer. These complex processes combined with geometrical effects can be handled accurately with the adoption of fourth-order analysis or namely computational fluid dynamics (CFD) analysis. A CFD simulator usually involves five essential steps.; First, a computational aided design software to define the geometry under study. Second, discretization of the geometry by a suitable meshing software. Third, applying multi-physics and suitable boundary conditions to describe the problem. Fourth, a suitable technique to convert the governing equations, which are normally sets of partial differential equations, into a set of algebraic equations by using the Finite Element Method (FEM) or the Finite Volume Method (FVM). The final step is post-processing the results to be assessed or compared to experimental results.

However, this approach is quite challenging and computationally expensive to model the engine as a whole. In terms of full engine CFD modelling, the thermal equilibrium used in porous media analysis for modelling the regenerator is believed to be a poor assumption in oscillating flow environment since several degrees of temperature difference between gas and solid matrix are reported [18].

The Navier-Stokes equations are either for laminar or turbulent regimes contrasting with the actual flow situation in Stirling environment and hence transition from laminar to turbulent can

occur from one spatial location to another over the cycle based on the published results of oscillating flow rig testing. Therefore, more understanding of flow physics is still required.

The deformation of engine domains due to pistons movement as a result of gas compression and expansion needs to be handled through a complex algorithm to support moving (dynamic) meshes during the simulation. The time step in transient analysis plays a crucial role on convergence and accuracy of the simulation. Movements of the pistons until reaching the dead points, where the mesh is densely compressed, may require smaller time steps for better convergence and hence adaptive time stepping can be a good strategy to return results more accurately. Therefore, using this approach needs more sophisticated codes, and sometime manual tuning is required, in order to return more reasonable and accurate results.

There have been fewer studies on using CFD approach than other analysis methods for modelling the Stirling engine in general and for modelling gamma-type in particular. Some of the conducted research are focused on modelling the engine as a whole and other are primarily focused on CFD simulations of parts of the engine including the heater or the regenerator. Mahkamov [80] performed a second-order and 3D CFD analysis on a gamma-type Stirling engine prototype to enhance its power. The CFD results revealed that power reduction was attributed to the high level of hydraulic losses in the regenerator, and the entrapment of the gas in the pipe connecting the two parts of the compression space and to its large dead volume. A further improvement in the engine design was only viable by adopting this multi-dimension approach within an acceptable range of accuracy, 18% when compared to experimental results.

Chen et al [81] developed a 3D CFD code for twin power piston gamma-type Stirling engine. Several time-dependent parameters such as temperature, heat input, heat output and engine

power were calculated. The results showed that impingement is the key mechanism for heat transfer in expansion and compression chambers with non-uniform temperature distribution across the engine volume.

Chen et al [82] developed an in-house CFD model to simulate gamma-type LTD Stirling engine. Effects of several geometrical and operational parameters including pistons strokes, radius of power piston, hot and cold temperature difference and speed on engine performance were investigated. It was found that the increase in power piston radius strongly affected engine performance due to the increased compression ratio.

Salazar and Chen [83] developed an in-house CFD model to simulate beta-type Stirling engine. Heat transfer characteristics during injection (gas flow through displacer gap during compression) and ejection (gas flow through displacer gap during expansion) phases of the cycle were investigated. Non-uniform heating or cooling of gas was observed due to impingement heat transfer. However, a realistic filling regenerator was not incorporated in their model and was replaced by a regenerative channel for simplification purposes.

Wilson et al [84] conducted a 2D CFD simulation for Stirling Radioisotope generator (SRG). The study aims to characterize the thermodynamic losses resulting from the conjugate heat transfer in the convertor. They observed that energy balance was not well established and the prediction of the indicated power was not of the correct order of magnitude and hence improvements to the modelling code are being sought.

Torre et al [85] developed a 2D CFD model for 300 cm³ beta-type Stirling engine simulation based on OpenFoam code, taking into account turbulence effects and porous media modelling.

Parametric study was carried out to investigate the effect of charge pressure, heat input to the heater and regenerator material thermal conductivity on engine power. It was found that increasing both charge pressure and heat input increase engine power. Meanwhile, lower thermal conductivity material of the regenerator enhances the engine performance due the reduced axial conduction in the regenerator. It was reported that when using helium against air as working fluid, no significant difference in power output was observed.

Mahkamov [86] performed axisymmetric 2D CFD simulation of a solar “V”-type Stirling engine to accurately calculate the dimensions of a parabolic concentrator in a dish/Stirling system. Standard κ - ϵ turbulence model and dynamic meshing were used to analyse the different working spaces of the engine. The results of gas pressure, temperature and velocity field were compared to second-order mathematical analysis based on hydraulic losses consideration. It was reported that better accuracy in engine performance prediction was obtained using CFD model. He found that the temperature distribution in compression space is varying spatially at a given moment in which it differs from the harmonic behaviour with time.

Martaj et al [87] performed a 2D CFD analysis on LTD gamma-type Stirling engine. The solid displacer was replaced by a moving porous media. Using COMSOL multiphysics software, mass, momentum and energy equations were solved for both free and porous domains to obtain the instantaneous local variables such as pressure, temperature, density, velocity and volume. The results were compared to an experimental test bench and they showed good agreement. The porous displacer was further optimized in terms of its volumetric porosity in the range of 40% to 60% and it was found that the maximum power and efficiency were achieved at a porosity of 40%.

Li et al [88] performed a theoretical analysis on a Stirling engine fitted with porous-sheet regenerator. The regenerator is hexagonal-shaped flow channels, each flow channel has a side length of 0.4 mm and a length of 73 mm. They performed reciprocating flow and heat transfer analysis in a single channel including heater and cooler using dynamic mesh CFD simulation. They validated the results with an existing analytical solution and then performed the simulation of the engine as a whole. They found that, under the same working conditions, the pressure drop for porous-sheet regenerator is lower compared to wire mesh. Optimizing both regenerators based on minimum entropy generation rate under given operating conditions showed that the porous-sheet regenerator had 38%-51% lower entropy generation rate compared to wire mesh, thus contributing to an increase in power and efficiency of the engine. However, real testing of the engine with porous-sheet regenerator was not reported in his study.

Costa et al [20] developed a CFD model based on finite volume method (FVM) to derive Nusselt number correlations of two types of regenerator matrices; stacked and wound woven wires. The stacked woven wire correlation was first compared to an existing experimental correlation to validate the numerical method. Then, a correlation for wound woven wire is proposed covering the investigated parameters of a diameter range from 0.08 to 0.11 mm and a porosity range from 0.60 to 0.68. While, the numerical results showed no clear influence of wire diameter on Nusselt number.

Xu et al [89] studied experimentally and numerically the fluid flow and heat transfer characteristics of sandwich structures of wire-screen mesh under steady-state condition. CFD simulations were carried out for laminar flow regime with uniform heat flux boundary condition applied at the bottom faceplate. The friction factor correlation was found similar to that found for a staggered-cylinder arrays. It was deduced that solid conduction and forced convection

were the key transport mechanisms of heat transfer. The heat dissipation rate was strongly affected by matrix porosity, the density of surface area and solid–fluid conductivity ratio. An optimal value of porosity (80%) and solid–fluid conductivity ratio (250) were reported in the study.

It can be concluded from the carried out review on the fourth order analysis that this analysis is more comprehensive by which the complex transport mechanisms taking place inside the engine can be captured accurately within the internal circuit of the gas. Moreover, fewer CFD studies were reported in literature than the first- and second-order analysis methods on the analysis of Stirling engines. This highlights that there is need for further development of the CFD approaches implemented on Stirling engine modelling.

2.3 Review of previous experimental work

Different experimental studies were reviewed in this section on the development of a Stirling engine or on a specific part of the engine such as the regenerator. Chen et al [90] constructed and tested a twin power piston gamma-type Stirling engine. The engine was incorporated with a moving regenerator housed inside its displacer and filled with a woven-screen material. The effects of different regenerator parameters on engine performance, including regenerator material, wire diameter, filling factor and stacking arrangements, were investigated. According to their results, copper material was found superior by 10%-20% to stainless steel on engine performance at the tested conditions and optimum filling factor of (0.00206) was proposed.

Gheith et al [91] conducted an experimental investigation on the optimum regenerator matrix material and porosity for gamma-type Stirling engine. Different materials were tested including

stainless steel, copper, aluminium and Monel 400. The results showed that stainless steel matrix with 85% porosity is the best configuration to maximize engine performance.

Gheith et al [92] studied experimentally a new phenomenon associated with gamma-type Stirling engine causing a thermal energy dissipation in the regenerator. They observed that a maximum temperature difference of 25 K between regenerator two sides can occur at heater temperature of 200 °C. The asymmetry of the engine and the one inlet of the cooling circuit were thought to cause this phenomenon. They carried out multi objective optimization to find the optimum operating values that minimizes this temperature difference in the regenerator and they found that heating temperature of 350 °C, initial pressure of 8 bar and cooling water flow rate 8.1 L/min can minimize this temperature difference to 17 K.

Cinar and Karabulut [93] fabricated and tested gamma-type Stirling engine using air and helium as working fluids and electrical furnace as a heat source. Heating temperatures were varied in the range of 700 to 1000 °C and the charge pressure in the range of 1 to 4.5 bar. It was found that maximum power was achieved by using helium at 1000 °C and 4 bar. On the other hand, two displacer cylinders were tested; one had smoother inner surface and the other had an augmented inner surface with triangular span-wise slots. The results showed that when heat transfer surface areas increased by 20%, the engine power had increased by 23%. These results were found encouraging to initiate a design of 1kW Stirling engine. The same author in another study [94] investigated two different displacer materials; aluminium alloy and medium density fibreboard (MDF). Hot end temperature was varied using liquefied petroleum gas burner. Maximum engine torque and power were obtained using MDF material because of its lower thermal conductivity and lower density compared to aluminium alloy.

Sripakagorn and Srikam [95] designed and tested a beta-type Stirling engine for solar power generation. Typical heating temperatures between 350-500 °C were aimed to be supplied by parabolic solar collector. The regenerator was filled with (#80) wire mesh. It was found higher specific power can be achieved when operating the engine at moderate temperature difference rather than at higher temperature ones based on West number which allows the adoption of simple engine design with low cost materials.

Karabulut et al [96] developed and fabricated a beta-type Stirling engine with new lever mechanism. Low and medium temperature heat sources were used to run the engine in the range of 200-500 °C. Two displacer cylinders were proposed; one had smoother inner surface and the other had an augmented inner surface. It was shown that power was boosted by 50% with the augmented cylinder compared to the smooth one. The results showed that adapting the new lever mechanism enabled the engine to approach ideal Stirling motion. Based on their analysis, the highest work per cycle was achieved using lever-drive compared to crank and rhombic-drive engines.

Damirchi et al [34] designed and tested a 580 cc helium-charged gamma-type Stirling engine run by biomass energy obtained by burning biomass and agriculture wastes. Schmidt theory was adopted to analyse the engine thermodynamically. The heat source temperature was in the range of 370 – 410 °C. The maximum measured brake power of 96.7W was obtained at heating temperature of 550 °C, charge pressure of 10 bar and speed of 700 rpm. It was found that most of the power (46 W) is produce from sawdust while trees wood generates low power of (21 W). This compares 4 min and 10 min, respectively as the ignition time required to burn sawdust against the pruned trees. The obtained results encouraged to start a new design of 1 kWe Stirling engine for rural electrification.

Isshiki et al [97] tested two atmospheric Stirling engines that were manufactured with pin-fin array heat exchangers for the heater and the cooler. The adoption of this configuration of heater allows the engine to be directly heated by solar energy or electric heating. The first engine was a large beta-type with total of 1.7 Litre swept volume and two types of regenerators were tested on this engine; layered-plate type regenerator and #5 stainless steel wire-mesh. The second engine was a small Yoke-Ross drive alpha-type fitted with #5 stainless steel wound wire-mesh. Measurements were carried out on the two engines to show the impact of pin-fin type heat exchangers and regenerators types on engines performance. It was concluded that the shaft power was improved by 36% for beta type and 17% for alpha type. Also, the maximum shaft power was achieved at lower temperature difference when using layered-plate type regenerator compared to the conventional wire-mesh.

Nam and Jeong [98] developed a parallel wire type regenerator. The friction factor was found to be 20-30% lower than the screen mesh regenerator, but the thermal performance of this new type was poor compared to the screen mesh type due to large axial conduction of parallel wires. The axial conduction losses were further alleviated by the segmentation of the continuous wires but the number of segmentation was limited due to the increased number of housings required to hold the wires.

Takizawa et al [99] proposed and developed a thin porous-sheet regenerator with small rectangular-shaped flow holes. The effect of this type regenerators and other two wire screens were tested on an experimental engine stand (NS03T). The results showed that the engine power output was improved by 15% compared to 200M wire sheet.

Ibrahim et al [100] developed a segmented-involute-foil regenerator to minimize the pressure drop effects of cylinder cross-flow and to avoid the large axial conduction losses such as in the case of parallel plates and tube bundles. Their test results showed that higher figure of merit was achieved closer to the ideal parallel-plate regenerators. However, the LiGA technique used for fabrication proved to be not cost effective.

Zhao and Cheng [101] investigated experimentally the cyclic pressure drop in packed columns of woven screen under oscillatory flow condition. The experimental results were based on 92 runs. It was found that the kinetic Reynolds number and the dimensionless fluid displacement were the key parameters influencing the oscillatory pressure drop factor. The results revealed that the cycle-averaged pressure drop through the packed column based on the oscillatory flow is several times higher than that of a steady flow at the same Reynolds number based on the cross-sectional mean velocity.

Yanagawa et al [102] reconstructed a cryogenic Stirling engine from beta-type Stirling refrigerator. The modified engine is heated by warm water at 40 °C and cooled by liquid N₂ (at -169 °C) or by dry-ice/methanol (at -69 °C). The helium-charged engine performance was investigated at different engine speeds and cooling temperatures. It was found that maximum power of (160 W) was achieved at engine speed of 1030 rpm and 1.24 MPa charge pressure. They obtained a figure of merit (FOM) of 1.35 which is defined as the ratio between the power output and the consumed cold energy. From their experimental results, they highlighted the potential of cryogenic Stirling engine to utilize the stored cold of liquid gases such as LN₂, LNG or liquefied oxygen.

Kato and Baba [103] proposed a methodology to evaluate the regenerator performance based on experiments. The experimental test facility was similar to that of a 180°-phase angle alpha-type Stirling engine. An electric heater was used to control the hot end temperature while the cold end temperature was controlled by a conditioned air. The LTD engine was tested with polyurethane foam and #18 stainless steel as regenerators. The regenerator effectiveness was calculated in terms of the measured temperature fluctuation between the hot and cold ends. The results showed that regenerator effectiveness of the stainless steel mesh layered parallel to gas flow direction was significantly less in comparison to that of the normal mesh layers while a significant pressure loss was observed for the polyurethane foam when fitted in cylinder/displacer gap.

Hirata et al [104] developed and analysed a small 100 W beta-type Stirling engine. The engine can be heated by either flue gases or directly by solar energy. A moving regenerator is fitted in the displacer piston. An isothermal thermodynamic analysis coupled with thermal, pressure, leakage in buffer space and mechanical losses was developed to predict the performance of the prototype. The engine was tested by using nitrogen and helium as working gases at different operating parameters. It was found that the indicated and brake powers in case of nitrogen is 10% higher than that of helium and this was attributed to that buffer space leakage in case of helium is twice of that nitrogen.

2.4 Review on transient testing techniques of heat exchangers

The proper utilization of energy resources can lead to a successful development of an efficient and cost-effective heat exchangers. A heat exchanger is a device that transfers thermal energy between a solid object and a fluid or between two or more fluids. Various types of heat exchangers are widely used in industry and production lines.

An accurate evaluation of heat transfer coefficient between fluid and solid interfaces in heat exchangers is required when fluid flow is so ill-defined. Based on the channel hydraulic diameter, heat exchangers can be classified into; conventional channels ($D_h > 3 \text{ mm}$), mini-channels ($3 \text{ mm} \geq D_h > 200 \mu\text{m}$) and micro-channels ($200 \mu\text{m} \leq D_h \leq 10 \mu\text{m}$) [105]. It is difficult to measure heat transfer coefficients in micro /mini channels heat exchangers due to small pore size and the unavailability of such tiny probes to measure the channels surface temperature.

The thermal performance of heat exchangers and thermal regenerators are commonly evaluated by single-blow technique. This transient technique is cost-effective and less time consuming compared to steady state method. The methodology is simple and it is composed of three steps; an experiment, theoretical model and a matching technique. In the test facility, the sample (heat exchanger) undergoes a step change in temperature at the inlet, depending on fluid type and matrix heat capacity, the outlet temperature breakthrough is sampled to be compared with any appropriate theoretical model.

Hausen [106] originally formulated a mathematical model for the transient method. Schumann [107] solved analytically the transient problem. Locke [108] showed that a unique relationship exists between the maximum slopes of the outlet response curves and the number of heat transfer units (NTU) for a step change for the fluid at the inlet of the heat exchanger but the effect of axial conduction was not accounted. The Schumann-Hausen model was found unrealistic based on the assumptions made. Loehrke [109] showed that it is not practical to conduct an experiment with an ideal temperature step change.

With the knowledge of the mathematical formulation of the inlet temperature curve, it became possible to use an arbitrary fluid temperature. Exponential fluid inlet variation was reported by Liang and Yang [110], Cai et al. [111] and Loehrke [112]. Moreover, the core matrix or heat exchanger is in contact with walls and in many applications, the adiabatic wall is a poor assumption. In other words, the outlet fluid temperature is influenced by the heat losses dissipated to the walls in the test section. Chen and Chang [113] showed that in their experiment that the NTU values were underestimated by 30% due to the adiabatic wall assumption. In addition, the Joule-Thomson effect is more common when the flow encountered a restriction causing the fluid temperature to rise or drop. Chen et al [114] showed that considering this effect for a wire regenerator (No 200), the drop in outlet temperature was 3% when higher pressure drop was achieved at 0.2 MPa.

Other researchers have improved the Schumann-Hausen model to correctly match the experiments of single-blow method. Pucci et al [115] included the effect of axial conduction and improved Locke's analysis. They showed that this effect is dominant when the NTU value >2 . It followed that some researchers included radial conduction effect due to the non-uniformity of flow [116]. Hegg and Burns [117] showed that neglecting longitudinal or transverse conduction or idealizing the temperature input function as an ideal step may cause inaccurate estimation of heat transfer processes.

A comprehensive review on transient techniques are provided in [118]. Different evaluation techniques have been developed to compare the predicted and measured fluid exit temperature histories; maximum slope method [108], Selected point matching technique [110], Differential fluid enthalpy method (DFEM) [119] and Direct curve matching [117]. Mismatching between the experiment and the model can be potential and far from correct even if two methods give

similar results. Loehrke [109] recommended pre-calibration of the test facility with a well-known core performance. However, more recently, both the maximum gradient technique and curve matching at multiple points are used [113], [116], [120], [121] and [122]. Optimization of heat emission and pressure drop of mini-channel by regulating the channel size and length has been recently investigated by [105].

Extensive reviews were conducted on micro/minichannels in terms of heat transfer and pressure drop characteristics of single and two-phase flow [123] and [124]. They showed that pressure drop from experimental data in little agreement with prediction. In terms of thermal behavior, the agreement is becoming closer when the hydraulic diameter increases for single phase flow. In small scale of microchannels ($1 \mu m$), the rarefied gas effects come into play [125]. Three regimes of flow are encountered depending on Knudsen number (mean free path/characteristic length); continuum flow, slip flow and free-molecular flow.

Mini-channel heat transfer is an active area of research due to its light weight, compactness and high heat transfer rate. Caney et al [126] conducted an experimental study on friction losses and heat transfer of single-phase flow in a mini-channel. They showed that the experimental frictional pressure drop measurements agree accurately with the conventional correlations while the temperature profile along the channel length deviates from the linear trend due to axial wall conduction. Liu and Yu [127] showed that mini-channel heat sink performance can be enhanced by using non uniform baffles at the inlet of channels which provide more uniformity of the temperature. On the other hand, Khoshvaght-Aliabadi et al [128] proposed sinusoidal-wavy mini-channel heat sink to enhance the cooling process. They found that the thermal performance was augmented when reducing wave length and increasing wave amplitude. The adoption of CFD specifically in the design and optimization of heat exchangers was intensively

reviewed by Bhutta et al [129] proving its efficiency and accuracy. Ranganayakulu et al [130] employed CFD simulations for the transient testing of offset and wavy fins of compact plate-fin heat exchangers. The NTU values of five samples were determined by using maximum slope method. The j-Colburn factors obtained from experiment and CFD were compared within 12% maximum deviation.

2.5 Summary and knowledge gap

From the conducted literature review, it can be concluded that modelling gamma-type Stirling engines with non-ideal adiabatic analysis was widely reported in literature. However, in all previous models, the connecting pipe that connects both the lower part of the expansion space and the compression space is always omitted from analysis. This dead volume (connecting pipe) is higher in this type of engine compared to other engine configurations. Therefore, the gas mass that transfers from the compression cell to the cooler back and forth is not correctly computed and hence the heat exchange in other spaces of the engine, based on Reynolds number, is under-estimated. On the other hand, this causes a deviation in minimum and maximum cyclic pressures and hence a deviation between the calculated average cyclic pressure from the model simulation and the predefined charge pressure.

On the other hand, CFD modelling of the current high temperature differential (HTD) Stirling engine prototype (ST05CNC) as a whole has not been reported in the literature. All previous studies [41, 76, 78] on the same engine configuration were based on second- and third-order models with a prediction accuracy ranging from 11-18%. Usually, such models were tuned to fit experimental data due to their dependency on empirical coefficients such as heat transfer leading to limited application. In contrast, CFD approach can be applied to any Stirling engine type as all variation of a parameter is inherently embedded in the Navier-Stokes equations.

Additionally, there has been little work conducted in the field of parallel-geometry regenerators for Stirling engine applications. Therefore, there is room for the investigation of new geometries and configurations. Finally, there has been very little research reported in open literature on using combined experimental and CFD approach in transient testing of heat exchangers.

CHAPTER 3

EXPERIMENTAL TEST FACILITY OF THE RESEARCH ENGINE

3.1 Introduction

In this chapter, a description of the Stirling engine test facility built at the department of Mechanical engineering of University of Birmingham was presented. The chapter is divided into four sections including engine description, instrumentations, performance analysis and uncertainty analysis.

3.2 Engine description

The engine was a gamma-type that was first designed by Dieter Viebach in 1992 in Germany to promote microgeneration with biomass fuels and since then was opened for research development [131]. The engine, shown in Figure 3-1, consists of power and displacer pistons with 90° phase angle, and three heat exchangers (heater, cooler and regenerator) and a connecting pipe.

The expansion and compression spaces are connected via a 30-mm concentric-cooled pipe. Meanwhile, the engine is heated up to 650 °C by an external electric heating unit and cooled by a circuit of cooling water normally at 15 °C. The geometrical and operational parameters of the engine are listed in Table 3-1.

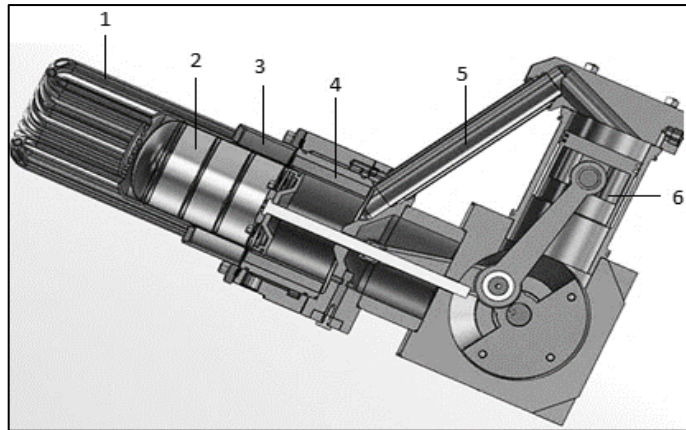


Figure 3-1 Engine components: 1-Heater, 2-Displacer piston, 3-Regenerator, 4-Cooler, 5-Connecting pipe, 6-Power piston.

Table 3-1 Engine’s geometrical and operational parameters.

Parameter	Value/description
Nominal rotational speed (rpm)	500
Stroke (mm)	75
Power piston bore (mm)	85
Displacer piston bore (mm)	96
Charge pressure (bar)	10
Working gas	N ₂
Heater type	Tubular
Cooler type	Finned
Regenerator type	Random fibre
Wire diameter (Micron)	31
Porosity	0.9
Hot source temperature (°C)	650
Inlet water temperature (°C)	15
Water flow rate (L/min)	3.5
Water cooling power (kW)	2.3
Compression ratio	1.3

The main heater of the engine is a tubular heat exchanger consisting of 20 tubes made of stainless steel with 6mm inner diameter. The engine is heated externally by an electrical heater hood (EHH70) shown in Figure 3-2. The heater assembly is designed to precisely control temperatures of the heater-head for laboratory experiments. The heater hood has some features

including; three-phase electrical heating, robust tubular heating elements with electrical heating capacity of 7kW to achieving temperatures up to 850 °C within the heater hood, thermally insulated heating chamber, coaxial stainless steel design with fan to cool outer surfaces, robust type 'K' (Chromel-Alumel) thermocouple for precise sensing and control of the hood-temperature, hot air fan within the heating chamber for even temperature distribution and efficient heat transfer and optional control cabinet with digital temperature controller and solid state relays (SSR).

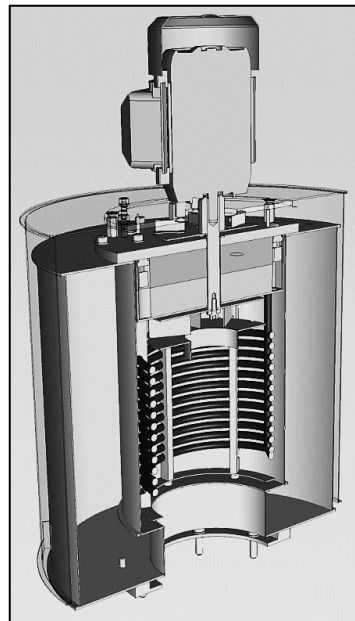


Figure 3-2 Electrical heater hood (EHH70).

The cooler, shown in Figure 3-3, is an aluminium finned type heat exchanger. The inner working gas passages are cooled by an external cooling water circuit in cross-flow heat exchanger configuration. The free flow area is structured with 144 internal fins, 1 mm by 10 mm cross sectional area each, with a volumetric porosity of 38.1%. The volumetric porosity was calculated from the internal dimensions of the cooler as,

$$Porosity_{cooler} = \frac{A_{free\ flow}}{A_{total}} = \frac{(10 * 1) * 144}{\frac{\pi}{4}(125^2 - 104^2)} = 0.381 \quad 3.1$$



Figure 3-3 Cooler of the engine.

The average value of the coolant power or heat rejection from the engine can be calculated directly from;

$$\dot{Q}_c = \dot{m}_w C_{pw} \Delta T \quad 3.2$$

Where, (ΔT) is the temperature difference between the measured coolant inlet and outlet temperatures, (C_{pw}) is the specific heat capacity of cooling water, calculated at inlet cooling temperature. The cooling water mass flow rate (\dot{m}_w) is calculated from the measured volume flow rate (\dot{V}_w) and the calculated water density at cooling inlet temperature (ρ_w) from eq. (3.3),

$$\dot{m}_w = \rho_w \dot{V}_w \quad 3.3$$

The calculation of the heat rejected by the engine is necessary to calculate the engine thermal efficiency in terms of shaft power and cooling power.

The regenerator (Figure 3-4) is fitted inside a housing cylinder of 134 mm outer diameter and 98 mm inner diameter and filled with a stainless steel random fibre of 31-micron wire diameter equally in a direction normal to the flow direction with 90% volumetric porosity. In order to precisely define the volumetric porosity of the matrix, a filing factor of 0.1 is normally obtained corresponding to a weight of the matrix of 250 g. A very important step in assembly to ensure that the wire matrix is free from any oil. To achieve this the matrix should be heated-up to 330 °C before stuffing, then any particles are removed using a compressed air jet. This will make the heater head as well free from impurities or wire particles.



Figure 3-4 Regenerator of the engine

3.3 Instrumentations and performance analysis

The engine is instrumented with eight k-type (NiCr-Ni; Chromel-Alumel) thermocouples with $\pm 0.75\%$ of overall range accuracy at steady state fitted in different locations of the engine, as shown in Figure 3-5, for local temperature measurements; compression space, cooling water inlet, cooling water outlet, cooler working gas, regenerator cold end, regenerator hot end, heater working gas and heater wall. The gas temperature thermocouple in heater tube is passed through a shield tube from the cooler then through the regenerator matrix and positioned in the middle of the tube. The heater wall is measured by single thermocouple positioned at the outer wall.

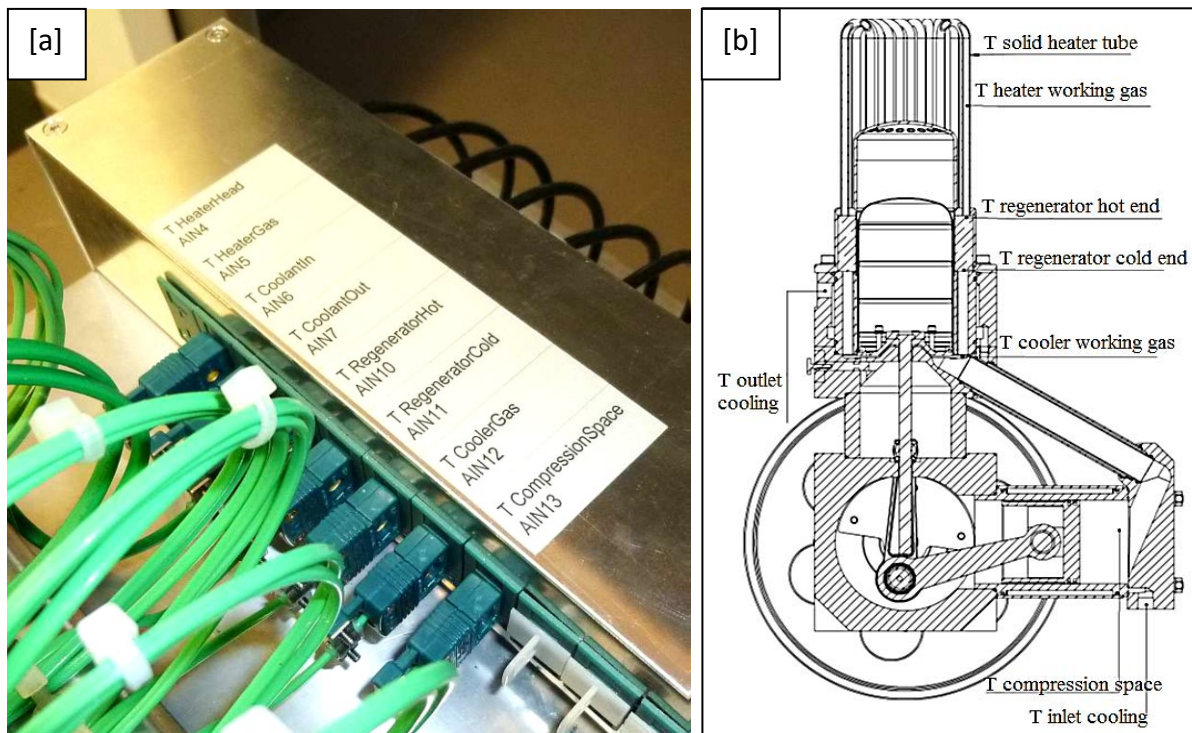


Figure 3-5 Thermocouples positions of the test engine, a) actual, b) schematic.

There is a limitation to measure the working gas pressure at the hot side of the engine, in which the sensor must be highly resistant against high temperatures and has low response time. Therefore, the gas pressure is measured in the power piston chamber which is maintained at the cold end temperature. A piezo-type pressure sensor, shown in Figure 3-6, with an accuracy of

0.04 bar (0.2% FSO) is fitted at the TDC of the compression space to measure the absolute gas pressure with a relatively high and constant sampling-rate of about 1 kHz, to ensure high sampling resolution with respect to the crank-shaft angle. This sampling-rate ensures that even at rotational crank-shaft velocities of 1500 rpm of the engine, at least every 10° of the rotation, a sample of the pressure will be taken. At lower velocities, the angular resolution will be even better, where a sample of the pressure can be every 1°. The pressure sensor body is kept at an acceptable range of temperature via a cooling adapter which is linked to the cooling water circuit. The power piston cylinder is specially designed to hold both sensor and cooling adapter.

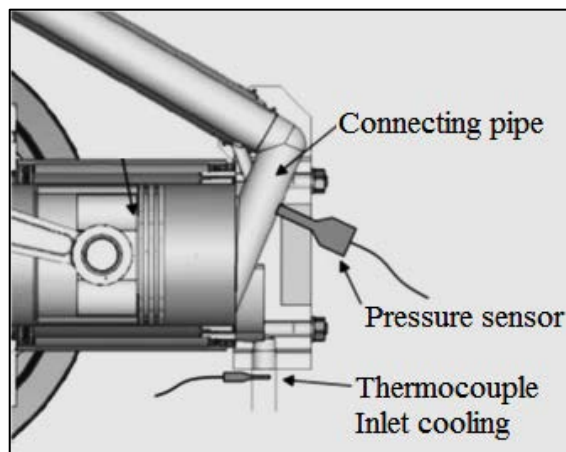


Figure 3-6 Pressure sensor location.

The whole test facility of the engine is shown in Figure 3-7. The engine is coupled with a dynamometer (6-pole 3-phase AC squirrel-cage asynchronous induction motor) in conjunction with a 3-phase frequency-inverter. Between the coupled dynamometer and the engine, a torque gauge, incremental encoder and an inductive initiator are installed to measure the torque, crank-shaft angle and engine speed, respectively.

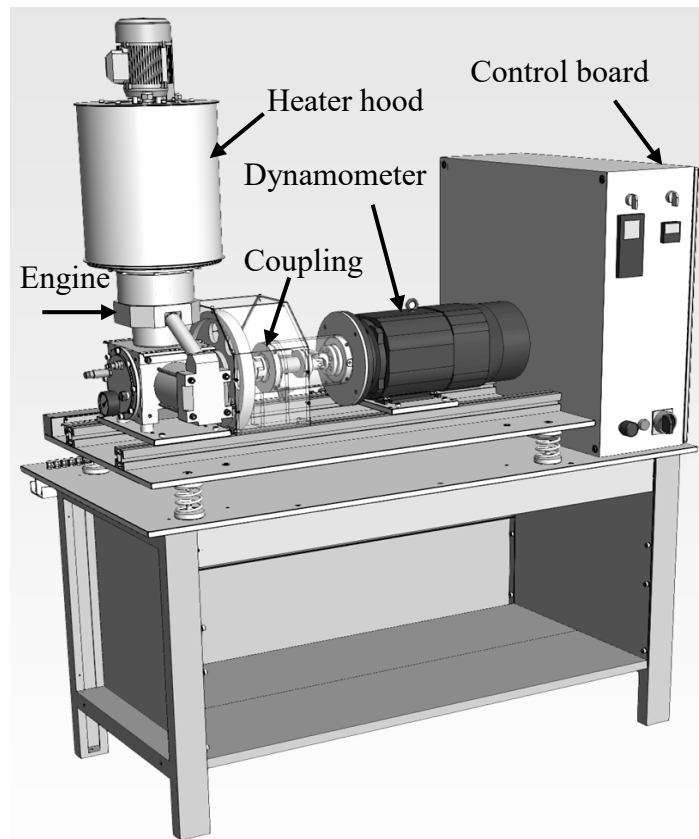


Figure 3-7 whole test facility of the engine.

The cyclic torque during one revolution, shown in Figure 3-8, is measured with a fast and accurate torque gauge of 0.05 N.m accuracy with a nominal measured value of 13 N.m up to a peak value of 50 N.m. The mean torque used for power calculation is based on the arithmetic mean of maximum and minimum cyclic torques. The measured speed by the incremental encoder is up to 1500 rpm with an accuracy of 4.2 rpm.

A reverse mode of operation (heat-pump or refrigerator) is also supported for the current test facility. The electrical power generated from the engine is dissipated in a thermal resistor rather being fed back to the mains power supply. The acquisition of all signals is handled by Ethernet-based data acquisition system (LabJack T7 Pro) which enables a LabVIEW-based PC to monitor and control the operation of the engine at different setting parameters including hot end

temperature, cold end temperature, charge pressure and engine speed. The volume variation is calculated by LabVIEW based on the crank-shaft angle and the kinematics of the engine. The equation of motions, eq. (3.4) and eq. (3.5), for each piston is predefined in LabVIEW environment and hence the volume variation is calculated for the generation of the indicated PV diagram as shown in Figure 3-8.

$$X_e = r \left[1 - \cos \theta + \frac{1}{\lambda_e} \left(1 - \sqrt{1 - \lambda_e^2 \sin^2 \theta} \right) \right] \quad 3.4$$

$$X_c = r \left[1 - \cos(\theta - \pi/2) + \frac{1}{\lambda_c} \left(1 - \sqrt{1 - \lambda_c^2 \sin^2(\theta - \frac{\pi}{2})} \right) \right] \quad 3.5$$

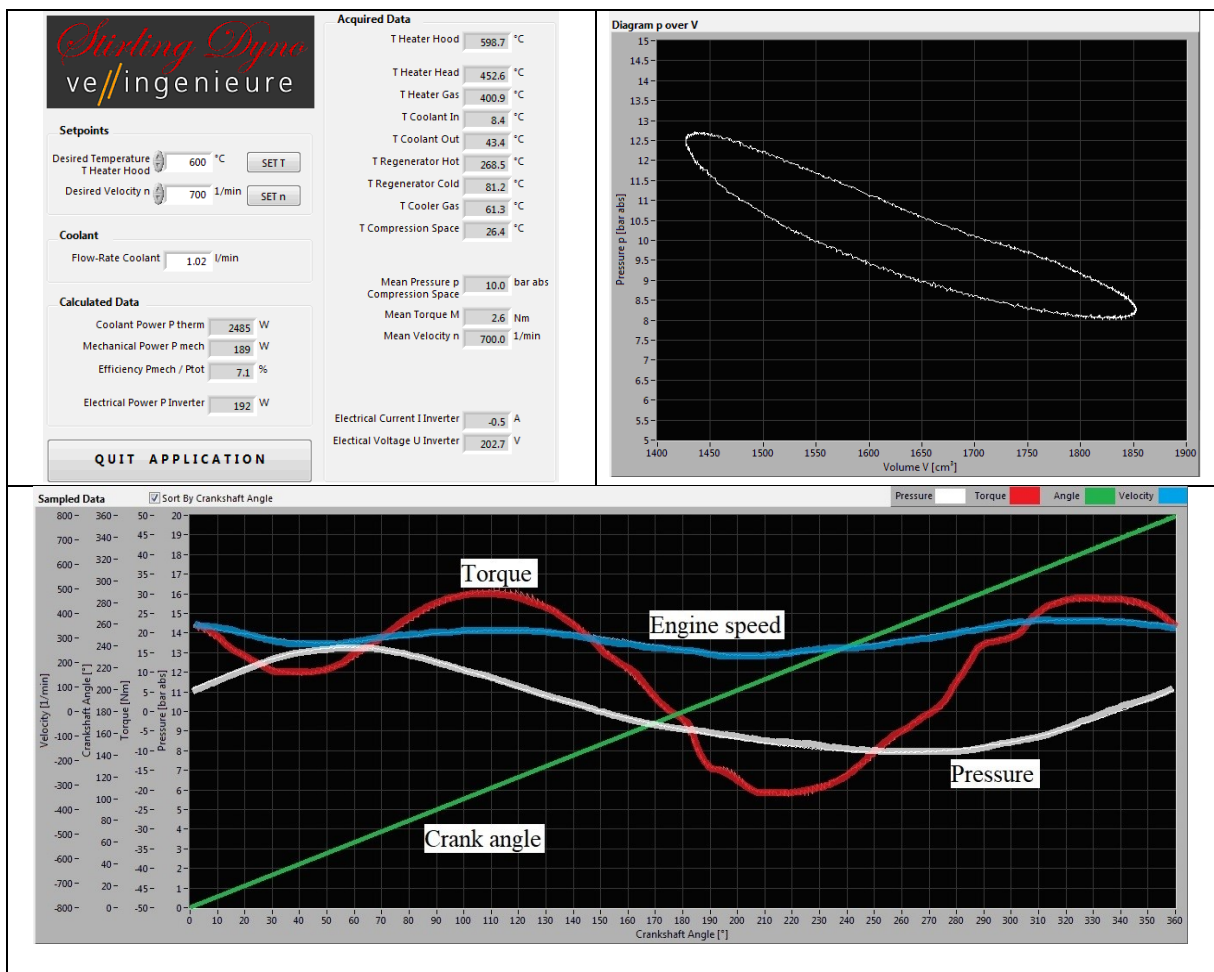


Figure 3-8 LabVIEW experimental data screen-shot.

The thermal power is reasonably assumed to be found in the coolant including any other thermal losses since the heater hood, which is the heat source, is perfectly insulated as well as the heat loss from the outer walls of the regenerator to the ambient is not significant due to the small surface area exposed to the surrounding. The procedure of calculating the thermal efficiency of the engine was further tested by the test facility manufacturer during the commissioning stage of the engine [131]. Based on the calculated shaft power (\dot{W}_s) from measured mean torque and rotational speed and the calculated coolant power (\dot{Q}_c) from eq.(3.2) and eq.(3.3), the thermal efficiency of the engine can be calculated from eq.(3.6),

$$\eta_c = \frac{\dot{W}_s}{\dot{Q}_h} \approx \frac{\dot{W}_s}{\dot{W}_s + \dot{Q}_c} \quad 3.6$$

3.4 Uncertainty analysis

Uncertainty analysis is performed on engine measured parameters using the method presented by Moffat [132]. All sources of uncertainties may be linked to the inaccuracies of sensors, data acquisition system, junctions and electrical disturbance. The effect of the uncertainty in a single measurement (X_i) on a calculated result (R), if only that one measurement were in error would be,

$$\delta R_{X_i} = \frac{\partial R}{\partial X_i} \delta X_i \quad 3.7$$

The partial derivative of (R) with respect to (X_i) is the sensitivity coefficient or the relative uncertainty for the result (R) with respect to the measurement (X_i). When several independent

variables are used in the function R, the individual terms are combined by a root-sum-square method.

$$R = \left\{ \sum_{i=1}^N \left(\frac{\partial R}{\partial X_i} \delta X_i \right)^2 \right\}^{\frac{1}{2}} \quad 3.8$$

This is the general equation of uncertainty analysis adopted from [132]. The uncertainties in measuring the indicated power (\dot{W}_I), coolant power (\dot{Q}_c), shaft power (\dot{W}_s) and thermal efficiency (η) of the engine using eq. (3.8), can be expressed in terms of their dependent variables as;

$$\frac{\partial \dot{W}_I}{\dot{W}_I} = \left[\left(\frac{\partial p}{p} \right)^2 + \left(\frac{\partial V}{V} \right)^2 \right]^{1/2} \quad 3.9$$

Where p and V are power piston pressure and volume variation, respectively.

$$\frac{\partial \dot{Q}_c}{\dot{Q}_c} = \left[\left(\frac{\partial T_{wi}}{T_{wi}} \right)^2 + \left(\frac{\partial T_{wo}}{T_{wo}} \right)^2 + \left(\frac{\partial \dot{V}}{\dot{V}} \right)^2 \right]^{1/2} \quad 3.10$$

Where (T_{wi}), (T_{wo}) and (\dot{V}) are measured inlet cooling temperature, outlet cooling temperature and cooling water flow rate, respectively.

$$\frac{\partial \dot{W}_s}{\dot{W}_s} = \left[\left(\frac{\partial \tau}{\tau} \right)^2 + \left(\frac{\partial \omega}{\omega} \right)^2 \right]^{1/2} \quad 3.11$$

Where (τ) and (ω) are the measured torque and engine speed, respectively.

$$\frac{\partial \eta}{\eta} = \left[\left(\frac{\partial \dot{W}_s}{\dot{W}_s} \right)^2 + \left(\frac{\partial \dot{Q}_c}{\dot{Q}_c} \right)^2 \right]^{1/2} \quad 3.12$$

All measured parameters and their uncertainties are tabulated in Table 3-2. The highest uncertainty, 2.88%, is recorded for thermal efficiency due to the relative uncertainties in measuring cooling water flow rate, inlet water cooling temperature, outlet water cooling temperature.

Table 3-2 Uncertainty analysis for measured parameters.

Device	Manufacturer	Measurement	Full Scale	Accuracy	Uncertainty
Torque-gauge	Lorenz	Torque	1-50 N.m	0.05 N.m	0.1%
Thermocouple, k-type	Thermibel	Temperature	-200-250 °C	2.5 °C	1%
Thermocouple, k-type	Thermibel	Temperature	-200-1100 °C	10 °C	0.9%
High pressure sensor	Kistler	Pressure	0-20 bar	0.04 bar	0.2%
Incremental encoder	Lorenz	Velocity	0-1500 rpm	4.2 rpm	0.28%
Flowmeter	Influx	Flowrate	1-10 L/min	0.25 L/min	2.5%
-	-	Indicated power	-	-	0.2%
-	-	Cooling power	-	-	2.87%
-	-	Shaft power	-	-	0.3%
-	-	Thermal efficiency	-	-	2.88%

CHAPTER 4

ENGINE THERMODYNAMIC MODELLING

4.1 Introduction

As reviewed in chapter 2, analysis techniques of Stirling engine were summarized. Ideal isothermal analysis or Schmidt analysis cannot be used to predict the actual performance of an engine as it assumes that the heat exchangers of a Stirling engine are redundant. It follows that the assumption of compression and expansion working spaces are kept at the respective cooler and heater temperatures will lead to a paradoxical statement that none of the heater or the cooler make a contribution to the net cyclic heat transfer and hence are redundant. In isothermal working spaces, all heat transfer is taking place across the boundaries which tends to be incorrect as the cylinder walls are not specifically designed for heat transfer. In real engines, the compression and expansion spaces tend to be adiabatic rather than isothermal. This implies that the heat exchangers must contribute to the net heat transferred over the cycle.

Therefore, in this chapter the development of an enhanced thermodynamic model based on a modified adiabatic analysis under second-order approach is described. This approach is widely used in literature as it is robust, computationally inexpensive and reasonably accurate compared to third- and fourth order methods. Then the next chapter (5) will be devoted for the development of a CFD approach for the simulation of gamma-type Stirling engine.

4.2 Thermodynamic model

The engine is reconfigured as six cells with the expansion and compression cells assumed to be adiabatic in which no heat is transferred to the surrounding. Energy is transported across the cells interfaces by means of enthalpy change in terms of mass flow and upstream temperature. As depicted in Figure 4-1, (c, k₁, k₂, r, h, e) represent the six engine cells; compression space, connecting pipe, cooler, regenerator, heater and expansion space, respectively. While (ck₁, k₁k₂, k₂r, rh, h_e) represent the five interfaces between cells. The system can be regarded as quasi-steady flow by neglecting the acceleration effects of the five mass flow variables. This can reduce the problem into a set of ordinary differential equations that can be solved simultaneously. Solving these equations can be more simplified by formulating them as an initial-value problem. Due to the cyclic nature of the system, the initial values can be arbitrarily defined, and then integrating the equations over several cycles until the cyclic steady state is reached.

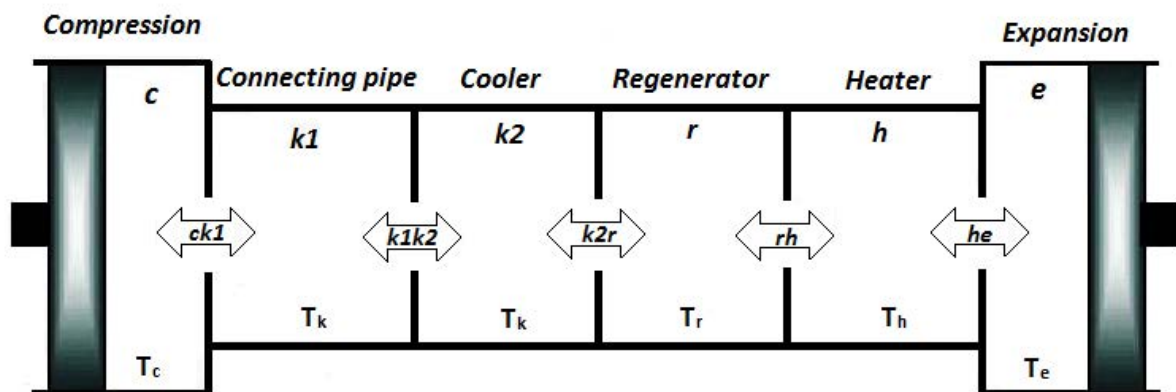


Figure 4-1 Reconfigured adiabatic model with six engine cells.

4.3 Derivation of real volume variation

The pistons of engines with conventional crank drives carry out an asymmetric, accelerated and decelerated motion. The crank shaft rotates with an almost simultaneous angular velocity. The movement of the connecting rods arises from the actions of the pistons and the crank shaft. The current distance of the piston to its upper dead point is called the piston motion S . For the derivation of the real piston motion Figure 4-2 is needed [58]. Thus:

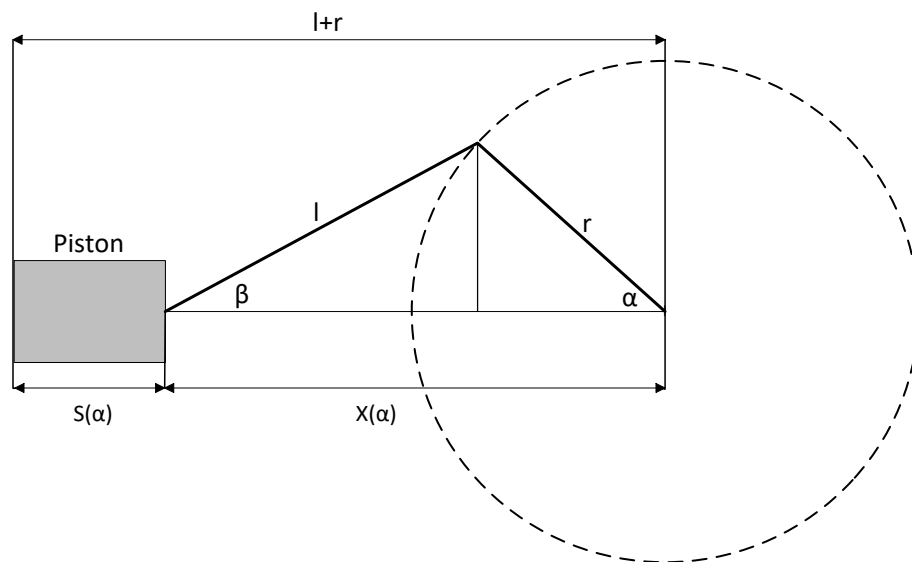


Figure 4-2 Sketch of conventional crank mechanism.

$$S(\alpha) + X(\alpha) = r + l \quad 4.1$$

$$S(\alpha) = r + l - X(\alpha) \quad 4.2$$

The distance of the piston to the bearing point of the crank shaft x can be derived as:

$$X(\alpha) = r \cos \alpha + l \cos \beta \quad 4.3$$

$$l^2 = (l \cos \beta)^2 + (r \sin \alpha)^2 \quad 4.4$$

$$l \cos \beta = \sqrt{l^2 - (r \sin \alpha)^2} \quad 4.5$$

Eq. (4.3) can be re-written as:

$$X(\alpha) = r \cos \alpha + \sqrt{l^2 - (r \sin \alpha)^2} \quad 4.6$$

Defining the connecting rod ratio, λ as

$$\lambda = r/l \quad 4.7$$

Then eq. (4.6) can be simplified further into:

$$X(\alpha) = r \cos \alpha + l \sqrt{1 - (\lambda \sin \alpha)^2} \quad 4.8$$

Setting this equation for x into eq. (4.2)

$$S(\alpha) = r + l - r \cos \alpha - l \sqrt{1 - (\lambda \sin \alpha)^2} \quad 4.9$$

$$S(\alpha) = r(1 - \cos \alpha) - l(1 - \sqrt{1 - \lambda^2 \sin^2 \alpha}) \quad 4.10$$

This leads to the exact definition of the piston motion S without any approximations:

$$S(\alpha) = r \left[1 - \cos \alpha + \frac{1}{\lambda} \left(1 - \sqrt{1 - \lambda^2 \sin^2 \alpha} \right) \right] \quad 4.11$$

Then, volume variation of expansion and compression spaces are evaluated, in terms of expansion and compression swept volumes, V_{SE} and V_{SC} , respectively, and crank radius to connecting rod ratios, λ_e and λ_c , respectively and crank angle (θ) by

$$V_e = C_{VE} + \frac{V_{SE}}{2} \left[1 - \cos \theta + \frac{1}{\lambda_e} \left(1 - \sqrt{1 - \lambda_e^2 \sin^2 \theta} \right) \right] \quad 4.12$$

$$V_c = C_{VC} + \frac{V_{SE}}{2} \left[1 + \cos \theta - \frac{1}{\lambda_e} \left(1 - \sqrt{1 - \lambda_e^2 \sin^2 \theta} \right) \right] \\ + \frac{V_{SC}}{2} \left[1 - \cos(\theta - \pi/2) + \frac{1}{\lambda_c} \left(1 - \sqrt{1 - \lambda_c^2 \sin^2 \left(\theta - \frac{\pi}{2} \right)} \right) \right] \quad 4.13$$

4.4 Ideal adiabatic model

The pressure is assumed to be uniform throughout the engine spaces. Applying the mass conservation law to the interior spaces of the engine leads to evaluating the instantaneous engine pressure,

$$p = mR / \left(\frac{V_c}{T_c} + \frac{V_{k1}}{T_k} + \frac{V_{k2}}{T_k} + \frac{V_r}{T_r} + \frac{V_h}{T_h} + \frac{V_e}{T_e} \right) \quad 4.14$$

The total mass of engine gas can be calculated in terms of the charge pressure and expansion swept volume from using Schmidt theory as

$$m = p_{ch} V_{SE} B \left(\sqrt{(1 + S^2)} / 2RT_k \right) \quad 4.15$$

Where B and S are constants dependent on geometrical and operational conditions of the engine. The regenerator temperature is assumed to vary linearly between hot and cold end temperatures and hence the regenerator temperature can be evaluated using the logarithmic mean temperature difference as

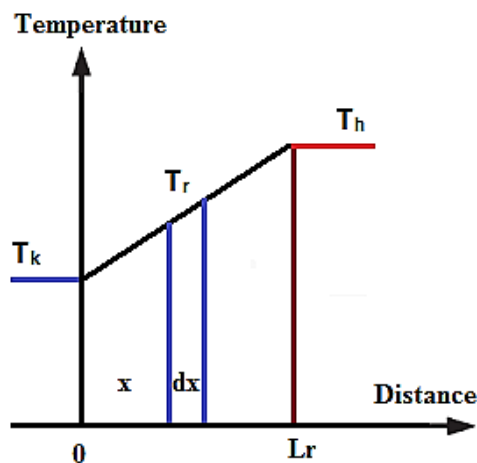


Figure 4-3 Regenerator temperature profile.

$$T_r = (T_h - T_k) / \ln(T_h / T_k) \quad 4.16$$

Where all temperature values are in Kelvin.

Applying equation of state, the mass variation through the connecting pipe, cooler, regenerator and heater are determined by

$$m_i = \frac{pV_i}{RT_i}; i = k_1, k_2, r, h \quad 4.17$$

Meanwhile, the mass accumulation in the compression and expansion cells can be determined as [9]

$$dm_c = (pdV_c + V_c dp/\gamma)/RT_{ck1} \quad 4.18$$

$$dm_e = (pdV_e + V_e dp/\gamma)/RT_{he} \quad 4.19$$

Where, the conditional temperatures, T_{ck1} and T_{he} are dependent on the flow direction as

$$\text{if } \dot{m}_{ck} > 0 \text{ then } T_{ck1} = T_c \text{ else } T_{ck1} = T_k \quad 4.20$$

$$\text{if } \dot{m}_{he} > 0 \text{ then } T_{he} = T_h \text{ else } T_{he} = T_e \quad 4.21$$

Thus, the mass flow rate at each of the cells interfaces can be evaluated by

$$\dot{m}_{ck1} = -dm_c/dt \quad 4.22$$

$$\dot{m}_{k1k2} = -\dot{m}_{ck1} - dm_{k1}/dt \quad 4.23$$

$$\dot{m}_{k2r} = -\dot{m}_{k1k2} - dm_{k2}/dt \quad 4.24$$

$$\dot{m}_{rh} = -\dot{m}_{k2r} - dm_r/dt \quad 4.25$$

$$\dot{m}_{he} = -\dot{m}_{rh} - dm_h/dt \quad 4.26$$

The pressure variation is obtained from eq. (4.14) as

$$dp = - \left[\frac{\gamma p [(dV_c/T_{ck1}) + (dV_e/T_{he})]}{\frac{V_c}{T_{ck1}} + \gamma \left(\frac{V_{k1}}{T_k} + \frac{V_{k2}}{T_k} + \frac{V_r}{T_r} + \frac{V_h}{T_h} \right) + \frac{V_e}{T_{he}}} \right] \quad 4.27$$

The cyclic temperatures of expansion and compression spaces are calculated using the equation of state in the differential form

$$dT_i = T_i(dp/p + dV_i/V_i - dm_i/m_i); \quad i = e, c \quad 4.28$$

From first law of thermodynamics, the heat transfer to the cooler, regenerator and heater can be obtained as

$$dQ_k = c_v(V_{k1} + V_{k2}) \frac{dp}{R} - c_p(T_{ck1}\dot{m}_{ck1} - T_k\dot{m}_{k2r}) \quad 4.29$$

$$dQ_r = \frac{c_v V_r dp}{R} - c_p(T_k\dot{m}_{k2r} - T_h\dot{m}_{rh}) \quad 4.30$$

$$dQ_h = \frac{c_v V_h dp}{R} - c_p (T_h \dot{m}_{rh} - T_{he} \dot{m}_{he}) \quad 4.31$$

The indicated work, heat absorbed by the heater and heat rejected from the cooler can be integrated over the cycles

$$W_i = \oint p dV_e + \oint p dV_c \quad 4.32$$

$$Q_k = \oint \delta Q_k \quad 4.33$$

$$Q_h = \oint \delta Q_h \quad 4.34$$

4.5 Losses consideration

Since the regenerator is imperfect, the actual heat transfer to the regenerator is dependent on its effectiveness and this can be obtained using the number of transfer units, NTU of the regenerator matrix,

$$\varepsilon = NTU / (1 + NTU) \quad 4.35$$

The *NTU* can be determined in terms of Nusselt number, *Nu* of the regenerator matrix using the *Scaling Parameter Approach* [18],

$$NTU = 4Nu(lr/dr)/(RePr) \quad 4.36$$

The correlations for flow friction and heat transfer in the random fibre regenerator matrix were based on oscillatory flow testing results which are presented in more detail by Geodon [133].

$$f_r = \frac{a_1}{Re} + a_2(Re)^{a_3} \quad 4.37$$

$$Nu = 1 + b_1(RePr)^{b_2} \quad 4.38$$

Thus, the heat loss in the regenerator due to imperfect regeneration can be determined based on regenerator effectiveness as

$$Q_{r,loss} = (1 - \varepsilon)(Q_{r,max} - Q_{r,min}) \quad 4.39$$

The actual gas temperatures in the heater and the cooler including the connecting pipe can be expressed in terms of the imperfect regeneration and heat exchange between the walls and the gas in these spaces as follows

$$Q_h = \frac{60}{n} h_h A_h (T_{wh} - T_{gh}) - Q_{r,loss} \quad 4.40$$

$$Q_k = \frac{60}{n} (h_{k1} A_{k1} + h_{k2} A_{k2})(T_{wk} - T_{gk}) + Q_{r,loss} \quad 4.41$$

The heat transfer coefficients in the heater, connecting pipe and cooler, h_h , h_{k1} and h_{k2} , respectively are based on Colburn J-factor found in Kays and London [134]

$$J = hPr^{2/3}/(\dot{m}C_p/A_f) \quad 4.42$$

If $Re < 3000$

$$J = \exp(0.337 - 0.812 \log(Re)) \quad 4.43$$

If $3000 < Re < 4000$

$$J = 0.0021 \quad 4.44$$

If $4000 < Re < 7000$

$$J = \exp(13.31 - 0.861 \log(Re)) \quad 4.45$$

If $7000 < Re < 10000$

$$J = 0.0034 \quad 4.46$$

If $Re > 10000$

$$J = \exp(-3.575 - 0.229 \log(Re)) \quad 4.47$$

The internal conduction losses in the regenerator and the shuttle losses due to oscillatory motion of the displacer are included to calculate the actual heat transferred to the heater [8]

$$Q_{d,loss} = \frac{k_r A_r}{l_r} (T_h - T_k) \quad 4.48$$

$$Q_{sh,loss} = \frac{0.4Z_d^2 k_d D_d}{J_d l_d} (T_e - T_c) \quad 4.49$$

$$Q_{act,h} = Q_h + Q_{d,loss} + Q_{sh,loss} \quad 4.50$$

The work loss due to pressure drop in connecting pipe, cooler, regenerator and heater can be obtained by

$$W_{loss} = \oint \Delta p_i dV_e \quad 4.51$$

The pressure drop for all heat exchangers can be expressed by an equation that satisfies the momentum conservation for positive and reversed flow [134] such as

$$\Delta p_i = -2f_r \mu u \left(\frac{V_i}{A_i d_i^2} \right); i = k_1, k_2, r, h \quad 4.52$$

The Reynolds friction factor, f_r , can be determined from Darcy friction factor and Reynolds number.

$$f_r = \left(\frac{f_D}{4} \right) Re \quad 4.53$$

Eq.(4.37) is used to quantify the pressure drop in the regenerator, while, the pressure drop in connecting pipe, cooler and heater is determined using friction factor evaluated by [135];

If $Re < 2000$

$$f_D = \frac{64}{Re} \quad 4.54$$

If $2000 < Re < 20000$

$$f_D = 0.316Re^{-0.25} \quad 4.55$$

If $Re > 20000$

$$f_D = 0.184Re^{-0.2} \quad 4.56$$

The forced work per cycle, \bar{W} , shown in Figure 4-4, can be evaluated by integrating the product of $(p-p_{ch})$ and dV over the portions of the cycle but with negative sign.

$$\bar{W} = \oint [(p - p_{ch}) dV]^- \quad 4.57$$

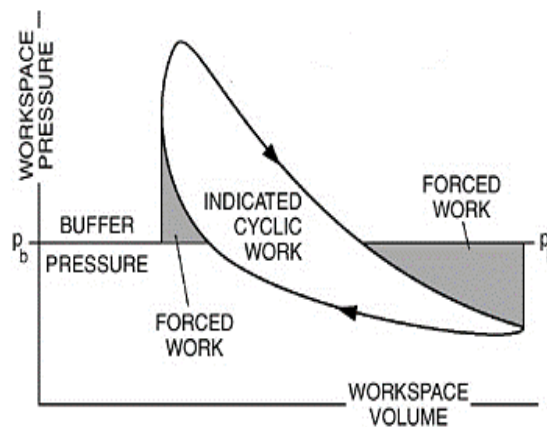


Figure 4-4 Schematic diagram of forced work [136].

The engine shaft work per cycle W_s can then be calculated in terms of the indicated work and the forced work based on Senft's theory [136] as,

$$W_s = E(W_i - W_{loss}) - (1/E - E)\bar{W} \quad 4.58$$

Where, E is the mechanism effectiveness which is related to the transformation of energy from engine piston to the flywheel in a cyclic manner. Due to the existence of the forced work, which is dependent on the pressure ratio, shape of indicated PV diagram and the buffer pressure, the mechanical efficiency is lower than the mechanism effectiveness. Detailed information on this theorem of heat engines can be found in [137]. For a heat engine, the mechanical effectiveness typically varies between 0.7 and 0.9. In present work, the mechanism effectiveness of the engine is calibrated to experiment and found to be 0.75. The mechanism effectiveness was calculated from eq. (4.58) with the knowledge of the calculated indicated power (W_i) from indicated PV diagrams, measured shaft power (W_s) and the calculated forced power eq. (4.57). All the data listed in Table 4-1 are based on the experimental indicated PV diagrams at normal engine speed of 500 rpm and different heater temperatures.

Table 4-1 Data used for calculation of engine mechanism effectiveness.

T_h	$(W_i - W_{loss})$	W_s	\bar{W}
450	536.66	303	175.5
500	603.41	349	182.5
550	654	404	153.2
600	709.41	460	128.5
650	753.08	490	133.2

The engine shaft power (\dot{W}_s) can be then obtained in terms of the shaft work and the engine speed as.

$$\dot{W}_s = W_s \left(\frac{n}{60} \right) \quad 4.59$$

Similarly, the engine torque can be expressed as

$$\tau = \left(\frac{\dot{W}_s}{\omega} \right) \quad 4.60$$

Finally, the thermal efficiency of the engine, can be calculated in terms of the shaft power and the actual heat input as

$$\eta_{th} = \left(\frac{\dot{W}_s}{\dot{Q}_{act,h}} \right) \quad 4.61$$

4.6 Method of solution

As mentioned in section 4.1 that the system can be treated as quasi-steady flow by neglecting the acceleration effects of the five mass flow variables. This can reduce the problem into a set of ordinary differential equations that can be solved simultaneously. Solving these equations can be more simplified by formulating them as an initial-value problem. All unknown variables can be collectively represented by the vector \mathbf{Y} . for example, $y[Tc]$ represents temperature of compression space and $y[We]$ for the work done by the expansion space, and so on. The initial values and the corresponding differential equations can be formulated, respectively in the form:

$$\mathbf{Y}(\theta = 0) = \mathbf{Y}_0 \quad 4.62$$

$$d\mathbf{Y} = \mathbf{F}(\theta, \mathbf{Y}) \quad 4.63$$

Using fourth-order Runge-Kutta method, the values of the derivatives are first computed numerically at θ_0 and proceeded incrementally to a new point $\theta_1 = \theta_0 + \Delta\theta$ to approximate the

true curves of $Y(\theta)$. The initial values can be arbitrarily defined due to the cyclic nature of the system, and then integrating the equations over several cycles until the cyclic steady state is reached. The flow chart of the developed algorithm, written in Matlab environment, is provided in Figure 4-5.

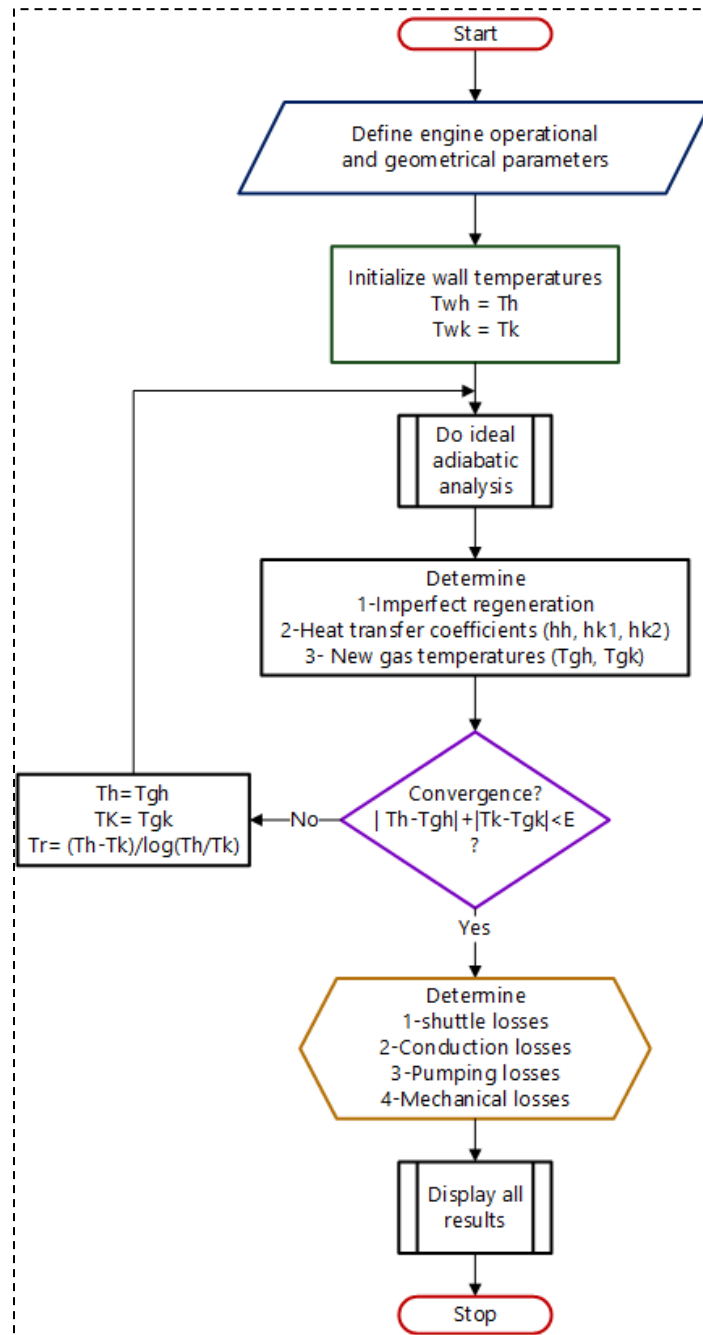


Figure 4-5: Flow chart of the developed algorithm.

While the ideal adiabatic analysis is performed, new gas temperatures in all heat exchangers are updated until the convergence criteria is met. The second step, all decoupled losses are evaluated and finally the engine performance parameters are obtained.

4.7 Model validation

In this section, a comparison of the results of the simulated engine and experiment using Nitrogen are presented. The operational conditions of the engine were listed previously in Table 3-1. The predicted indicated PV diagrams are compared to experimental results at the two extremes of hot end temperatures and charge pressures as shown in Figure 4-6 and Figure 4-7 at engine nominal speed of 500 rpm.

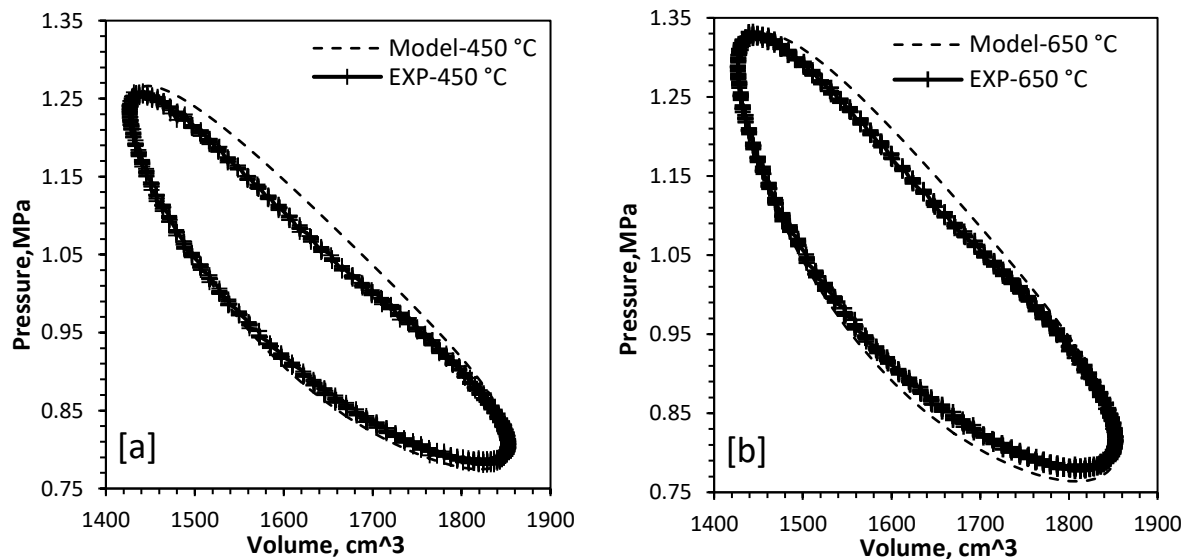


Figure 4-6 Comparison of indicated PV diagrams between the model and experiment at fixed charge pressure (10bar) and different heater temperatures, (a) at 450 °C and (b) at 650 °C.

It can be said that the minimum and the maximum pressures predicted by the model are very similar to experimental results. This suggests that calculating the instantaneous pressure based

on gas equation of state is reasonably accurate. However, the gap areas in indicated PV diagrams between model and experimental results are observed.

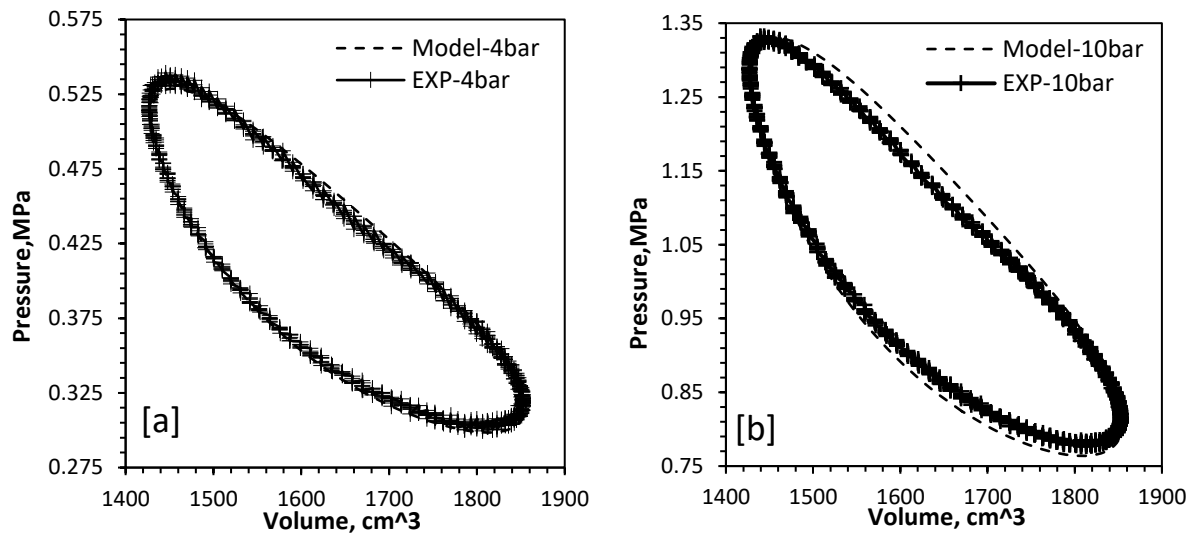


Figure 4-7 Comparison of indicated PV diagrams between the model and experiment at Fixed heater temperature (650 °C) and different charge pressures, (a) at 4 bar and (b) at 10 bar.

The indicated PV diagram obtained from experiment is based on actual pressure drop in all spaces of the engine. Meanwhile, the pressure drop in the current model is decoupled from the indicated PV diagram and added in the final evaluation of engine performance. In general, the maximum deviation in predicting the indicated power is 15% compared to experimental results observed at lower hot end temperatures.

In Figure 4-8, a comparison between the model and experimental results in predicting shaft power and engine thermal efficiency at different hot end temperatures is presented. As can be seen, the shaft power increases with increasing the hot end temperature. The maximum shaft power reaches 470 W at 500 rpm for both model and experimental results at the maximum hot end temperature of 650 °C.

In general, the shaft power is over-predicted with a maximum deviation of 15% which occurs at lower hot end temperature of 450 °C. For engine efficiency, the trend is similar with a maximum value of 16.49 % achieved at maximum hot end temperature of 650 °C. A 7.5 % maximum deviation is depicted at lower hot end temperature of 450 °C.

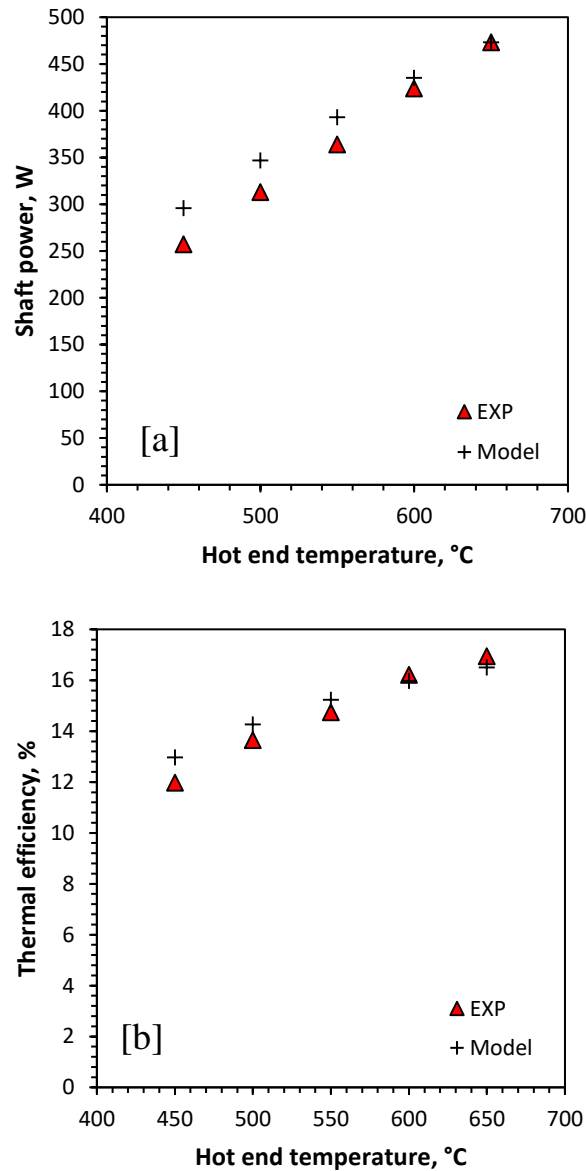


Figure 4-8 Comparison of N₂ results between the present model and experiment at constant charge pressure (10 bar), speed of 500 rpm and different heater temperatures, (a) shaft power and (b) engine efficiency.

In Figure 4-9, the shaft power predicted at different charge pressures are very similar to the experimental results. In terms of thermal efficiency, the trend is similar to experiment. However, the efficiency is under-predicted with a maximum deviation of 8% which occurs at charge pressures of 7 and 8 bar. This may be attributed to the uncertainty in measuring the flow rate and inlet and outlet cooling temperatures, which affects the calculation of thermal efficiency, accordingly.

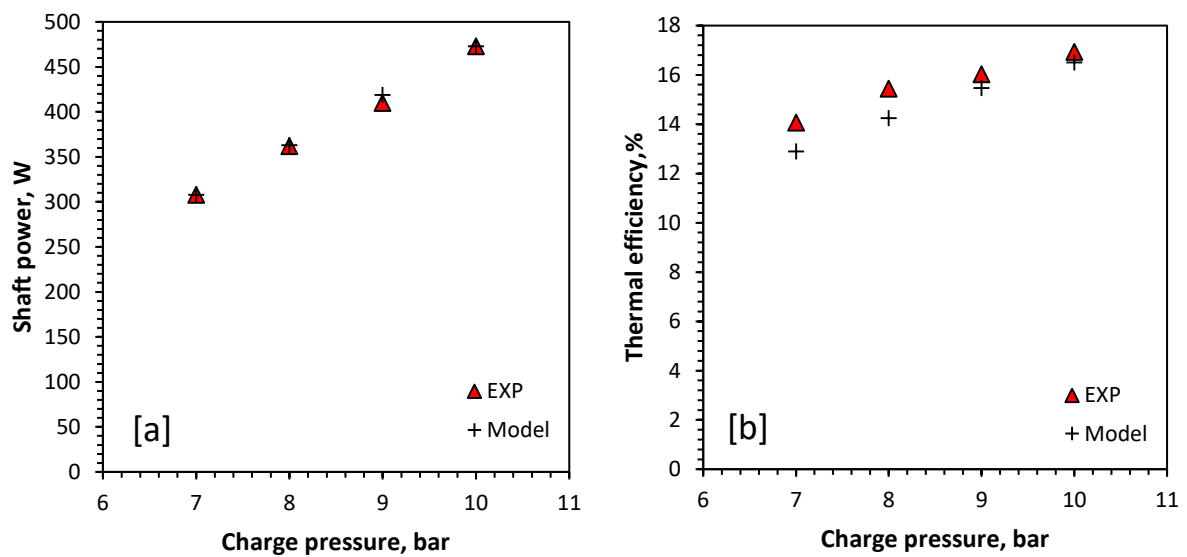


Figure 4-9 Comparison of N₂ results between the present model and experiment at constant heater temperature (650 °C), speed of 500 rpm and different charge pressures, (a) shaft power and (b) engine efficiency.

Figure 4-10 compares the predicted shaft power with experiment at different engine speeds and two extreme hot end temperatures. It can be found that with increasing the speed, the shaft power reaches its maximum at an optimum speed and then falls down. This is attributed to that pressure drop is more pronounced at higher speeds due to elevated frictional losses. The optimum speed, predicted and from experiment, is very similar which reads 600 rpm at hot end temperature of 650 °C compared to 500 rpm at hot end temperature of 450 °C.

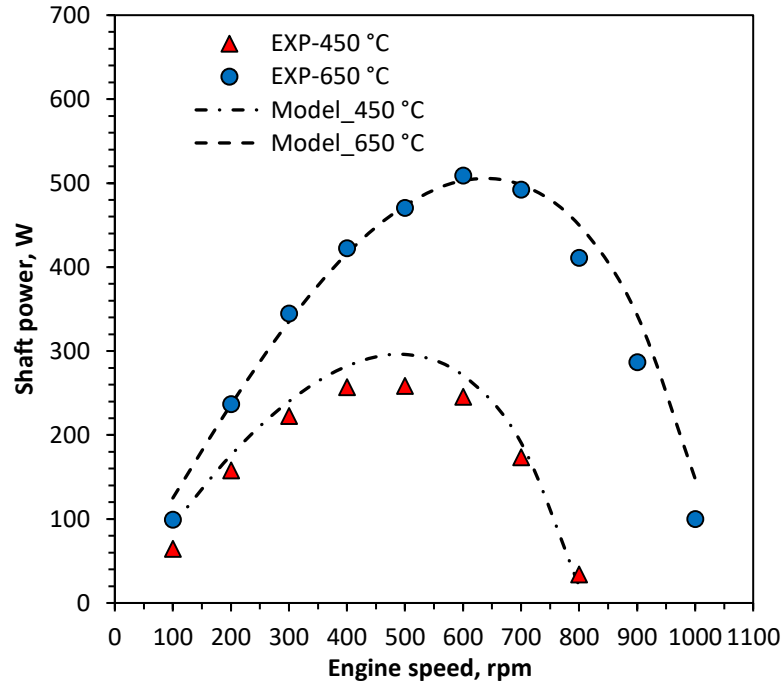


Figure 4-10 Comparison of N₂ results of shaft power versus engine speed between the present model and experiment at constant charge pressure (10 bar) and different heater temperatures (450 °C and 650 °C).

4.8 Summary

An enhanced thermodynamic model based on non-ideal adiabatic analysis, is developed to simulate gamma-type Stirling engine (ST05-CNC). The engine is reconfigured with six engine cells to include the connecting pipe for better accuracy. Random fibre correlations for flow friction and heat transfer, based on oscillatory flow testing were used to model the regenerator. The real pistons motion was adopted and hence the real volume variation was included in the model. The pumping losses in the heat exchangers were evaluated depending on the type of flow regime. Thermal losses such as shuttle and conduction losses are accounted for as well as the mechanical losses to estimate the shaft power. A maximum deviation of 15% was found between model and experimental results. The maximum deviation of the model prediction is lower than that of most published work.

CHAPTER 5

ENGINE CFD MODELLING

5.1 Introduction

In this chapter, the development of a CFD model for the simulation of gamma-type Stirling engine is described. The model has been developed based on a commercially available software (Comsol multiphysics 5.2) [138]. Specific features within Comsol environment will first be introduced including porous media modelling and dynamic meshing. Then the governing equations for the problem will be presented. In addition, the strategies implemented to obtain the porous media characteristics for the regenerator and cooler will be described. The choice of meshing techniques, boundary conditions and solution scheme will be discussed. Finally, the validation of the model with experimental data will be presented.

5.2 Heat transfer in porous media

Based on the mixture rule on energies appearing in solid and fluid heat transfer equations, the heat transfer equation for porous media is derived [139]. Two approaches are widely used in porous media in which the accuracy of each depends on the specific field of application; local thermal equilibrium (LTE) and local thermal non-equilibrium (LTNE) models.

5.2.1 Local thermal equilibrium

Modelling heat transfer in porous media using classical local equilibrium hypothesis is based on pointwise equality of both solid and fluid temperatures. The (LTE) approach is one energy

equation that can be applied when infinite heat transfer exists between the solid and the fluid phases. Most slow motion problems and steady conduction problems can be treated by this approach if volumetric internal heating do not differ in both materials [140]. One shortcoming of this approach is that entropy generation due to the radial heat transfer is totally omitted because of the temperature difference between the two phases is locally zero.

In general, the validity of (LTE) assumption in Stirling regenerator applications was assessed by many researchers. Some experimental results on a wire-screen Stirling regenerator reported by Schreiber [141] and other results obtained from Sage 1-D models [142], supported the existence of several degrees difference between the gas and the solid phases. This proves that the (LTE) is inappropriate in oscillating-flow environment and heat storage applications such as Stirling regenerators.

The other disadvantage of this approach is the underestimation of enthalpy-flux losses in the regenerator [143]. This requires that the solid heat capacity must be infinite compared to that of the gas for accurate estimation. Other researchers [144, 145] showed the departure from this approach in porous media when rapid heating and cooling is predominant which led to significant errors depending on the thermophysical properties.

The energy equation is formulated as

$$(\rho C_p)_{eff} \frac{\partial T}{\partial t} + \rho C_p \mathbf{u} \cdot \nabla T + (\nabla \cdot (-k_{eff} \nabla T)) = Q \quad 5.1$$

The effective heat capacity, $(\rho C_p)_{eff}$ and thermal conductivity, k_{eff} are calculated based on the volume fractions of the fluid and the solid. Since the heat conduction occurs in parallel in

the solid and the fluid, then the effective thermal conductivity is usually calculated by three models proposed for an isotropic medium namely; volume average model, reciprocal average model and power law model which can be found in more detail in [139].

5.2.2 Local thermal non-equilibrium

Local Thermal Non-Equilibrium heat transfer in porous media is used when the temperatures of the porous matrix and the fluid are not in local equilibrium. The governing equations are the usual heat transfer equations for solids and fluids, but multiplied by the volume fractions θ_p and $(1 - \theta_p)$ respectively, and with an additional source term quantifying exchanged heat between both phases [139].

$$\theta_p \rho_s C_{ps} \frac{\partial T_s}{\partial t} + \nabla \cdot (-\theta_p k_s \nabla T_s) = q_{sf}(T_f - T_s) + \theta_p Q_s \quad 5.2$$

$$\begin{aligned} (1 - \theta_p) \rho_f C_{pf} \frac{\partial T_f}{\partial t} + (1 - \theta_p) \rho_f C_{pf} \mathbf{u}_f \nabla T_f + \nabla \cdot (-(1 - \theta_p) k_f \nabla T_f) \\ = q_{sf}(T_s - T_f) + (1 - \theta_p) Q_f \end{aligned} \quad 5.3$$

Where,

θ_p is the solid volume fraction.

ρ_s and ρ_f are the solid and fluid densities (kg/m^3).

C_{ps} and C_{pf} are the solid and fluid heat capacities at constant pressure ($\text{J/kg}\cdot\text{K}$).

k_s and k_f are the solid and fluid thermal conductivities ($\text{W/m}\cdot\text{K}$).

q_{sf} is the interstitial convective heat transfer coefficient ($\text{W/m}^3\cdot\text{K}$).

Q_s and Q_f are the solid and fluid heat sources (W/m^3).

\mathbf{u}_f is the fluid velocity vector (m/s).

The fluid velocity is often deduced from a porous velocity \mathbf{u}_p , coming for example from Darcy's law or Brinkman equations, according to [146]:

$$\mathbf{u}_f = \frac{\mathbf{u}_p}{1 - \theta_p} \quad 5.4$$

so that the heat transfer equations in the fluid domain reduces to:

$$\begin{aligned} (1 - \theta_p)\rho_f c_{pf} \frac{\partial T_f}{\partial t} + \rho_f c_{pf} \mathbf{u}_p \nabla T_f + \nabla \cdot (-(1 - \theta_p)k_f \nabla T_f) \\ = q_{sf}(T_s - T_f) + (1 - \theta_p)Q_f \end{aligned} \quad 5.5$$

As can be seen that two exchanged opposite heat sources are added in eq.(5.2) and eq.(5.5), $q_{sf}(T_f - T_s)$ and $q_{sf}(T_s - T_f)$ which represent the rate of heat received or released from one phase to another when their respective temperatures are different. The interstitial convective heat transfer coefficient, q_{sf} is defined as the product of the heat transfer coefficient and the specific surface area of the solid as

$$q_{sf} = a_{sf} h_{sf} \quad 5.6$$

The heat transfer coefficient, h_{sf} is determined from an appropriate empirical or numerical-based correlation depending on the type and configuration of the porous matrix.

5.3 Moving mesh

As the Stirling engine works by gas expansion and compression processes, the deformation of respective domains due to pistons movement needs to be handled through a complex algorithm to support moving (dynamic) meshes during the simulation. The choice of continuum kinematical description in developed computer codes fundamentally determines the resolution accuracy of interfaces and moving boundaries of the material in relationship with the deforming continuum and mesh of computing zones.

Two classical descriptions of motion are widely used in algorithms; the *Eulerian* formulation and the *Lagrangian* formulation [147, 148]. The Eulerian is a good choice for a flow model except with moving boundaries or with free surface. This is due to the fixed points in space in which the physical quantities are referred to, while domain boundaries spatial points change with time causing high distortion when they follow the motion. The Lagrangian is favourable for “confined fluids” when there is a relatively small displacement due to small motion. The inherent disadvantage of pure Lagrangian approach is that it cannot follow large deformations of the computational domain until re-meshing strategy is supported.

The *Arbitrary Lagrangian-Eulerian* (ALE) is a combination of the best features in both Lagrangian and Eulerian formulation- it enables moving boundaries without a restriction for the moving mesh to follow the material based on a moving imaginary mesh [149, 150]. If the velocity of the domain is denoted by w , it would be equal to zero in the Eulerian approach, and equal to the velocity of the fluid particles in the Lagrangian approach.

In the ALE approach, w equals neither to zero nor to fluid particles velocity, but it varies arbitrarily and smoothly between both of them. The movement of an object inside of a domain is actually a boundary value problem. Knowing the boundary displacements, the deformation of the mesh can be defined within the domain interiors.

Four approaches to compute the mesh deformation within each domain are supported in Comsol environment; Laplace, Winslow, Hyperelastic, and Yeoh smoothing types. Their choice is governed by the application of the problem and complexity. The Laplace smoothing is suitable for most cases as it is computationally cheap and it uses single equation for each coordinate direction. The following partial differential equation is solved within the domain using Laplace smoothing approach:

$$\frac{\partial^2 x}{\partial X^2} + \frac{\partial^2 y}{\partial Y^2} + \frac{\partial^2 z}{\partial Z^2} \quad 5.7$$

Where the lowercase (x, y, z) are the deformed positions of the mesh and the uppercase (X, Y, Z) are the original, undeformed positions.

5.4 Linear translation

In a finite element method (FEM) software, linear translation of an object within a domain, which is similar to a piston motion in Stirling engine, can be efficiently handled in Comsol using deformed geometry or moving mesh modules based on ALE approach. An example is given in Figure 5-1 to demonstrate the technique setting up a large linear motion of an object within a domain Figure 5-1-(a).

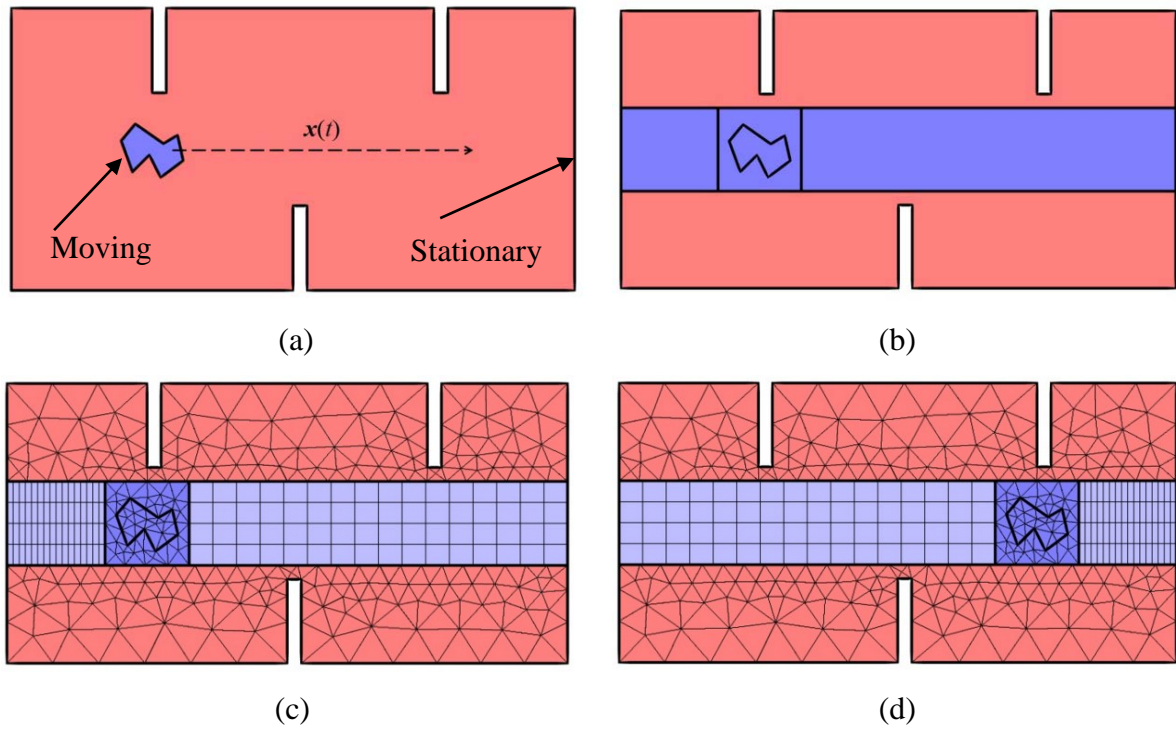


Figure 5-1 Motion of solid object along a linear path inside a complicated domain [151].

First, the domain is subdivided into two different geometry objects, as depicted in the Figure 5-1-(b) where the red coloured domains are stationary and the blue one is translating linearly. Then, it is followed by an assembly formulation to create identity pairs to maintain field continuity across these boundaries.

In Figure 5-1-(c), the red domains are not deforming while the dark blue domain is moving with a prescribed deformation and the light blue domains are freely moving following the dark blue domain by using bilinear interpolation. Usually mapped meshing is adopted in the light blue domains since mesh stretching and compressing is required (Figure 5-1-(c) and Figure 5-1-(d)).

When looking into the computed temperature contours in this example (Figure 5-2) around the moving object, it shows smooth transition over the boundary where the mesh is discontinuous [138].

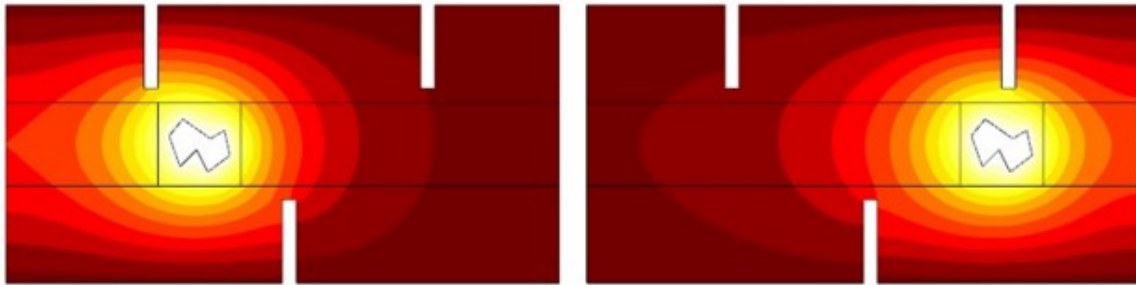


Figure 5-2 The temperature fields of a moving object and its surrounding over time [151].

5.5 Governing equations

The main physical processes in the engine are unsteady, transient, oscillating, laminar or turbulent, compressible flow and heat transfer. These processes along with geometrical effects can be handled within COMSOL Multiphysics environment [138]. The Arbitrary Lagrangian-Eulerian (ALE) method was used to handle the deformed geometry and the moving boundaries due to compression and expansion of the gas inside the engine. Meanwhile, compressible laminar non-isothermal flow is used to solve for fluid flow and heat transfer in the domains except the regenerator and the cooler (shown in Figure 5-3).

The regenerator and the cooler are modelled as porous media using Brinkman equation for fluid flow and the two Local Thermal Non-Equilibrium (LTNE) heat transfer equations for gas and solid phases as given in eq. (5.2) and eq. (5.5).



Figure 5-3 Porous media domains, (a) regenerator, (b) cooler.

The governing equations in the porous domains, including continuity, momentum and energy equations for the gas phase [143] are:

$$\frac{\partial \rho}{\partial t} = \frac{\nabla \cdot (\rho \mathbf{u})}{\varepsilon} \quad 5.8$$

$$\frac{\rho}{\varepsilon} \left[\frac{\partial \mathbf{u}}{\partial t} + (\mathbf{u} \cdot \nabla) \frac{\mathbf{u}}{\varepsilon} \right] = -\nabla p - \frac{\nabla \cdot \bar{\tau}}{\varepsilon} - \left(\frac{\mu}{K} + \beta_F |\mathbf{u}| \right) \mathbf{u} \quad 5.9$$

$$\begin{aligned} \rho C_p \left[\varepsilon \frac{\partial T}{\partial t} + (\mathbf{u} \cdot \nabla) T \right] \\ = \nabla \cdot (k \nabla T) + \frac{\bar{\tau} \cdot \nabla \mathbf{u}}{\varepsilon} + \varepsilon \frac{Dp}{Dt} - Nu \frac{k}{d_h} a_{sf} (T - T_s) \end{aligned} \quad 5.10$$

Where the viscous tensor, $\bar{\tau}$ is defined by

$$\bar{\tau} = (\mu)[\nabla\mathbf{u} + (\nabla\mathbf{u})^T] - \frac{2}{3}(\mu)(\nabla \cdot \mathbf{u}) \quad 5.11$$

The three last terms in eq. (5.10), represent viscous dissipation, pressure work and non-equilibrium heat source, respectively.

Assuming the gas to be ideal, the state equation is,

$$\rho = p/RT \quad 5.12$$

In the solid phase, the energy equation is

$$(1 - \varepsilon)\rho_s C_{ps} \partial T_s / \partial t = \nabla \cdot (\bar{k}_e \nabla T_s) + Nu \frac{k}{d_h} a_{sf} (T - T_s) \quad 5.13$$

Where, the solid effective thermal conductivity, \bar{k}_e is calculated based on volume average as,

$$\bar{k}_e = k \varepsilon + (1 - \varepsilon)k_s \quad 5.14$$

Non-isothermal compressible laminar flow equations are applied on the other domains of the engine. In the gas region, the governing equations of continuity, momentum and energy, respectively are,

$$\frac{\partial \rho}{\partial t} = \nabla \cdot (\rho \mathbf{u}) \quad 5.15$$

$$\rho \left[\frac{\partial \mathbf{u}}{\partial t} + (\mathbf{u} \cdot \nabla) \mathbf{u} \right] = -\nabla p - \nabla \cdot \bar{\tau} \quad 5.16$$

$$\rho C_p \left[\frac{\partial T}{\partial t} + (\mathbf{u} \cdot \nabla) T \right] = \nabla \cdot (k \nabla T) + \bar{\tau} \cdot \nabla \mathbf{u} + \frac{Dp}{Dt} \quad 5.17$$

The working gas inside the engine is nitrogen (N₂) where its density is calculated using eq.(5.12) while its other properties are predefined in Comsol using piecewise polynomials covering the temperature variation in the range of 200 to 1200 K [151].

The dynamic viscosity of nitrogen is defined by

$$\mu = 1.772E^{-6} + (6.274E^{-8})T - (3.472E^{-11})T^2 + (1.012E^{-14})T^3 \quad 5.18$$

The heat capacity of nitrogen is defined by

$$C_p = 1088.22 - (0.3659)T + (7.887E^{-4})T^2 - (3.7492E^{-7})T^3 \\ + (3.17592E^{-11})T^4 \quad 5.19$$

And finally, thermal conductivity of nitrogen is defined by

$$k = 3.696E^{-4} - (9.743E^{-5})T + (4.0758E^{-8})T^2 - (7.684E^{-12})T^3 \quad 5.20$$

5.6 Permeability, Forchheimer Drag Coefficient and Nusselt number

5.6.1 Regenerator

In the fluid momentum eq. (5.9), the permeability, K , and Forchheimer drag coefficient, β_F can be evaluated for the regenerator from the following one dimensional Darcy- Forchheimer and Darcy equations [143], respectively

$$\frac{\Delta p}{L} = \frac{\mu}{K} u + \beta_F u^2 \quad 5.21$$

$$\frac{\Delta p}{L} = \frac{1}{2} \frac{f}{d_h} \rho u^2 \quad 5.22$$

The friction-factor correlation for random fibre eq. (5.23) and its parameters (a_1 , a_2 , a_3) can be found in more details in [133].

$$f_r = \frac{a_1}{Re} + a_2 Re^{a_3} \quad 5.23$$

Where Reynolds number,

$$Re = \frac{\rho u d_h}{\mu} \quad 5.24$$

The hydraulic diameter, d_h of a random fibre, in terms of porosity and wire diameter is determined by,

$$d_h = \frac{\varepsilon}{1 - \varepsilon} d_w \quad 5.25$$

Substituting the expression for friction-factor and the definition of Reynolds number into eq.(5.22), and then equating the right-hand sides of equations eq.(5.21) and eq.(5.22), it can be determined that:

$$K = \frac{2d_h^2}{a_1} \quad 5.26$$

$$\beta_F = \frac{1}{2d_h} \rho (a_2 R_e^{a_3}) \quad 5.27$$

In energy eq. (5.10) and eq. (5.13), the Nusselt number, Nu and the solid surface area per unit volume, a_{sf} are calculated as

$$Nu = (1 + b_1 P_e^{b_2}) \quad 5.28$$

$$a_{fs} = \frac{4\varepsilon}{d_h} \quad 5.29$$

The correlation parameters (b_1 , b_2) can be found in more details in [133].

5.6.2 Cooler

Due to the computationally expensive modelling of cooler real geometry in the current 2D CFD model, instead of cooler was treated as a porous media similar to the regenerator. The flow resistance and convection coefficient are determined from steady state simulation of 3D sector of the cooler as described below. The outer wall of the cooler is maintained at a constant wall temperature corresponding to the average temperature of the water jacket, while the gas velocity was varied up to 15m/s. A sample of the pressure, velocity and temperature contours is shown in Figure 5-4 to Figure 5-6 for gas velocity of 2 m/s.

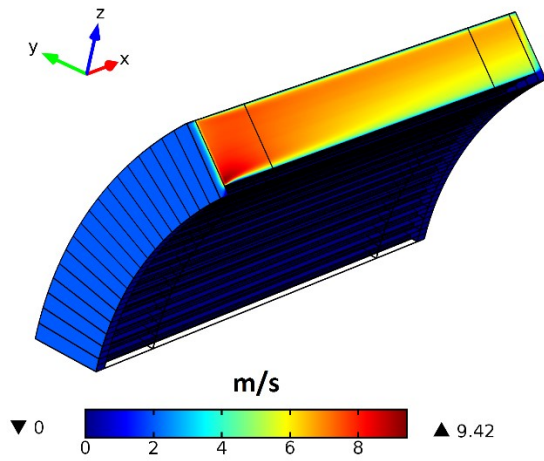


Figure 5-4 Velocity contours inside a sector of the real engine cooler.

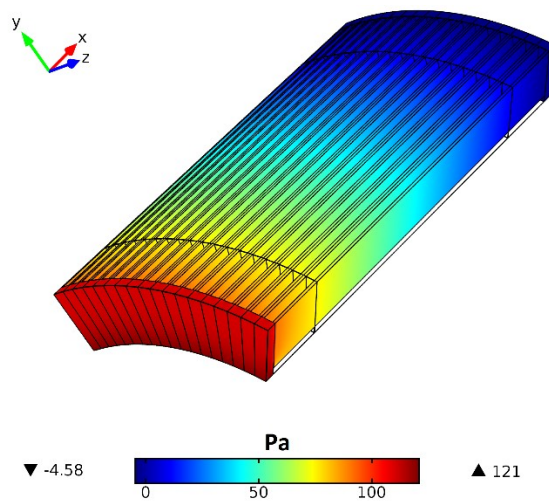


Figure 5-5 Pressure contours inside a sector of the real engine cooler.

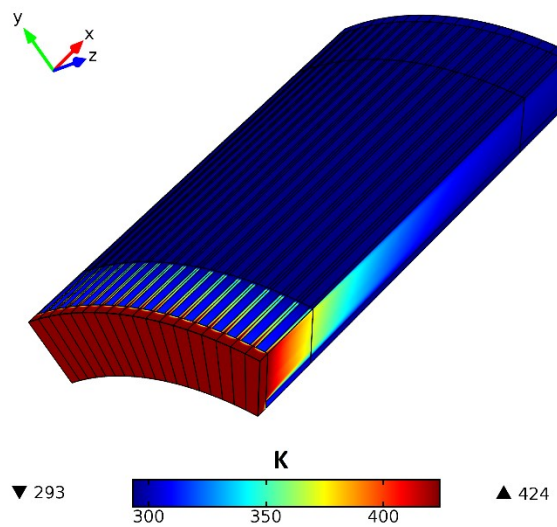


Figure 5-6 Temperature contours inside a sector of the real engine cooler.

The velocity-pressure drop relationship for the cooler is shown in Figure 5-7. The permeability ($K = 9.87E-09 \text{ m}^2$), and Forchheimer drag coefficient ($\beta_F = 293 \text{ kg/m}^4$) are evaluated by fitting the data of velocity-pressure drop with eq. (5.21) using the least square method. The average interstitial convective heat transfer coefficient, which was previously defined in eq. (5.6), as the product of average heat transfer coefficient and the solid surface area per unit volume is found from simulation to be ($1E+06 \text{ W/m}^3 \cdot \text{K}$).

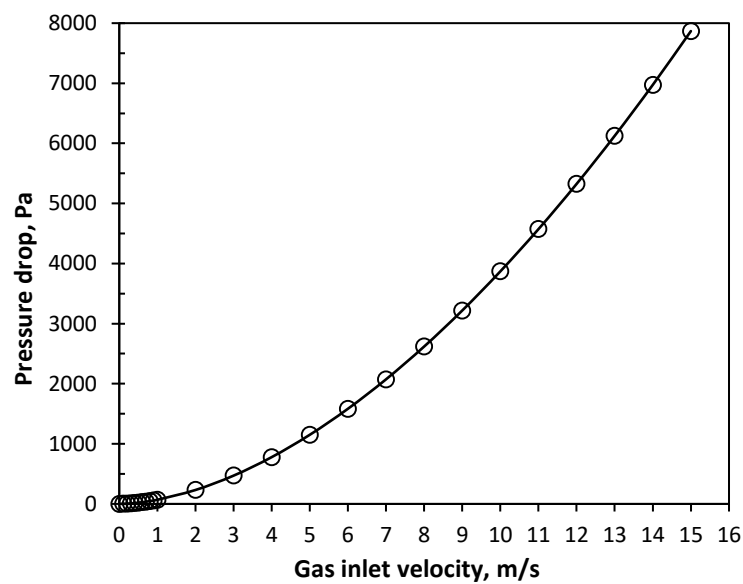


Figure 5-7 Pressure drop through cooler using steady state simulations.

The indicated PV power, was obtained and integrated over the total cycles using Simpson's rule, and calculated by:

$$\dot{W}_I = \left[\oint p dV dt \right]_{Expansion} - \left[\oint p dV dt \right]_{Compression} \quad 5.30$$

The coolant thermal power was calculated from the total heat output through the cooler surfaces over the cycles.

$$\dot{Q}_c = \left[\oint Q dt \right] \quad 5.31$$

5.7 Meshing sequence

In CFD modelling, the speed and accuracy of the solution is determined by the mesh quality. Therefore, the CFD model was carefully set up with respect to the meshing size, time stepping and tolerances. The computational domain of the engine geometry demonstrated in Figure 5-8, captures closely the real geometry of the engine including all solid walls of heater tubes, displacer cylinder, regenerator and cooler and the displacer as a solid material is included as well. Moreover, the appendix gap between the displacer and the cylinder is included in the geometry (see Figure 5-9). Fluid dynamics meshing scheme is adopted in this study with globally controlled meshing size for investigating the suitable mesh for the simulation. Table 5-1 shows the effect of three different meshing sizes on CFD results.

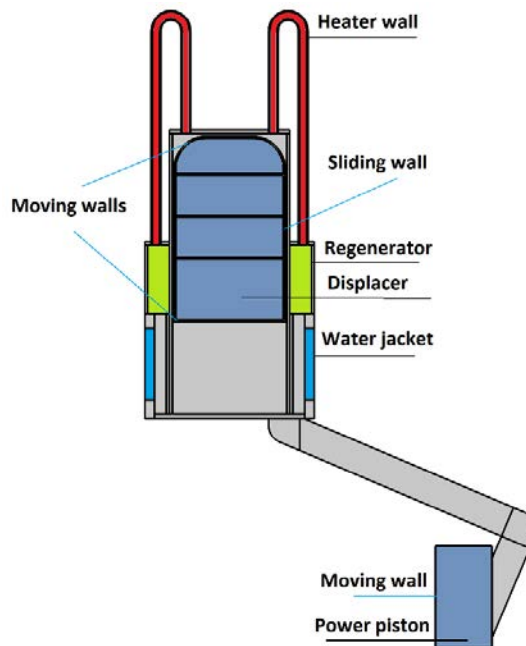


Figure 5-8 The 2D computational domain of the engine.

Table 5-1 Mesh sequence and CFD results.

Mesh sequence	No of elements	Indicated power	Cooling power
Coarse	12389	691W	2466W
Fine	23813	708W	2416W
Extra-fine	39193	718W	2390W

The indicated power increases with refining the mesh due to the decrease in the cooling power. However, the difference in power when changing from coarse to fine is 17W but when changing from fine to extra fine it is 10W which is less than 1.4%. Extra-fine meshing size was then selected for the simulation with manual adjustment in the appendix gap (red circle) which was meshed with extremely fine triangular meshing, as shown in Figure 5-9, to reduce the time required for re-meshing in this zone due to the large deformation of the mesh.

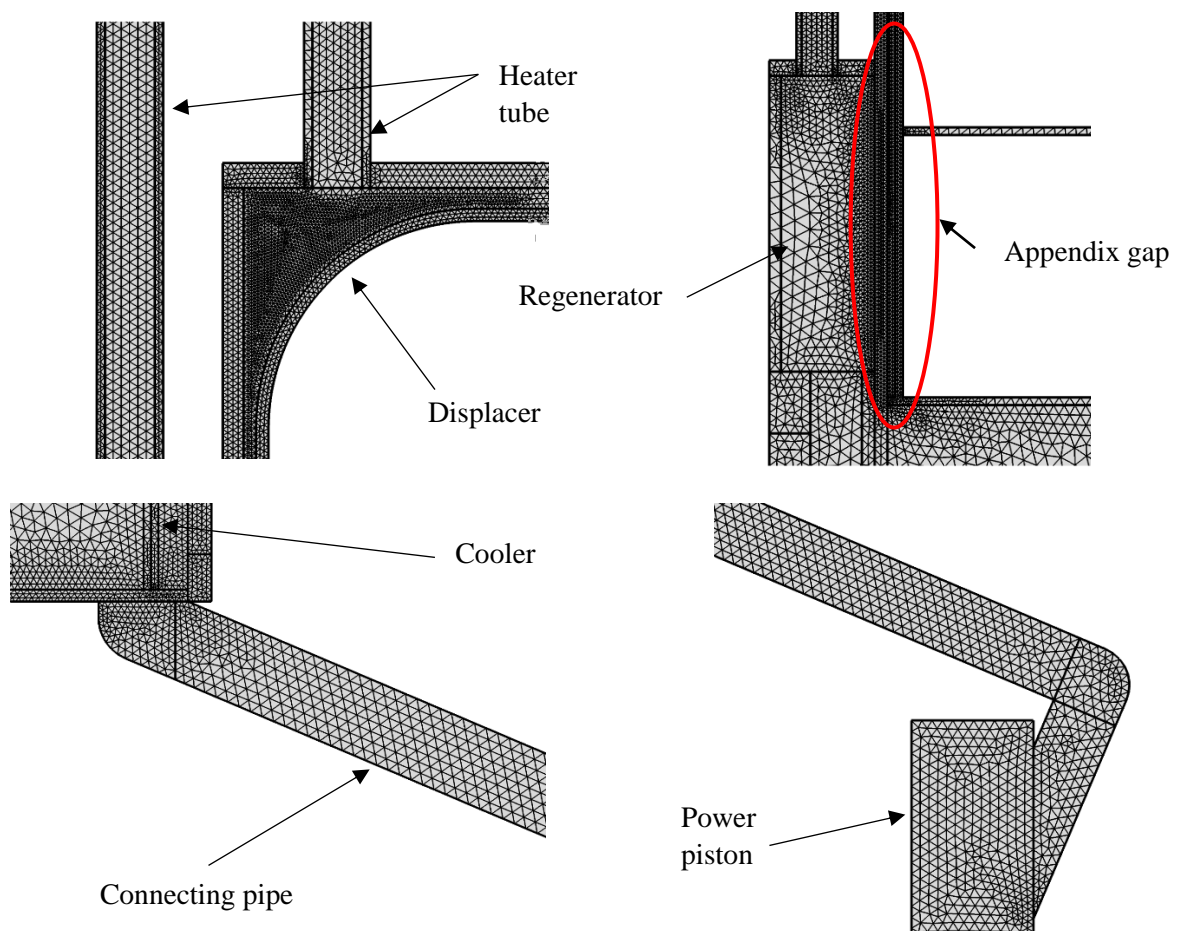


Figure 5-9: Meshing of engine domains.

Automatic re-meshing is activated based on a minimum element relative volume of 0.01 so that this will stop the solution if any element is inverted (its volume becomes negative) and re-mesh afterwards for better resolution. The time stepping is resolved by 100 times over one cycle.

5.8 Boundary Conditions and Solution Scheme

Moving and sliding walls are applied on the displacer and power pistons walls. The moving boundaries of the displacer and power pistons are predefined from equations of real motion of the pistons adopted from [58] as

$$X_e = r \left[1 - \cos \theta + \frac{1}{\lambda_e} \left(1 - \sqrt{1 - \lambda_e^2 \sin^2 \theta} \right) \right] \quad 5.32$$

$$X_c = r \left[1 - \cos(\theta - \pi/2) + \frac{1}{\lambda_c} \left(1 - \sqrt{1 - \lambda_c^2 \sin^2(\theta - \frac{\pi}{2})} \right) \right] \quad 5.33$$

All outer walls of the displacer are moving wall except the vertical wall in y direction are sliding walls. The inner vertical walls of the cylinder holding the displacer are freely moving following the prescribed motion of the displacer. The power piston walls are treated as moving wall for the boundary in physical contact with the piston in x direction and the other two walls (parallel to x direction) are freely moving following the prescribed motion of the piston. Free deformation is only activated for the compression and expansion spaces and has been avoided for other domains (regenerator, heater, cooler and piping's) for faster simulation running-time.

Except constant temperature walls of heater and cooler, the other walls are treated as adiabatic walls. The unsteady time-dependent solution of the governing equations was initialized with

steady state solution of heat transfer with no flow condition (no pistons motion). The computational time can be significantly reduced with the adoption of steady state solution as the temperature gradient is well established throughout the engine. All simulations are carried out on a PC with configuration of Intel(R) core(TM) CPU i7-4820K, runs at speed of 3.7 GHz with 48 GB RAM memory. Typically, each simulation run takes up to 12hrs with normally 10 cycles to reach periodic steady state due to the difference in heat capacities of the working gas and the regenerator. The modelling set-up of the current engine using Comsol multiphysics 5.2 is described in Appendix A.

5.9 Model Validation

5.9.1 Replication of a previously published work ‘CFD Simulation of porous regenerative displacer LTD Stirling engine’

In order to gain some knowledge and explore the features of CFD modelling using Comsol software, a previously published work [87] was replicated which was meant to simulate a LTD gamma-type Stirling engine (Figure 5-10). The engine is featured with solid displacer that is replaced by a moving porous media.

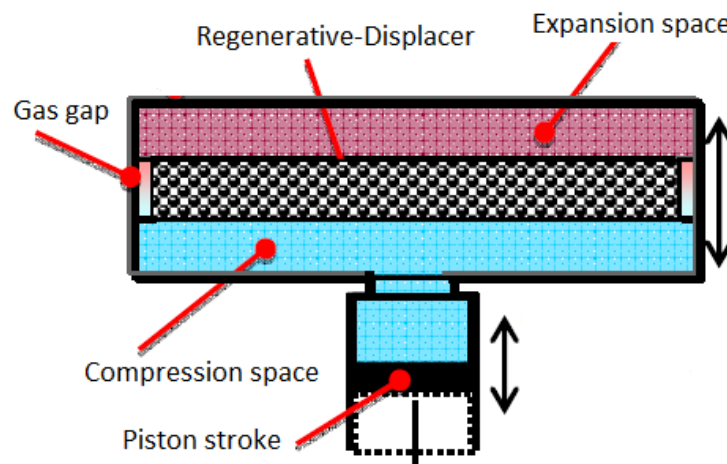


Figure 5-10 LTD gamma-type Stirling engine.

Figure 5-11 shows the temperature contours across the engine during the 10th cycle, where a linear temperature gradient is predominant. The indicated PV diagram (Figure 5-12) of the replicated results compares well with the author's experimental data [87].

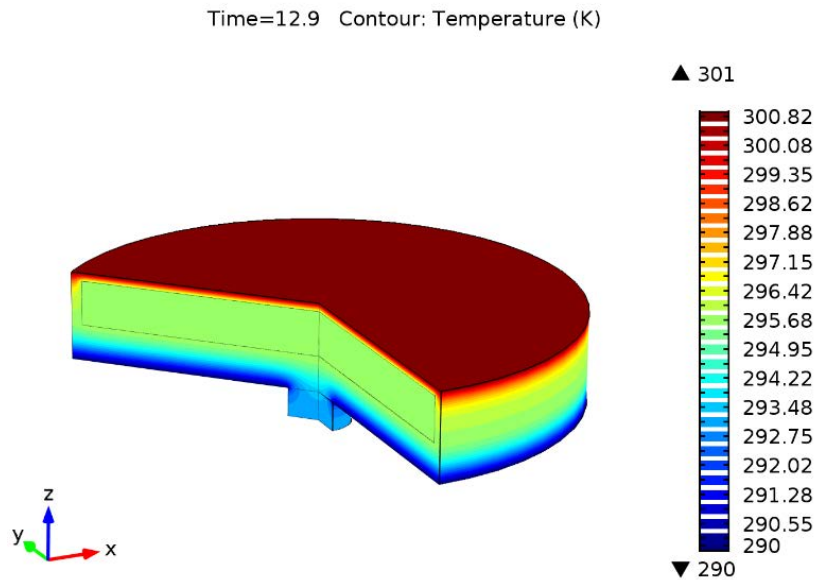


Figure 5-11 Temperature contours of the simulated engine during the 10th cycle.

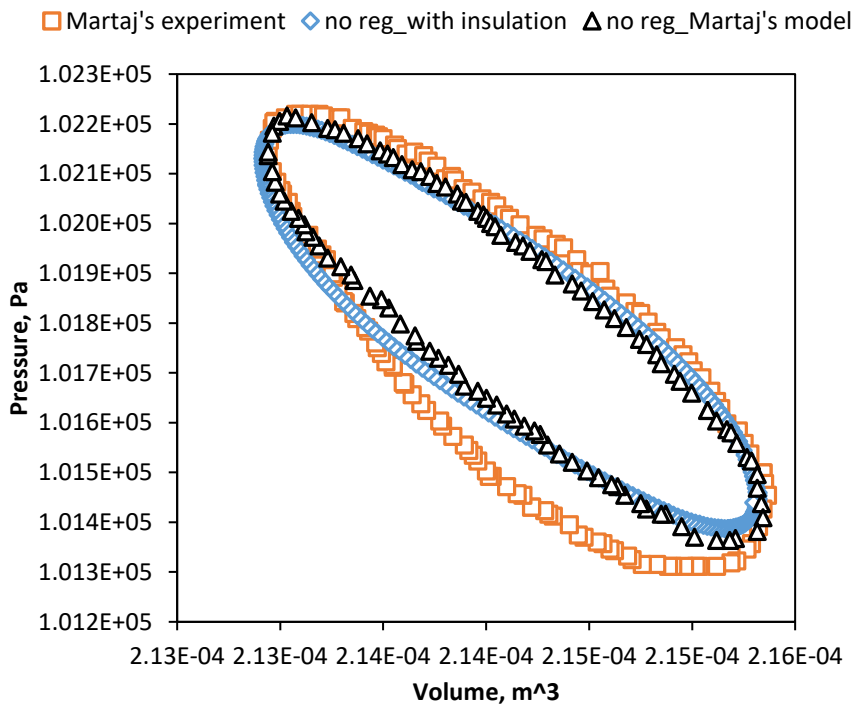


Figure 5-12 Comparison of CFD results and experiment.

As the author investigated the effect of volumetric porosity of the regenerator on engine power, the replicated results obtained showed closer agreement with the authors work as depicted in Figure 5-13, where a volumetric porosity of 0.4 produced the maximum power. This has given a confidence in modelling methodology gained to further proceed with simulating the engine under research.

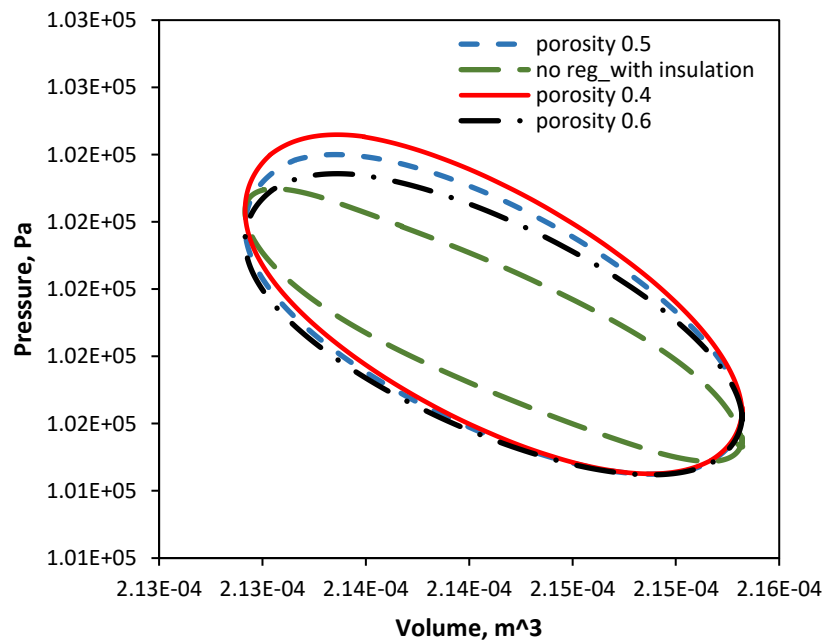


Figure 5-13 Effect of regenerator porosity on indicated PV diagram.

5.9.2 Validation with experimental data of the engine under research

In order to check the validity of CFD results for gamma-type Stirling engine, the indicated PV diagram predicted by the model was compared with experimental results at normal operating conditions as depicted in Figure 5-14. It can be seen that the minimum and the maximum pressures predicted by the model are very close to experimental results. However, the gap areas in indicated PV diagrams between the model and experimental results are observed. This may be attributed to that the porous media characteristics obtained for the cooler using steady state simulation is underestimated.

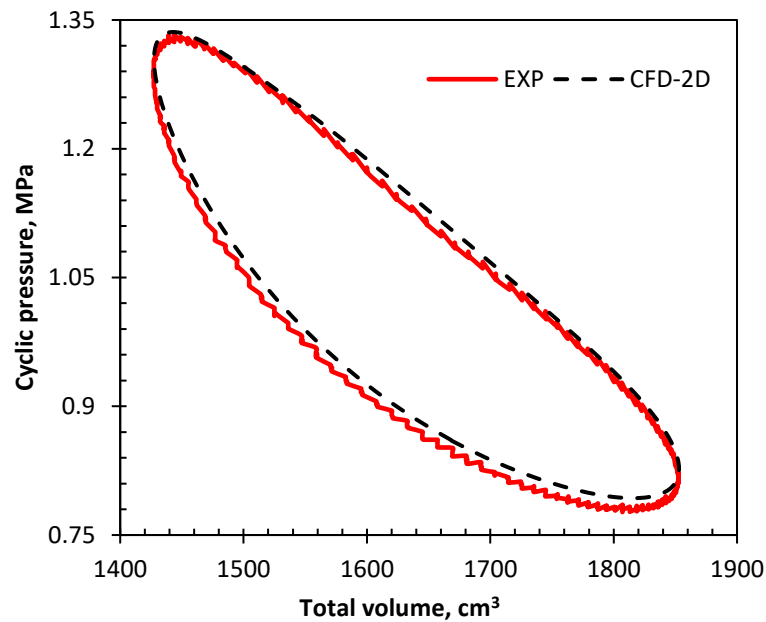


Figure 5-14 Comparison of indicated PV diagrams between CFD model and experiment at normal operating conditions.

In such oscillatory flow environment of Stirling engine, the pressure drop tends to be higher than steady flow [39]. In general, the maximum deviation in predicting the indicated power is 9% compared to experimental results.

The effect of hot end temperature on engine indicated and cooling powers (Figure 5-15) was investigated for further comparison between CFD model and experimental results, with a variation of hot end temperature from 450 °C to 650 °C, at nominal engine speed of 500 rpm and fixed charge pressure of 10 bar.

As can be seen that the CFD model results showed a similar increasing trend to experimental results of indicated and cooling powers with increasing the hot end temperature up to the maximum temperature of the heater with a maximum deviation of 9% and 5%, respectively.

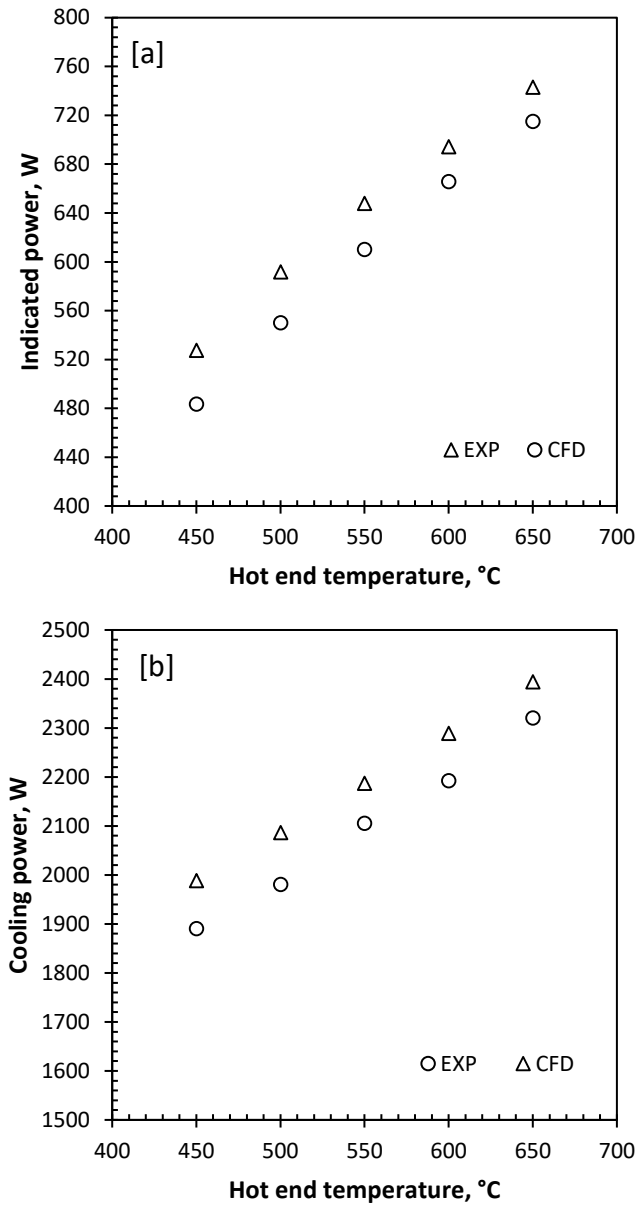


Figure 5-15 Comparison between CFD model and experimental results at constant charge pressure (10 bar) and different heater temperature, (a) indicated power and (b) cooling power.

5.10 Summary

A comprehensive 2D CFD model was developed and validated against experimental data to simulate gamma-type Stirling engine. The 2D engine computational domain resembles the real geometry of the engine including; power and displacer pistons, heater, regenerator, cooler and connecting pipe. The model was based on a realistic Local Thermal Non-Equilibrium (LTNE)

approach for porous domains in the engine (cooler and regenerator). Compressible laminar non-isothermal flow modelling was used to model the free flow domains while Brinkman equation was used to model porous domains. The Arbitrary Lagrangian-Eulerian (ALE) method was used to handle the deformed geometry and the moving boundaries due to compression and expansion of the gas inside the engine. The simulation results showed an acceptable degree of accuracy of 9% and 5%, respectively when comparing with experimental results in predicting the indicated and cooling powers at different heating temperatures. The CFD model is maturing and can be extended for 3D simulations for better understanding of fluid flow and heat transfer characteristics inside the engine. Parametric study of different operational and geometrical parameters affecting engine performance will be conducted in chapter 7.

CHAPTER 6

DEVELOPMENT OF CHANNEL REGENERATORS

6.1 Introduction

In this chapter new circular-shaped mini-channel regenerators will be developed to be adopted for gamma-type Stirling engine (ST05CNC). A CFD model was developed on a 3D sector of the proposed geometry using transient conjugate heat transfer simulations to determine the fluid flow and heat transfer characteristics of five different configurations. Three configurations were fabricated using 3D printing technique and a test facility was built to perform transient testing of the regenerators. This will be presented at the end of the current chapter. The real geometry of regenerators is then converted into an equivalent porous media so that the engine performance fitted with channels regenerator can be evaluated using the full engine CFD model developed in chapter (5). The performance of these regenerators will be evaluated in chapter (7).

6.2 Conventional and parallel-geometry regenerators

Enhancing Stirling engine performance is being sought by many researchers and developers. The successful development of an efficient and cost-effective Stirling engine will have a significant impact on the recovery of the available waste heat sources leading to significant reduction in fossil fuel consumption and CO₂ emissions. The regenerator, as reviewed previously, is an essential part of the engine and engine performance can be enhanced by

optimizing this component. The original regenerator in the subject Stirling engine was a wire mesh (woven or random fibre) type. As micro-fabrication techniques have recently shown great advances, regular-shaped mini-channel regenerator type can be as good a choice as a parallel-geometry regenerator. Some attempts were reported in the literature for the development of new conceptual parallel-geometry regenerators that were reported to have superior performance to the traditional wire mesh types [88, 97-100, 103].

Theoretically, a regenerator, which has its heat transfer surfaces parallel to an oscillatory flow can have better performance than conventional mesh regenerator types [152]. Because of lower pressure losses, due to the minimum flow separation, and a smaller dead volume, which means that they can be more fabricated. However, the intrinsic axial conduction losses are larger due to the continuity of solid material and this crucial disadvantage can significantly degrade its performance.

The proposed regenerators performance is often evaluated experimentally on a real engine test-stand or on a tailor-made test-stand based on unidirectional flow or oscillatory flow. However, in recent years, numerical models and the sophisticated CFD packages for Stirling engine analysis have emerged which reduces the amount of experimental test time, required [35].

6.3 Mini-channel regenerator

Figure 6-1 shows the conceptual design of mini-channel regenerator which is scaled to the original regenerator dead volume on the test engine. The proposed geometry is composed of constant diameter circular-shaped mini-channels cutting through the solid matrix. Different diameters were selected for the investigation of the channels 0.4, 0.5, 0.6, 1, 1.5 (mm) with

channel length equal to the regenerator length of 57 mm. The material used to manufacture all regenerators was stainless steel (SS304), the properties of which are listed in Table 6-1.

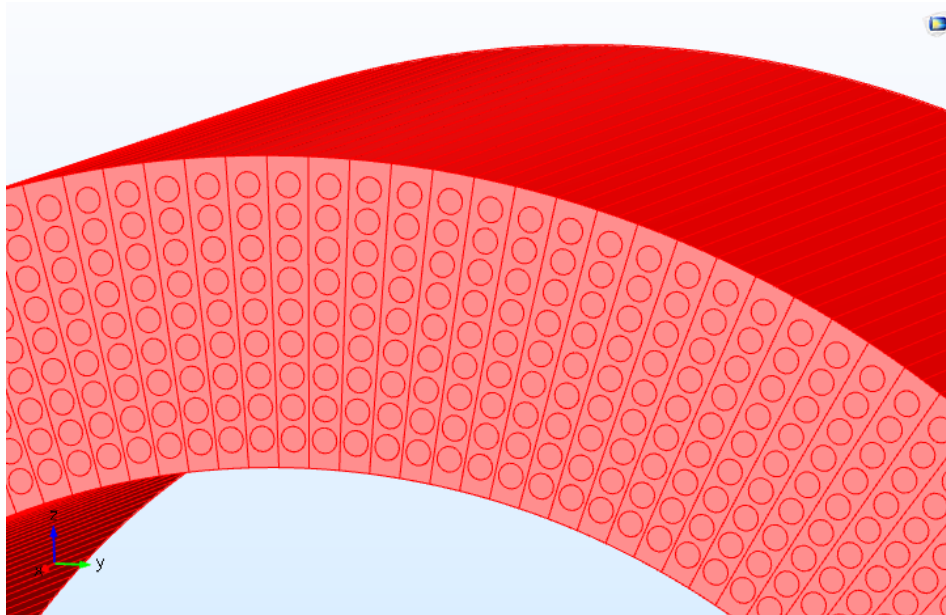


Figure 6-1 Conceptual design of mini-channel regenerator.

Table 6-1 Regenerator material thermal properties (SS304)

Property	Value
Density (kg/m ³)	7500
Specific heat capacity (J/kg. K)	502
Thermal conductivity (W/m. K)	16

The circular channels were distributed with radial and angular pitches that must satisfy the minimum thermal penetration depth required, which was defined as the distance that heat can diffuse into the solid matrix during single blow time, $t_p = (1/\pi f_{req})$, where f is the frequency of the engine [67]. Since the engine under consideration can operate at speed ranging from 100 to 1000 rpm, then the thermal penetration depth was calculated by eq.(6.1) [67] and plotted in Figure 6-2;

$$\delta = \sqrt{(k/\pi f_{req} \rho C_p)}$$

6.1

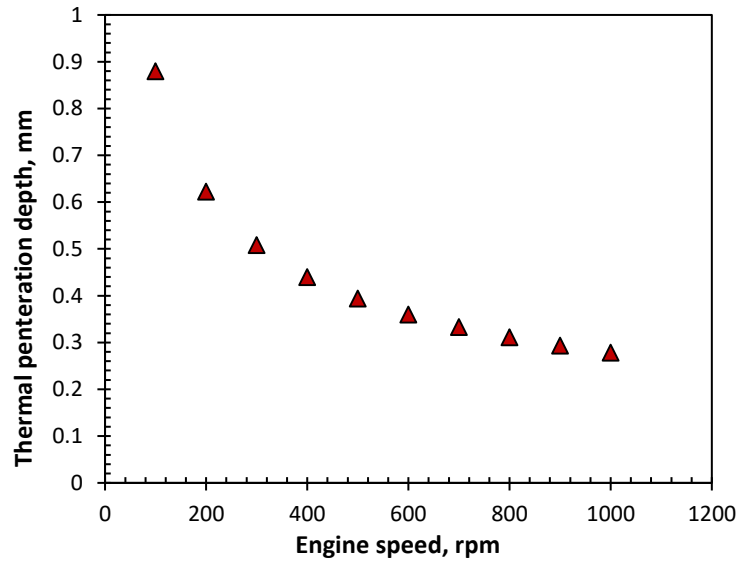


Figure 6-2 Thermal penetration depth vs. engine speed.

The radial and angular pitches are calculated based on the minimum thermal penetration depth of 0.25 obtained at maximum engine speed as shown in Figure 6-2. The geometrical parameters of the regenerator configuration shown in Figure 6-3 can be calculated from eq.(6.2) and eq.(6.3), respectively.

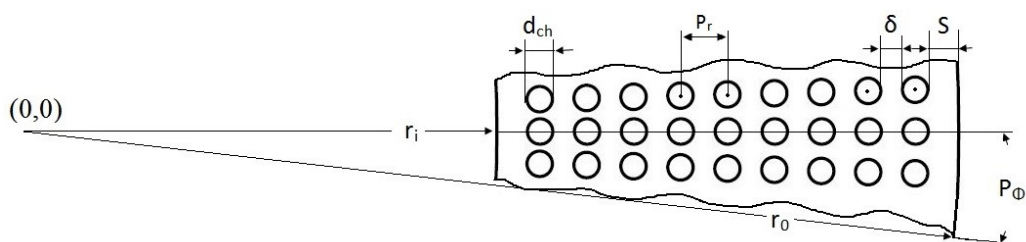


Figure 6-3 Geometrical parameters of channels regenerator.

$$P_r = \delta + d_{ch}$$

6.2

Where the radial pitch (P_r) is measured from centre to centre of consecutive channels

$$P_\phi = 2 * \sin^{-1}(((d_{ch}/2) + \delta) / ((d_{ch}/2) + r_i + S)) \quad 6.3$$

The angular pitch (P_ϕ) in eq. (6.3) is based on the trigonometric relation between the three parameters (d_{ch} , δ and S) at the first row of channels as demonstrated in Figure 6-4.

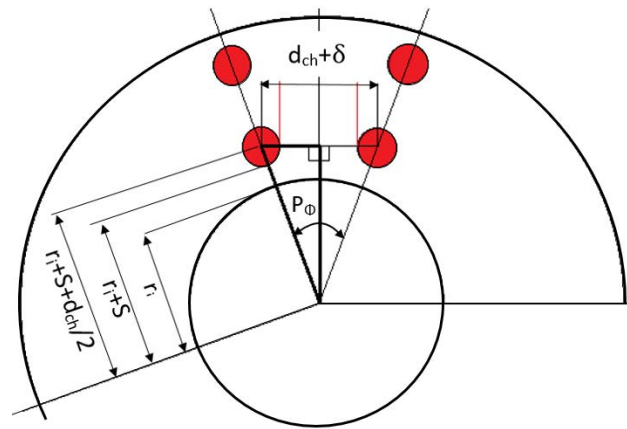


Figure 6-4 Radial pitch definition in terms of regenerator parameters (not to scale).

The geometrical parameters are calculated for channel diameter ranging from 0.4 mm to 1.5 mm and fixed δ value and tabulated in Table 6-2 where the porosity is defined as the ratio of free flow area to the total area in flow direction.

Table 6-2 Regenerators configurations and parameters.

Configuration	Angular pitch P_ϕ (°)	Vertical pitch P_r (mm)	Tubes/sector	Tubes/annulus	Porosity (%)
0.4mm	0.85	0.65	26	500	0.248
0.5mm	0.85	0.75	22	500	0.286
0.6mm	0.9	0.85	20	400	0.343
1.0mm	1.42	1.25	13	253	0.391
1.5mm	2	1.75	9	180	0.433

6.4 CFD model

COMSOL Multiphysics 5.2 CFD commercial code was used to analyse the 3D transient, conjugate heat transfer of the regenerator, the following steps were conducted to set up the CFD analysis;

- Simulation of a fluid flowing inside a short smooth circular tube under constant wall temperature boundary condition.
- Validation of the CFD results for Nusselt number (Nu) with data for thermally developing flow correlations from the literature.
- Comparison of the product of friction factor - Reynolds number (fRe) obtained from simulation with existing correlations from the literature.

6.5 Fluid flow and heat transfer in channels

The average friction factor and heat transfer coefficient for a whole tube are reported to be enhanced due to the effect of the entrance length [153]. This enhancement is significant for a shorter tube rather than a longer one as the skin shear stress and the heat transfer coefficient are large at the entrance of the tube where the boundary layer thickness is very small. In the developing flow regime, both the velocity and thermal boundary layers are growing in the flow direction where the velocity and temperature profile are locally varying up to a certain distance downstream of the tube then the flow become fully developed. As depicted in Figure 6-5, the flow is said to be *fully developed*, and the *parabolic profile* is obtained for laminar flow in a circular tube. In the entrance region, the boundary layer of the developing flow needs to be captured by the computational grid for accurate solutions.

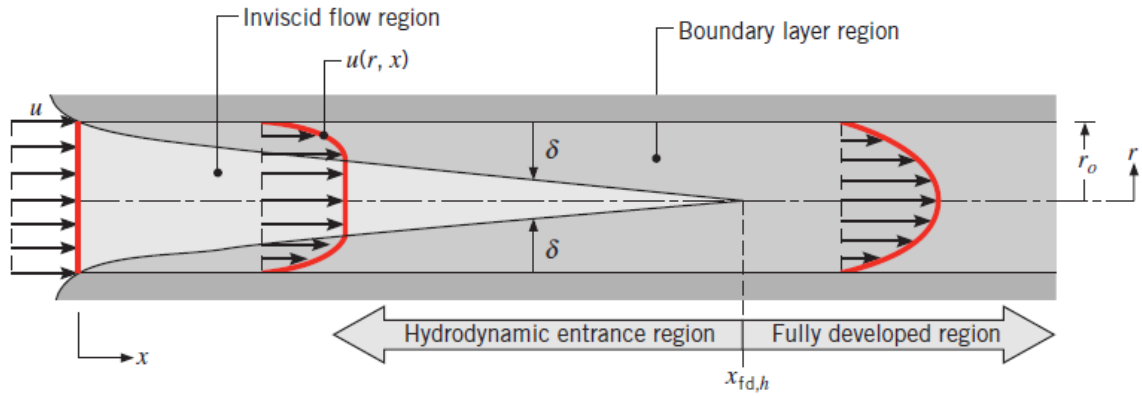


Figure 6-5 The developing velocity profile of a fluid entering a tube [135].

The hydrodynamic entry length, for laminar flow ($Re < 2300$), can be expressed in the form [154].

$$\left(\frac{x_{fd,h}}{D}\right) \approx 0.05Re \quad 6.4$$

In the fully developed region, the pressure gradient is constant and the velocity profile is recalled from [154] as

$$u(r) = 2u_m \left[1 - \left(\frac{r}{R}\right)^2\right] \quad 6.5$$

It follows that the ratio of the maximum and average velocities in the fully developed region

$$u_{max} = 2u_m \quad 6.6$$

According to Shah and London [155], the Fanning friction factor – Reynolds number product (fRe) for laminar fully developed flow is

If the tube surface is maintained at either uniform temperature or uniform heat flux (Figure 6-6), conduction and convection heat transfer occurs and the *boundary layer* begins to develop thermally until the fully developed temperature profile is reached.

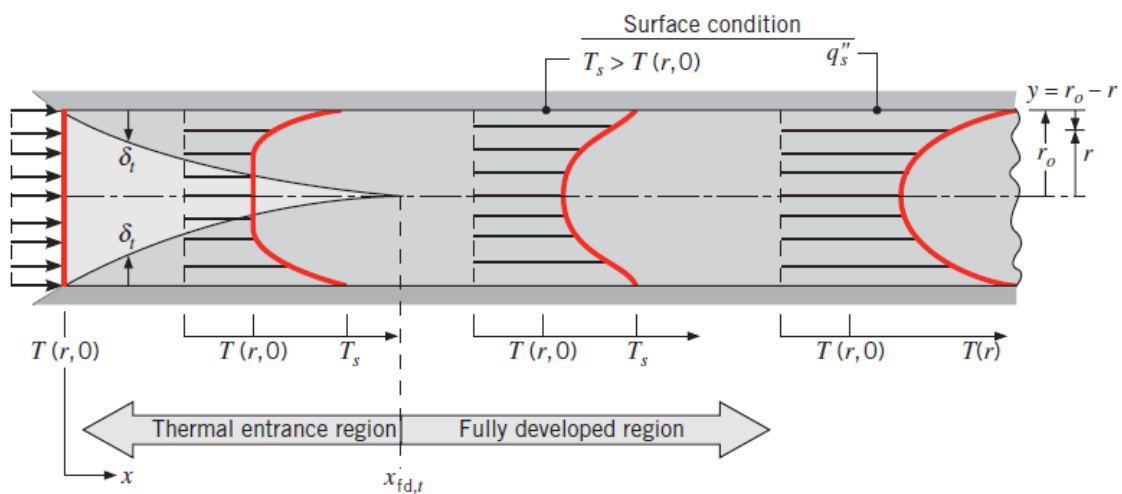


Figure 6-6 The developing temperature profile of a fluid entering a tube [135].

The *thermal entry length* for laminar flow can be expressed as [154].

$$\left(\frac{x_{fd,t}}{D}\right) \approx 0.05 Re Pr \quad 6.8$$

When a tube flow is considered, heat transfer occurs by conduction when the fluid layers are stationary near the wall and by forced convection when the fluid is flowing through the tube. The ratio of the convective heat flux to the conductive heat flux is referred to, Nusselt number (Nu) and it is defined as

$$Nu = \frac{h_x D_h}{k_f} \quad 6.9$$

In a horizontal tube, under constant wall temperature boundary condition, the thermal characteristics of the flow is defined by the fluid bulk temperature, heat transfer coefficient, heat flux, and the Nusselt number. The fluid bulk temperature, is obtained in terms of the true energy advection over an arbitrary cross section of the pipe.

Therefore, T_m is defined by

$$T_{m,x} = \frac{\int \rho u C_p T dA_c}{m C_p} \quad 6.10$$

The other important parameter is the heat transfer coefficient which is defined by

$$h_x = \frac{q''_x}{(T_w - T_{m,x})} \quad 6.11$$

Where

$$q''_x = k_f \left[\left(\frac{\partial T}{\partial r} \right)_{w,m} \right]_x \quad 6.12$$

Where $\left(\frac{\partial T}{\partial r} \right)_{w,m}$ represents the peripheral average temperature gradient at wall.

As a special case for a fully developed laminar flow in case of constant wall temperature in a circular tube, *the rate of net energy transfer to the control volume by mass flow is equal to the*

net rate of heat conduction in the radial direction, leading to the common value of Nusselt number,

$$Nu = 3.66 \quad 6.13$$

It is worth noting that this discussion is limited to laminar flow regime as the flow is typically laminar inside all the different channel regenerators based on the maximum gas velocity in the range of engine operating speed from 100 rpm to 1000rpm (see section 6.7).

6.6 Governing equations and solution methodology

For steady-state incompressible viscous flow, the Navier-Stokes equations which describe the velocity, pressure, temperature, and density of a moving fluid based on conservation of mass, momentum and energy for the computational domain can be written as;

$$\rho \nabla \cdot (\mathbf{u}) = 0 \quad 6.14$$

$$\rho (\mathbf{u} \cdot \nabla) \mathbf{u} = \nabla \cdot [-p\mathbf{I} + \mu (\nabla \mathbf{u} + (\nabla \mathbf{u})^T)] + \mathbf{F} \quad 6.15$$

$$\rho C_p \mathbf{u} \cdot \nabla T + \nabla \cdot k \nabla T = Q \quad 6.16$$

These coupled differential equations are solved by finite element-based CFD software (Comsol multiphysics). In order to carry out the simulation, a prerequisite of mesh sensitivity analysis is initialized to ensure that the numerical solutions obtained are grid-independent. Using symmetry can provide faster solution in which a quarter of the current 3D tube is selected as the computational domain as shown in Figure 6-7. The tube has (0.0254 m) diameter and

(0.3048 m) length which is subdivided into six sections in order to calculate the developing Nusselt number downstream of the inlet.

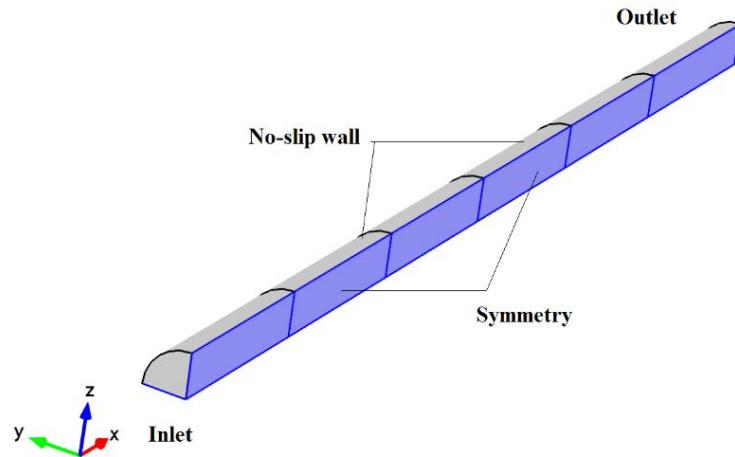


Figure 6-7 Computational domain of the channel.

The boundary conditions are applied as follows;

- Constant wall temperature of 310 K is applied on the outer walls of the pipe.
- Uniform inlet velocity (based on $Re = 100$) at constant temperature of 300 K is applied at the tube inlet.
- Outlet pressure of 101,325 kPa with no back flow is applied at the tube outlet.
- Free-slip symmetry walls with zero normal velocity components and normal gradients of all velocity components.

The meshing sequence is varied from coarse, normal fine and finer size as shown in Figure 6-8. This will define mesh size that gives an accurate solution with less computational time required to perform the CFD simulation. The face elements then are swept over the length of the tube based on each sequence. Table 6-3 summarises the details of each meshing sequence and the obtained solution of Nusselt number.

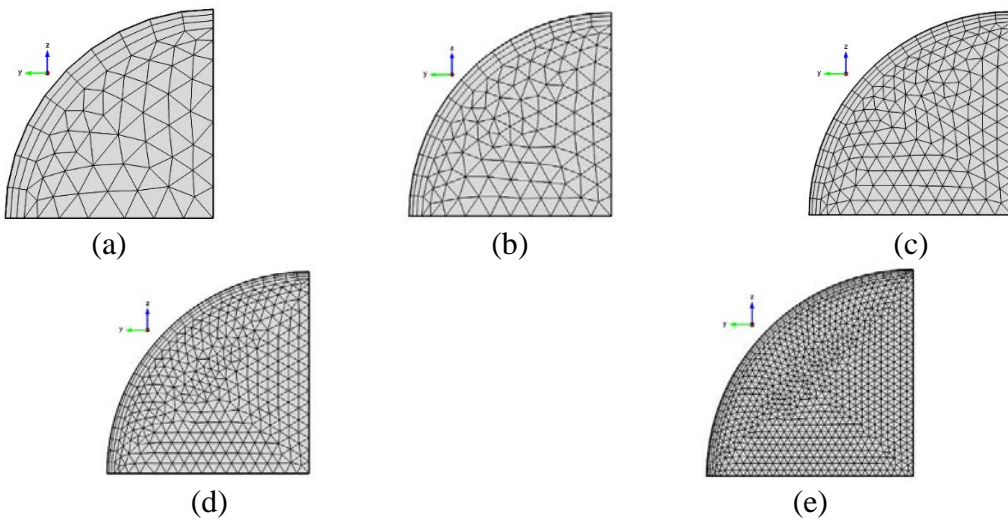


Figure 6-8 Meshing sequence, a) coarse, b) normal, c) fine and d) finer, e) extra-fine.

Table 6-3 Mesh sequence and CFD results

Mesh sequence	No of elements	Mesh quality	Growth rate	Nu
Coarse	19908	0.6558	1.344	6.2728
Normal	57354	0.7324	1.317	6.1937
Fine	103840	0.7747	1.269	6.1387
Finer	283920	0.8139	1.229	6.0173
Extra-fine	1,116,220	0.8614	1.189	5.9435

From the data presented in Table 6-3, finer meshing sequence can be selected for the investigation as the change of Nusselt number is less than 1.3% compared to the extra-fine sequence. The velocity, temperature and pressure contours are plotted in Figure 6-9 to Figure 6-13. It is clearly shown that both hydrodynamic and thermal boundary layers are developing downstream of the tube inlet.

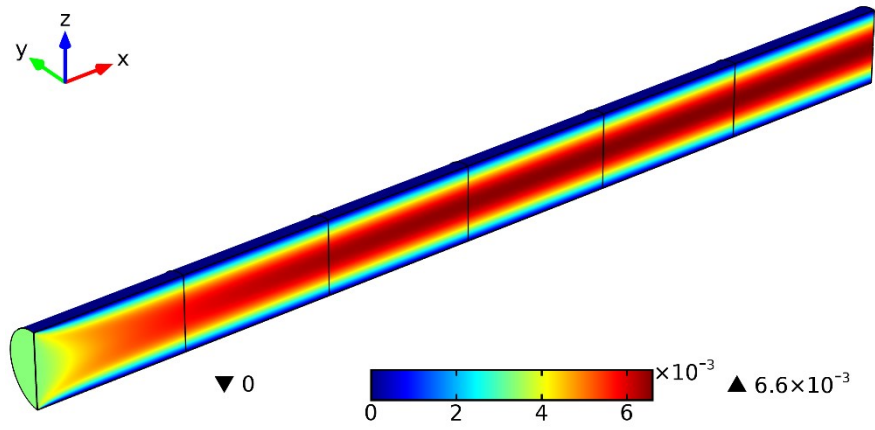


Figure 6-9 Velocity contours (m/s) along the tube.

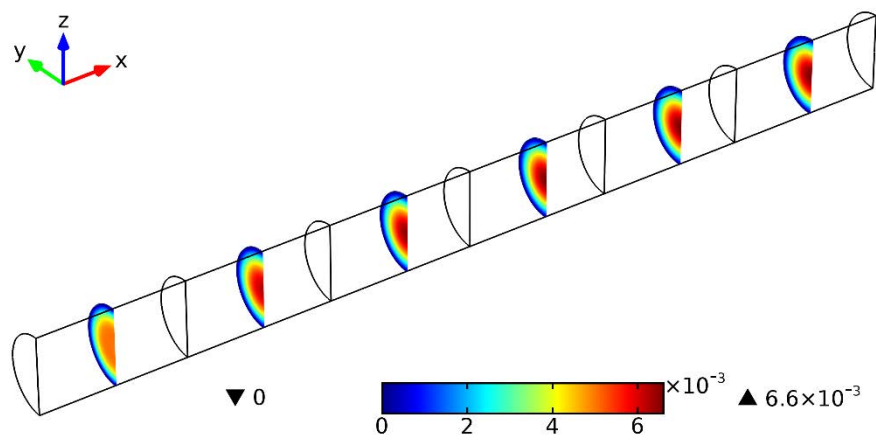


Figure 6-10 Sectional velocity contours (m/s) at different positions of the pipe.

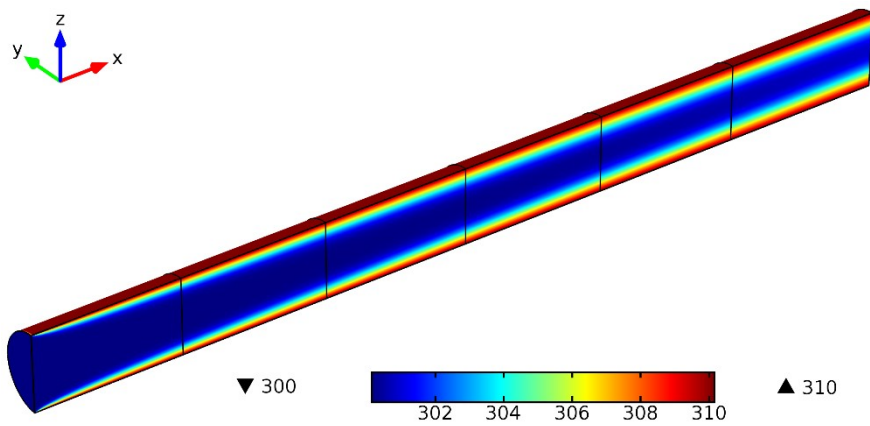


Figure 6-11 Temperature contours (K) along the tube

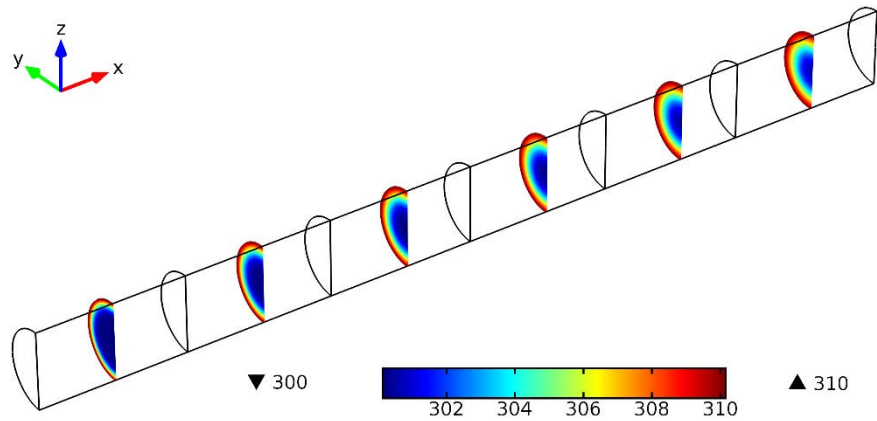


Figure 6-12 Sectional temperature contours (K) at different positions of the pipe.

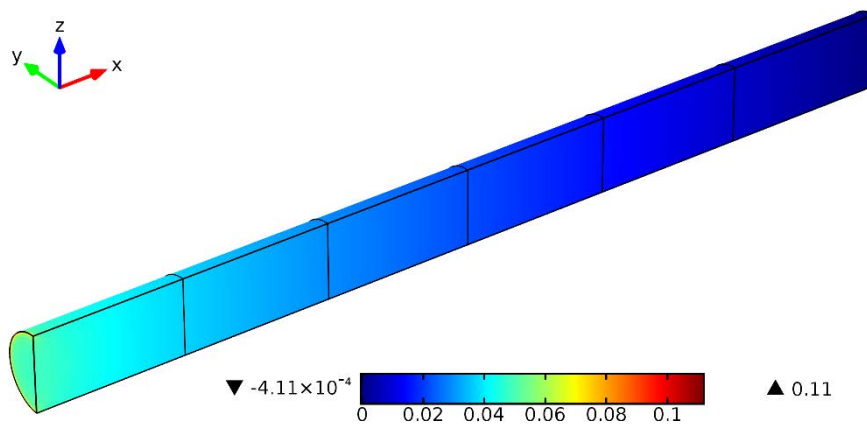


Figure 6-13 Pressure contours along the tube.

A first check to carry out was to calculate the ratio of the maximum velocity magnitude to the average velocity magnitude at the end of the pipe and the product of Reynolds number with friction factor. It is recalled that from the analytical solutions available in literature eq. (6.6) that this ratio is double since the pressure gradient is constant in the fully developed region. Since the entry length required for this tube is calculated from eq. (6.4) equals 12.7 cm which means that the flow should be hydrodynamically fully developed at the end of the pipe and the product of Reynolds number with friction factor equals to 16. The comparison made in Table 6-4 has shown good agreement with the available analytical solution.

Table 6-4 Comparison between CFD results and analytical data for fully developed tube flow.

Parameter	CFD	Analytical solution [154]	Difference %
u_{\max}/u_{mean}	1.97	2	1.5
f_f, Re	17.4	16	8

In order to validate the CFD results of the obtained Nu number in the case of developing flow, reference [156] was selected for the comparison which is recommended for a combined entry length under constant wall boundary condition. The results of Nusselt number was compared to Hausen's correlation in Figure 6-14 where both results are in good agreement with maximum deviation of 11%.

$$\overline{Nu_D} = 3.66 + \left[\frac{0.0668 G_{ZD}}{1 + 0.04 G_{ZD}^{\frac{2}{3}}} \right] \quad 6.17$$

Where, G_Z is Graetz number which is defined as

$$G_Z = \left(\frac{D}{x} \right) \cdot Re \cdot Pr \quad 6.18$$

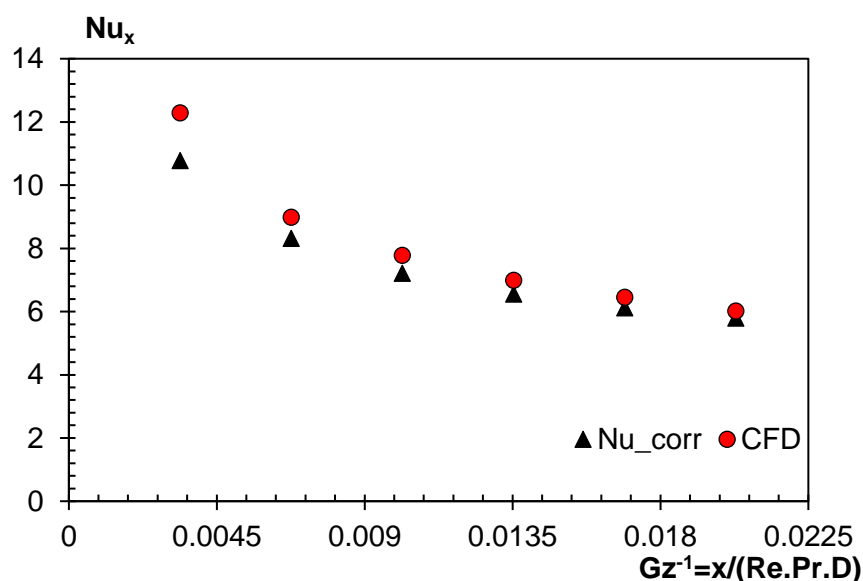


Figure 6-14 Nusselt number for laminar developing pipe flow.

As can be seen, the Nusselt number predicted by CFD for the developing flow correlates well with Hausen's correlation. This gives confidence in the CFD methodology and the meshing sequence used thus the calculation of Nusselt number will be adopted for the regenerator CFD simulation in the next section.

6.7 Regenerator modelling

From a microscopic point of view, it is not feasible to model the regenerator as a whole as depicted in Figure 6-1. Therefore, more simplification is realized when a certain sector is repeated in the angular-direction with a certain pitch (P_θ), as illustrated in section 6.3, it resembles the flow through regenerator annulus. The depth of the sector is taken as whole regenerator length.

Inlet velocity at constant temperature of 650 °C is specified at channels inlet, while pressure outlet at 10 bar with outflow boundary is prescribed at the outlet. These boundary conditions are similar to the actual operating conditions of the engine during single hot blow period. The maximum inlet velocity to the sector channels, is varied according to the engine frequency and displacer swept volume, and is calculated by [101];

$$u_{max} = \pi \cdot f_{req} \cdot V_{SE} / A_{ff} \quad 6.19$$

The outer walls and the inner wall of the sector are adiabatic and the reference pressure is the charge pressure of the engine pressure. Transient conjugate heat transfer simulations were carried out for all configurations following the same procedure of meshing sequence described in section 6.6. A sample of the obtained results of temperature contours was presented in Figure 6-15 and Figure 6-16 for 1.5mm channels sector. It can be seen that most of the heat is

transferring in the radial direction depending on the gas inlet velocity through the channels. The parabolic shape of temperature contours in Figure 6-16 appears to be a result of adiabatic walls and the pronounced axial conduction in the flow direction. As the inlet velocity to the regenerator sector increases from 100 rpm (Figure 6-15) to 1000rpm (Figure 6-16), more energy is transferred to the solid matrix due to the forced convection giving a rise to the average solid temperature of the matrix. As can be seen that the minimum temperature of the matrix at 100 rpm is 500 K compared to 865 K at 1000 rpm.

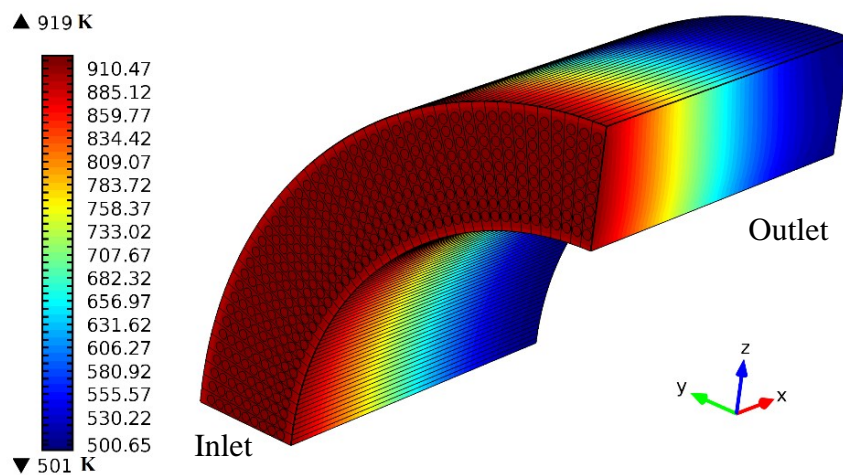


Figure 6-15 Temperature contours for 1.5mm channels regenerator at speed of 100 rpm and time of 30 s.

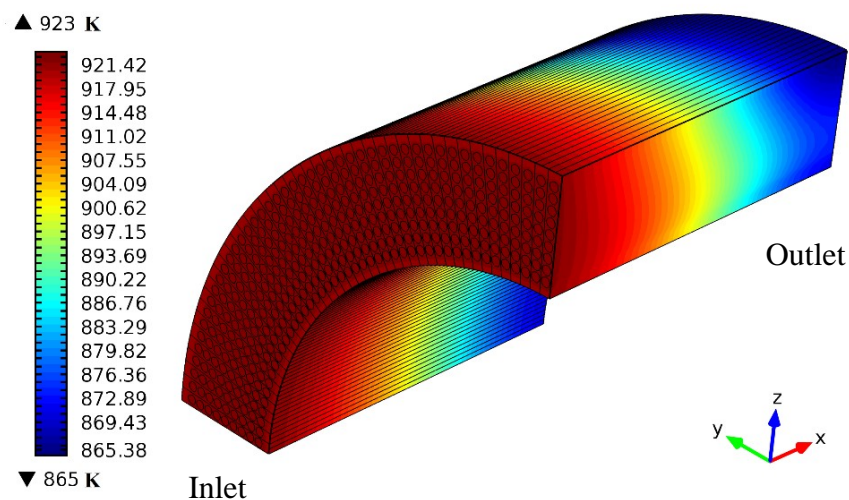


Figure 6-16 Temperature contours for 1.5mm channels regenerator at speed of 1000 rpm and time of 30 s.

The fluid flow and heat transfer characteristics were obtained from CFD simulations for each configuration and are plotted in Figure 6-17 to Figure 6-19. It can be seen that data of pressure loss (Figure 6-17) shows almost linear trends with gas inlet velocity for all regenerator configurations. The inertial pressure loss part is not significant in the channels due to the absence of flow separation and vortices. The highest pressure loss is observed for 0.4mm channels regenerator.

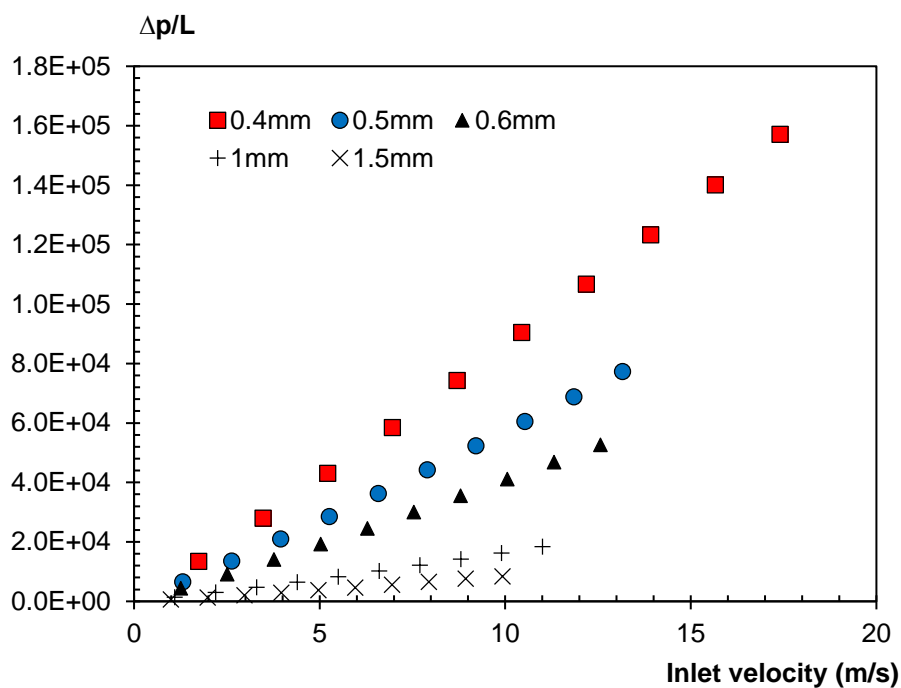


Figure 6-17 Pressure loss per unit length vs. maximum gas inlet velocity to the regenerator for different channels regenerators.

The simulation results for friction factor and Nusselt number were plotted in Figure 6-18 to Figure 6-19. Figure 6-18 shows that the average friction factor has a decreasing trend with increasing Reynolds number for all configurations, in which the friction factor correlations are similar to Darcy friction factor for laminar flow.

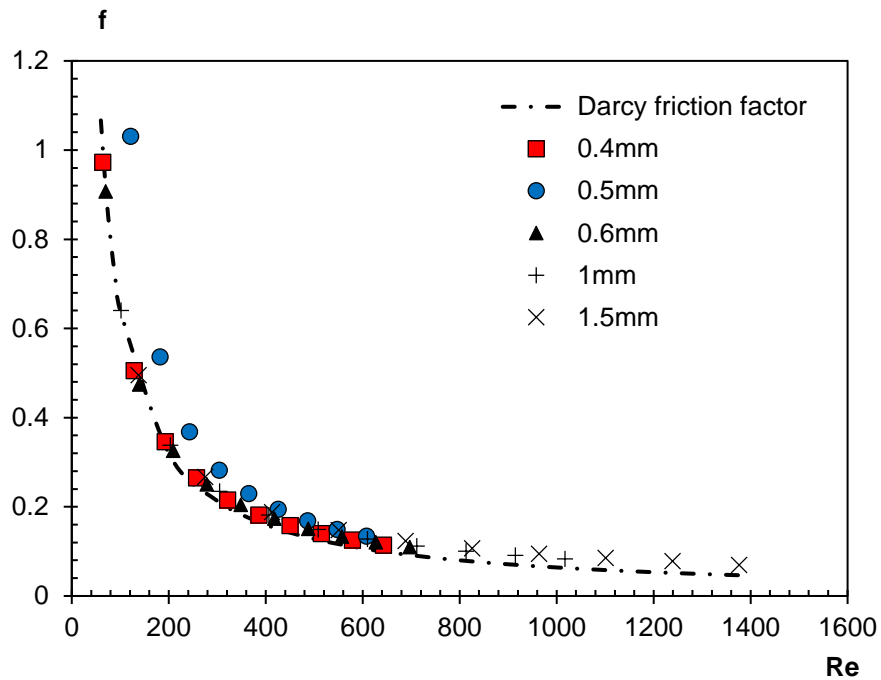


Figure 6-18 Darcy friction factor vs. Reynolds number for different channels regenerators.

Figure 6-19 shows that the average Nusselt number increases with the fluid flow velocity. This result agrees with the principles of forced convection. For larger diameter channels, higher values of Nusselt number is depicted in Figure 6-19 due to the higher values of hydraulic diameters.

However, the small channels regenerators indicate faster thermal response at a small range of Reynolds number (100 to 700) compared to larger diameter channels (100 to 1400). In terms of heat transfer coefficient, larger diameter channels experience low heat transfer coefficients due to the limited heat transfer surface area.

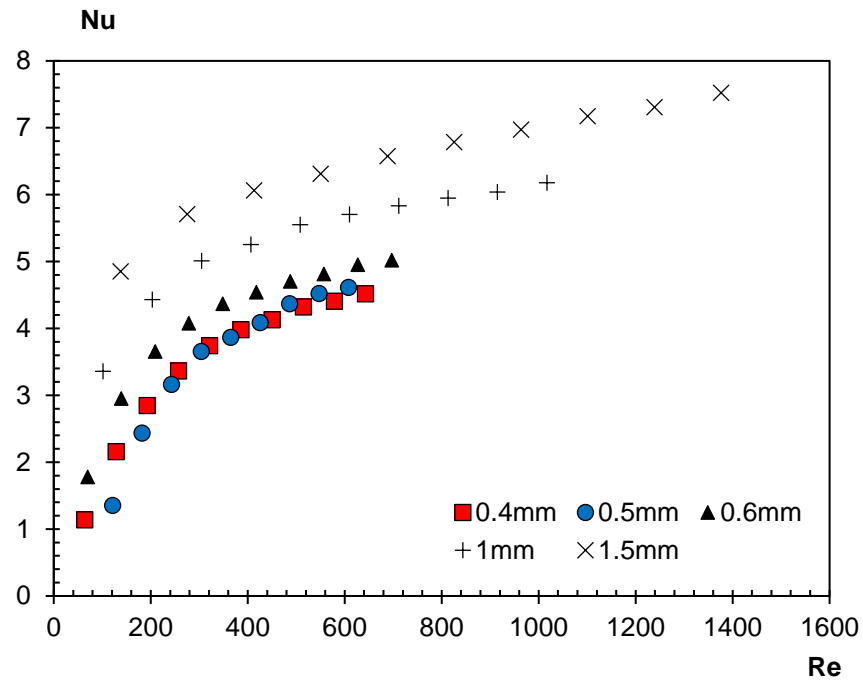


Figure 6-19 Nusselt number vs. Reynolds number for different channels regenerators.

The pressure drop-velocity data of each regenerator was fitted to Forchheimer-Darcy equation eq. (5.21) using the least square method in order to obtain the equivalent porous media parameters (porosity, Forchheimer drag coefficient and permeability).

$$\frac{\Delta p}{L} = \frac{\mu}{K} u + \beta_F u^2 \quad 6.20$$

All simulation results such as Nusselt number correlations and porous media parameters were tabulated in Table 6-5. This data of each configuration will be used as input parameters to the engine CFD model to evaluate the performance of the engine with each configuration. This will include evaluating the indicated and cooling powers of the engine to investigate the effects of the various mini-channel regenerators configurations.

Table 6-5 Equivalent porous media characteristics of the five proposed regenerators.

Regenerator type	Permeability, K (m ²)	Forchheimer drag coefficient, β_F (kg/m ⁴)	Nusselt number	Specific surface area (1/m)
0.4mm	4.95E-09	61.375	$0.124\text{Re}^{0.5747}$	2475
0.5mm	7.73E-09	59	$0.195\text{Re}^{0.5126}$	2617
0.6mm	1.1E-08	49.2	$0.34\text{Re}^{0.4249}$	2284
1.0mm	3E-08	32.925	$1.143\text{Re}^{0.2488}$	1565
1.5mm	6.26E-08	23	$2.018\text{Re}^{0.1812}$	1156

6.8 Regenerator test facility

The three mini-channel regenerative heat exchangers (MCRHXs), having hydraulic diameters of 0.5, 1 and 1.5mm, were 3D printed after the development phase. Figure 6-20 shows a sample of the fabricated MCRHX of 0.5mm.

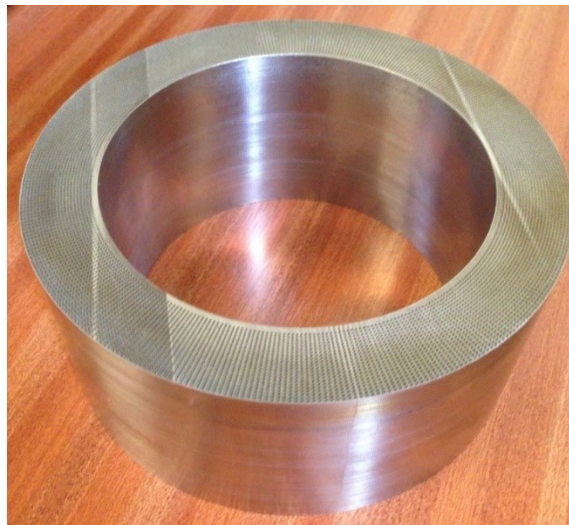


Figure 6-20 3D printed 0.5mm MCRHX.

A test facility was purposely designed for transient testing of annular type heat exchangers based on unidirectional flow condition as represented schematically in Figure 6-21.

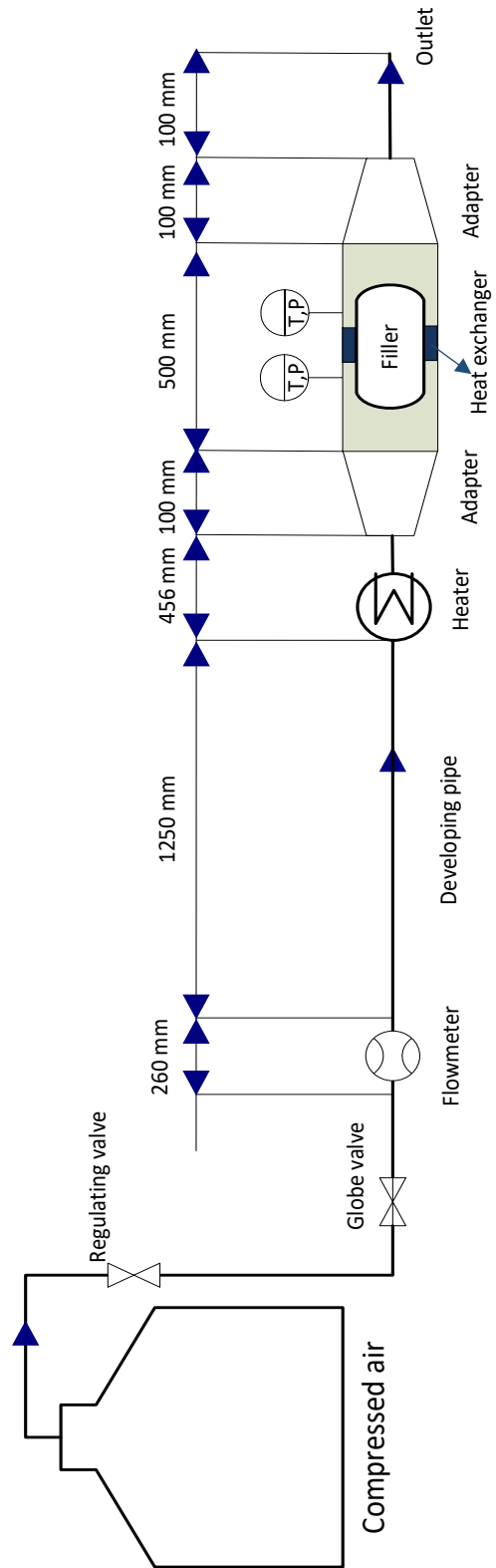


Figure 6-21 schematic of experimental test facility.

It consists of an open airflow circuit, test section and instrumentations. The test facility is supplied with a compressed air at a certain pressure level from a compressor-vessel system. The air is allowed to flow in a 2-in (50.8mm) pipe and then heated via a 2000 W inline heater (*Omega AHF-14240*), shown in Figure 6-22-(a), before entering the test section. The mean air velocity is measured at the outlet with an anemometer (*TECPEL 712*), shown in Figure 6-22-(b), calibrated with a gas flow meter (*Omega FLMG-10050AL*).

The heating power of the heater can be controlled using a Variac transformer (*Carroll & Meynell LTD.*), shown in Figure 6-22-(c). The test section is comprised of two conical adaptors (2 in to 5 in) (Figure 6-22-(d)), two housing cylinders with an inner step of 1mm to hold the MCRHX in the middle of the two cylinders (Figure 6-22-(e)), and the MCRHX and the filler assembly (Figure 6-22-(f)).

The filler is made of stainless steel with ellipsoidal shape that is hollow from inside with 6 mm thickness and it functions as a flow guide to the MCRHX. The filler and the two conical adaptors were designed and optimised using CFD simulations. The ellipsoidal shape of the filler was adopted as a uniform velocity profile was achieved at the inlet of the regenerator compared to the spheroidal shape. All MCRHXs are made of stainless steel and the thermophysical properties are summarized in Table 6-1.



Temperature probes (type T) of 3 mm diameter and 0.1 °C accuracy, were used to measure temperatures; at inlet and outlet of the heater and at four positions (90° offset) at the inlet and the outlet of each MCRHX, as shown in Figure 6-23. The transient response of temperature signals is sampled using two data takers (*Pico TC08*) (Figure 6-22-(h)) at a sample rate of 2 Hz connected to a PC. The pressure drop is measured across the test section using (*D and D/2*) pressure tapings connected to a micromanometer (Figure 6-22-(i)) with a minimum scale division of 0.1 mbar and a full scale 50 mbar.

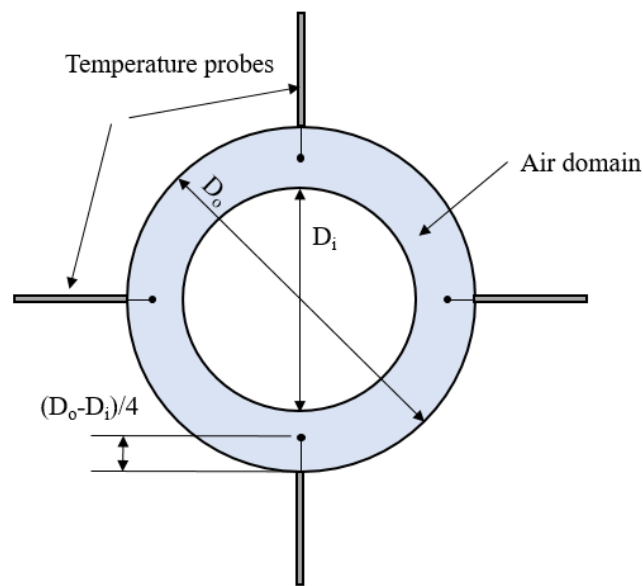


Figure 6-23 Positions of thermocouples at inlet and outlet of MCRHX.

Once the desired heat exchanger configuration was fitted in the test section, the flow rate was set at the desired amount. For isothermal and Non-isothermal flow experiments, the flow rate was varied in the range from 10 to 50 SCFM and the readings of pressure drop were recorded at isothermal condition. For the Non-isothermal experiments, the heater then was switched on and each test run was allowed for a period of time (normally 1 hour). At that stage, readings of all temperatures were recorded. The maximum outlet temperature of the heater was maintained around 100 °C at each specific flow rate.

6.9 Theoretical model for transient testing method

Since the MCRHX is composed of mini-channels of circular shape, internal fluid flow and heat transfer are the major physics. In experiment, the hot air passes through the channels transporting energy to the MCRHX and temperature responses of the air are measured at inlet and outlet of the MCRHX. Due to the complexity of inserting thermocouples in the miniature channels to measure the solid wall temperature inside the channels, similar approach to single-blow transient method was proposed in this work.

The current technique is robust and cost effective compared to single-blow method and steady-state heat transfer measurements. In the conventional single-blow method, the analytical solution of this method imposed an ideal step change in inlet fluid temperature to a constant value to be met in experiment until the new equilibrated temperature is reached. This requires a special controlled compact heater, or using two-fluid streams with a fast response valve, or any mechanism to switch between the two streams, which adds more time and complexity and hence cost to the experimental set-up. In the current set-up, a low heat capacity heater was used to heat up the test core gradually without a step change from a room temperature for a period of time so that the inlet and outlet temperature profiles are measured and sampled for analysis.

The heat transfer characteristics can be evaluated by the transient response of the air outlet temperature. Transient conjugated heat transfer simulations were performed on 3D sector of the MCRHX using Comsol multiphysics 5.2a. The inlet thermal response obtained from experiment was entered to the CFD model as inlet boundary condition using piecewise cubic interpolation function. The outlet thermal response predicted is iteratively matched as a whole curve with experiment for each test run. Once the thermal responses are matched within a

minimum acceptable deviation, heat transfer coefficient can be determined from CFD. Table 6-6 summarizes the main differences between the current approach and the single-blow method.

Table 6-6 Comparison between current testing technique and single-blow method.

Condition	Transient testing technique	
	Current technique	Single-blow method
Inlet temperature	Arbitrary change	Step change
Fluid properties	Temperature dependent	constant
Steady-state	Not required	required
Thermal losses	Included (non-adiabatic walls, radial and axial conduction)	Non-adiabatic walls and axial conduction can be included
Numerical model	CFD (Conjugate heat transfer)	Analytical (Schumann-Hausen model)
Evaluation technique	Direct curve matching	Depends on NTU value but maximum slope method is recommended.

The computational model is based on the following assumptions:

- The gas is weakly compressible that is its density is only constant with pressure and all other fluid properties are strongly dependent on the temperature field.
- The inlet velocity and the inlet temperature profiles are uniform
- The effective thermal conductivity of solid matrix (deducing the channels volume) is accounted in simulations.

The governing equations are the continuity, momentum and energy equations given as;

$$\frac{\partial \rho}{\partial t} + \rho \nabla \cdot (\mathbf{u}) = 0 \quad 6.21$$

$$\rho \frac{\partial \mathbf{u}}{\partial t} + \rho (\mathbf{u} \cdot \nabla) \mathbf{u} = \nabla \cdot [-p\mathbf{I} + \mu (\nabla \mathbf{u} + (\nabla \mathbf{u})^T)] \quad 6.22$$

$$\text{For fluid} \quad \rho C_p \left(\frac{\partial T}{\partial t} + \mathbf{u} \cdot \nabla T \right) + \nabla \cdot k \nabla T = Q \quad 6.23$$

$$\text{For solid} \quad (1 + \zeta) \rho_s C_{ps} \frac{\partial T}{\partial t} = \nabla \cdot (1 - \varepsilon) k_s \nabla T \quad 6.24$$

The computational domain is a 3D sector of the heat exchanger as illustrated in Figure 6-24. Inlet boundary condition is imposed at the inlet with constant velocity in x-direction and the temperature profile measured from experiment.

$$T = T_{inlet}, u = U_m, v = 0, w = 0 \quad 6.25$$

The outlet boundary condition is set across the gas outlet such that convection heat transfer is dominant. The temperature gradient in the normal direction is zero thus,

$$-\mathbf{n} \cdot \mathbf{q}'' = 0 \quad 6.26$$

The outlet pressure is set to zero (gauge pressure) and backflow is suppressed. The walls between the fluid and the solid are set as no slip. The symmetry boundary conditions imposed on the two faces of the sector lie in Y-X planes to account for similar physics. Thermally resistive layers are added on the faces lying in X-Z planes to account for the conduction resistance through housing cylinder inner and filler outer walls. A thermal insulation layer (0.04 W/m·K conductance) boundary condition of 12 mm thickness was applied on the outer walls of the housing cylinders. The time step was fixed for all simulations to be 1 second as the normal

sampling rate. The mesh sequence was based on sweeping the meshed inlet faces (free triangular elements) over the total length of the sector so that the resultant elements are composed of prism and hexahedral elements. The mesh sensitivity analysis showed that when the mesh was further refined below 156,636 total elements, simulation results only changed by less than 1%.

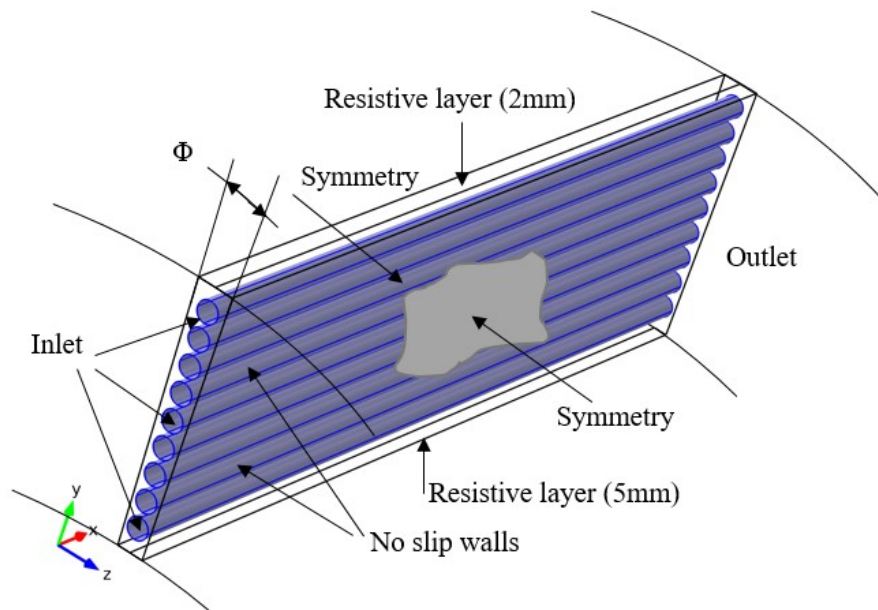


Figure 6-24: Computational domain of 3D sector of the heat exchanger.

It should be emphasized that the results of the CFD model were scaled by introducing the factor (ζ) into eq. (6.24) to overweigh any boundary condition that cannot be feasibly included in the considered computational domain [157]. In the current CFD model, the computational domain considered is only a 3D sector of the heat exchanger (test core) including the inner and outer walls of the housing cylinders and the filler attached to the heat exchanger with a length equals the heat exchanger length as shown in Figure 6-24. However, these walls attached to MCRHX (designated as resistive layers in the figure) extend 3 times and 8 times the heat exchanger

length, as shown in Figure 6-22(f), for the filler walls and housing walls, respectively. Therefore, heat capacity of these walls and the heat loss by axial conduction starting from the outlet of the heater which are not captured in the current computational domain, were overweighed. This constant is varied by trial and error and their values at different flow conditions are summarized in Table 6-7. The absolute value of the total residual between measurement and prediction data points are minimized by using least square criterion [117].

$$R = \left[\sum_{n=1}^{3600} (T_{cal} - T_{exp})^2 \right]^{0.5} \quad 6.27$$

Table 6-7 (ζ) values under different flow conditions.

MCRHX type					
1.5mm		1mm		0.5mm	
Re	ζ	Re	ζ	Re	ζ
146	5.35	146	6	58	4.75
229	5.75	229	4.75	97	4.25
374	4.75	373	4.28	152	3.8
507	4.5	475	4.5	196	4
684	4.3	641	4	242	3.25

The total heat flux entered to the MCRHX, \mathbf{q}''_{-tot} , can be calculated in terms of the air temperature difference measured at the inlet and outlet, the specific heat capacity, mass flow rate and internal surface area of the MCRHX,

$$\mathbf{q}''_{-tot} = \dot{m}C_p\Delta T/A_s \quad 6.28$$

The net heat flux transferred to the MCRHX, \mathbf{q}''_{-net} , is calculated from CFD by

$$\mathbf{q''}_{-net} = k_f \left[\left(\frac{\partial T}{\partial r} \right)_{wall} \right]_x \quad 6.29$$

The factor (ζ) adds an artificial heat capacity of the walls attached to the test core that extends beyond the considered computational domain as previously explained and hence the transient axial conduction loss through these walls starting from the heater outlet up to the outlet of the MCRHX, is accounted for accordingly. In the base case, this factor approaches zero value if the heater is located just upstream the MCRHX. The results of the total heat flux and the net heat flux transferred to the MCRHX at different flow rates, were depicted in Figure 6-25 to demonstrate the importance of this factor.

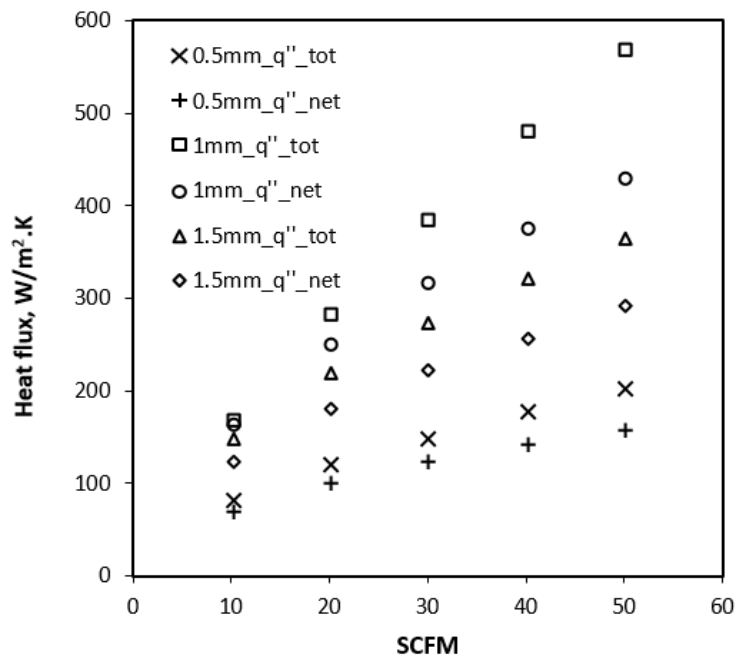


Figure 6-25 Total and net heat flux transferred to the three MCRHX's at different flow rates.

It is clear that heat flux shows an increasing trend with flow rate due to the forced convection. As depicted, the difference between total and net heat flux represents the heat loss from the test core (MCRHX). The highest heat loss of 142 W was observed for 1mm MCRHX at the

maximum flow rate of 50 SCFM compared to 41 W and 74 W for 0.5 mm and 1.5 mm MCRHX's, respectively.

The temperature histories of inlet and outlet from experiment and CFD can be expressed in a nondimensionalized form as a temperature incremental rate for comparison as

$$\theta = \frac{T - T_{ref}}{T_{final} - T_{ref}} \quad 6.30$$

Since the maximum slope method is not used in this work, the nondimensionalized time variable can be conveniently expressed as the ratio between transient response and the total time elapsed during experiment.

$$\tau = \frac{t}{t_{final}} \quad 6.31$$

6.10 Data analysis and uncertainty

Friction factors. The friction factor for each MCRHX is calculated from the predicted pressure drop and the mean air velocity,

$$f = \left(\frac{\Delta P_{cal}}{\frac{1}{2} \rho U_m^2} \right) \frac{D_H}{L} \quad 6.32$$

Since the maximum deviation between predicted pressure drop, ΔP_{cal} and experimental pressure drop, ΔP_{exp} is 8% and the individual uncertainties for ΔP_{exp} and U_m are 0.2% and

1.4%, respectively, the maximum uncertainty in calculating f is less than 9% based on reference [132].

Heat transfer coefficient. Heat transfer coefficient is calculated from CFD after matching the air temperature responses at the outlet of the MCRHX with experiment. From the knowledge of net heat flux, average bulk temperature and the average wall temperature, the average heat transfer coefficient can be calculated from,

$$h = \frac{\mathbf{q}''_{-net}}{T_b - T_w} \quad 6.33$$

The errors in estimating heat transfer coefficients are mainly due to uncertainty in temperature measurement and the deviation in temperatures between measured and predicted values (the root-mean-square difference). The uncertainty in temperature measurement by temperature probes and data taker resolution is 1% (the calibration of the probes is provided in Appendix A). The maximum deviation in temperatures recorded between predicted and measured values is less than 9%. Therefore, the maximum uncertainty in calculating h is less than 10%.

6.11 Summary

A combined approach based on experiment and CFD was proposed to investigate heat transfer and flow friction of three mini-channel regenerative heat exchangers (MCRHX), having channel hydraulic diameters of 1.5, 1 and 0.5 mm. Experiments were conducted to measure pressure drop and the transient thermal responses at the inlet and outlet of each MCRHX. The thermal response predicted from CFD, based on transient conjugated heat transfer simulations,

was iteratively solved until it matched the experimental data within an acceptable deviation. The results of heat transfer and fluid flow characteristic of the three MCRHX will be presented in chapter 7, section 7.8.

CHAPTER 7

RESULTS AND DISCUSSION

7.1 Introduction

This chapter is devoted for discussing the results obtained from the developed thermodynamic model, developed CFD model of the engine described in chapter 3 and the feasibility of the new proposed channel regenerators. The validation process of the developed thermodynamic and 2D CFD model with experiments was described in chapters 4 and showing good agreement. This chapter will be divided into different sections. In the first section, all simulation results of the engine obtained from the developed thermodynamic model will be presented. The second section is devoted to the results obtained from the engine 2D CFD model. Results from other 3D CFD approaches are presented and in section 8 the results from transient model testing of the three regenerators and engine performance using channel regenerators are presented.

7.2 Results of thermodynamic model

The variation of total, expansion space, compression space volumes versus the crank angle are shown in Figure 7-1. The compression ratio is the ratio of maximum to minimum total volumes, as read, 1850 cm³ and 1425 cm³, respectively. The compression space volume is that volume of the working gas confined between the top of power piston and the bottom of displacer piston. It follows that the maximum volume of the compression space is larger than that of the expansion space.

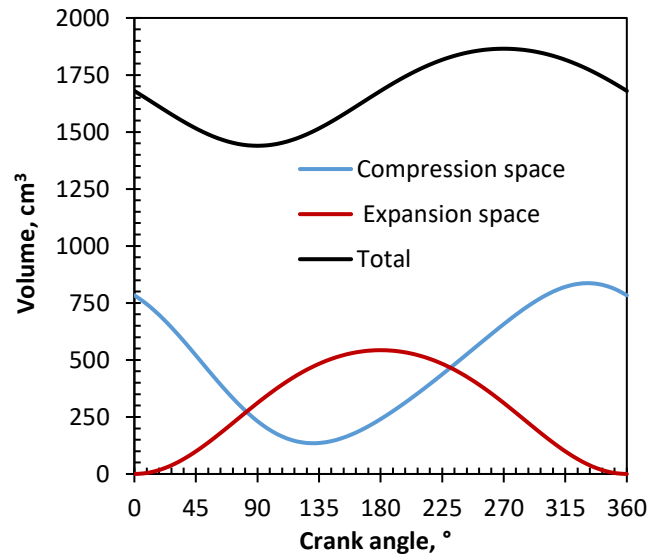


Figure 7-1 Variation of total, expansion, compression volumes versus crank angle.

The pressure variation with crank angle is shown in Figure 7-2 over one cycle. The maximum and minimum pressure amplitudes occur during the compression and expansion processes, respectively at different phase angles of 120° and 320° . The pressure variation is a result of temperature variation between hot and cold end temperatures.

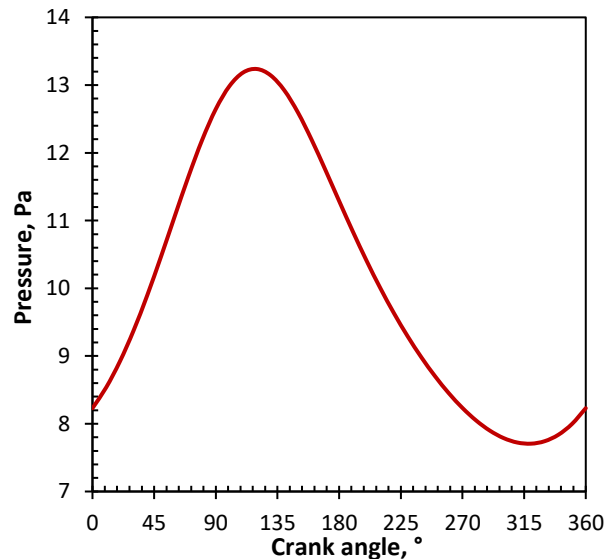


Figure 7-2 Cyclic pressure vs. crank angle over a cycle.

The temperature variation in the working spaces against crank angle is presented in Figure 7-3. As can be seen that a large cyclic temperature variation of the gas was observed in the expansion space ($> 100\text{ }^{\circ}\text{K}$). The average value is less than heater wall temperature of 923 K . Similarly, in the compression space, the average gas temperature is higher than the cooling water temperature. This is most likely a direct result of the adiabatic assumption of the working spaces by which the operated temperature extremes are remarkably reduced, thus, reducing the thermal efficiency of the cycle to a value less than that of the Carnot efficiency.

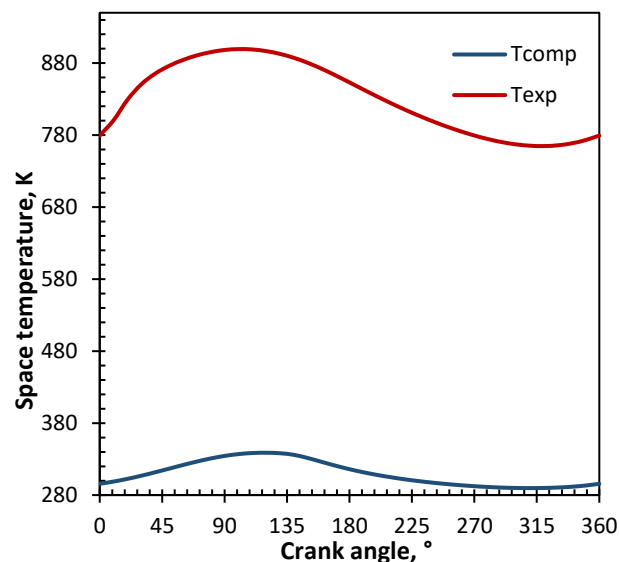


Figure 7-3 Variation of space temperatures vs. crank angle.

Predicted energy rates at different spaces of the engine vs. crank angle are depicted in Figure 7-4. This diagram shows the heat rates accumulated and transferred in, and by the heat exchangers, the compression power, the expansion power and the power output of the engine. It is observed that the power (W_{exp}) begins the cycle with positive slope up to half of the cycle- this is due to higher power generated during expansion process and then returns to a negative slope as this power is consumed by the compression process (W_{comp}). Therefore, the net power output at the end of the cycle is positive.

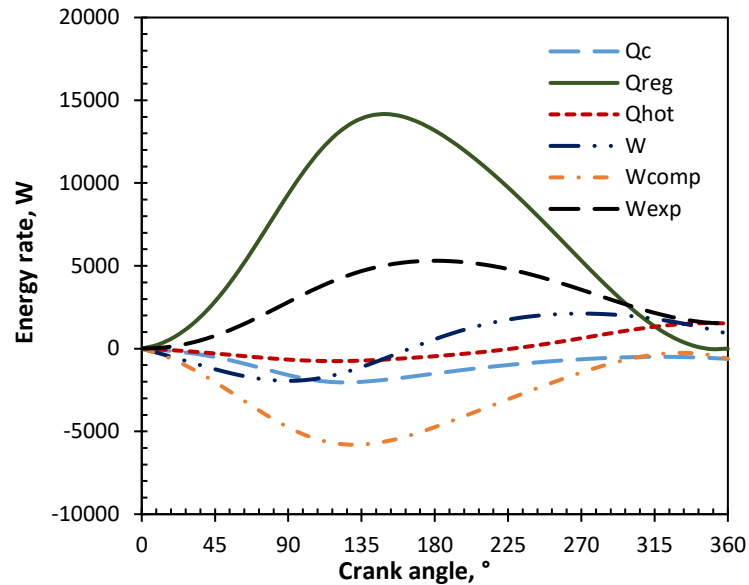
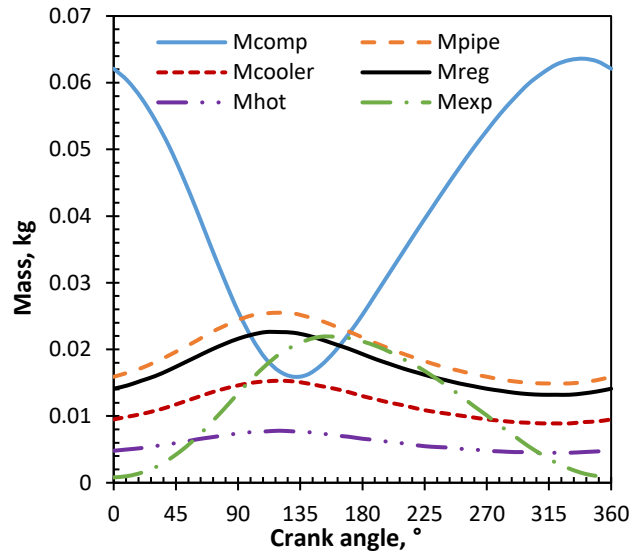


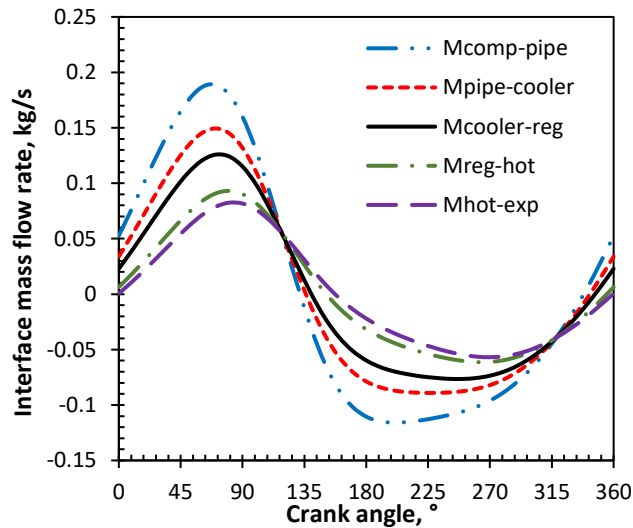
Figure 7-4 Energy rates vs. crank angle within engine spaces.

It is worth noting in this graph how significant the amount of heat rate absorbed and released by the regenerator matrix over the cycle is. The amount of heat rate in the regenerator is nine times that of the heat rate transferred to the heater per cycle. As can be seen that the amount of energy released and absorbed during the first half and second half of the cycle is equal, thus the net heat rate transferred to the regenerator over a cycle is zero. This indicates how the engine performance is strongly affected by the regenerator effectiveness and its heat transfer area to accommodate higher heat fluxes. It is conceivable that Schmidt [38] ignored the regenerator from his analysis and did not appreciate its importance and its function in the engine originally patented with a regenerator about 100 years ago.

The mass flow rates at different locations of the engine are shown in Figure 7-5. Most of the mass flow rates variations are of a sinusoidal behaviour. Closer look into Figure 7-5-(a), suggests that a larger mass of the gas exists in the connecting pipe of 0.0255 kg compared to other masses in the engine dead volumes.



(a)



(b)

Figure 7-5 Masses and mass flow rates vs. crank angle, a) masses of engine spaces b) mass flow rates of spaces interfaces.

The largest mass variation occurs in the compression space as the mass in this space is a combination of the mass in the compression space and the mass of the lower part of the expansion space. The mass flow rates through the interfaces of engine cells are depicted in Figure 7-5-(b). It is based on the arithmetic average of the mass flow rate at the inlet and the outlet of each engine cell. Again, the large variation is observed at the interface between the compression space and the connecting pipe.

7.3 Parametric study of developed thermodynamic model

7.3.1 Effect of phase angle

In most gamma-type Stirling engines, the phase angle can be adjusted for maximum shaft power based on the operating conditions. The optimum phase angle is usually assumed to be 90° for practical purposes [40]. However, the results shown in Figure 7-6, shows that maximum shaft power of 525 W occurs at phase angle of 100° compared to 503 W at angle of 90° . On the other hand, maximum thermal efficiency is still at 90° angle.

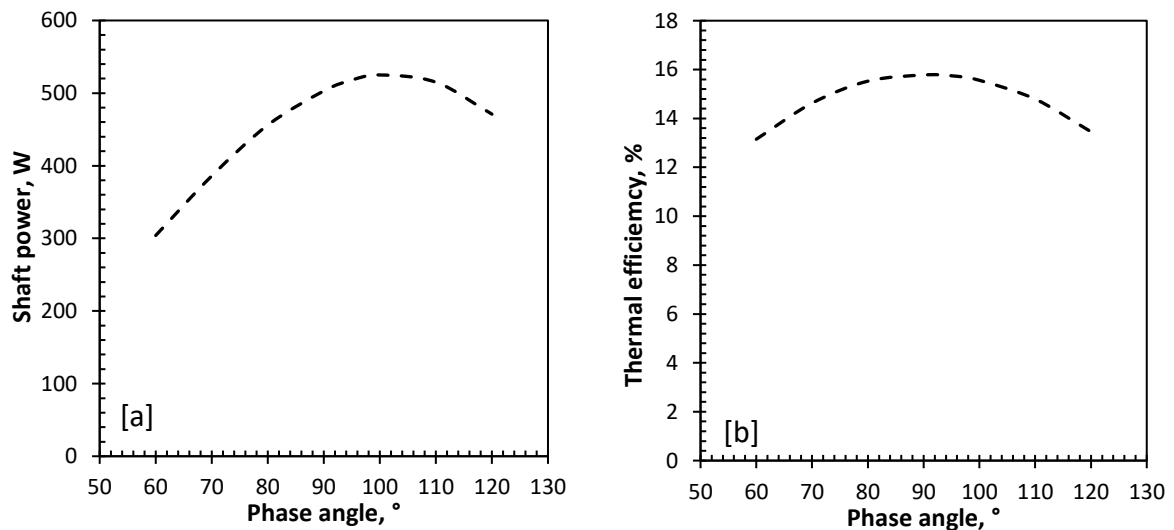


Figure 7-6 Effect of phase angle on, (a) shaft power and (b) engine efficiency.

7.3.2 Effect of regenerator matrix type

The engine was originally fitted with random fibre regenerator (type 3) in Table 7-1. Three random fibre configurations, listed in Table 7-1, were investigated.

Table 7-1 Random fibre configurations [133].

Type	Commercial name	Wire diameter, μm	Porosity, %	Material
1	1 mil Brunswick	27.4	82	stainless steel
2	12 micron Bekaert	13.4	89.7	stainless steel
3	31 micron Bekaert	31	90	stainless steel

The difference in engine performance using different regenerator fillings is demonstrated in Figure 7-7. Both shaft power and thermal efficiency increased with engine speed till the optimum speed for all configurations. It can be seen that type 3 is superior to type 1 and type 2, with shaft power produced 503 W, 316 W and 255 W, respectively. Type 3 has the largest wire diameter and porosity so that the heat transfer rate is increased due to the increased surface area leading to higher shaft power. On the other hand, type 1 combines moderate wire diameter and porosity. The optimum speed occurs when the negative effects of elevated pressure drop are balanced with the positive effects of increased heat transfer. The optimum speed for type 2, type 1 and type 3 occurs at 400 rpm, 500 rpm and 600 rpm, respectively. For the thermal efficiency, the optimum speed occurs at 300 rpm, 400 rpm and 500 rpm for type 2, type 1 and type 3, respectively.

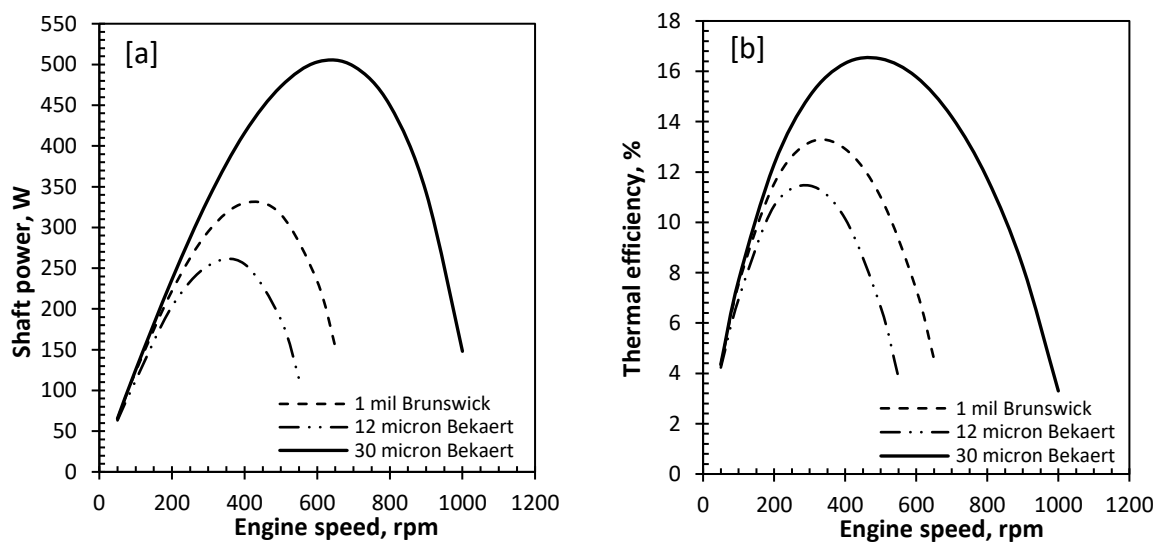


Figure 7-7 Effect of regenerator matrix on engine performance at ($T_h = 650\text{ }^\circ\text{C}$, $T_k = 15\text{ }^\circ\text{C}$ and $p_{ch} = 10\text{ bar}$), (a) shaft power and (b) engine efficiency.

7.3.3 Effect of gas type

Most developed Stirling engines can run faster when charged with helium than with air [5]. Helium possesses greater power density due to its low viscosity and higher thermal

conductivity. In this regard, the effect of gas type on engine performance at different engine speeds is presented in Figure 7-8 for charge pressure and hot end temperature maintained at their maximum values of 10 bar and 650 °C, respectively. It is observed that when helium is used, the shaft power exhibits superior values than nitrogen at higher engine speeds. Up to speed of 500 rpm, no significant difference of shaft power is observed between the two gases.

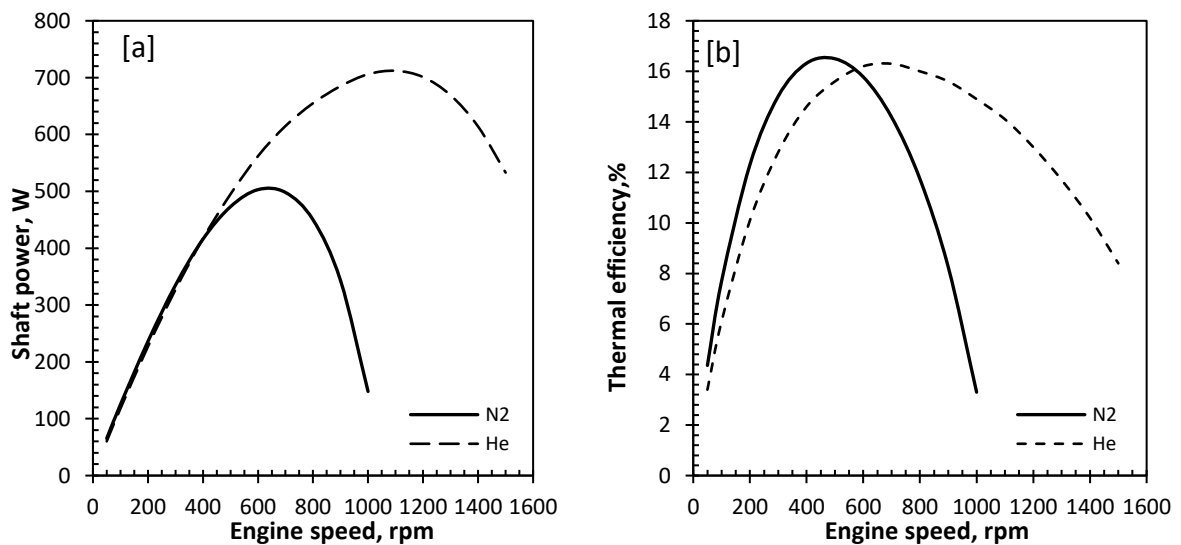


Figure 7-8 Effect of gas type on engine performance at ($T_h = 650$ °C, $T_k = 15$ °C and $p_{ch} = 10$ bar), (a) shaft power and (b) engine efficiency.

At 1100 rpm the engine produces maximum power of 712 W when using helium compared to 503 W at 600 rpm when using nitrogen. The thermal efficiency drops steeply from 16.5% to 3% when using nitrogen between 500 to 1000 rpm. Meanwhile, the thermal efficiency using helium drops steadily from 16.3% to 8.4% between 700 to 1500 rpm.

7.3.4 Effect of low temperature cooling

The use of liquid air/LN2 as media for storing thermal energy is becoming an increasingly important technology with high storage density of 0.77 [MJ/kg]. Surplus electricity (off-peak) and/or the renewable energy sources can be used to liquefy air/N2 in which energy can be stored

and transported using the well-developed cryogenic industry infrastructure. In this context, the feasibility of utilizing the stored cold energy of LN2 to maximize the shaft power of the engine was investigated. Figure 7-9 shows the effect of low cooling temperature, in the range of (15 °C to -150 °C), on the shaft power and thermal efficiency for nitrogen and helium as working gases.

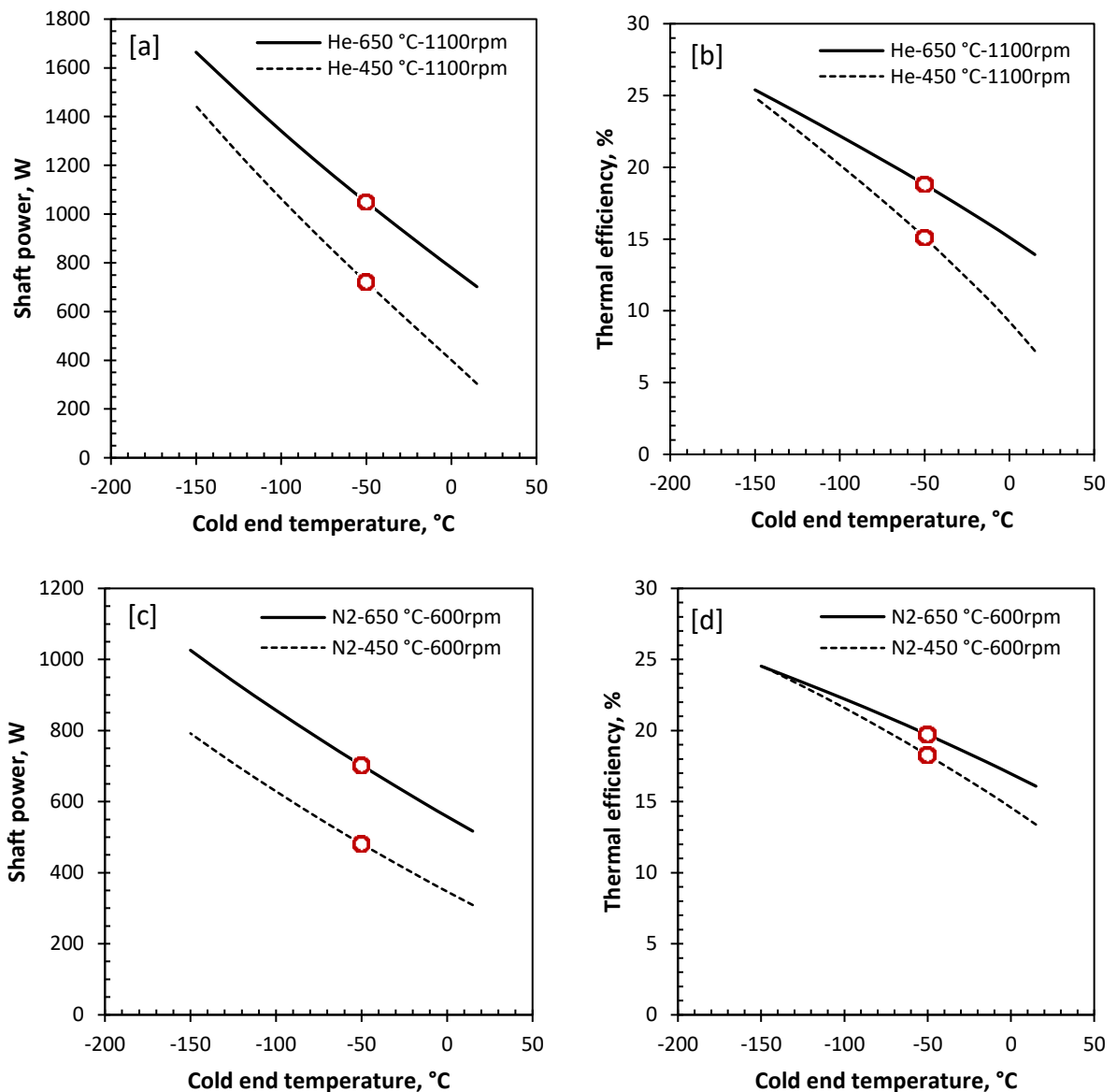


Figure 7-9 Effect of cold end temperature on engine performance at different hot end temperatures for helium (a, b) and nitrogen (c, d).

In all figures [a, b, c and d], both shaft power and thermal efficiency increase with lowering the cooling temperature for helium and nitrogen. As cooling temperature decreases, the minimum cyclic pressure is reduced giving rise to the pressure amplitude thus producing higher power density. Similarly shaft power and thermal efficiency is increased when hot end temperature is increased from 450 °C to 650 °C. As heating temperature is increased from 450 °C to 650 °C, a 49% enhancement of shaft power is achieved for helium at -50 °C reaching 1 kW and 35% for Nitrogen reaching 700 W. This compares to a 35% enhancement of thermal efficiency for helium at -50 °C reaching 18.8% and 23% enhancement for Nitrogen reaching 19.7% when compared to that at normal cooling temperature of 15 °C.

7.3.5 Effect of dead volume (connecting pipe)

The dead-volume of the connecting pipe can be reduced to enhance the engine performance [80]. The effect of pipe diameter, connecting both parts of the compression space, on N₂-charged engine performance was illustrated in Figure 7-10.

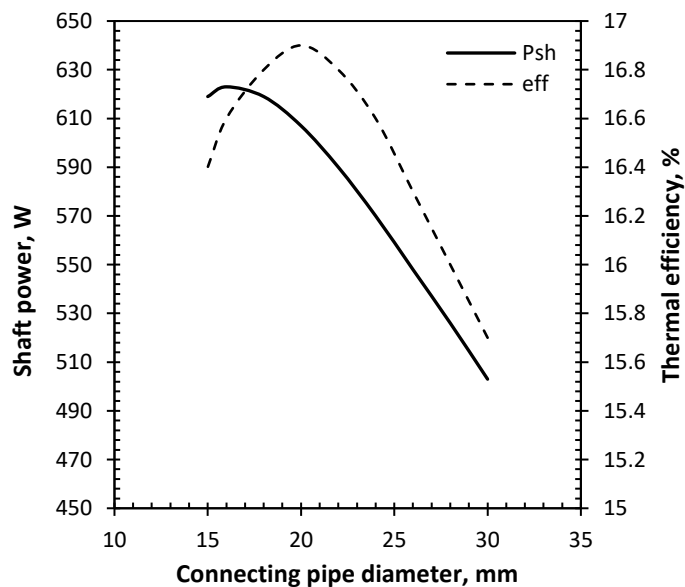


Figure 7-10 Effect of connecting pipe diameter on engine performance at ($T_h = 650\text{ }^\circ\text{C}$, $T_k = 15\text{ }^\circ\text{C}$ and $p_{ch} = 10\text{ bar}$), shaft power and engine efficiency.

It can be seen that as pipe diameter is reduced, from 30 mm to 15 mm, the dead volume is reduced by 50%, the shaft power is enhanced by 20% reaching a maximum of 623 W at pipe diameter of 16 mm. The thermal efficiency is similarly enhanced by 5% reaching 16.9% but at different optimum diameter of 20 mm.

7.3.6 Effect of heater tube diameter

The effect of heater tube diameter on engine performance is shown in Figure 7-11. As it is represented, within the investigated range of tube diameter, an optimum value exists for maximum shaft power and thermal efficiency. The optimum value was found to be 5.5 mm diameter which is close to the original (6mm) heater of the engine. Below this value, the heater cannot exchange the heat required for engine operation due to the reduced surface area of the heater and the increased pressure drop. On the other hand, above this value a degradation in engine performance occurs due to the increased dead volume which lowers the compression ratio of the engine.

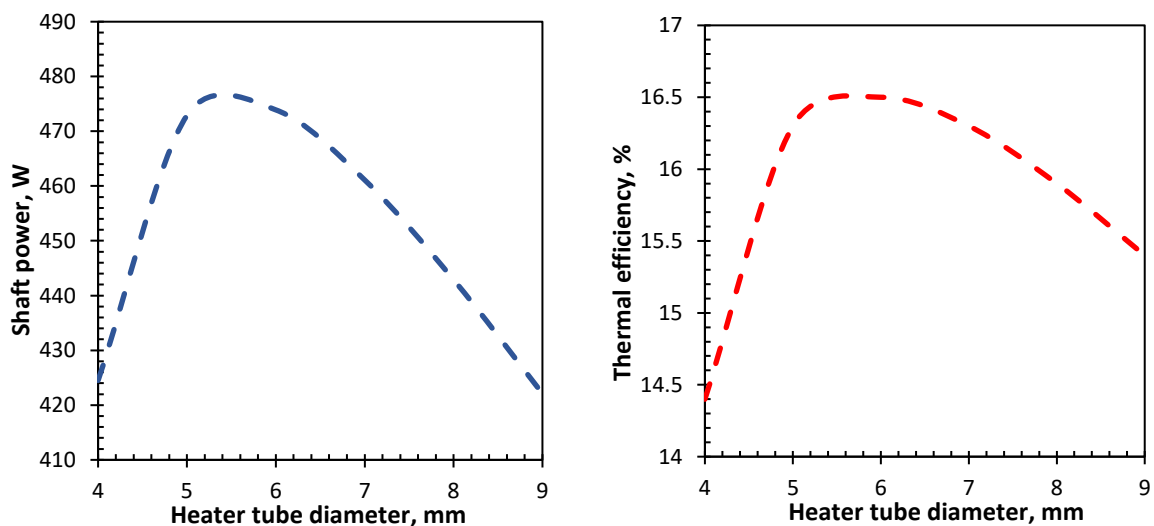


Figure 7-11 Effect of heater tube diameter on engine at ($T_h = 650\text{ }^\circ\text{C}$, $T_k = 15\text{ }^\circ\text{C}$ and $p_{ch} = 10\text{ bar}$), a) shaft power and b) thermal efficiency.

7.4 Results of engine 2D CFD model

The PV diagrams for compression and expansion spaces are illustrated in Figure 7-12. It is noticeable that the positive expansion work is larger in magnitude than the negative compression work giving rise to the net output work from the engine.

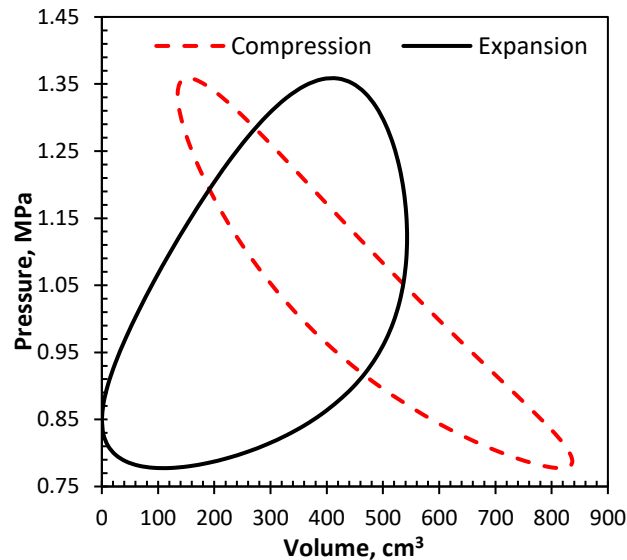


Figure 7-12: PV diagrams for expansion and compression volumes within an engine cycle at 500 rpm, based on 2D CFD model.

The velocity, pressure and temperature contours are plotted in Figure 7-13 to Figure 7-15 at the end of the 5th cycle ($t = 0.6$ s) at engine nominal speed. It can be seen that the engine has asymmetric geometry near the connecting pipe which affects the uniformity of fluid flow in the engine. Due to the combined motion of the power piston and displacer, gas moves forward and backward through the engine domains.

In Figure 7-13, the gas flows from compression space through the connecting pipe with an average velocity of (5 m/s), where it splits into two streams due to asymmetric geometry. Part of the gas mass enters the cooler, meanwhile, the bulk flow is strongly jetting into the lower part of the expansion space causing flow vortexes as a result of jet impingement on the lower

surface of the displacer. While, most of the gas is confined at the lower part of the engine, engine is cooled by a cooling water jacket. At this instant ($t = 0.6$ s), as the power piston moves to the right and the displacer moves down, compression process takes place at the beginning of the new cycle and is completed when power piston reaches top dead centre (TDC), while displacer piston reaches bottom dead centre (BDC).

Pressure gradient is established across the engine spaces giving rise to cyclic pressure during compression process as seen from Figure 7-14. The maximum pressure drop during the cycle normally occurs in the regenerator due to the elevated inertia losses in the pore volumes of the matrix. The gas continues the thermodynamic cycle; heat is being supplied by the electric heater causing the gas to expand and more positive power is generated from the engine.

The temperature contours of the gas phase across the engine spaces are shown in Figure 7-15 with almost linear gradient across the engine spaces between hot and cold end temperatures. The gas coming from the heater enters the regenerator, releases energy to the matrix and exits with a temperature normally higher than the cold end temperature. This depends on the regenerator effectiveness and thermal losses that occur in the regenerator. The higher thermal losses in the regenerator the higher cooling power rejected from the engine. When the cooled gas is reversed during cold blow, the gas absorbs an amount of heat stored in regenerator matrix reducing the total amount of heat flow to the heater, hence boosting engine efficiency.

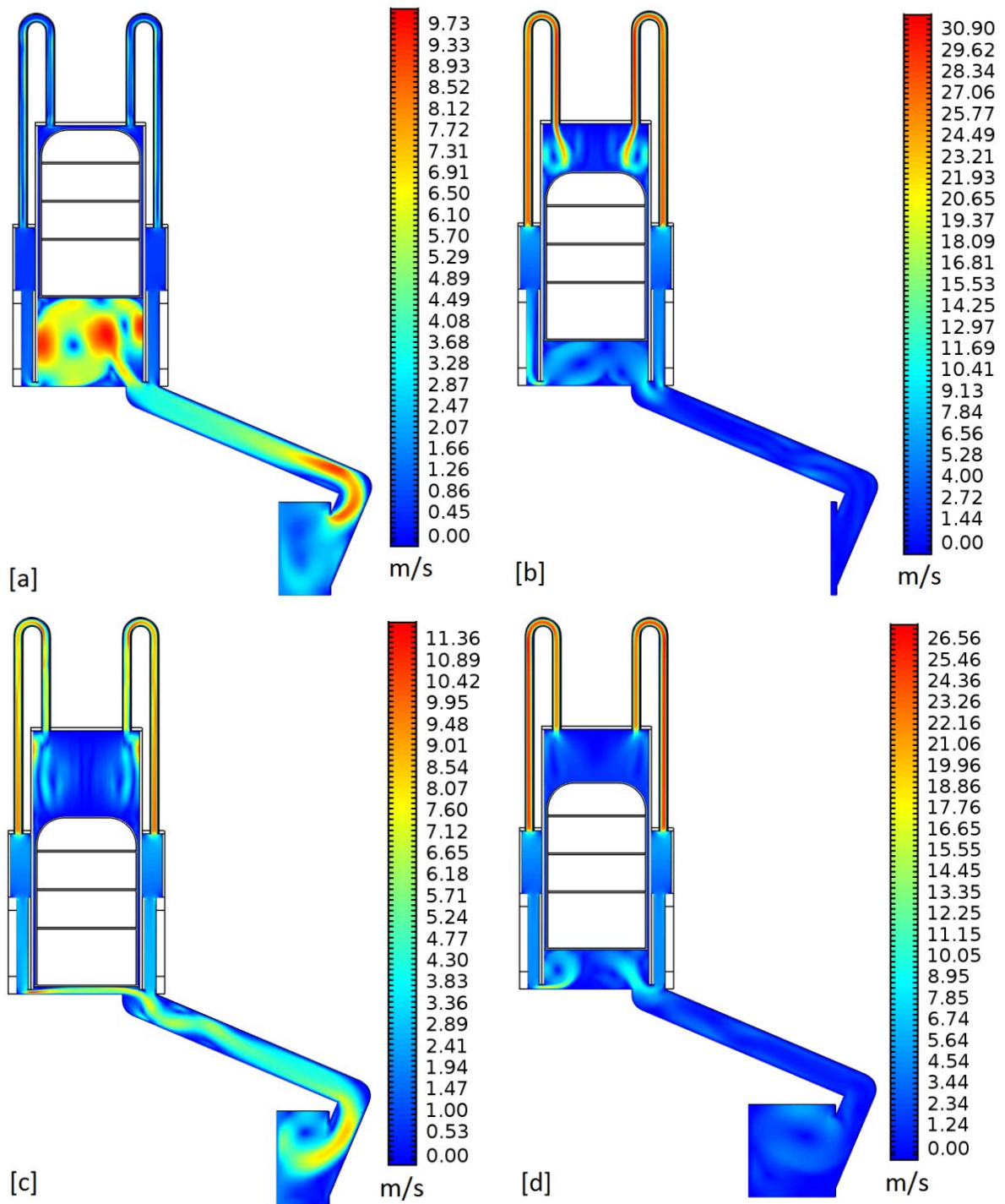


Figure 7-13 Velocity contours during the 5th cycle ($t = 0.6$ s) at different crank angles, a) $\Theta = 0^\circ, 360^\circ$, b) $\Theta = 90^\circ$, c) $\Theta = 180^\circ$, d) $\Theta = 270^\circ$.

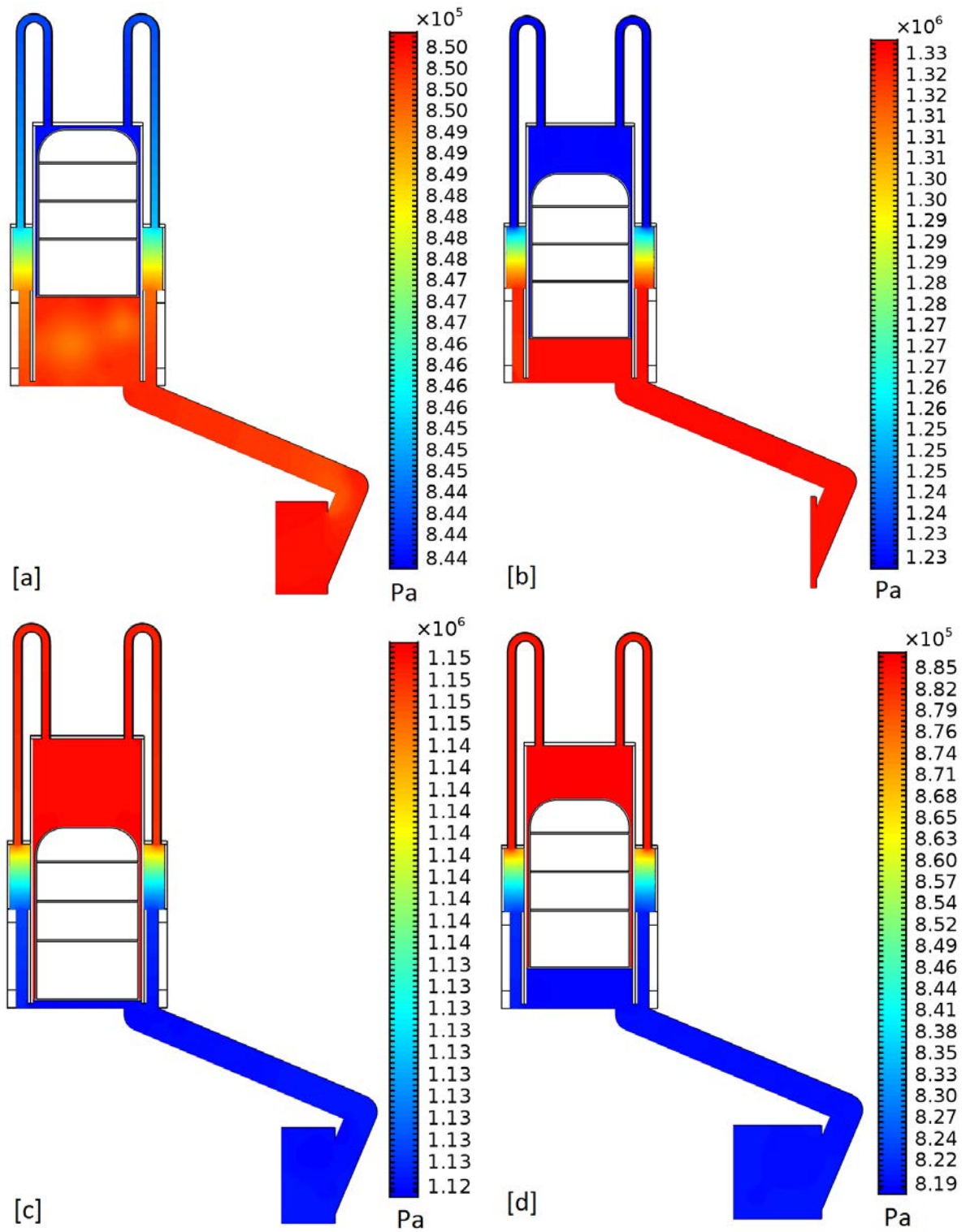


Figure 7-14 Pressure contours during the 5th cycle ($t = 0.6$ s) at different crank angles, a) $\Theta = 0^\circ, 360^\circ$, b) $\Theta = 90^\circ$, c) $\Theta = 180^\circ$, d) $\Theta = 270^\circ$.

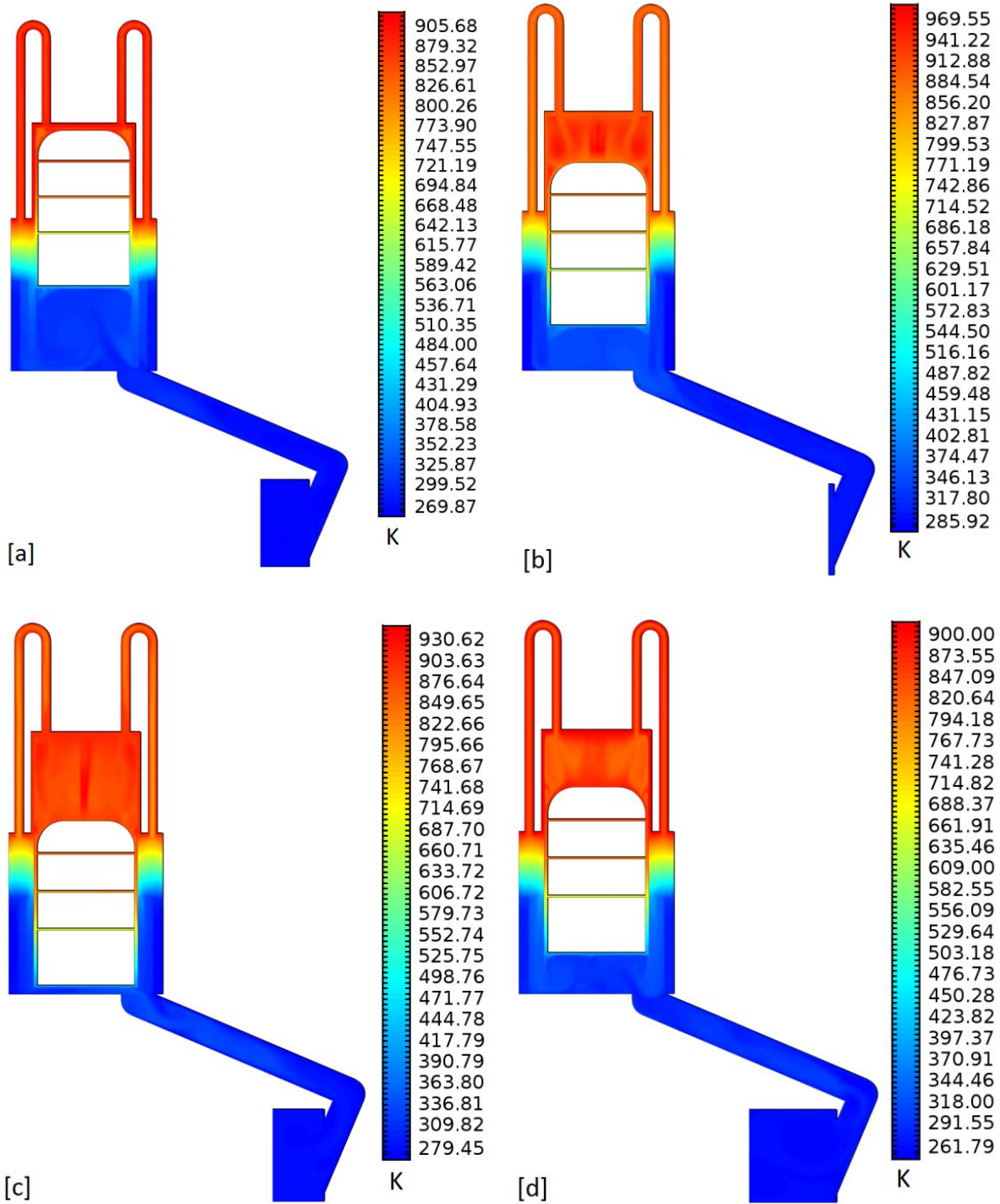


Figure 7-15 Temperature contours during the 5th cycle ($t = 0.6$ s) at different crank angles, a) $\Theta = 0^\circ, 360^\circ$, b) $\Theta = 90^\circ$, c) $\Theta = 180^\circ$, d) $\Theta = 270^\circ$.

Figure 7-16 shows the temperature contours in the two porous media (regenerator and cooler), respectively. The average regenerator matrix temperature was found to be 580 K after a few cycles, which is slightly higher than the logarithmic mean temperature difference that is widely evaluated in second-order analysis as, $T_r = (T_h - T_k)/\ln(T_h/T_k) = 549$ K. It is worth noting that the connecting pipe is two concentric pipes cooled by the cooling water circuit but most of the heat is rejected from the main cooler.

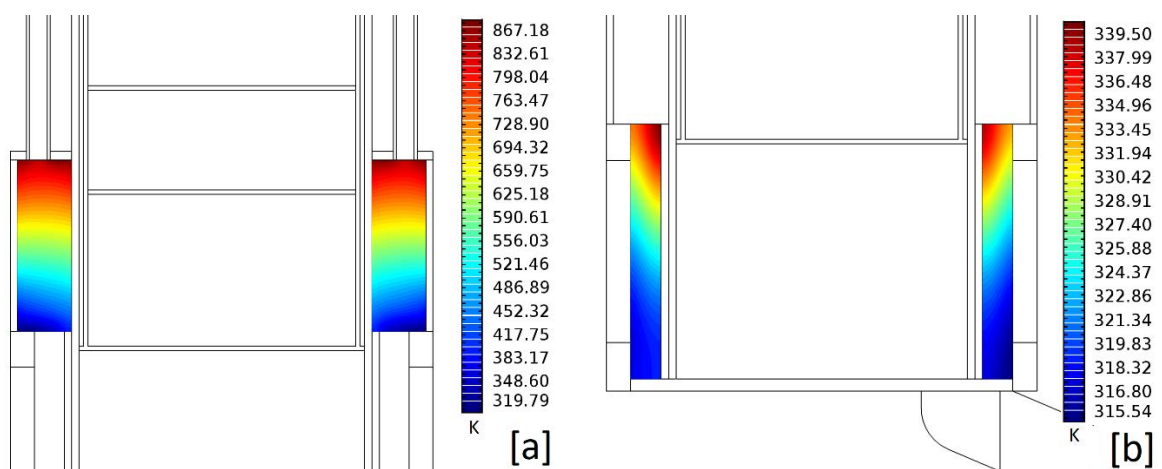


Figure 7-16 Temperature contours of porous domains during the 5th cycle ($t = 0.6$ s) at engine normal operating conditions, (a) Regenerator, (b) Cooler.

The variation of Average-Weighted temperatures in different spaces of the engine, are shown in Figure 7-17. The cyclic temperature variation is nearly sinusoidal except for heater tubes and cooler. For the expansion space temperature, the peak-to-peak magnitudes are nearly 923 K and 825 K, respectively, with the maximum peak value occurring at crank angle of 90°.

The compression space temperature fluctuates between 308 K and 270 K, respectively. Meanwhile, the regenerator cyclic temperature is nearly constant with an amplitude of 5 K. It is worth noting that the heat is supplied to the heater tube walls as well as the outer walls of the cylinder containing the displacer. This justifies that the temperature variation of the gas in the

expansion space, between phase angles [50° to 200°], is showing higher values than that of heater tubes.

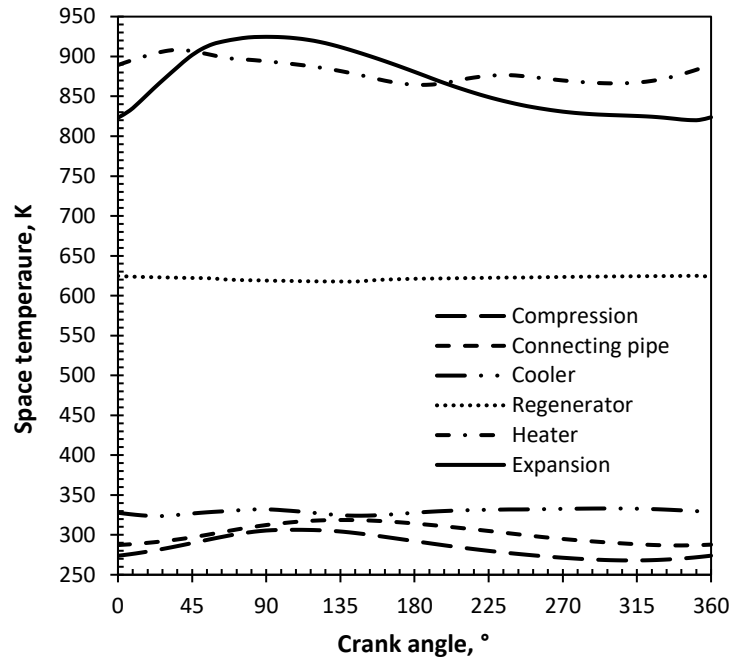


Figure 7-17 Spaces cyclic temperatures vs. crank angle during the 5th cycle at engine normal operating conditions.

As mentioned previously in chapter 2 (section 2.2.5), the thermal equilibrium in the regenerator is a poor assumption, where due to the limited heat capacity and heat transfer in the regenerator, solid matrix temperatures differ a few degrees from the gas temperature in actual Stirling engines.

In the present CFD model, the thermal non-equilibrium model for porous media was considered. Figure 7-18 presents the temperature oscillations with crank angle over one cycle, where an amplitude of two degrees was observed between the gas and matrix temperatures during the cycle. The process of heat regeneration occurs due to heat release and storage in the matrix. During cold blow period, the gas enters the regenerator with a temperature greater than

the matrix temperature. However, in the hot blow period, the gas temperature becomes greater than that of the matrix.

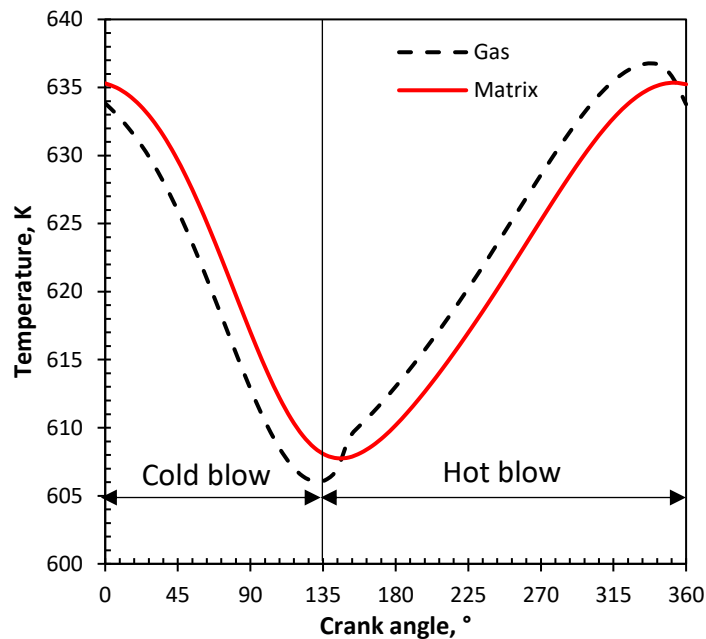


Figure 7-18 Gas and matrix variation in the regenerator over one cycle based on 2D CFD model.

7.5 Parametric study using the developed CFD model

7.5.1 Effect of phase angle

It is a common understanding that maximum power output is obtained at a phase angle of 90° . In fact, most gamma-type Stirling engines with standard crank mechanism are phased out with 90° for practical reasons and not because of its optimal thermodynamic behaviour.

On the other hand, variation of phase angle was acknowledged as one of the effective ways for controlling Stirling engine power. As a result of phase angle choice, three major effects on engine parameters are expected; it influences the pressure amplitude, the total volumetric change of the gas, and heat transfer and hence affecting engine indicated power. The total

volume variation with phase angle shown in Figure 7-19, indicates that the maximum and the minimum volumes are unchanged. However, there is a shift of angles at which minimum and maximum volumes occur. At phase angle of 120° , large volume variation is observed during compression process starting from 1769 cm^3 to 1429 cm^3 . On the other hand, at lower phase angle of 60° , compression volume varies from 1556 cm^3 to 1429 cm^3 .

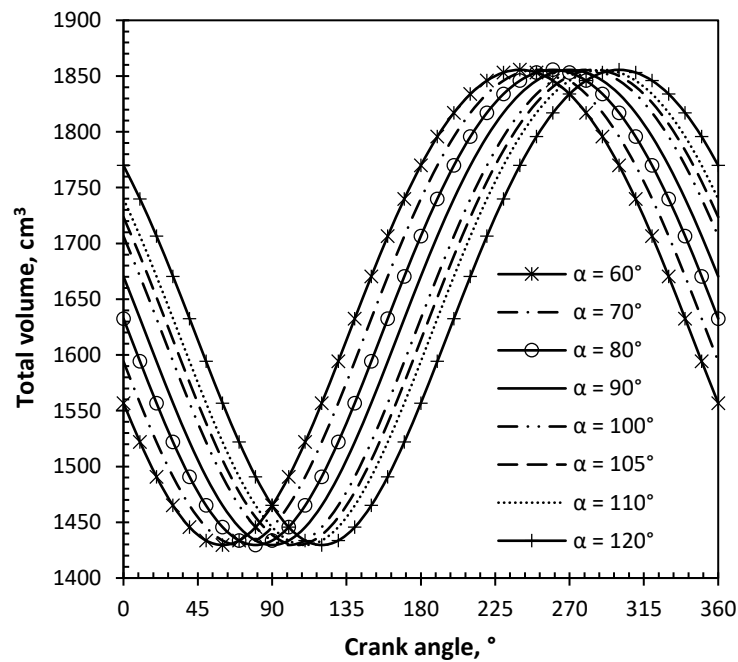


Figure 7-19 Total volume vs. crank angle at different phase angles.

The effect of phase angle variation on cyclic pressure drop across the regenerator is shown in Figure 7-20. For all phase angles shown, it can be seen that the pressure loss variation is sinusoidal. Though, peak-to-peak values of pressure loss exhibit different values during the hot and cold blow times of the cycle. This may be attributed to differences of gas properties and gas velocities as such higher gas volumes are exchanged during the hot blow by the movement of the relatively larger displacer.

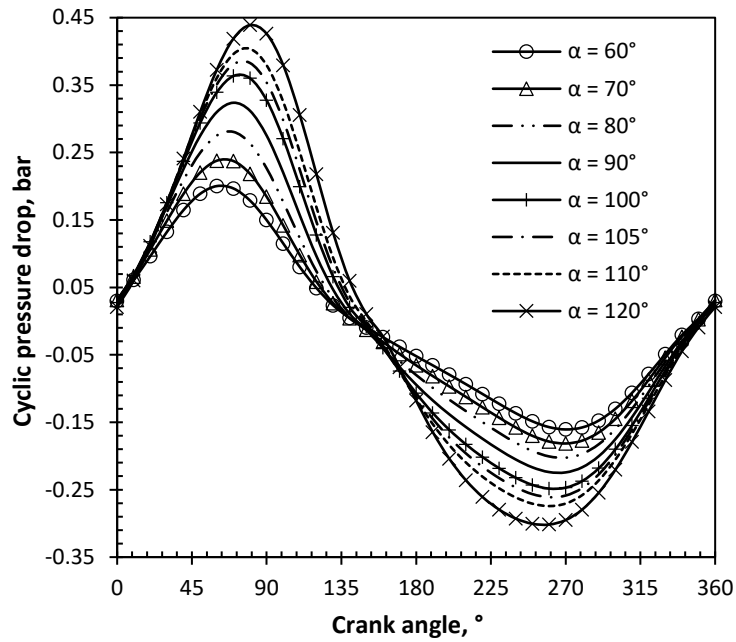


Figure 7-20 Pressure drop across the regenerator vs. crank angle at different phase angles.

For the standard case of 90° phase angle, the maximum pressure drop in the regenerator reaches 0.31 bar, with maximum charge pressure of 10 bar. As the phase angle increases from 60° to 120° , the maximum pressure drop increases from 0.19 bar to 0.42 bar. There is almost a shift of 10° at which minimum and maximum pressure drop normally occurs. At any given combination of operating condition, there would be a balance between the favourable increased heat transfer rate and the elevated pressure drop and hence the optimum phase angle value for engine performance is achieved.

The effect of phase angle on indicated PV diagrams is demonstrated in Figure 7-21. It can be seen that the larger phase angles the higher the pressure amplitude. The pressure amplitude is most likely a result of temperature variation rather than the gas compression. It is worth noting that a maximum indicated power was found to be 750 W at a phase angle of 105° . This optimum phase angle agrees closely with the results found in [48]. While a minimum value was found to be 440 W at a phase angle of 60° . The indicated power generated at a phase angle of

90° is 714 W, which is 5% lower than that at 105°. This difference could be more pronounced at higher engine frequencies [77]. The optimum value of indicated power is most likely a result of balance between the negative effect of pressure drop (specifically, across the regenerator) and the positive effects caused by the increase in heat transfer rate due to the increased volumetric gas exchange, compression and pressure ratios.

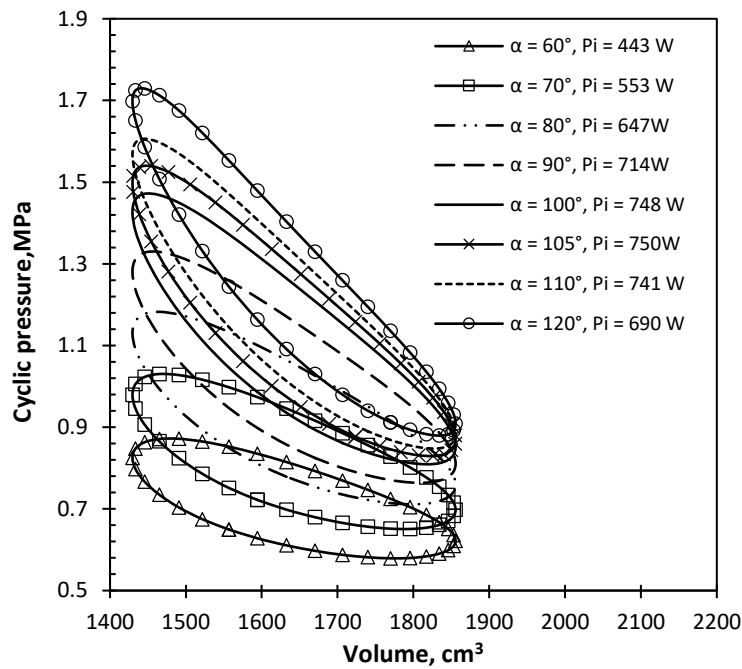


Figure 7-21 Indicated PV diagrams at different phase angles.

The indicated power and power loss due to pressure drop in the regenerator are presented in Figure 7-22 at different phase angles. The indicated power loss is calculated based on the difference between indicated power at each phase angle to the indicated power at optimum phase angle of 105°. It can be seen that the maximum power loss occurs at the smaller phase angle (60°) of the investigated range.

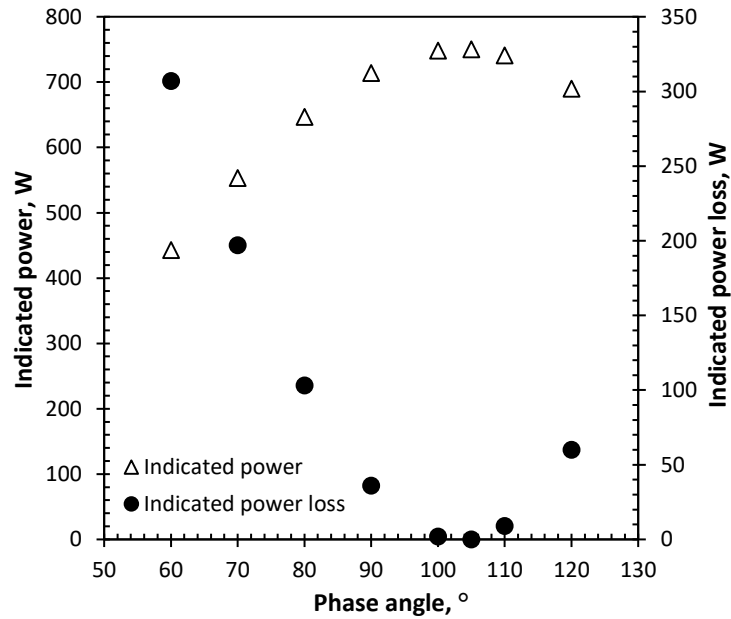
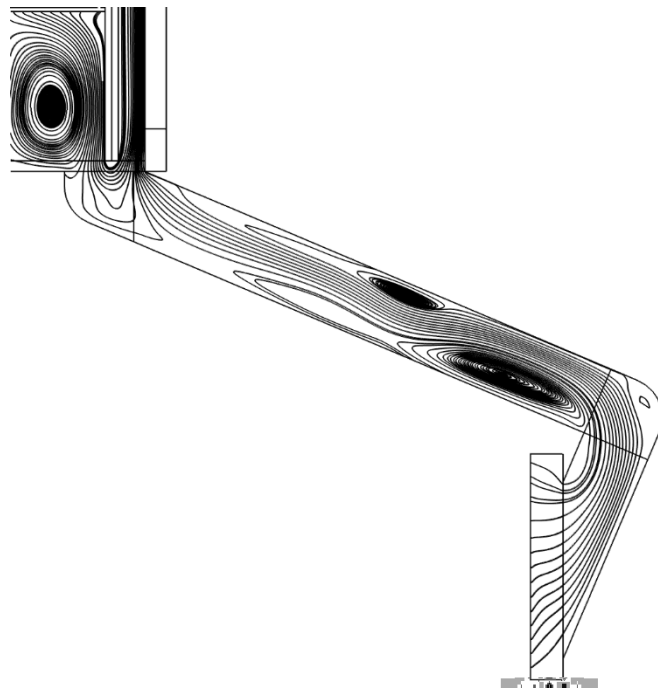


Figure 7-22 Indicated power and indicated power loss at different phase angles.

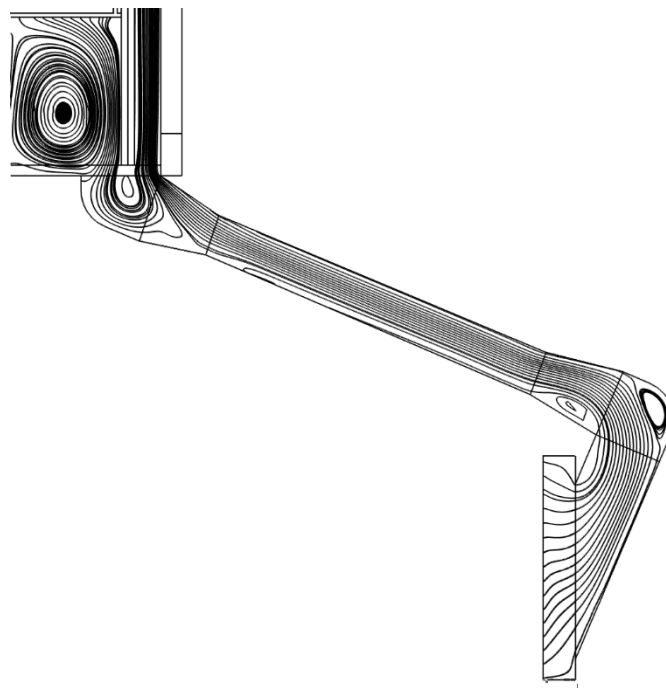
7.5.2 Effect of dead volume (connecting pipe)

Realizing that dead space is harmful to Stirling engine leads to Finkelstein' generalization [73]; 'harmful dead space to be minimized'. In theory, this unswept volume should be kept minimum which contradicts with real engines that can have up to 50% dead volume of its total gas volume. A closer inspection of the current engine indicates that the connecting pipe which connects the compression space and the lower part of the expansion space, is relatively large compared to other dead spaces of the engine (heat exchangers).

The reduction of connecting pipe diameter, and hence the dead volume, can be achieved without alteration of the general layout of the engine, using reduced pipe diameters and two adaptors as geometrically depicted in Figure 7-23. The recirculation and vortex separation of velocity streamlines is strongly pronounced in the original pipe compared to the suggested reduced pipe.



(a)



(b)

Figure 7-23 Effect of connecting pipe diameter on velocity streamlines during the 5th cycle, (a) original pipe and (b) reduced pipe.

With reducing the pipe diameter from 30 mm to 15 mm, its effect on engine performance can be seen in Figure 7-24. The indicated power (Figure 7-24-(a)) increases until reaching a maximum value of 887 W at pipe diameter of 15 mm and then falls down. This may be attributed to the increased pressure ratio as the dead volume decreases.

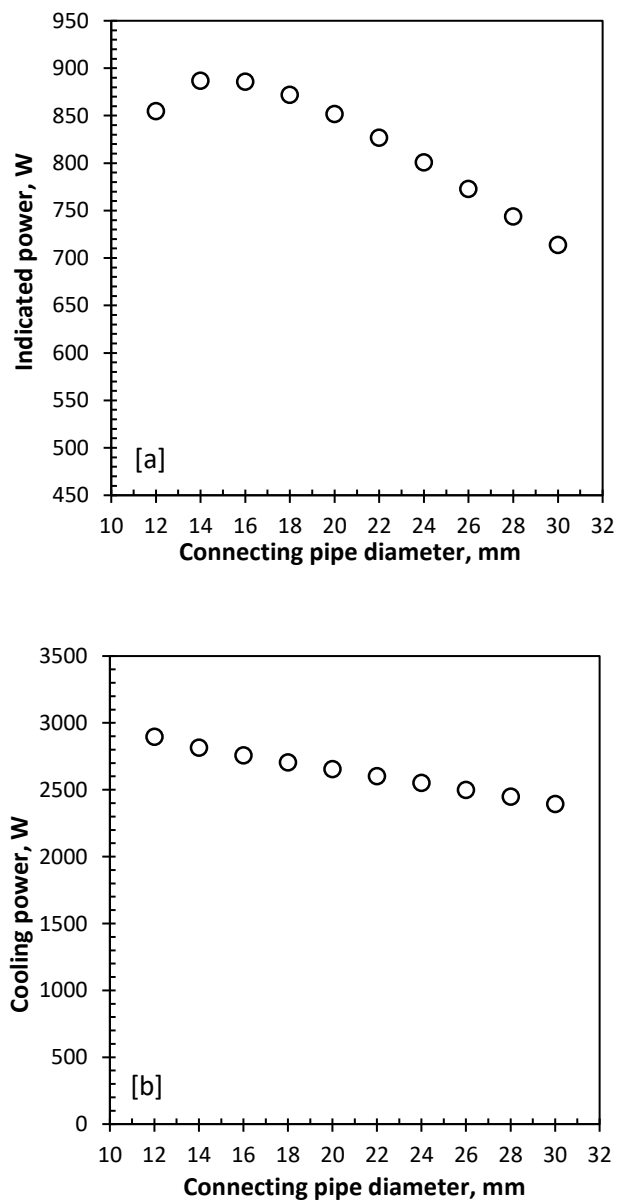


Figure 7-24 Effect of connecting pipe diameter on engine performance, (a) indicated power and (b) cooling power.

At lower values of pipe diameter, the pressure in the pipe increases which means that the displacer experiences more resistance when it moves down during compression process. Therefore, more useful power is consumed to overcome this resistance and the net indicated power drops down. On the other hand, the cooling power (Figure 7-24-(b)) is showing an increasing trend with reducing the connecting pipe diameter.

7.5.3 Effect of regenerator porosity

For gamma-type Stirling engine, the optimum matrix porosity of the conventional regenerator type is around 0.9. Increasing the regenerator porosity causes a decrease in the contact surface area between the gas and the matrix due to the increase in the pore volume. This effect reduces the residence time of the gas in the regenerator and hence degrade the regenerator performance. Figure 7-25 shows that the optimum indicated power of the engine is somewhere between 0.85 and 0.9. As the porosity increases above 0.9 to 0.95, both indicated and cooling power decrease.

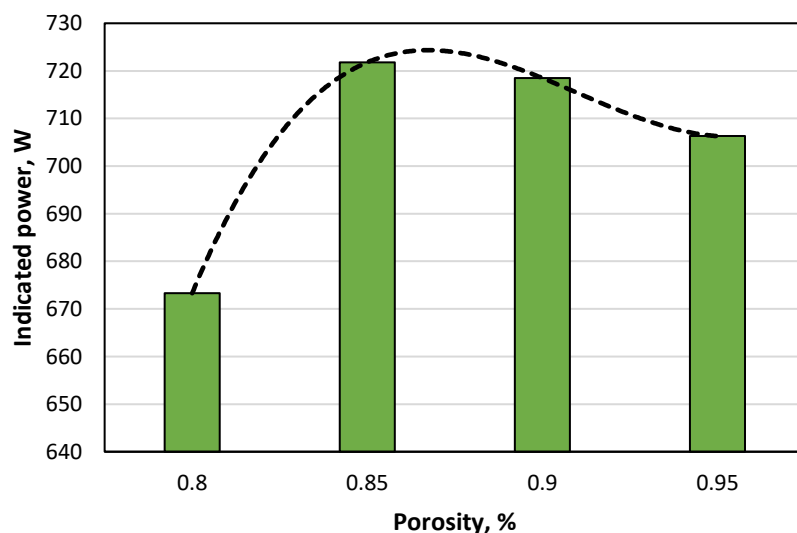


Figure 7-25: Indicated power vs. different regenerator porosities.

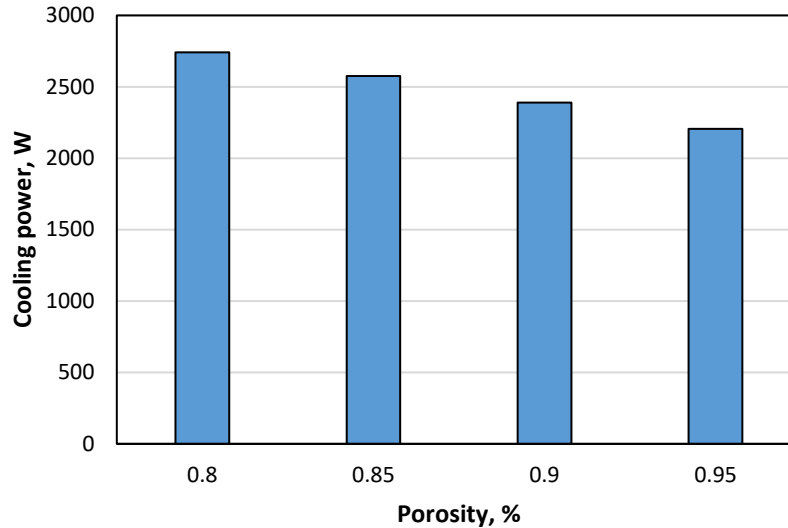


Figure 7-26: Cooling power vs. different regenerator porosities.

7.6 3D half engine CFD modelling

CFD Modelling of the current engine in 3D is computationally expensive due to the complex geometry which consists of a twenty heater pipes, the finned shaped cooler, displacer material and solid walls. In this section, half of the engine as a symmetric object about z-axis, was modelled.

The same approach discussed in chapter 5 was adopted here in terms of boundary conditions, meshing and solution technique. Free tetrahedral meshing sequence is adopted for all engine domains. The tetrahedral mesh generator (algorithm) creates an *unstructured mesh* — that is, a mesh with irregular connectivity — it is well suited for complex-shaped geometries requiring a varying element size. The algorithm further improves the quality of the meshes and also features an option for reducing the risk of obtaining inverted curved elements as well as an option for avoiding the creation of elements that are too large. The critical domain in the engine is the appendix gap within the expansion space as shown in Figure 7-27. Due to the displacer motion, the appendix gap and the expansion space elements can deform largely.

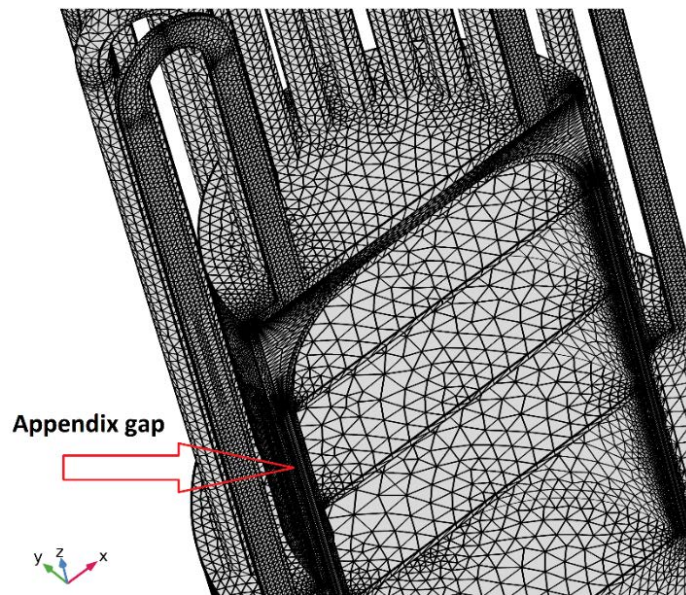


Figure 7-27: 3D meshing of appendix gap.

The tetrahedral elements which conform to the topology of these domains are set to be compressed in z direction at initial position at time ($t=0$) with a reasonable scaling factor of 5 so that the elements quality is maintained at the same level during expansion or stretching. The total number of tetrahedral elements was 878,239. Further refinement of the computational grid resulted in the increase of the computational time to such extent that it became unfeasible to carry out numerical modelling with the PC allocated to the project with the configuration of Intel(R) core(TM) CPU i7-4820K, runs at speed of 3.7 GHz with 48 GB RAM memory.

The simulation results are presented in Figure 7-28, for the temperature contours at different crank angles of the fifth cycle. The contours are similar to those obtained using 2D CFD simulations discussed in chapter 5. The linear temperature gradient across the whole engine is predominant. All simulation runs carried out taking up to three days to reach periodic steady state. It is worth mentioning that initializing the solution with steady state study (no motion) had significantly reduced the simulation time to half.

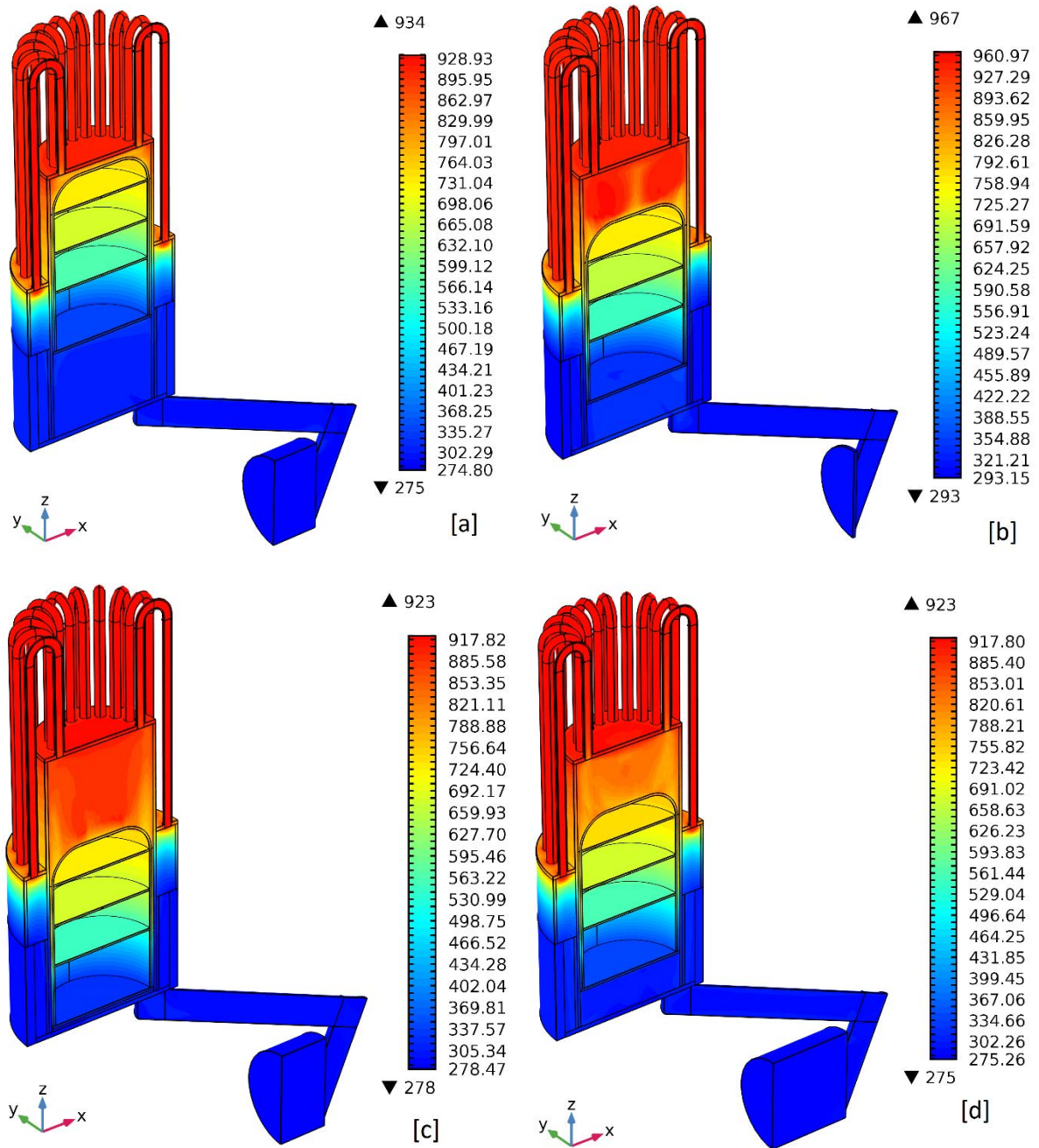


Figure 7-28 3D half engine temperature contours during fifth cycle at different crank angles, a) $\Theta = 0^\circ, 360^\circ$, b) $\Theta = 90^\circ$, c) $\Theta = 180^\circ$, d) $\Theta = 270^\circ$.

3D engine sector CFD modelling of the engine is regarded to be less computationally expensive compared to 3D half engine modelling thus 18-degree sector of the engine is considered and presented below.

7.7 3D engine sector CFD modelling

One way to reduce the computational domain of the engine is to find a proper symmetry on geometrical planes. As previously presented that the engine has a symmetrical plane on z-x plane which allows to model the engine as half domain to reduce the computational time. The asymmetric nature of the current engine is caused by the connecting pipe which connects both compression space and the lower part of the expansion space. In the current approach, the original connecting pipe was replaced by a straight pipe parallel to z-axis and the power piston was reverted to move along z-axis as shown in Figure 7-29.

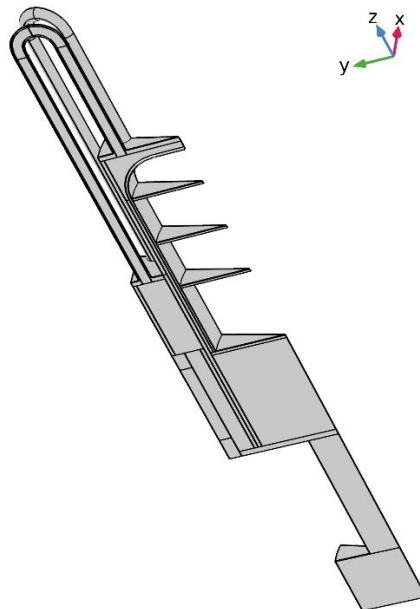


Figure 7-29: Computational domain of 18-degree 3D sector of the engine.

The dead volume of the new connecting pipe was kept the same as the old one. Knowing the pipe length (fixed to 100 mm), the pipe diameter can be obtained from the dead volume which is found to be 38mm. The 3D sector of the engine is 18° based on the heater tubes positions which are 18° separated each about the symmetry axis (z-axis). The same sequence of meshing is applied using tetrahedral elements with a total number of 294,643 and each simulation run

takes up to one day to reach periodic steady state. The temperature contours are presented in Figure 7-30 at different crank angles with a linear gradient. The maximum temperature of the gas (957.7 K) is reached at the end of the compression stroke, then expansion process starts causing a reduction in the gas temperature.

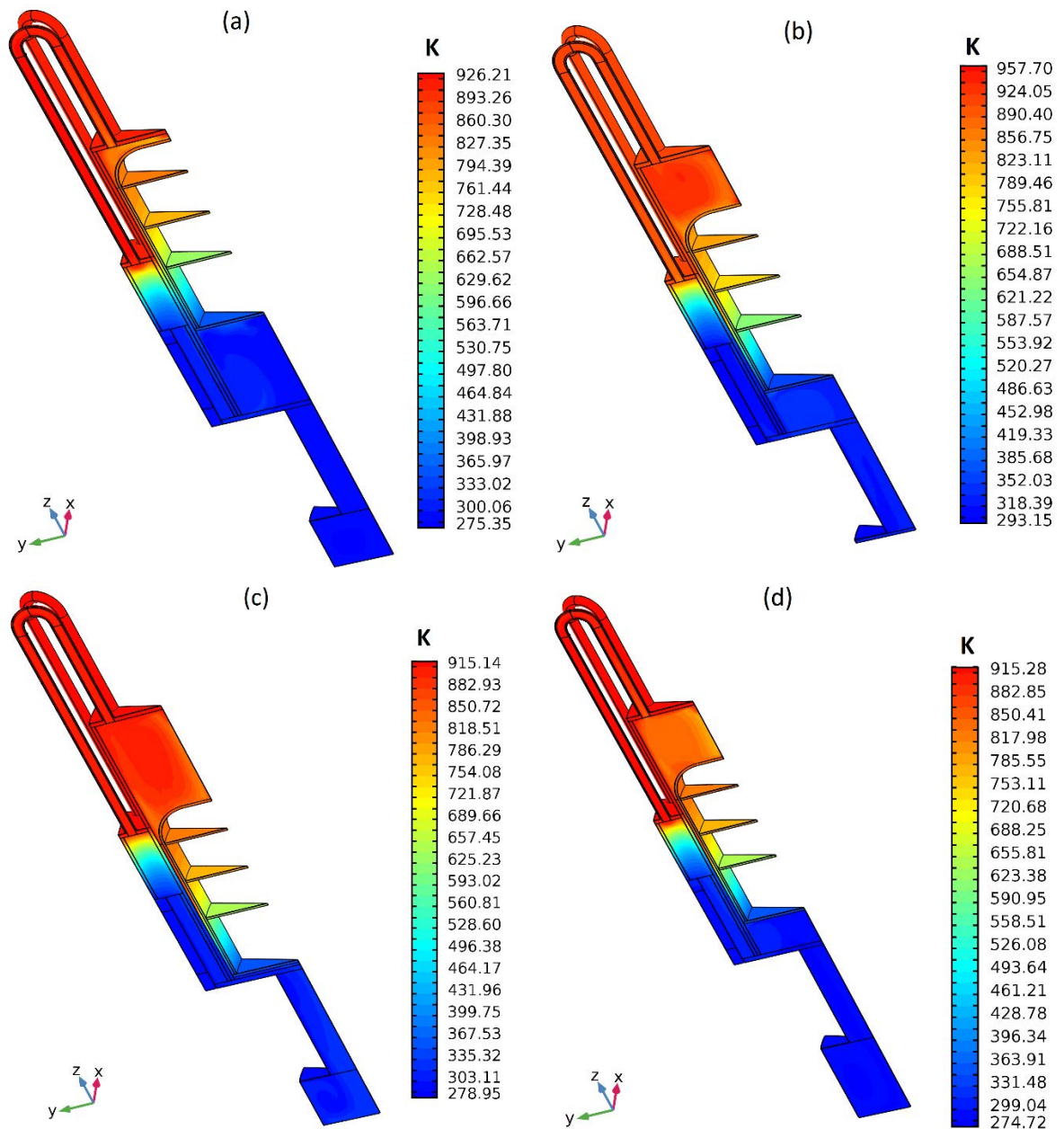


Figure 7-30 (3D) sector temperature contours during fifth cycle at different crank angles, a) $\Theta = 0^\circ, 360^\circ$, b) $\Theta = 90^\circ$, c) $\Theta = 180^\circ$, d) $\Theta = 270^\circ$.

The indicated PV diagrams of the different CFD approaches are compared in Figure 7-31 with the experimental PV diagram at engine normal operating conditions. In general, slight deviation was observed in the expansion processes of the 3D approaches compared to experiment. However, the calculated indicated powers (Table 7-2) showed that the power generated from 3D half engine is close to experiment, while 3D sector generates 10% higher power than that of the experiment. It is believed that the 3D sector is totally different from the original layout of the engine but this approach was meant to reduce the computational time with maintaining the 3D capability of simulation. Also, the 2D approach adopted in this work compares very well with experiment. It is worth mentioning that 2D meshing of the engine domain is controllable and feasible with free triangular elements with even a very fine mesh size which makes the 2D CFD a better approach for parametric study.

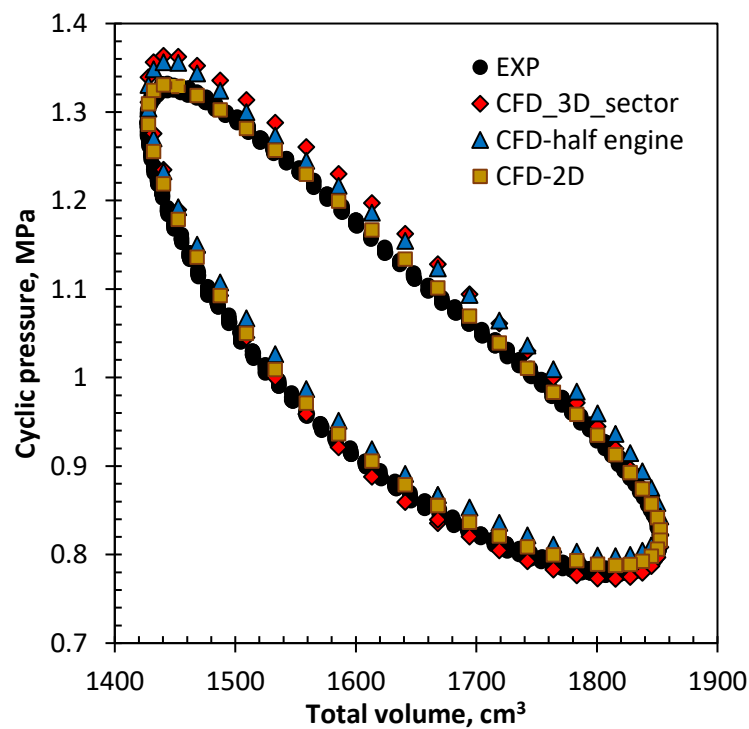


Figure 7-31 Indicated PV diagrams of different CFD modelling.

Table 7-2: CFD comparison of indicated PV powers.

2D	3D sector	3D half engine	Exp.
718 W	824 W	744 W	750 W

7.8 Results of channel regenerators

7.8.1 Transient testing method results

A sample of the temperature contours of the three MCRHXs at 10 SCFM and test run time of (3600 s) were presented in Figure 7-32. As can be seen, the isothermal contours of the solid temperature are not uniform along the whole length of MCRHX in the flow direction (x-axis). The profile gradually becomes a curved-shape near the outlet due to heat loss to the attached walls and axial conduction.

The typical plots of air inlet and outlet temperatures histories for the three MCRHXs are presented in Figure 7-33 to Figure 7-35. The inlet measured temperature history was entered to the CFD model and hence the predicted and measured outlet temperature histories were compared (square solid points represent measured values and the dashed line represents predicted values). In general, the predicted values are in good agreement with the measured ones.

This has given confidence in the developed test facility and the developed computational approach. The heating period was maintained for 1 hour for all tests. It should be noted that due to the restriction that the heater has a fixed heating power and the outlet temperature of the heater is merely dependent on the flow rate, the maximum temperature of the air was set to roughly 100 °C with ± 5 °C for all test runs.

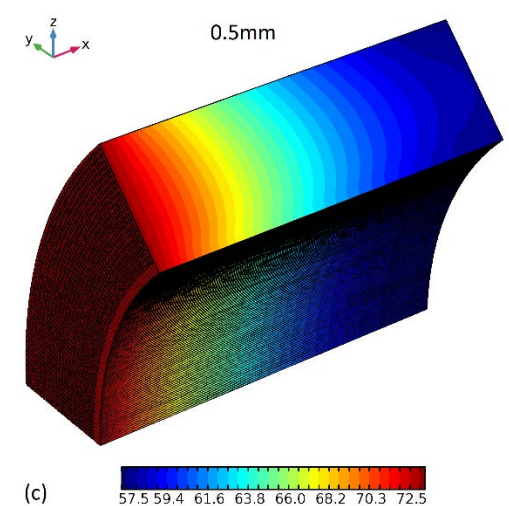
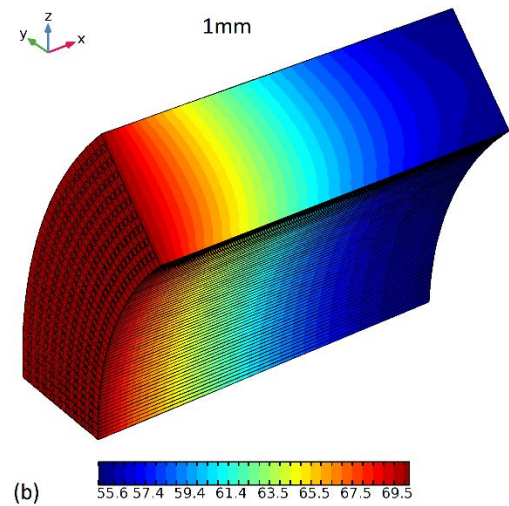
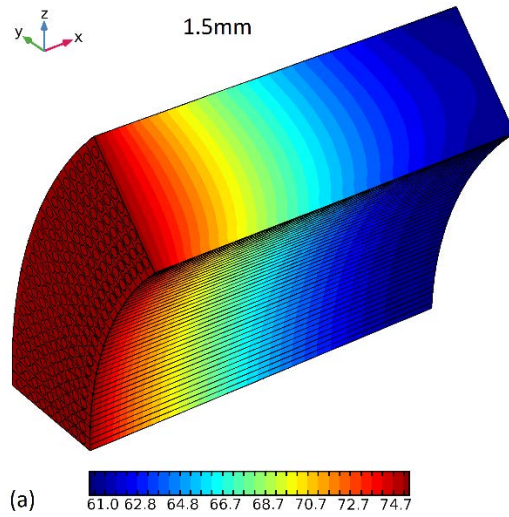


Figure 7-32 Sample of temperature contours (in °C) of the three MCRHXs at 10 SCFM and $t = 3600$ s.

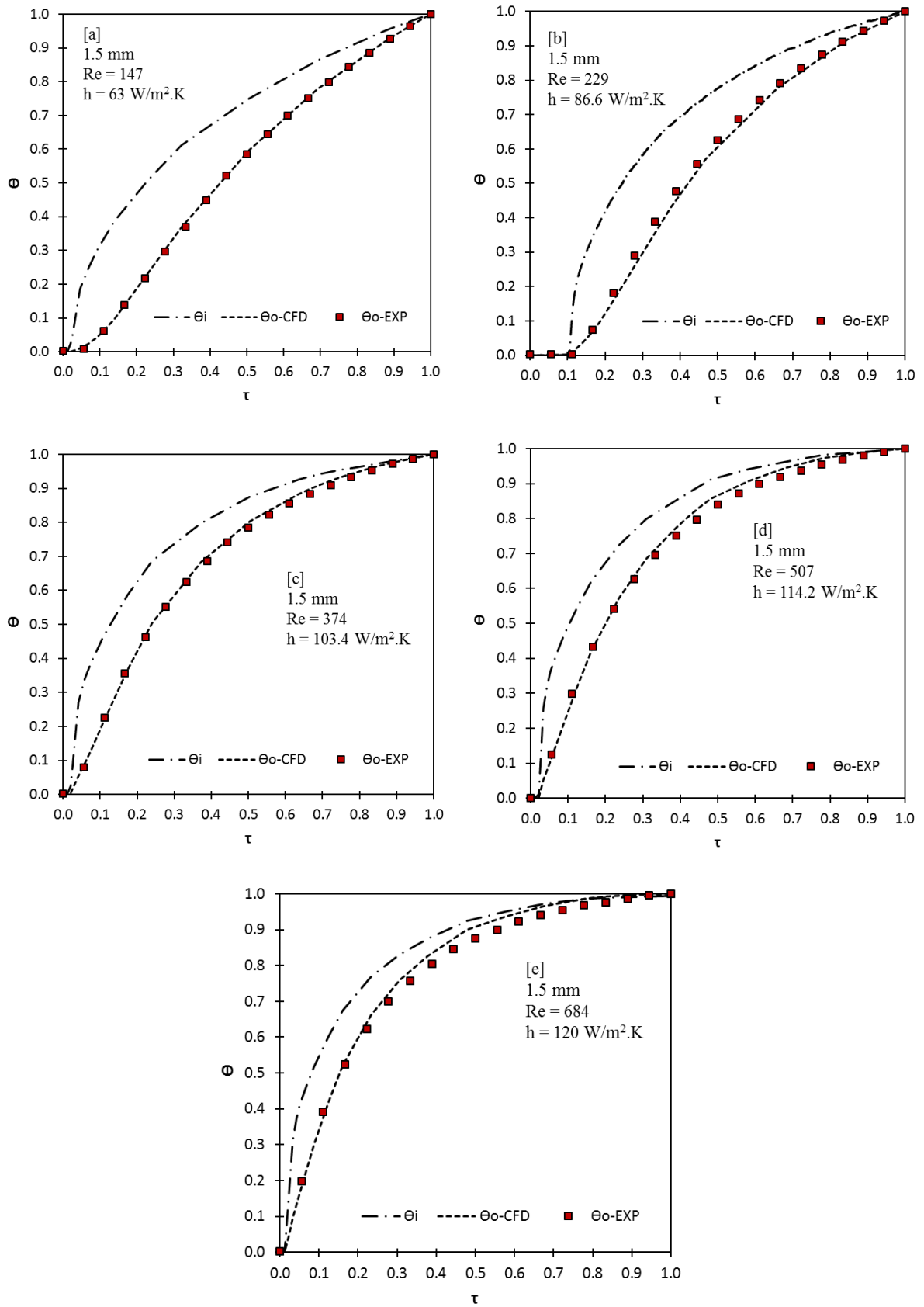


Figure 7-33 Comparison of inlet and outlet temperatures histories for 1.5 mm MCRHX.

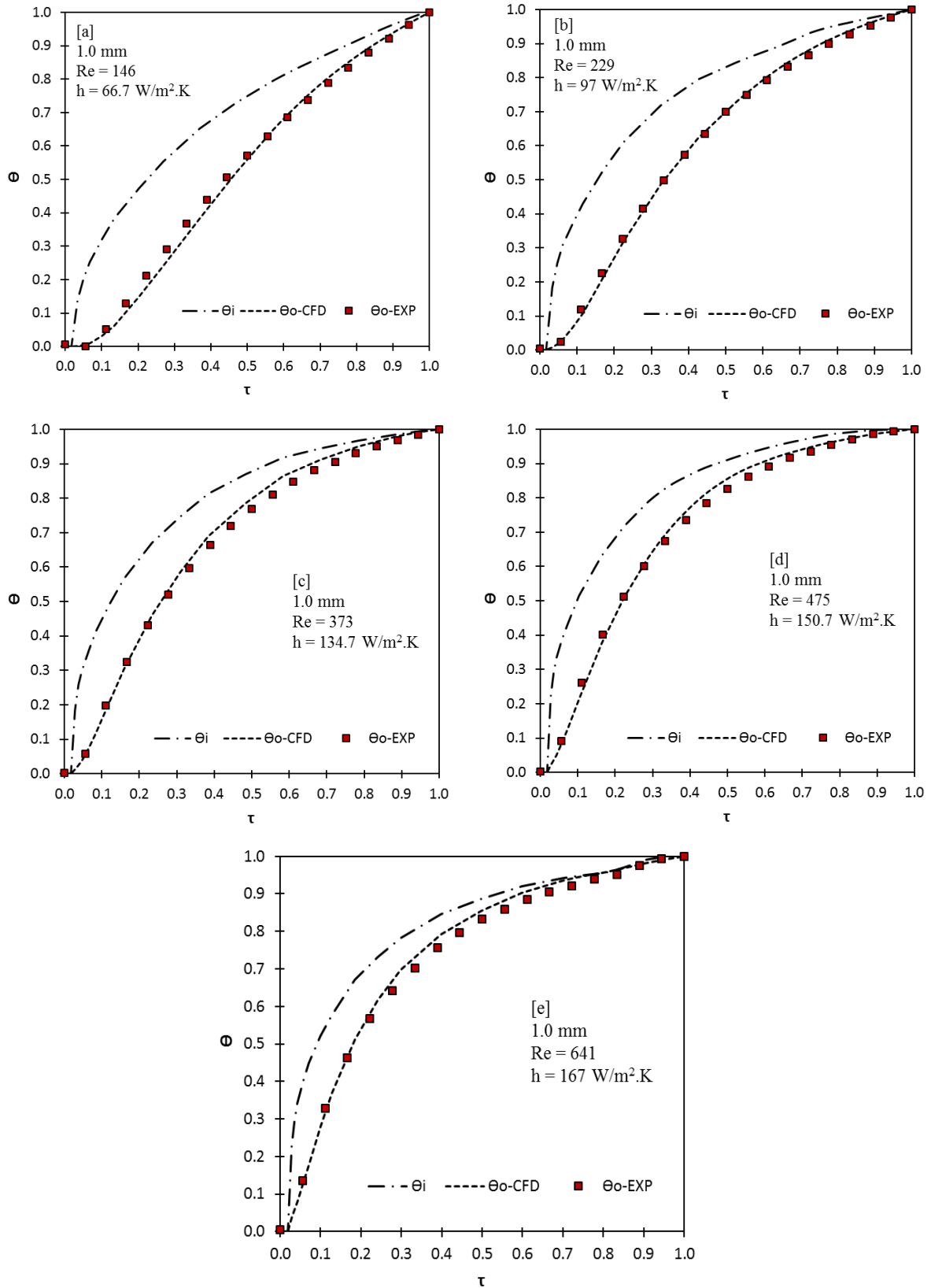


Figure 7-34 Comparison of inlet and outlet temperatures histories for 1 mm MCRHX.

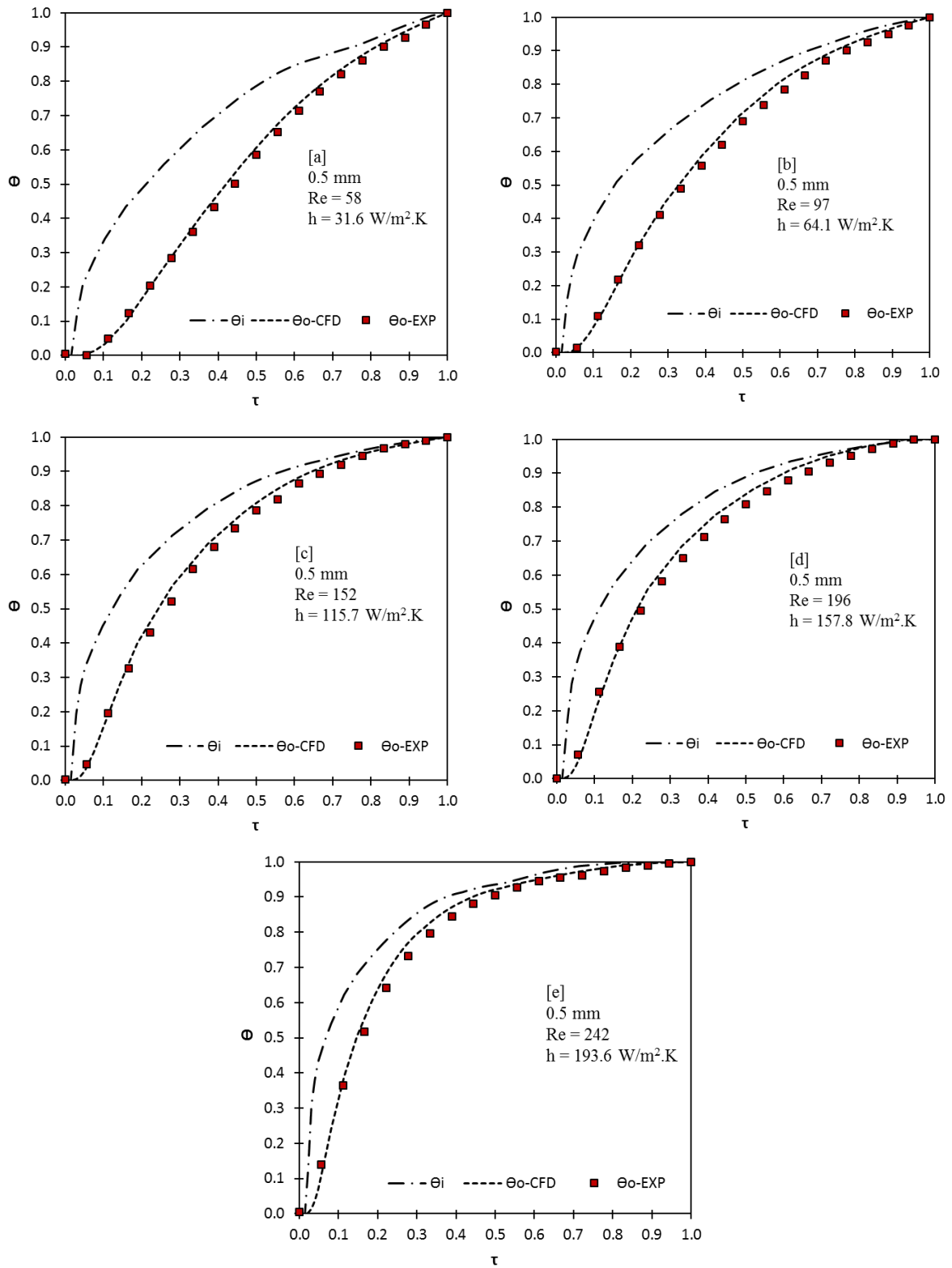


Figure 7-35 Comparison of inlet and outlet temperatures histories for 0.5 mm MCRHX.

As shown in Figure 7-33(a)-(e), as inlet velocity increases, the incremental rate in temperature, Θ increases. For example, at a time ratio of 0.3 and different Re number, 147 and 684,

respectively, the temperature incremental rate reads 0.325 and 0.724. This result is natural and it agrees with the principles of forced convection and it was observed for all configurations. The (ζ) values were varied by trial and error until the corresponding thermal responses at outlet are matched between CFD and measurements. At each test case, the heat transfer coefficient was calculated from CFD and was shown on the legend. For 1.5 mm MCRHX, the heat transfer coefficient varies from 63 to 120 W/m². K as Reynolds number increases from 147 to 684. For 1 mm MCRHX, as depicted in Figure 7-34(a)-(e), the heat transfer coefficient varies from 66.7 to 167 W/m². K as Reynolds number increases from 146 to 641. Similarly, the heat transfer coefficient varies from 31.6 to 193.6 W/m². K at Reynolds number ranging from 58 to 242 for the 0.5 mm MCRHX, as depicted in Figure 7-35(a)-(e).

In terms of heat transfer coefficient, larger diameter channels experience relatively low heat transfer coefficients at higher Reynolds number (over 240) due to the limited heat transfer surface area. In order to quantify the interstitial heat transfer coefficient (q_{sf}), the specific solid surface area is used for each configuration which is defined as the ratio of the matrix surface area exposed to the gas to the volume of the matrix and can be calculated in terms of volumetric porosity (ϵ) and hydraulic diameter (D_h). The calculated specific areas for 0.5 mm, 1 mm and 1.5 mm configurations are 2617, 1565 and 1156, respectively. The interstitial heat transfer coefficients vs. Reynolds number are shown in Figure 7-36 for the three MCRHXs.

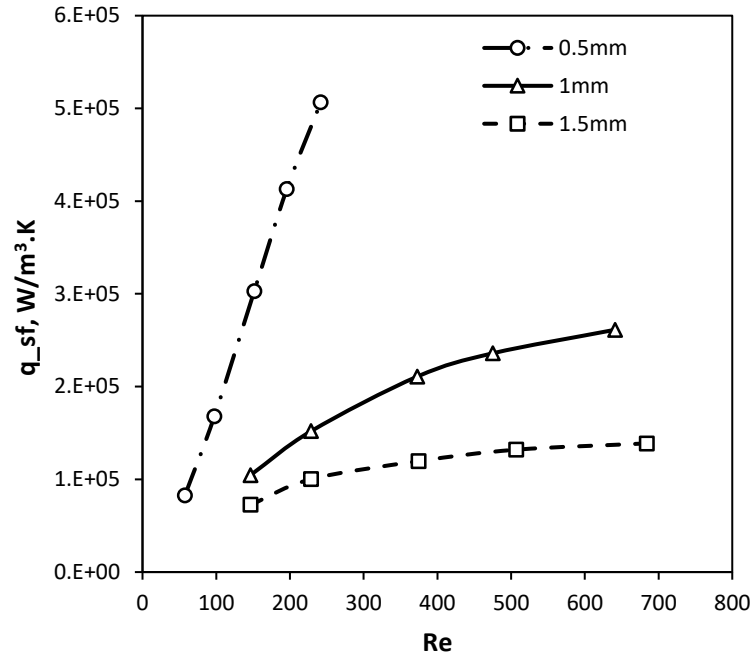


Figure 7-36 interstitial heat transfer coefficients vs. Reynolds number for the three heat exchangers.

It can be seen that the specific surface area exposed to the working gas plays an important role in maximizing the thermal performance of the heat exchanger. Since heat transfer resistance between the gas and the solid is much higher than the resistance inside the MCRHX. Therefore, higher values of interstitial heat transfer coefficients were obtained for 0.5 mm configuration compared to 1 mm and 1.5 mm ones due to the increased specific surface area.

Figure 7-37 shows that the average Nusselt number increases with Reynolds number. For larger diameter channels, higher values of Nusselt number is depicted due to the higher values of hydraulic diameters. However, the small hydraulic diameter indicates faster thermal response at a small range of Reynolds number (60 to 250) compared to larger diameter channels (150 to 700). For smaller channels (0.5 mm), it is clear that Nusselt number almost varies linearly with Reynolds number with a slope higher than that of larger diameter ones. It is noteworthy that at

Reynolds number higher than 300, the Nusselt number values of small diameter MCRHX will be superior to large ones.

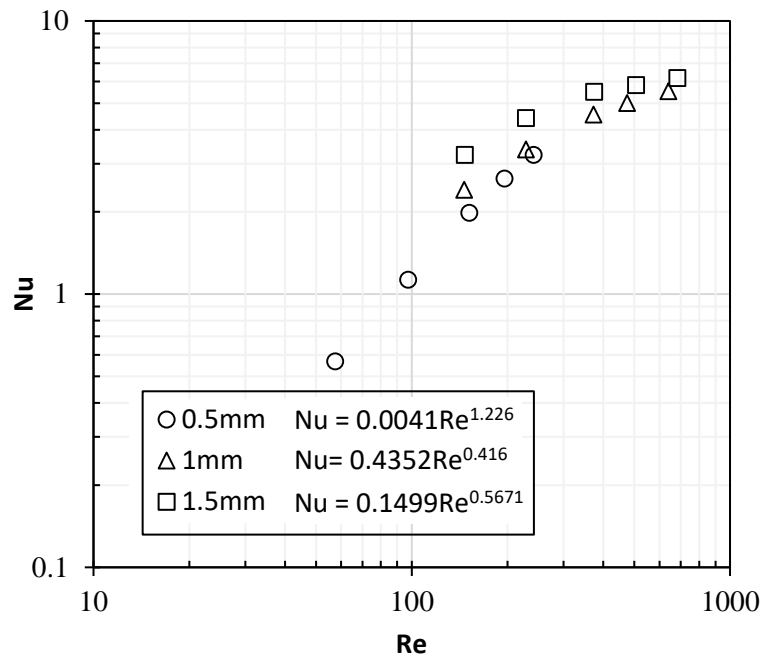


Figure 7-37 Average Nusselt number vs. Reynolds number for the three heat exchangers.

The fluid flow characteristics, in terms of pressure drop, were obtained from CFD simulations for each configuration and compared to experiment as shown in Figure 7-38. As can be seen that data of pressure loss compares well with experiment with maximum deviation of 9%. The trends are almost linear with fluid inlet velocity for all MCRHX configurations. The inertial loss part is not significant in the channels due to the absence of flow separation and vortices. The highest pressure loss is observed for the 0.5 mm MCRHX.

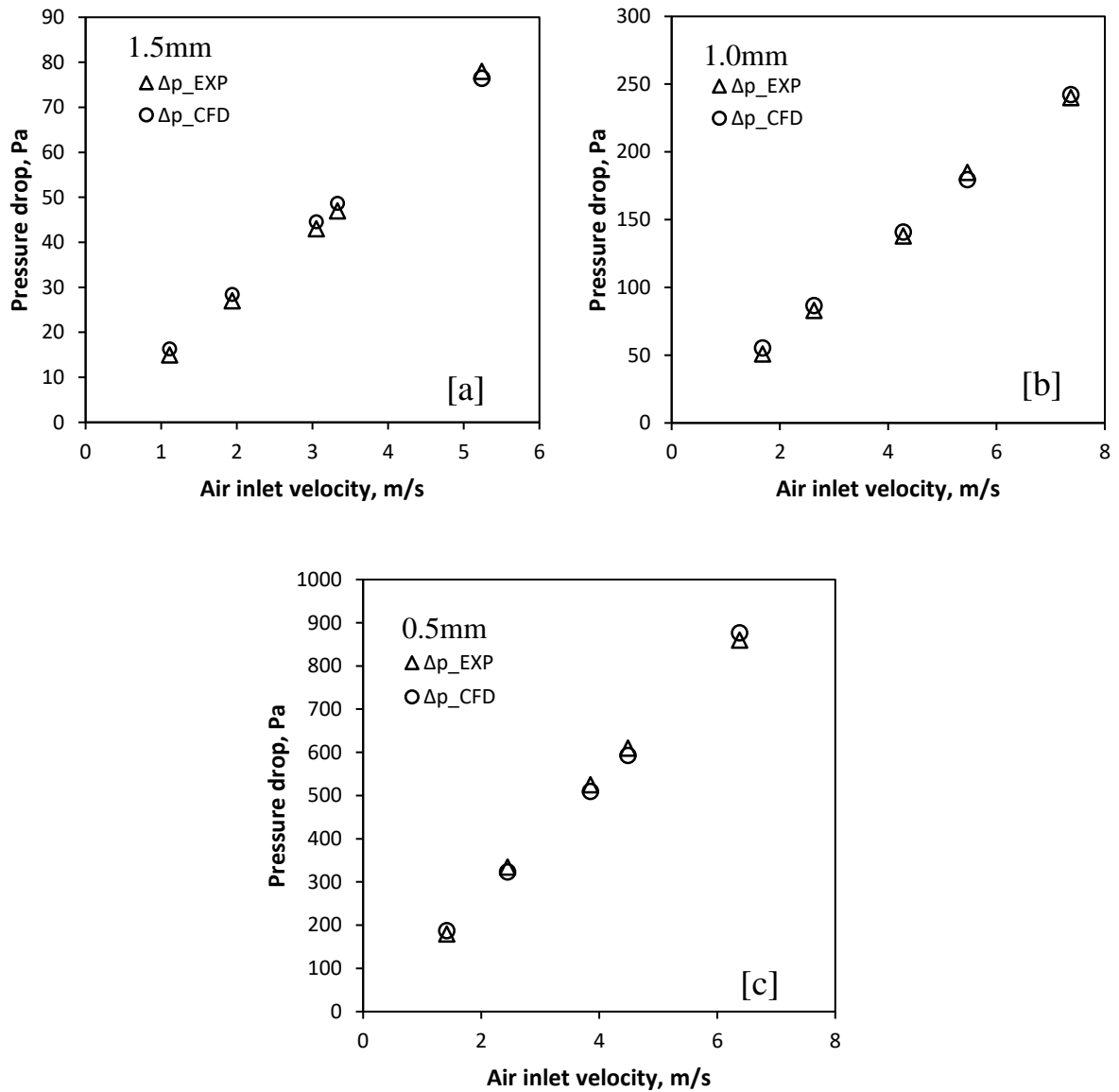


Figure 7-38 comparison of pressure drop across the three heat exchangers between CFD and experiment.

The simulation results for friction factors were plotted in Figure 7-39 showing a decreasing trend with increasing Reynolds number for all configuration. The friction factor correlations are close to Darcy friction factor for laminar flow. This indicated that the use of classical friction correlation for mini-channels accurately apply in the present investigated range.

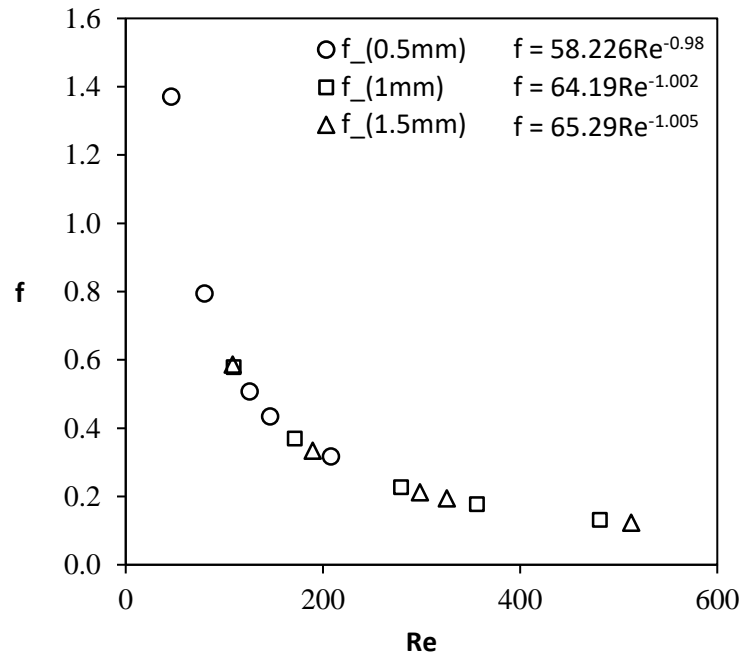


Figure 7-39 Friction factor vs. Reynolds number for the three MCRHXs.

7.8.2 Engine performance with mini-channel regenerators

In order to evaluate the performance of mini-channel regenerators on Gamma-type Stirling engine performance, the full 2D CFD model of the engine developed in chapter 5 was used. The porous media data obtained for all channel regenerators were defined as input parameters to the full engine CFD model. Figure 7-40 shows the engine indicated PV diagrams for mini-channels regenerators and random fibre. As depicted in Figure 7-41, the indicated power of 0.5 mm regenerator is 4% lower than that of the random fibre regenerator. As the channels diameter increases, the indicated power deteriorates reaching a reduction of 31% for 1.5 mm regenerator compared to that of random fibre. Although pressure drop of mini-channels regenerator is significantly lower than that of conventional regenerators, the performance of the engine is governed by the heat transfer characteristics of the regenerator.

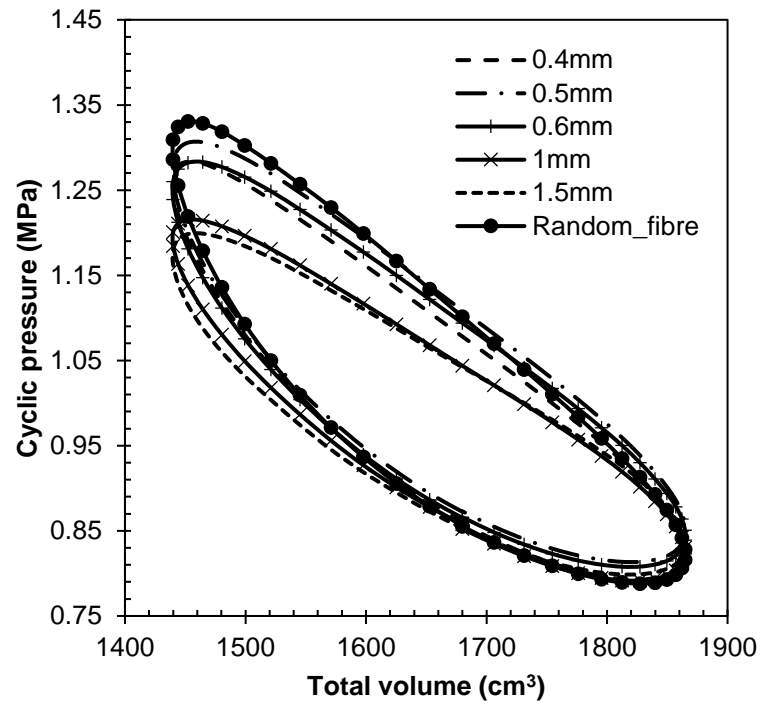


Figure 7-40 Indicated PV diagrams for channels regenerator and random fibre.

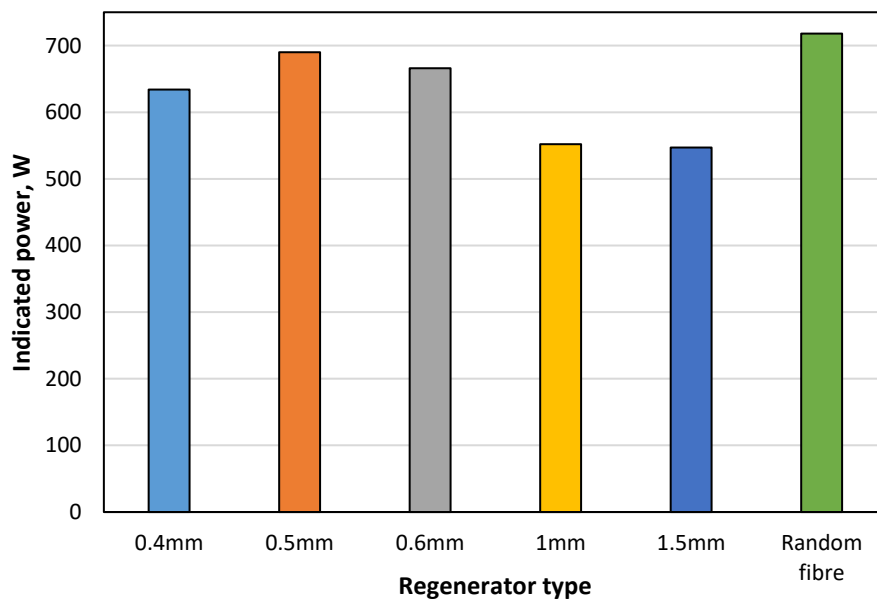


Figure 7-41 Indicated power for channels regenerator and random fibre.

Figure 7-42 shows a comparison of the heat rejected from the engine's cooler for mini-channels regenerator and random fibre where the maximum heat rejected from the engine is observed for the 1mm channel regenerator which is 17% higher than that of the random fibre. One important factor of regenerator performance is the specific surface area exposed to the working gas. Since heat transfer resistance between the gas and the solid is much higher than the resistance inside the regenerator. Therefore, transferring the heat from the gas to the regenerator can be enhanced by increasing the specific surface area.

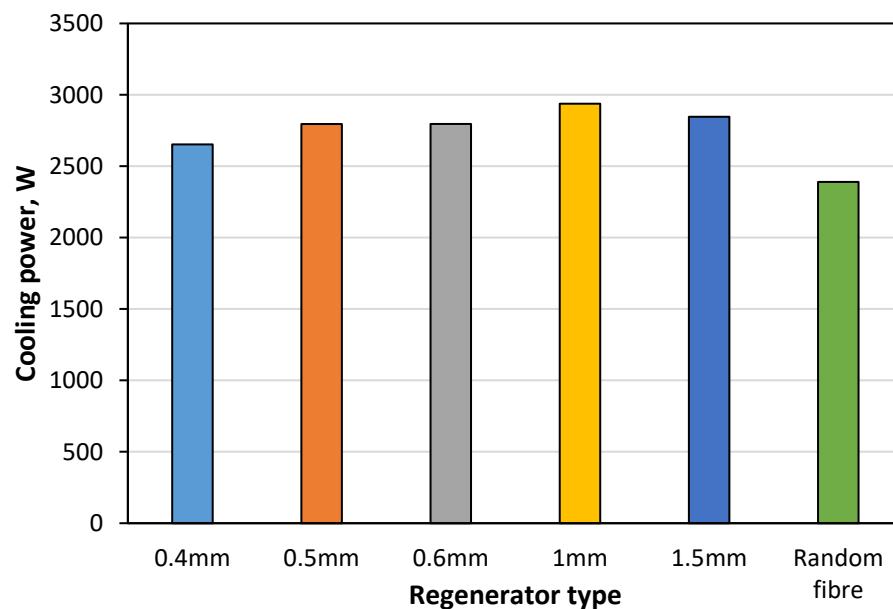


Figure 7-42 Cooling power for channels regenerator and random fibre.

A closer comparison of the solid specific area between the random fibre and channel regenerators showed that the surface area of all channel regenerators is limited which is 80% lower than that of random fibre. However, the volumetric heat capacity of the channel regenerator is significantly higher than that of random fibre due to a lower porosity.

One critical issue with mini-channel regenerators was their excessive conduction loss due to high longitudinal thermal conductivity. Therefore, the regenerator's NTU is reduced due to the reduction of the temperature difference between the working gas and matrix.

However, the ineffectiveness of mini-channels regenerators can be alleviated by optimizing the matrix material and the segmentation of the whole regenerator. The thermal performance of the regenerator is governed by the choice of its material. A material with good heat capacity allows to absorb/release maximum energy to/from the working gas and a material with lower thermal conductivity reduces conduction losses. Different materials such as Stainless steel, Monel 400, ceramic (ZrO₂), copper and aluminium with different thermal properties, were investigated for the 0.5 mm channels regenerator using the engine full CFD model. The thermal properties of those material are listed in Table 7-3.

Table 7-3 Material thermal properties of regenerator matrix [91].

Properties	Stainless steel (304L)	Copper	Aluminium	Monel 400	Ceramic (ZrO ₂)
Density (kg m ⁻³)	7850	8920	2700	8800	6050
Thermal capacity (J kg ⁻¹ K ⁻¹)	475	385	902	430	460
Thermal conductivity (J kg ⁻¹ K ⁻¹)	26*	390	237	22	3

*recommended for Stirling engine environment based on oscillatory flow condition [8]

Monel 400 and Stainless steel have the highest volumetric heat capacity (material density times the specific heat capacity) among those materials and lower thermal conductivity. Therefore, it is expected that those two materials will show better performance compared to copper and aluminium with higher thermal conductivities. In order to investigate the effect of those materials on engine performance, the maximum heater temperature of the engine was

maintained at 500 °C to avoid approaching the melting point of aluminium (660 °C). As depicted in, Figure 7-43 higher indicated power was obtained using Monel 400 and Stainless steel, while copper has the lowest indicated power. In terms of the cooling power rejected from the engine, ceramic (ZrO₂) and Monel 400 had the lowest cooling power while copper had the highest value. This proves that the best regenerator material should have a reasonable high volumetric heat capacity and a lower thermal conductivity.

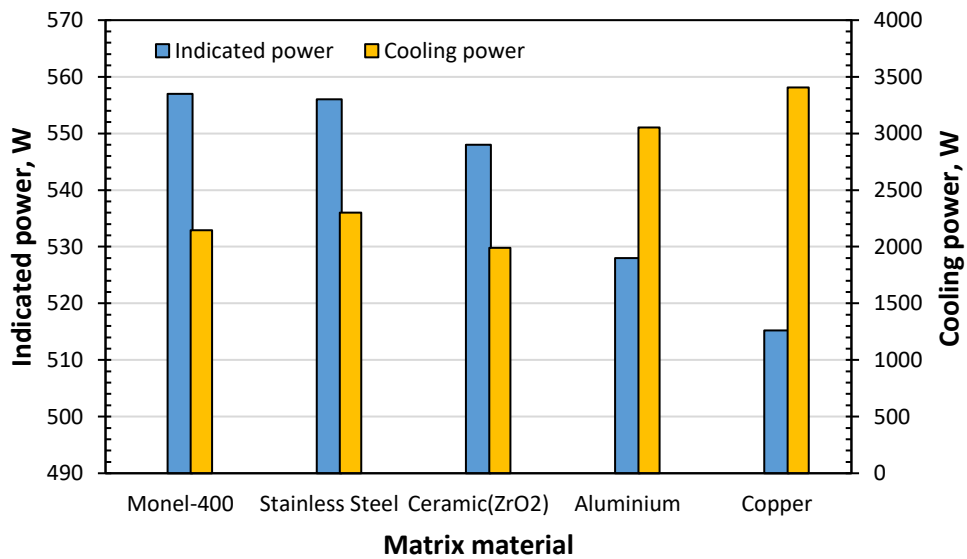


Figure 7-43 Indicated and cooling powers for different matrix materials.

The ineffectiveness of channels regenerators can be alleviated by the segmentation of the whole regenerator. Segmentation adds thermal contact resistance to each consecutive sheet so that the axial conduction loss is minimized due the interruption of the solid continuity. Similar behaviour was observed by authors [98, 158] where they conducted an experimental study to find the optimum number of segmentations for parallel wire regenerator. The theoretical investigation of segmentation of a parallel geometry regenerator was not reported in literature due to the lack in defining thermal contact characteristics that resembles the real cutting properties of the sheets such as surface roughness (height and slope), hardness of the material, contact pressure and the gap conductance.

7.8.3 Summary

From the results presented in this chapter, the engine performance can be improved by altering some operational parameters such as: the working gas, phase angle and cold end temperature, and some geometrical parameters such as the connecting pipe diameter. On the other hand, mini-channel regenerators can have as good potential to generate power as random fibre using materials such as ceramic (ZrO₂) and Monel 400.

CHAPTER 8

CONCLUSIONS AND RECOMMENDATIONS

Nowadays, a great effort is applied for developing Stirling engines to be used in numerous applications. Stirling engines can be environmentally and economically competitive if they are integrated with renewable sources of energy.

In this context, thermodynamic and CFD models are developed to simulate HTD gamma-type Stirling engine prototype (ST05-CNC), available at Mechanical Engineering Department of University of Birmingham. Once they are validated with experimental results, a parametric study was carried out to improve the engine performance.

Due to the complex geometry of the investigated engine (twenty heater pipes, finned shaped cooler, displacer material and solid walls), 3D CFD Modelling of the current engine was computationally expensive. Also, it is not possible to model the engine as 2D axisymmetric configuration due to the asymmetric feature of engine geometry (heater pipes and connecting pipe). Therefore, the engine was modelled as 2D plane which represents all engine components and divides the whole engine into two symmetrical domains.

Using this technique along with converting the 3D structure of the regenerator and cooler into an equivalent 2D porous media, made this approach computationally inexpensive compared to the 3D model approaches represented in this work (3D half engine and 3D engine sector CFD approaches).

Although the predicted power generated from 3D half engine is close to experiment, while 3D sector generates 10% higher power than that of the experiment, the 2D approach generates 5% lower power than that of the experiment with simulation time considerably less than that of other 3D approaches (normally 5 hours for the 2D approach compared to 3 days of the 3D half engine approach).

The alteration of some operational and the geometrical parameters of the engine can improve the engine performance. Using a gas of higher power density such as helium can enhance the shaft power at higher speeds to (712 W at 1100 rpm) compared to nitrogen (503 W at 600 rpm). Reducing the dead volume (connecting pipe) from 30 mm to 15 mm can enhance the shaft power by up to 20% as the dead volume is minimized. Adjusting the phase angle value to 105° increases the shaft power by 5%. Lowering the cooling temperature up to (-50°C) using the stored cold energy of cryogenic fluids during surplus electricity or using renewable energy sources can boost the shaft power by 49% for helium reaching 1000 W and 35% for Nitrogen reaching 700 W. Theoretically, the shaft power can reach up to 1664 W for helium compared to 1026 W for nitrogen when the temperature is lowered to -150°C . However, further study is required to consider the behaviour of engine materials and instrumentations at low temperatures and its effect on heat transfer characteristics.

As the regenerator is a key part in the engine, a new parallel-geometry type was developed to investigate its potential of enhancing the engine performance and in the first stage, different configurations were investigated. In mini-channels regenerators, most of the heat between fluid and solid is transferred in the radial direction and the surface area plays an important role in maximizing the thermal response in order to overcome the higher thermal resistance between

gas and solid due to gas lower thermal conductivity. The small hydraulic diameter of channels regenerators can have good potential to generate power as random fibre one. However, the axial conduction loss in mini-channels regenerators is intrinsically higher than the conventional regenerator type.

The transient testing of the three-fabricated mini-channels regenerators using the combined approach of CFD and experiment showed that the (0.5mm) channel regenerator had the highest interstitial heat transfer coefficient compared to other investigated configurations tested due to the increased surface area of the matrix. It was demonstrated in this work that the performance of the (0.5mm) channel regenerator can be further enhanced by the appropriate selection of material. Using matrix materials such as ceramic (ZrO₂) and Monel 400 with lower thermal conductivity and higher volumetric heat capacity can enhance its performance and alleviate these losses compared to stainless steel. The power generated using Monel 400 is similar to that of stainless steel while ceramic (ZrO₂) generates power 1.4% less than that of stainless steel. However, by using ceramic (ZrO₂) and Monel 400, the engine rejects cooling power 13.4% and 6.5%, respectively lower than using stainless steel by which the engine thermal efficiency is improved.

Recommendations

More research is needed to optimize the performance of mini-channels regenerators. Therefore, an investigation of heat transfer and fluid flow characteristics of single channel of the regenerator, under oscillatory flow condition similar to engine operating conditions is essential in optimization phase. Future work should be focused on the following;

- Constructing more useful dimensionless thermodynamic analysis to correlate engine power and efficiency with a wide range of operating conditions including the variation of compression ratio.
- Cryogenic storage can be more feasible by recovering cold energy from other applications to the engine. Therefore, further study on best scenario of supplying LN₂/liquid air as cooling medium to the engine is required.
- Improving the performance of 0.5 mm channel regenerator. Using segmentation of the whole regenerator into compact porous sheets will alleviate the axial conduction loss and hence improve its thermal performance. Therefore, a theoretical and experimental work is required to investigate the optimum number of segmentations.

REFERENCES

- [1] R. Stirling, "Stirling patent of 1816/1817," *The Philips Stirling engine, Elsevier Science Publishers BV, Amsterdam, The Netherlands*, 1991.
- [2] A. J. Organ, *The air engine: Stirling cycle power for a sustainable future*: Elsevier, 2007.
- [3] C. Hargreaves, "The hot-air engine," *The Philips Stirling engine, Elsevier Science Publishers BV, Amsterdam, The Netherlands*, pp. 1-25, 1991.
- [4] C. Hargreaves, "The twentieth century revival," *The Philips Stirling engine, Elsevier Science Publishers BV, Amsterdam, The Netherlands*, pp. 27-81, 1991.
- [5] G. Walker, *Stirling-cycle machines*: Oxford University Press, 1973.
- [6] J. R. Senft, *Ringbom stirling engines*: Oxford University Press, USA, 1993.
- [7] B. Kongtragool and S. Wongwises, "A review of solar-powered Stirling engines and low temperature differential Stirling engines," *Renewable and Sustainable energy reviews*, vol. 7, pp. 131-154, 2003.
- [8] I. Urieli and D. M. Berchowitz, *Stirling cycle engine analysis*: Taylor & Francis, 1984.
- [9] D. Thombare and S. Verma, "Technological development in the Stirling cycle engines," *Renewable and Sustainable Energy Reviews*, vol. 12, pp. 1-38, 2008.
- [10] A. Ross, *Making stirling engines: Ross experimental*, 1993.
- [11] R. Bowman, F. Ritzert, and M. Freedman, "Evaluation of candidate materials for a high-temperature stirling convertor heater head," 2003.
- [12] D. Isaac Jr, "Stirling engine with high pressure fluid heat exchanger," ed: Google Patents, 2004.
- [13] C.-H. Cheng, H.-S. Yang, and L. Keong, "Theoretical and experimental study of a 300-W beta-type Stirling engine," *Energy*, vol. 59, pp. 590-599, 2013.
- [14] B. STIRLING ENERGY s.r.o., "Cleanergy C9G Microcogeneration Unit," 2017.
- [15] M. Kanzaka and M. Iwabuchi, "Study on heat transfer of heat exchangers in the stirling engine: performance of heat exchangers in the test stirling engine," *JSME international journal. Ser. 2, Fluids engineering, heat transfer, power, combustion, thermophysical properties*, vol. 35, pp. 647-652, 1992.
- [16] F. d. Monte, "Thermal analysis of the heat exchangers and regenerator in Stirling cycle machines," *Journal of propulsion and power*, vol. 13, pp. 404-411, 1997.

- [17] G. Walker and J. R. Senft, "Free-piston Stirling engines," in *Free Piston Stirling Engines*, ed: Springer, 1985, pp. 23-99.
- [18] A. J. Organ, *The regenerator and the Stirling engine*: wiley, 1997.
- [19] M. B. Ibrahim and R. C. Tew Jr, *Stirling convertor regenerators*: CRC Press, 2011.
- [20] S. Costa, H. Barrutia, J. A. Esnaola, and M. Tutar, "Numerical study of the heat transfer in wound woven wire matrix of a Stirling regenerator," *Energy Conversion and Management*, vol. 79, pp. 255-264, 2014.
- [21] M. Iasiello, S. Cunsolo, M. Oliviero, W. M. Harris, N. Bianco, W. K. Chiu, "Numerical Analysis of Heat Transfer and Pressure Drop in Metal Foams for Different Morphological Models," *Journal of Heat Transfer*, vol. 136, p. 112601, 2014.
- [22] A. J. Organ, *Thermodynamics and gas dynamics of the Stirling cycle machine*: Cambridge University Press, 1992.
- [23] S. Mekhilef, R. Saidur, and A. Safari, "A review on solar energy use in industries," *Renewable and Sustainable Energy Reviews*, vol. 15, pp. 1777-1790, 2011.
- [24] M. Z. Jahromi, M. M. H. Bioki, and R. Fadaeinedjad, "Simulation of a stirling engine solar power generation system using Simulink," in *International Aegean Conference on Electrical Machines and Power Electronics and Electromotion, Joint Conference*, 2011, pp. 676-681.
- [25] A. Asnaghi, Ladjevardi, SM, Saleh Izadkhast, P Kashani, AH, "Thermodynamics performance analysis of solar stirling engines," *ISRN Renewable Energy*, vol. 2012, 2012.
- [26] DAILYTECH, "MSI Showcases Stirling Engine Heatsink," 2008.
- [27] B. Van Arsdell, "Around the World by Stirling Engine," *American Stirling Company*, 2003.
- [28] N. Badea and S. DomneascÄf, "Design for Micro-Combined Cooling, Heating and Power Systems," *London: Springer London. doi*, vol. 10, pp. 978-1, 2015.
- [29] N. P. Nightingale, "Automotive Stirling engine: Mod 2 design report," 1986.
- [30] L. Figueroa, O. R. Fauvel, and G. T. Reader, "Performance of stirling engine hybrid electric vehicles: A simulation approach," SAE Technical Paper 0148-7191, 2001.
- [31] A. De Waele, "Basic operation of cryocoolers and related thermal machines," *Journal of Low Temperature Physics*, vol. 164, pp. 179-236, 2011.
- [32] D. Y. Goswami and F. Kreith, *Handbook of energy efficiency and renewable energy*: Crc Press, 2007.

- [33] U. Kumar and M. Karimi, "Low grade Waste Heat Recovery for Optimized Energy Efficiencies and Enhanced Sustainability in Process Industries: A Comprehensive Review," *International Journal of Multidisciplinary Sciences and Engineering*, vol. 5, 2014.
- [34] H. Damirchi, G. Najafi, S. Alizadehnia, R. Mamat, C. S. N. Azwadi, W. Azmi, *et al.*, "Micro Combined Heat and Power to provide heat and electrical power using biomass and Gamma-type Stirling engine," *Applied Thermal Engineering*, vol. 103, pp. 1460-1469, 2016.
- [35] W. R. Martini, *Stirling engine design manual*: US Department of Energy, Office of Conservation and Solar Applications, Division of Transportation Energy Conservation, 1978.
- [36] W. T. Beale, J. Wood, and B. Chagnot, "Stirling engines for developing countries," in *Intersociety energy conversion engineering conference. 15*, pp. 1971-1975, 1980.
- [37] C. West, "Dynamic analysis of the Fluidyne," in *Proc., Intersoc. Energy Convers. Eng. Conf.:(United States)*, 1983.
- [38] G. Schmidt, "Classical analysis of operation of Stirling engine," *A report published in German engineering union (Original German)*, vol. 15, pp. 1-12, 1871.
- [39] A. Organ, P. LONG, and L. VASCIAVEO, "Back-to-back test for determining the pumping losses in a Stirling cycle machine," *IECEC'82*, pp. 1856-1861, 1982.
- [40] J. R. Senft, "Optimum Stirling engine geometry," *International Journal of Energy Research*, vol. 26, pp. 1087-1101, 2002.
- [41] J. C. Bert, Daniela Sophy, Tonino Le Moyne, Luis Sirot, Frédéric, "Simulation, experimental validation and kinematic optimization of a Stirling engine using air and helium," *Energy*, vol. 78, pp. 701-712, 2014.
- [42] R. Li, L. Grosu, and D. Queiros-Condé, "Losses effect on the performance of a Gamma type Stirling engine," *Energy Conversion and Management*, vol. 114, pp. 28-37, 2016.
- [43] F. Formosa and G. Despesse, "Analytical model for Stirling cycle machine design," *Energy Conversion and Management*, vol. 51, pp. 1855-1863, 2010.
- [44] E. Eid, "Performance of a beta-configuration heat engine having a regenerative displacer," *Renewable Energy*, vol. 34, pp. 2404-2413, 2009.
- [45] A. H. El-Ehwany, GM Eid, EI El-Kenany, EA, "Development of the performance of an alpha-type heat engine by using elbow-bend transposed-fluids heat exchanger as a heater and a cooler," *Energy Conversion and Management*, vol. 52, pp. 1010-1019, 2011.
- [46] N. G. Martaj, Lavinia Rochelle, Pierre, "Thermodynamic study of a low temperature difference Stirling engine at steady state operation," *International Journal of Thermodynamics*, vol. 10, pp. 165-176, 2007.

- [47] P. Puech and V. Tishkova, "Thermodynamic analysis of a Stirling engine including regenerator dead volume," *Renewable Energy*, vol. 36, pp. 872-878, 2011.
- [48] C.-H. Cheng and H.-S. Yang, "Optimization of geometrical parameters for Stirling engines based on theoretical analysis," *Applied energy*, vol. 92, pp. 395-405, 2012.
- [49] C.-H. Cheng and H.-S. Yang, "Optimization of rhombic drive mechanism used in beta-type Stirling engine based on dimensionless analysis," *Energy*, vol. 64, pp. 970-978, 2014.
- [50] H. Hosseinzade, H. Sayyaadi, and M. Babaelahi, "A new closed-form analytical thermal model for simulating Stirling engines based on polytropic-finite speed thermodynamics," *Energy Conversion and Management*, vol. 90, pp. 395-408, 2015.
- [51] T. Finkelstein, "analogue simulation of Stirling engine," *Simulation*, vol. 2, 1975.
- [52] A. Altman, "SNAP 2002-a Stirling numerical analysis program a second generation program," in *Energy Conversion Engineering Conference, 2002. IECEC'02. 2002 37th Intersociety*, pp. 497-502, 2004.
- [53] B. Thomas and D. Pittman, "Update on the evaluation of different correlations for the flow friction factor and heat transfer of Stirling engine regenerators," in *Energy Conversion Engineering Conference and Exhibit, 2000.(IECEC) 35th Intersociety, 2000*, pp. 76-84.
- [54] R. B. G. Paula, José L Cobas, Vlamir RM Lora, Electo ES, "THEORETICAL ASSESSMENT OF A STIRLING ENGINE'AMAZON'BY USING PROSA AND MATHCAD," 2011.
- [55] H. Hachem, R. Gheith, F. Aloui, and S. B. Nasrallah, "Numerical characterization of a γ -Stirling engine considering losses and interaction between functioning parameters," *Energy Conversion and Management*, vol. 96, pp. 532-543, 2015.
- [56] J. A. C. Araoz, Evelyn Salomon, Marianne Alejo, Lucio Fransson, Torsten H, "Development and validation of a thermodynamic model for the performance analysis of a gamma Stirling engine prototype," *Applied Thermal Engineering*, vol. 83, pp. 16-30, 2015.
- [57] M. Mabrouk, A. Kheiri, and M. Feidt, "Displacer gap losses in beta and gamma Stirling engines," *Energy*, vol. 72, pp. 135-144, 2014.
- [58] N. W. Parlak, Andreas Elsner, Michael Soyhan, Hakan S, "Thermodynamic analysis of a gamma type Stirling engine in non-ideal adiabatic conditions," *Renewable Energy*, vol. 34, pp. 266-273, 2009.
- [59] I. Tlili and A. Sa'ed, "Thermodynamic evaluation of a second order simulation for Yoke Ross Stirling engine," *Energy Conversion and Management*, vol. 68, pp. 149-160, 2013.
- [60] Y. Timoumi, I. Tlili, and S. B. Nasrallah, "Design and performance optimization of GPU-3 Stirling engines," *Energy*, vol. 33, pp. 1100-1114, 2008.

- [61] R. Gheith, H. Hachem, F. Aloui, and S. B. Nasrallah, "Experimental and theoretical investigation of Stirling engine heater: Parametrical optimization," *Energy Conversion and Management*, vol. 105, pp. 285-293, 2015.
- [62] K. Kraitong, "Numerical modelling and design optimisation of stirling engines for power production," Northumbria University, 2012.
- [63] S. Schulz and F. Schwendig, "A general simulation model for stirling cycles," *Journal of engineering for gas turbines and power*, vol. 118, pp. 1-7, 1996.
- [64] K. K. Makhkamov and D. Ingham, "Analysis of the working process and mechanical losses in a Stirling engine for a solar power unit," *Journal of solar energy engineering*, vol. 121, pp. 121-127, 1999.
- [65] C. J. Paul and A. Engeda, "Modeling a complete Stirling engine," *Energy*, vol. 80, pp. 85-97, 2015.
- [66] C. J. Paul and A. Engeda, "A Stirling engine for use with lower quality fuels," *Energy*, vol. 84, pp. 152-160, 2015.
- [67] D. Shendage, S. Kedare, and S. Bapat, "Investigations on performance of Stirling engine regenerator matrix," in *ASME/JSME 2011 8th Thermal Engineering Joint Conference*, 2011, pp. T20044-T20044-8.
- [68] S. Oberweis and T. Al-Shemmeri, " γ -Stirling engine—The effect of different working gases and pressures," *in practice*, vol. 7, p. 9, 2010.
- [69] H. Hosseinzade and H. Sayyaadi, "CAFS: The Combined Adiabatic–Finite Speed thermal model for simulation and optimization of Stirling engines," *Energy Conversion and Management*, vol. 91, pp. 32-53, 2015.
- [70] M. Babaelahi and H. Sayyaadi, "Simple-II: A new numerical thermal model for predicting thermal performance of Stirling engines," *Energy*, vol. 69, pp. 873-890, 2014.
- [71] M. Babaelahi and H. Sayyaadi, "A new thermal model based on polytropic numerical simulation of Stirling engines," *Applied Energy*, vol. 141, pp. 143-159, 2015.
- [72] M. Babaelahi and H. Sayyaadi, "Modified PSVL: A second order model for thermal simulation of Stirling engines based on convective–polytropic heat transfer of working spaces," *Applied Thermal Engineering*, vol. 85, pp. 340-355, 2015.
- [73] T. Finkelstein, "Generalized thermodynamic analysis of Stirling engines," SAE Technical Paper 0148-7191, 1960.
- [74] R. W. Dyson, S. D. Wilson, and R. C. Tew, "Review of computational stirling analysis methods," in *Collect. Tech. Pap. Int. Energy Convers. Eng. Conf*, 2004, pp. 511-531.
- [75] S. Huang, "HFAST-A harmonic analysis program for Stirling cycles," SAE Technical Paper 0148-7191, 1992.

- [76] M. Hooshang, R. A. Moghadam, S. A. Nia, and M. T. Masouleh, "Optimization of Stirling engine design parameters using neural networks," *Renewable Energy*, vol. 74, pp. 855-866, 2015.
- [77] B. Hoegel, D. Pons, M. Gschwendtner, A. Tucker, and M. Sellier, "Thermodynamic peculiarities of alpha-type Stirling engines for low-temperature difference power generation: Optimisation of operating parameters and heat exchangers using a third-order model," *Proceedings of the Institution of Mechanical Engineers, Part C: Journal of Mechanical Engineering Science*, vol. 228, pp. 1936-1947, 2014.
- [78] M. Hooshang, R. A. Moghadam, and S. AlizadehNia, "Dynamic response simulation and experiment for gamma-type Stirling engine," *Renewable Energy*, vol. 86, pp. 192-205, 2016.
- [79] S. Toghyani, A. Kasaeian, S. H. Hashemabadi, and M. Salimi, "Multi-objective optimization of GPU3 Stirling engine using third order analysis," *Energy Conversion and Management*, vol. 87, pp. 521-529, 2014.
- [80] K. Mahkamov, "Design improvements to a biomass Stirling engine using mathematical analysis and 3D CFD modeling," *Journal of Energy Resources Technology*, vol. 128, pp. 203-215, 2006.
- [81] W.-L. Chen, K.-L. Wong, and Y.-F. Chang, "A computational fluid dynamics study on the heat transfer characteristics of the working cycle of a low-temperature-differential γ -type Stirling engine," *International Journal of Heat and Mass Transfer*, vol. 75, pp. 145-155, 2014.
- [82] W.-L. Chen, Y.-C. Yang, and J. L. Salazar, "A CFD parametric study on the performance of a low-temperature-differential γ -type Stirling engine," *Energy Conversion and Management*, vol. 106, pp. 635-643, 2015.
- [83] J. L. Salazar and W.-L. Chen, "A computational fluid dynamics study on the heat transfer characteristics of the working cycle of a β -type Stirling engine," *Energy Conversion and Management*, vol. 88, pp. 177-188, 2014.
- [84] S. D. Wilson, R. W. Dyson, R. C. Tew, and M. B. Ibrahim, "Multi-D CFD modeling of a free-piston Stirling convertor at NASA GRC," in *Proc. 2nd International Energy Conversion Engineering Conference, AIAA*, 2004.
- [85] A. Della Torre, A. Guzzetti, G. Montenegro, T. Cerri, A. Onorati, and F. Aloui, "CFD MODELLING OF A BETA-TYPE STIRLING MACHINE," in *5th European Conference on Computational Mechanics (ECCM V), Barcelona*, 2014.
- [86] K. Mahkamov, "An axisymmetric computational fluid dynamics approach to the analysis of the working process of a solar Stirling engine," *Journal of solar energy engineering*, vol. 128, pp. 45-53, 2006.
- [87] N. Martaj, P. Rochelle, L. Grosu, R. Bennacer, and S. Savarese, "Multiphysics CFD simulation of an Stirling engine with a porous regenerator," *Diffusion in Solids and Liquids DSL, Paris,(05-07July 2010)*.

- [88] Z. Li, Y. Haramura, Y. Kato, and D. Tang, "Analysis of a high performance model Stirling engine with compact porous-sheets heat exchangers," *Energy*, vol. 64, pp. 31-43, 2014.
- [89] J. Xu, J. Tian, T. Lu, and H. Hodson, "On the thermal performance of wire-screen meshes as heat exchanger material," *International journal of heat and mass transfer*, vol. 50, pp. 1141-1154, 2007.
- [90] W.-L. Chen, K.-L. Wong, and H.-E. Chen, "An experimental study on the performance of the moving regenerator for a γ -type twin power piston Stirling engine," *Energy Conversion and Management*, vol. 77, pp. 118-128, 2014.
- [91] R. Gheith, F. Aloui, and S. B. Nasrallah, "Determination of adequate regenerator for a Gamma-type Stirling engine," *Applied Energy*, vol. 139, pp. 272-280, 2015.
- [92] R. Gheith, F. Aloui, and S. B. Nasrallah, "Study of temperature distribution in a Stirling engine regenerator," *Energy Conversion and Management*, vol. 88, pp. 962-972, 2014.
- [93] C. Cinar and H. Karabulut, "Manufacturing and testing of a gamma type Stirling engine," *Renewable energy*, vol. 30, pp. 57-66, 2005.
- [94] C. Çınar, F. Aksoy, and D. Erol, "The effect of displacer material on the performance of a low temperature differential Stirling engine," *International Journal of Energy Research*, vol. 36, pp. 911-917, 2012.
- [95] A. Sripakagorn and C. Srikam, "Design and performance of a moderate temperature difference Stirling engine," *Renewable Energy*, vol. 36, pp. 1728-1733, 2011.
- [96] H. Karabulut, H. S. Yücesu, C. Çınar, and F. Aksoy, "An experimental study on the development of a β -type Stirling engine for low and moderate temperature heat sources," *Applied Energy*, vol. 86, pp. 68-73, 2009.
- [97] S. Isshiki, H. Sato, S. Konno, H. Shiraishi, N. Isshiki, I. Fujii, *et al.*, "The Experimental Study of Atmospheric Stirling Engines Using Pin-Fin Arrays' Heat Exchangers," *Journal of Power and Energy Systems*, vol. 2, pp. 1198-1208, 2008.
- [98] K. Nam and S. Jeong, "Development of parallel wire regenerator for cryocoolers," *Cryogenics*, vol. 46, pp. 278-287, 2006.
- [99] H. Takizawa, N. Kagawa, A. Matsuguchi, and S. Tsuruno, "Performance of new matrix for Stirling engine regenerator," in *Energy Conversion Engineering Conference, 2002. IECEC'02. 2002 37th Intersociety*, 2004, pp. 491-496.
- [100] M. B. Ibrahim, D. Danila, T. Simon, S. Mantell, L. Sun, D. Gedeon, "A Microfabricated Segmented-Involute-Foil Regenerator for Enhancing Reliability and Performance of Stirling Engines: Phase II Final Report for the Radioisotope Power Conversion Technology NRA Contract NAS3-03124," 2007.
- [101] T. Zhao and P. Cheng, "Oscillatory pressure drops through a woven-screen packed column subjected to a cyclic flow," *Cryogenics*, vol. 36, pp. 333-341, 1996.

- [102] D. Yanagawa, K. Kogure, A. Yamashita, I. Yamashita, and K. Hamaguchi, "Experimental Study of Cryogenic Stirling Engine II (Effect of Regenerator Matrices on Engine Performance)," in *Proceedings of the 9th Symposium on Stirling Cycle*, 2005, pp. 9-10.
- [103] Y. Kato and K. Baba, "Empirical estimation of regenerator efficiency for a low temperature differential Stirling engine," *Renewable Energy*, vol. 62, pp. 285-292, 2014.
- [104] K. Hirata, S. Iwamoto, F. Toda, and K. Hamaguchi, "Performance evaluation for a 100 W Stirling engine," in *Proceedings of 8th International Stirling Engine Conference*, 1997, pp. 19-28.
- [105] S. G. Kandlikar and W. J. Grande, "Evolution of Microchannel Flow Passages--Thermohydraulic Performance and Fabrication Technology," *Heat transfer engineering*, vol. 24, pp. 3-17, 2003.
- [106] H. Hausen, "Über die Theorie des Wärmeaustausches in Regeneratoren," *ZAMM-Journal of Applied Mathematics and Mechanics/Zeitschrift für Angewandte Mathematik und Mechanik*, vol. 9, pp. 173-200, 1929.
- [107] T. E. Schumann, "Heat transfer: a liquid flowing through a porous prism," *Journal of the Franklin Institute*, vol. 208, pp. 405-416, 1929.
- [108] G. Locke, "HEAT TRANSFER AND FLOW FRICTION CHARACTERISTICS OF POROUS SOLIDS. Technical Report No. 10," Stanford University, 1950.
- [109] R. Loehrke, "Evaluating the results of the single-blow transient heat exchanger test," *Experimental Thermal and Fluid Science*, vol. 3, pp. 574-580, 1990.
- [110] C. Liang and W.-J. Yang, "Modified single-blow technique for performance evaluation on heat transfer surfaces," *ASME J. Heat Transfer*, vol. 97, pp. 16-21, 1975.
- [111] Z. Cai, M. Li, Y. Wu, and H. Ren, "A modified selected point matching technique for testing compact heat exchanger surfaces," *International journal of heat and mass transfer*, vol. 27, pp. 971-978, 1984.
- [112] R. Loehrke, "A transient heat exchanger evaluation test for arbitrary fluid inlet temperature variation and longitudinal core conduction," 1986.
- [113] P.-H. Chen and Z.-C. Chang, "Measurements of thermal performance of cryocooler regenerators using an improved single-blow method," *International journal of heat and mass transfer*, vol. 40, pp. 2341-2349, 1997.
- [114] P.-H. Chen, Z.-C. Chang, and B.-J. Huang, "Effect of oversize in wire-screen matrix to the matrix-holding tube on regenerator thermal performance," *Cryogenics*, vol. 36, pp. 365-372, 1996.

- [115] P. Pucci, C. Howard, and C. Piersall, "The single-blow transient testing technique for compact heat exchanger surfaces," *Journal of Engineering for Power*, vol. 89, pp. 29-38, 1967.
- [116] Z.-C. Chang, M.-S. Hung, P.-P. Ding, and P.-H. Chen, "Experimental evaluation of thermal performance of Gifford–McMahon regenerator using an improved single-blow model with radial conduction," *International journal of heat and mass transfer*, vol. 42, pp. 405-413, 1999.
- [117] P. Heggs and D. Burns, "Single-blow experimental prediction of heat transfer coefficients: A comparison of four commonly used techniques," *Experimental Thermal and Fluid Science*, vol. 1, pp. 243-251, 1988.
- [118] K. Krishnakumar, A. K. John, and G. Venkatarathnam, "A review on transient test techniques for obtaining heat transfer design data of compact heat exchanger surfaces," *Experimental Thermal and Fluid Science*, vol. 35, pp. 738-743, 2011.
- [119] B. Baclic, D. Gvozdenac, D. Sekulic, and E. Becic, "Laminar heat transfer characteristics of a plate-louver fin surface obtained by the differential fluid enthalpy method," *Adv. Heat Exch. Des*, vol. 66, pp. 21-27, 1986.
- [120] L. Younis and R. Viskanta, "Experimental determination of the volumetric heat transfer coefficient between stream of air and ceramic foam," *International Journal of Heat and Mass Transfer*, vol. 36, pp. 1425-1434, 1993.
- [121] X. Luo, W. Roetzel, and U. Lüdersen, "The single-blow transient testing technique considering longitudinal core conduction and fluid dispersion," *International Journal of Heat and Mass Transfer*, vol. 44, pp. 121-129, 2001.
- [122] K. Shaji and S. K. Das, "The effect of flow maldistribution on the evaluation of axial dispersion and thermal performance during the single-blow testing of plate heat exchangers," *International Journal of Heat and Mass Transfer*, vol. 53, pp. 1591-1602, 2010.
- [123] M. Asadi, G. Xie, and B. Sunden, "A review of heat transfer and pressure drop characteristics of single and two-phase microchannels," *International Journal of Heat and Mass Transfer*, vol. 79, pp. 34-53, 2014.
- [124] T. Dixit and I. Ghosh, "Review of micro-and mini-channel heat sinks and heat exchangers for single phase fluids," *Renewable and Sustainable Energy Reviews*, vol. 41, pp. 1298-1311, 2015.
- [125] D. Reay, C. Ramshaw, and A. Harvey, *Process Intensification: Engineering for efficiency, sustainability and flexibility*: Butterworth-Heinemann, 2013.
- [126] N. Caney, P. Marty, and J. Bigot, "Friction losses and heat transfer of single-phase flow in a mini-channel," *Applied thermal engineering*, vol. 27, pp. 1715-1721, 2007.
- [127] X. Liu and J. Yu, "Numerical study on performances of mini-channel heat sinks with non-uniform inlets," *Applied Thermal Engineering*, vol. 93, pp. 856-864, 2016.

- [128] M. Khoshvaght-Aliabadi, M. Sahamiyan, M. Hesampour, and O. Sartipzadeh, "Experimental study on cooling performance of sinusoidal–wavy minichannel heat sink," *Applied Thermal Engineering*, vol. 92, pp. 50-61, 2016.
- [129] M. M. A. Bhutta, N. Hayat, M. H. Bashir, A. R. Khan, K. N. Ahmad, and S. Khan, "CFD applications in various heat exchangers design: A review," *Applied Thermal Engineering*, vol. 32, pp. 1-12, 2012.
- [130] C. Ranganayakulu, X. Luo, and S. Kabelac, "The single-blow transient testing technique for offset and wavy fins of compact plate-fin heat exchangers," *Applied Thermal Engineering*, vol. 111, pp. 1588-1595, 2017.
- [131] Ve-ingenieure. ST05-CNC Stirling engine [Online].
- [132] R. J. Moffat, "Describing the uncertainties in experimental results," *Experimental thermal and fluid science*, vol. 1, pp. 3-17, 1988.
- [133] D. Gedeon and J. Wood, "Oscillating-flow regenerator test rig: hardware and theory with derived correlations for screens and felts," 1996.
- [134] W. M. Kays and A. L. London, "Compact heat exchangers," 1984.
- [135] T. L. Bergman, F. P. Incropera, D. P. DeWitt, and A. S. Lavine, *Fundamentals of heat and mass transfer*: John Wiley & Sons, 2011.
- [136] J. R. Senft, *An introduction to Stirling engines*: Moriya Press, 1993.
- [137] J. R. Senft, "Extended mechanical efficiency theorems for engines and heat pumps," *International Journal of Energy Research*, vol. 24, pp. 679-693, 2000.
- [138] C. Multiphysics, "The Platform for Physics-Based Modeling and Simulation," Available at: <https://www.comsol.com/>, 2015.
- [139] D. A. Nield and A. Bejan, *Convection in porous media*: Springer Science & Business Media, 2006.
- [140] D. Nield, "Effects of local thermal nonequilibrium in steady convective processes in a saturated porous medium: forced convection in a channel," *Journal of porous media*, vol. 1, pp. 181-186, 1998.
- [141] J. G. Schreiber and L. G. Thieme, "Accomplishments of the NASA GRC Stirling technology development project," in *Proceedings of the International Energy Conversion Engineering Conference*, 2004.
- [142] D. Gedeon, "Sage Stirling-Cycle Model-Class Reference Guide," *Gedeon Associates*, vol. 16922, 1999.
- [143] R. C. Tew, T. Simon, D. Gedeon, M. Ibrahim, and W. Rong, "An initial non-equilibrium porous-media model for CFD simulation of Stirling regenerators," in *Proceedings of the 4th International Energy Conversion Engineering Conference*, 2006, pp. 65-77.

- [144] W. Minkowycz, A. Haji-Sheikh, and K. Vafai, "On departure from local thermal equilibrium in porous media due to a rapidly changing heat source: the Sparrow number," *International journal of heat and mass transfer*, vol. 42, pp. 3373-3385, 1999.
- [145] K. Muralidhar and K. Suzuki, "Analysis of flow and heat transfer in a regenerator mesh using a non-Darcy thermally non-equilibrium model," *International journal of heat and mass transfer*, vol. 44, pp. 2493-2504, 2001.
- [146] R. G. Carbonell and S. Whitaker, "Heat and mass transfer in porous media," in *Fundamentals of transport phenomena in porous media*, ed: Springer, 1984, pp. 121-198.
- [147] J. Donea, P. Fasoli-Stella, and S. Giuliani, "Finite element solution of transient fluid-structure problems in Lagrangian coordinates," 1976.
- [148] J. Donéa, P. Fasoli-Stella, and S. Giuliani, "Lagrangian and Eulerian finite element techniques for transient fluid-structure interaction problems," in *Structural mechanics in reactor technology*, ed, 1977.
- [149] T. J. Hughes, W. K. Liu, and T. K. Zimmermann, "Lagrangian-Eulerian finite element formulation for incompressible viscous flows," *Computer methods in applied mechanics and engineering*, vol. 29, pp. 329-349, 1981.
- [150] M. A. Fernández and M. Moubachir, "Sensitivity analysis for an incompressible aeroelastic system," *Mathematical Models and Methods in Applied Sciences*, vol. 12, pp. 1109-1130, 2002.
- [151] C. Multiphysics®, "v5.2 user's guide," *COMSOL AB, Stockholm, Sweden*.
- [152] R. Radebaugh and B. Louie, "A simple, first step to the optimization of regenerator geometry," *Proc. of the 3rd Cryocooler Conf.* pp. 177-198, (SEE N86-11367 02-31), 1985.
- [153] C. Yunus and J. Afshin, "Heat and Mass Transfer: Fundamentals and Applications," ed: Tata McGraw-Hill, New Delhi, India, 2011.
- [154] S. Kakaç, R. K. Shah, and W. Aung, *Handbook of single-phase convective heat transfer*: Wiley, New York, 1987.
- [155] R. K. Shah and A. L. London, *Laminar flow forced convection in ducts: a source book for compact heat exchanger analytical data*: Academic press, 2014.
- [156] H. Hausen, "Darstellung des Wärmeüberganges in Rohren durch verallgemeinerte Potenzbeziehungen," *Z. VDI Beih. Verfahrenstech*, vol. 4, pp. 91-98, 1943.
- [157] J. Hwang, G. Hwang, R. Yeh, and C. Chao, "Measurement of interstitial convective heat transfer and frictional drag for flow across metal foams," *TRANSACTIONS-AMERICAN SOCIETY OF MECHANICAL ENGINEERS JOURNAL OF HEAT TRANSFER*, vol. 124, pp. 120-129, 2002.

- [158] F. Barari, "Metal foam regenerators; heat transfer and pressure drop in porous metals," University of Sheffield, 2014.

APPENDIX A

CALIBRATION OF THERMOCOUPLES

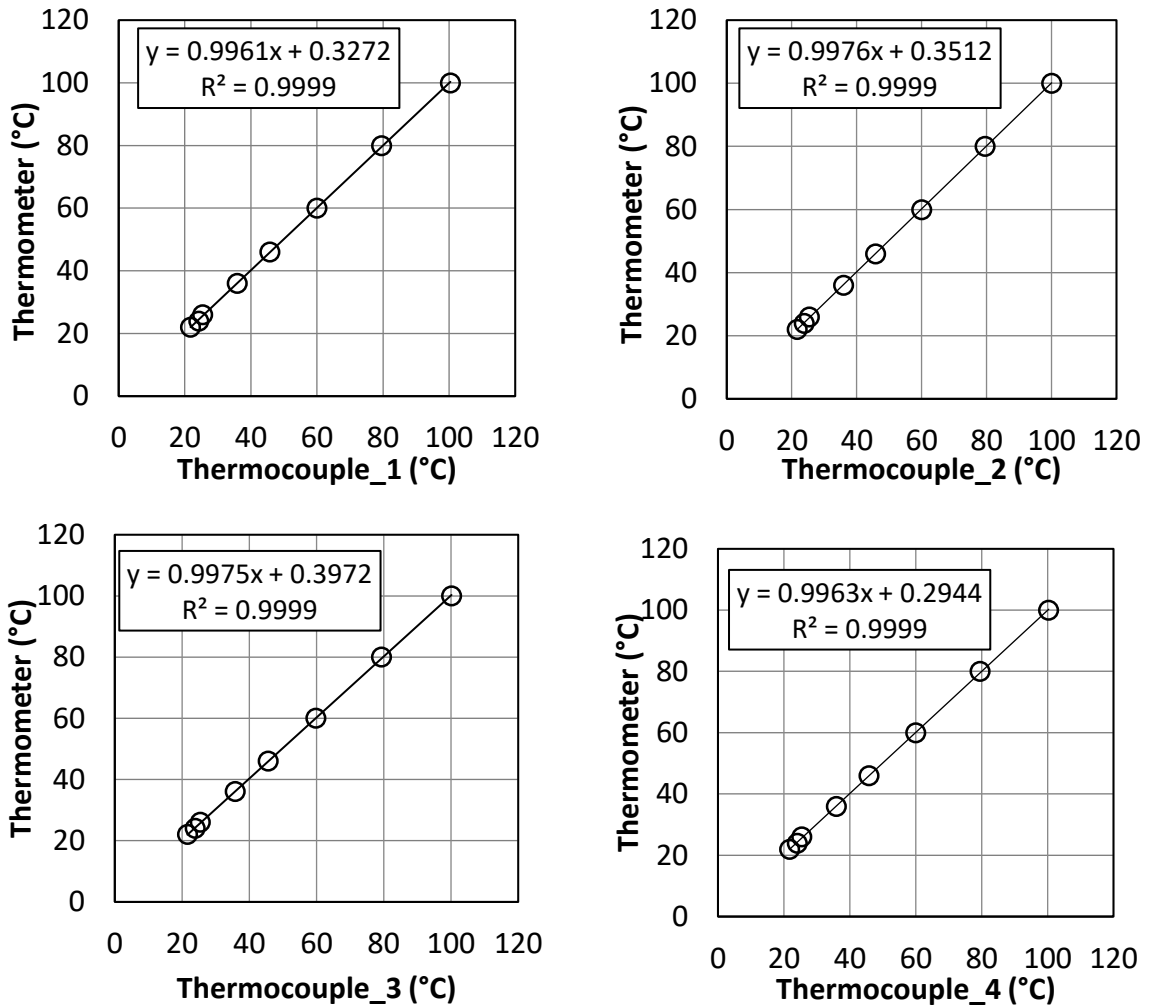


Figure A.1 Relationship between thermocouples readings (inlet of MCRHX) and thermometer readings.

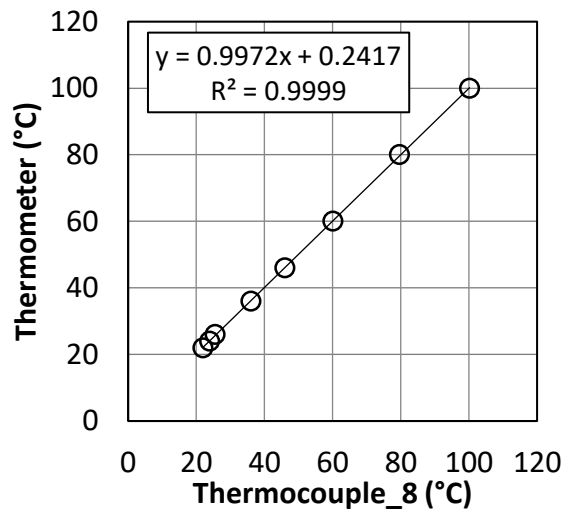
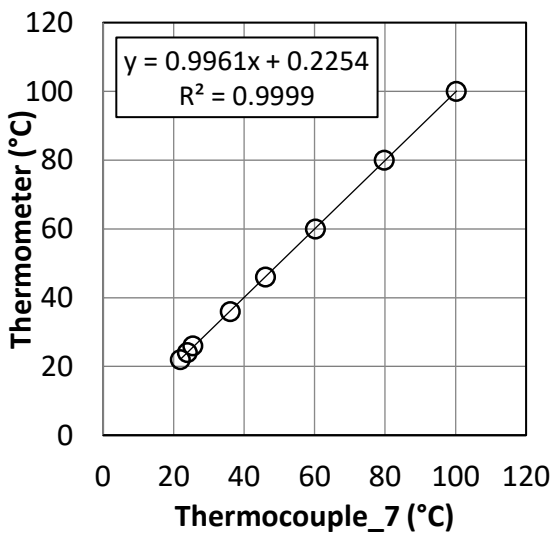
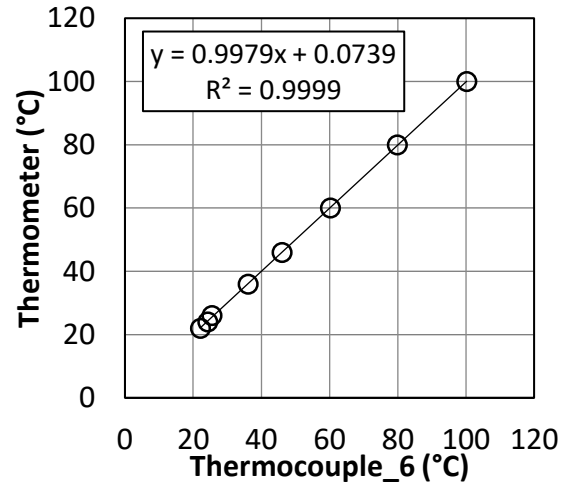
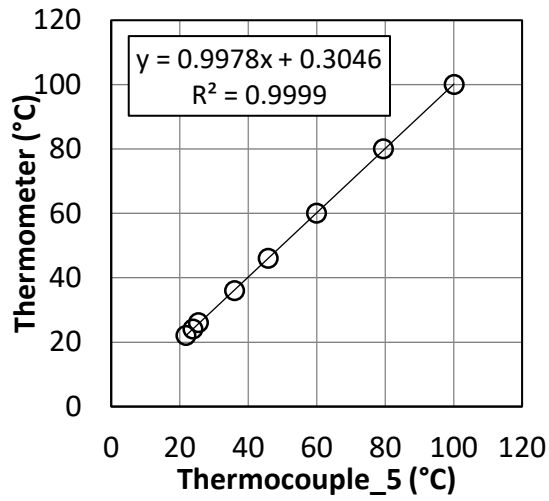


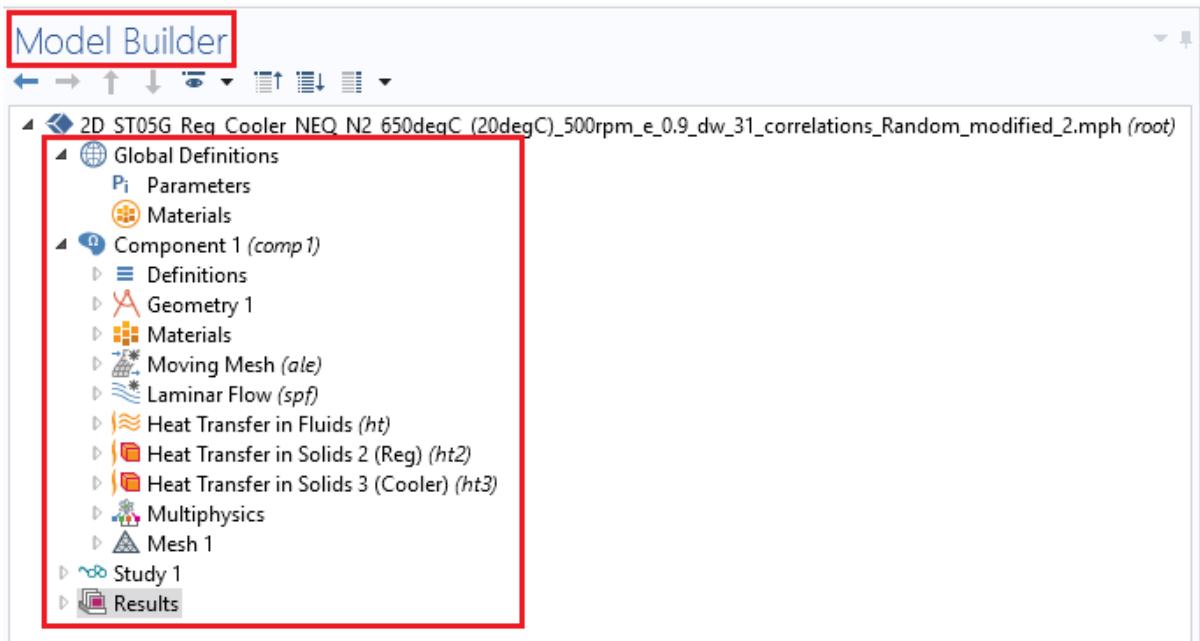
Figure A.2 Relationship between thermocouples readings (outlet of MCRHX) and thermometer readings.

APPENDIX B

SET UP OF CFD MODEL WITHIN COMSOL MULTIPHYSICS

1. Model builder environment

- a) Parameters
- b) Variables
- c) Geometry
- d) Material
- e) Moving mesh
- f) Laminar flow
- g) Heat transfer in fluids
- h) Heat transfer in solids (Regenerator)
- i) Heat transfer in solids (Cooler)
- j) Multiphysics
- k) Mesh
- l) Study (Solution)
- m) Postprocessing (Results)



2. Variables

The screenshot shows the COMSOL Model Builder interface. On the left, the 'Model Builder' tree has 'Variables 1' highlighted with a red box and an arrow pointing to the 'Variables' table in the 'Properties' window on the right.

Name	Expression	Unit	Description
theta	omega*t	rad	
term_e	$\sqrt{1-(\text{lamda_e}^2 \sin(\text{theta})^2)}$		
term_c	$\sqrt{1-(\text{lamda_c}^2 \sin(\text{theta}-\text{alpha})^2)}$		
Xe	$Xe0 - re^*(1 - \cos(\text{theta}) + (1/\text{lamda_e})^2 \sin^2(\text{theta}))$	m	
Xc	$Xc0 - rc^*(1 - \cos(\text{theta}-\text{alpha}) + (1/\text{lamda_c})^2 \sin^2(\text{theta}-\text{alpha}))$	m	
Ue	$d(Xe,t)$	m/s	
Uc	$d(Xc,t)$	m/s	
VVe	$(\text{vswe}/2)^*(1 - \cos(\text{theta}) + (1/\text{lamda_e})^2 \sin^2(\text{theta}))$	m ³	
VVc	$(\text{vswe}/2)^*(1 + \cos(\text{theta}) - (1/\text{lamda_c})^2 \sin^2(\text{theta}-\text{alpha}))$	m ³	
VT	$VVc + VVe + V_off$	m ³	
Re_br	$\text{spf.rho}*(\text{spf.U}/\text{e_sg})*\text{dh}/\text{spf.mu}$		
Cf	$a2^2 * \text{Re_br}^{\text{a3}} / (\text{sqrt}(2^{\text{a1}}))$		
Bf_reg	$\text{Cf} * \text{spf.rho} / \text{sqrt}(\text{kappa_reg})$	kg/m ⁴	
Nu	$(1 + (b1^2 * (\text{Re_br} * \text{Pr})^{\text{b2}}))$		
h_fs	$\text{Nu} * \text{ht.kmean} / \text{dh}$	W/(m ² ·K)	
Power	$\text{intop1}(2 * \text{pi} * y * p * Uc)$	W	
q_reg	$h_fs * a_fs$	W/(m ³ ·K)	

3. Moving mesh set up

The screenshot shows the COMSOL Model Builder interface. On the left, the 'Model Builder' tree has 'Moving Mesh (ale)' highlighted with a red box. On the right, the 'Properties' window shows the settings for the 'Moving Mesh' node.

Moving Mesh

Name: ale

Domain Selection

Selection: All domains

Active: 1, 2, 3, 4, 5, 6

Equation

Frame Settings

Material frame coordinates:

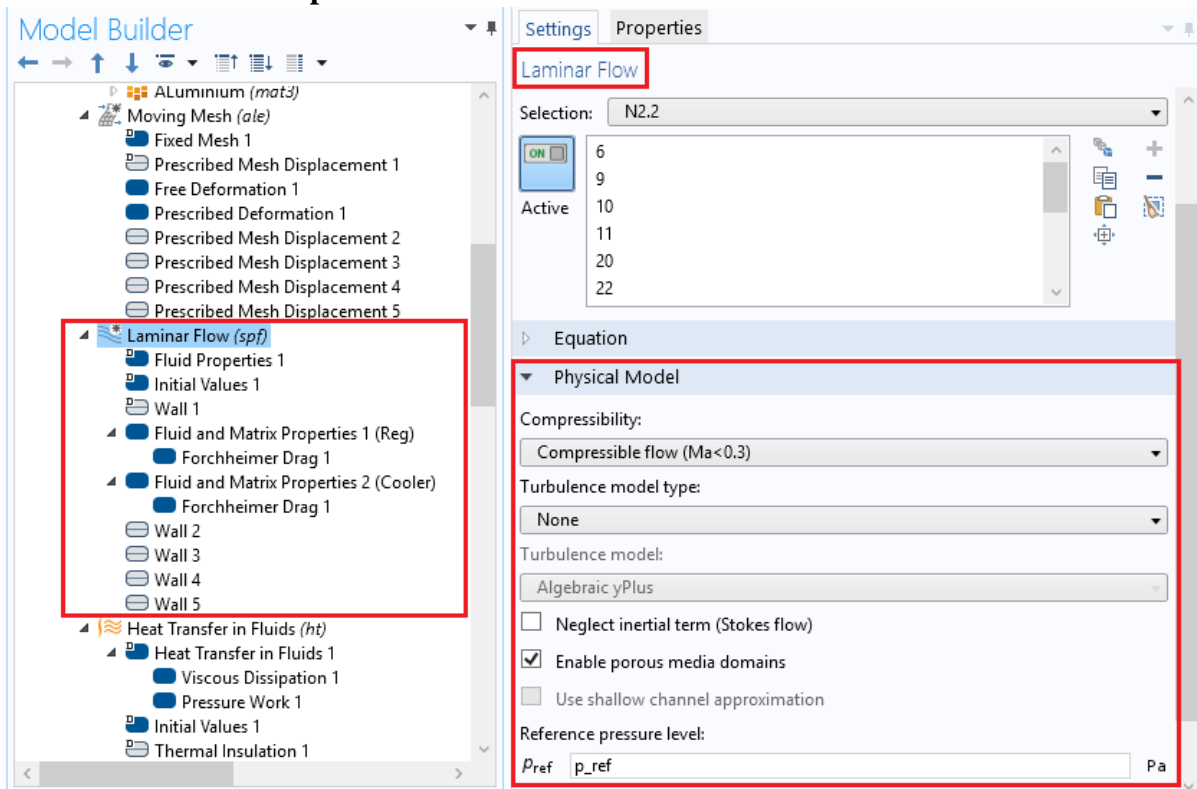
First	Second	Third
X	Y	Z

Geometry shape order: 2

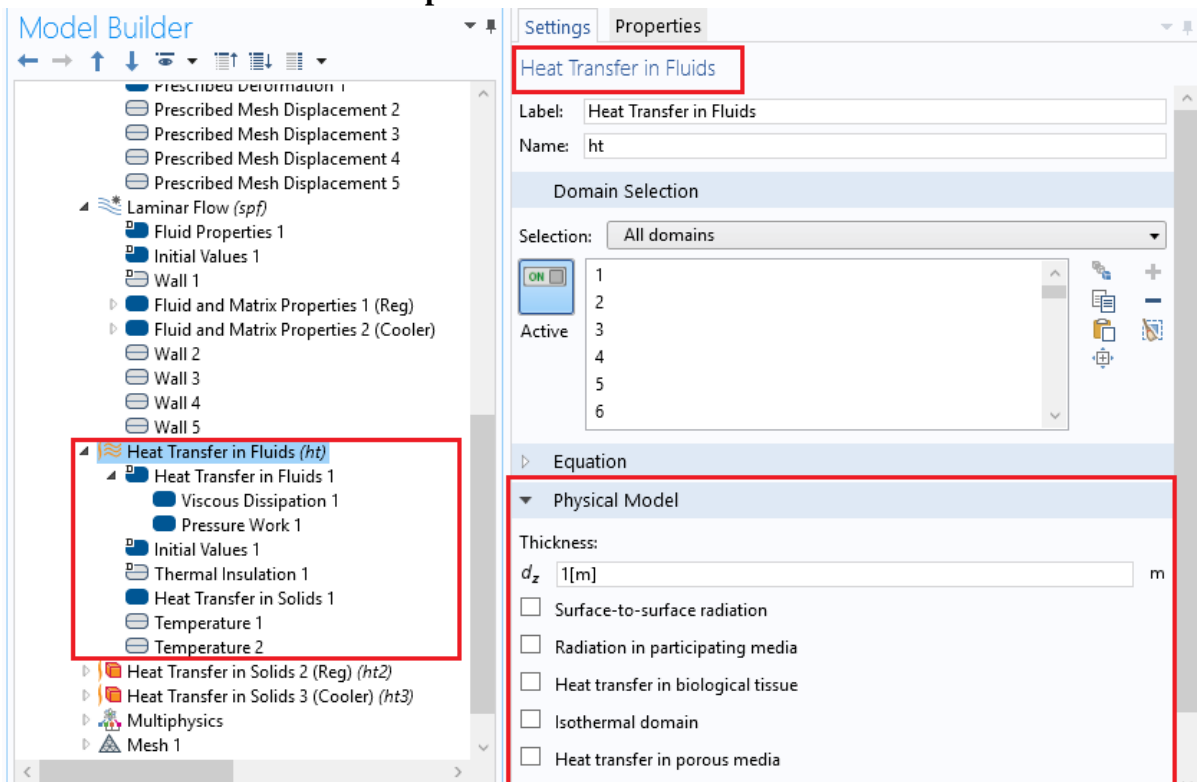
Free Deformation Settings

Mesh smoothing type: Hyperelastic

4. Laminar flow set up



5. Heat transfer in fluids set up



6. Heat transfer in regenerator

Model Builder

Settings Properties

Heat Transfer in Solids

Label: Heat Transfer in Solids 2 (Reg)

Name: ht2

Domain Selection

Selection: Manual

ON 6
40

Active

Equation

Physical Model

Thickness:

d_z 1[m] m

Surface-to-surface radiation

Radiation in participating media

Heat transfer in biological tissue

Isothermal domain

Heat transfer in porous media

7. Heat transfer in cooler

Model Builder

Settings Properties

Heat Transfer in Solids

Label: Heat Transfer in Solids 3 (Cooler)

Name: ht3

Domain Selection

Selection: Manual

ON 11
42

Active

Equation

Physical Model

Thickness:

d_z 1[m] m

Surface-to-surface radiation

Radiation in participating media

Heat transfer in biological tissue

Isothermal domain

Heat transfer in porous media

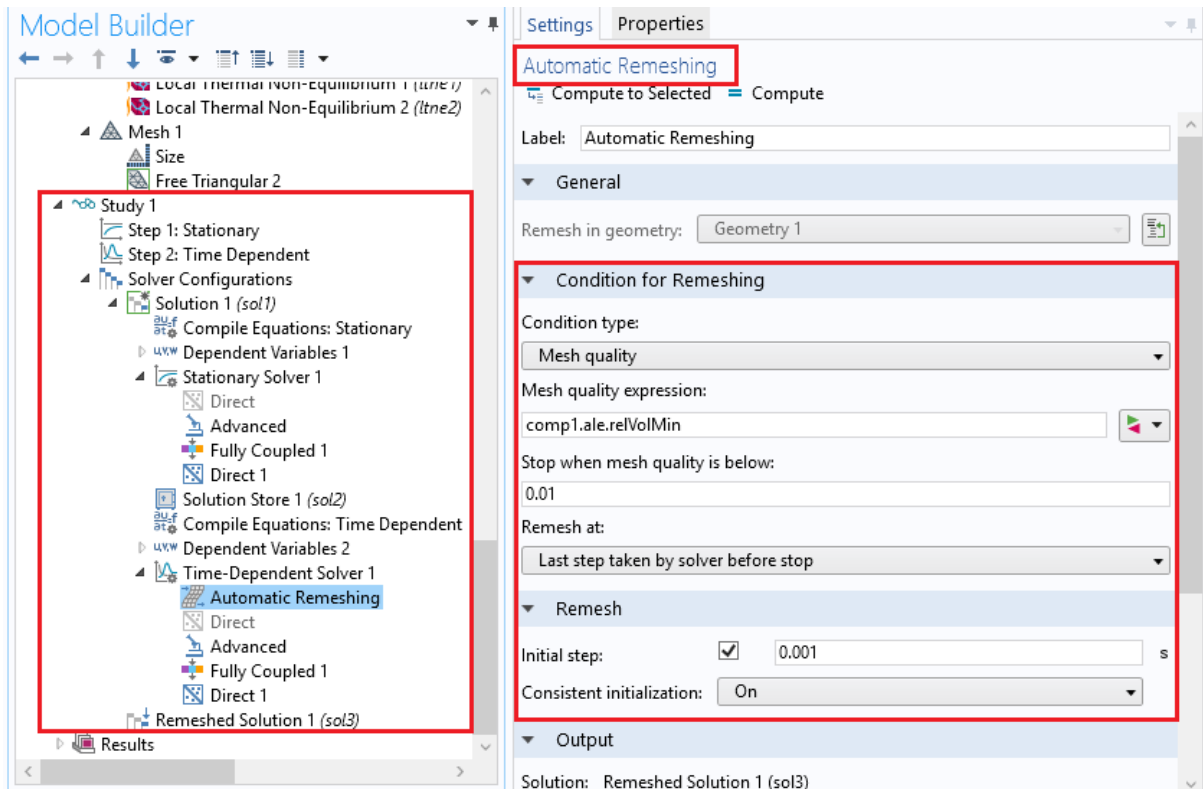
8. Local thermal non-equilibrium (regenerator)

The screenshot shows the COMSOL Multiphysics interface. On the left, the Model Builder tree is visible, with 'Local Thermal Non-Equilibrium 1 (ltne1)' selected under the 'Multiphysics' node. On the right, the 'Settings' pane for 'Local Thermal Non-Equilibrium' is shown. The 'Domain Selection' section has 'Manual' selected, and domains 6 and 40 are listed as 'Active'. The 'Equation' section is expanded to show 'Local Thermal Non-Equilibrium Settings'. The 'Solid volume fraction' is set to $\theta_p = 1 - e_{sg}$ with a value of 1. The 'Interstitial convective heat transfer coefficient' is set to 'User defined' with a variable q_{sf} and units $W/(m^3 \cdot K)$. The 'Coupled Interfaces' section shows 'Heat transfer in solids' set to 'Heat Transfer in Solids 2 (Reg) (ht2)' and 'Heat transfer in fluids' set to 'Heat Transfer in Fluids (ht)'.

9. Local thermal non-equilibrium (cooler)

The screenshot shows the COMSOL Multiphysics interface. On the left, the Model Builder tree is visible, with 'Local Thermal Non-Equilibrium 2 (ltne2)' selected under the 'Multiphysics' node. On the right, the 'Settings' pane for 'Local Thermal Non-Equilibrium' is shown. The 'Domain Selection' section has 'Manual' selected, and domains 11 and 42 are listed as 'Active'. The 'Equation' section is expanded to show 'Local Thermal Non-Equilibrium Settings'. The 'Solid volume fraction' is set to $\theta_p = 1 - e_{sg1}$ with a value of 1. The 'Interstitial convective heat transfer coefficient' is set to 'User defined' with a variable q_{sf} and units $W/(m^3 \cdot K)$. The 'Coupled Interfaces' section shows 'Heat transfer in solids' set to 'Heat Transfer in Solids 3 (Cooler) (ht3)' and 'Heat transfer in fluids' set to 'Heat Transfer in Fluids (ht)'.

10. Automatic Remeshing set up



11. Postprocessing (results)

